Inaugural dissertation

for

obtaining the doctoral degree

of the

Combined Faculty of Mathematics, Engineering and Natural Sciences

of the

Ruprecht - Karls - University

Heidelberg

Presented by

M.Sc. Severina Klaus

Born in Mainz, Germany

Oral examination: 24.10.2022

Deciphering the spatiotemporal organization and regulation of *Plasmodium falciparum* schizogony

Referees: Prof. Dr. Michael Lanzer
Prof. Dr. Friedrich Frischknecht

Summary

Despite decades-long' efforts to combat malaria, it is still responsible for the death of over half a million people each year. All clinical symptoms of malaria are caused by the rapid asexual proliferation of parasites of the genus *Plasmodium* in the blood of patients. Here, *Plasmodium* replicates via schizogony: an atypical form of replication, where nuclei multiply asynchronously. Only once approximately twenty nuclei are formed, daughter cells assemble. However, the coordination of DNA replication and nuclear division as well as the molecular determinants of asynchronous nuclear multiplication are unknown.

In my thesis, I investigated the organization and regulation of asynchronous nuclear multiplication during schizogony in *Plasmodium falciparum* (*P. falciparum*), which causes the most severe form of human malaria. I first determined that *P. falciparum* proliferates via alternating rounds of DNA replication and nuclear division, with nuclei seemingly acting as 'cells-within-cells'. By showing that the episomally expressed replication fork protein PCNA1::GFP transiently accumulates only in those nuclei that undergo DNA replication, I established a marker for DNA replication compatible with life-cell imaging. In combination with the marker 3xNLS::mCherry for the nuclei, imaging of PCNA1::GFP allowed me to track DNA replication and nuclear division in nuclei of single parasites as they underwent schizogony. I then quantified the overall dynamics of nuclear multiplication as well as the dynamics and organization of the individual DNA replication and nuclear division events. To establish a mathematical model of nuclear multiplication, I collaborated with P. Binder, showing that DNA replication is influenced by a limiting factor and that asynchronous nuclear divisions enable rapid parasite proliferation. I also investigated the molecular basis of the transient accumulation of PCNA1::GFP in nuclei during S-phase and found that this is most likely caused by association of PCNA1 with the DNA during replication. As PCNA1 shuttles between the cytoplasm and the nucleus, I also analyzed sequence motifs potentially important for the nucleo-cytoplasmic transport of PCNA1 and found that PCNA1 may contain a classical nuclear export signal (NES), which should facilitate nuclear export via the export receptor exportin-1. Yet, this NES may not be functional, as chemical inhibition of exportin-1 in an engineered cell line which is sensitive to the exportin-1 inhibitor leptomycin B (LMB), did not affect nuclear accumulation or export of PCNA1::GFP.

Together, I characterized the spatiotemporal organization of nuclear multiplication, defining the basic organization and regulation of the cell cycle in *P. falciparum* in the blood stage of infection. This may not only help to uncover novel targets for malaria intervention but also to expand our understanding of the unusual cell cycle biology of an early-branching eukaryote.

Zusammenfassung

Trotz jahrzehntelangen Anstrengungen Malaria zu bekämpfen, ist sie immer noch für den Tod von mehr als einer halben Million Menschen pro Jahr verantwortlich. Alle klinischen Malaria Symptome werden durch die schnelle asexuelle Vermehrung von Parasiten des Genus *Plasmodium* im Blut der Patienten verursacht. Dabei vermehrt sich *Plasmodium* durch Schizogonie: eine atypische Form der Replikation, bei der sich die Kerne asynchron vermehren. Erst wenn etwa zwanzig Kerne vorliegen, bilden sich Tochterzellen. Die Koordination von DNA-Replikation und Kernteilung sowie die molekularen Determinanten der asynchronen Kernvermehrung sind jedoch unbekannt.

In meiner Dissertation untersuchte ich die Organisation und Regulierung der asynchronen Kernvermehrung während der Schizogonie im Parasiten *Plasmodium falciparum* (*P. falciparum*), der die schwerste Form der humanen Malaria verursacht. Zunächst stellte ich fest, dass sich *P. falciparum* durch abwechselnde Runden von DNA-Replikation und Kernteilung vermehrt, wobei die Kerne anscheinend wie "Zellen in Zellen" agieren. Durch den Nachweis, dass sich das episomal exprimierte Replikationsgabelprotein PCNA1::GFP vorübergehend nur in den Kernen anreichert, die eine DNA-Replikation durchlaufen, konnte ich einen Marker für die DNA-Replikation etablieren, der mit der Mikroskopie von Lebendzellen kompatibel ist. In Kombination mit dem Marker 3xNLS::mCherry für die Zellkerne konnte ich über die Mikroskopie von PCNA1::GFP die DNA-Replikation und Kernteilung in den Kernen einzelner Parasiten während der Schizogonie verfolgen. Ich habe dann die Gesamtdynamik der Kernvermehrung sowie die Dynamik und Organisation der einzelnen DNA-Replikations- und Kernteilungsereignisse quantifiziert. Um ein mathematisches Modell der Kernvermehrung zu erstellen, arbeitete ich mit P. Binder zusammen und zeigte, dass die DNA-Replikation durch einen limitierenden Faktor beeinflusst wird und dass asynchrone Kernteilungen eine schnelle Vermehrung der Parasiten ermöglichen. Ich untersuchte auch die molekulare Grundlage der vorübergehenden Akkumulation von PCNA1::GFP in Kernen während der S-Phase und fand heraus, dass diese wahrscheinlich durch die Assoziation von PCNA1 mit der DNA während der Replikation verursacht wird. Da PCNA1 zwischen Zytoplasma und Zellkern pendelt, analysierte ich auch Sequenzmotive, die für den nukleo-zytoplasmatischen Transport von PCNA1 wichtig sein könnten, und fand heraus, dass PCNA1 ein klassisches Kernexportsignal (NES) enthält, das den Kernexport über den Exportrezeptor exportin-1 ermöglichen sollte. Dieses NES ist jedoch möglicherweise nicht funktionell, da die chemische Hemmung von Exportin-1 in einer gentechnisch veränderten Zelllinie, die gegenüber dem Exportin-1-Inhibitor Leptomycin B (LMB) empfindlich ist, die nukleäre Akkumulation und den Export von PCNA1::GFP nicht beeinflusste.

Zusammenfassend habe ich die räumliche und zeitliche Organisation der Kern-vermehrung charakterisiert und die grundlegende Organisierung und Regulierung des Zellzyklus in *P. falciparum* während des Blutstadiums der Infektion definiert. Dies könnten nicht nur dazu beitragen, neue Angriffspunkte für Malaria-bekämpfung zu finden, sondern auch unser Verständnis der ungewöhnlichen Zellzyklusbiologie eines frühen Eukaryoten zu erweitern.

Abbreviations

µl (unit)	Microliter
µM (unit)	Micromolar
3D	3 dimensional
A (nucleobase)	Adenine
A (amino acid)	Alanine
ACT	Artemisinin-based combination therapy
Amp	Ampicillin
Apo	Apochromat
Ark	Aurora-related kinases
A. gossypii	*Ashbya gossypii*
bp	Base pairs
BSD	Blasticidin S Deaminase
C (nucleobase)	Cytosine
C (amino acid)	Cysteine
Cam	Calmodulin
CDC	Cell division control
CDK	Cyclin-dependent kinase
Cdt1	Chromatin licensing and DNA replication factor 1
CINCH	Coordinator of nascent cell detachment
CLEM	Correlative light and electron microscopy
CMG	CDC45, MCM, GINS
CRISPR	Clustered regularly interspaced short palindromic repeats
CRK	CDK-related kinase
cRPMI	Complete RPMI
DDK	Dbf4-dependent kinase
DHFR	Dihydrofolate reductase
DIC	Differential interference contrast
DLS	Dynamic light scattering
DMSO	Dimethyl sulfoxide
DNA	Deoxyribonucleic acid
DPBS	Dulbecco's phosphate-buffered saline
DPSS	Diode pumped solid state
DTT	Dithiothreitol
E. coli	*Escherichia coli*
e.g.	For example
EDTA	Ethylenediaminetetraacetic acid
eGFP	enhanced GFP
EGTA	Ethylene glycol-bis(β-aminoethyl ether)-N,N,N′,N′-tetraacetic acid
EM	Electron microscopy
EM-CCD	Electron-multiplying charge-coupled device
ER	Endoplasmic reticulum
ERC	Endoplasmic reticulum-resident calcium-binding protein
F (amino acid)	Phenylalanine
F (unit)	Farad
Fen	Flap endonuclease
Fiji	Fiji is just ImageJ
FP	Forward primer
FRAP	Fluorescence recovery after photobleaching
FUCCI	Fluorescent Ubiquitination-based Cell Cycle Indicator

G (nucleobase)	Guanine
G1	Gap 1 phase
G2	Gap 2 phase
GFP	Green fluorescent protein
GINS complex	Go-Ichi-Ni-San complex
GO	Gene ontology
gRNA	Guide RNA
GS	Glycine-serine
h (unit)	Hour
h (species)	Human
H (protein)	Histone
HC	Harmonic Compound
HeNe	Helium-Neon
HEPES	4-(2-hydroxyethyl)-1-piperazineethanesulfonic acid
hpi	Hours post invasion
Hsp	Heat shock protein
I (amino acid)	Isoleucine
IC_{50}	Half maximal inhibitory concentration
i.e.	That is
IFA	Immunofluorescence assay
iRBC	Infected RBC
iRPMI	Incomplete RPMI
K (amino acid)	Lysine
kb	Kilobase
l (unit)	Liter
LB	Lysogeny broth
LC-MS	Liquid chromatography–mass spectrometry
LMB	Leptomycin B
LSM	Laser scanning microscopy
M (amino acid)	Methionine
M (unit)	Molar
MCM	Minichromosome maintenance protein
min (unit)	Minute
ml (unit)	Milliliter
MORN	Membrane occupation and recognition nexus
Nek	NimA-related kinase
NES	Nuclear export sequence
NimA	Never in mitosis A
NLS	Nuclear localization signal
NP-40	Nonidet-40
ORC	Origin recognition complex
P. falciparum	*Plasmodium falciparum*
POI	Protein of interest
SDS-PAGE	Sodium dodecyl sulfate polyacrylamide gel electrophoresis
PAM	Protospacer adjacent motif
PBS	Phosphate-buffered saline
PCNA	Proliferating cell nuclear antigen
PCR	Polymerase chain reaction
Pf	*Plasmodium falciparum*
PK5	Protein Kinase 5

PL	Field planarity
Pol	Polymerase
Pre-IC	Pre-initiation complex
Pre-RC	Pre-replication complex
RBC	Red blood cell
RFC	Replication factor C
RIPA	Radioimmunoprecipitation assay
RNA	Ribonucleic acid
ROI	Region of interest
RP	Reverse primer
RPA	Replication protein A
RPMI medium	Roswell Park Memorial Institute medium
RT	Room temperature
S (amino acid)	Serine
SDS	Sodium dodecyl sulfate polyacrylamide
sec (unit)	Second
SIM	Structured illumination microscopy
SINE	Selective inhibitors of nuclear export
SiR	Silicon-rhodamine
Sld	Synthetic lethality with dpb11
T (nucleobase)	Thymine
TAE	Tris-acetate-EDTA
TAP	Transporter associated with antigen processing
TE	Tris-EDTA
UTR	Untranslated region
UV	Ultraviolet
V (unit)	Volt
WT	Wild type
XPO-1	Exportin-1
Y (amino acid)	Tyrosine
γ-TuRC	γ-Tubulin ring complex

List of Figures

List of Tables

Content

1 Introduction

"Malaria penetrates you bones with the bread that you eat and every time you open your mouth to speak, […] For malaria seizes the inhabitants in the empty lane or strikes them down by the sun-bleached house door, shaking with fever in their overcoats, with all the blankets in the house heaped upon their shoulders […]"

Giovanni Verga, Novelle Rusticane 1883 (M.J. Dobson, the malariology centenary, Parassitologia 1999)

No other illness has had such a profound effect on humanity as malaria. The history of the modern human is tightly intertwined with that of malaria, with some scientists estimating that malaria is responsible for the death of half of all humans that ever lived (Whitfield, 2002). Apart from its impact on human society, malaria is considered one of the strongest drivers for the development of inheritable diseases in humans and implicated in the evolution of many blood cell abnormalities such as sickle-cell disease, thalassemia and glucose-6-phosphatase deficiency, which are protective against malaria (Carter and Mendis, 2002; Kwiatkowski, 2005).

Malaria is caused by protozoan parasites of the genus *Plasmodium* that infect the red blood cells of their vertebrate hosts (Laveran, 1881). Human-infecting malaria parasites are transmitted through the bite of female mosquitoes of the genus *Anopheles* (Grassi, 1900), which are found on all continents except Antarctica (Sinka, 2013). Even today half of the world's population is at risk for malaria (World Health Organisation, 2021), despite decades' worth of effort to eradicate both mosquito vectors and the parasites themselves, and malaria is still the sixth leading cause of death in low-income countries (World Health Organisation, 2020), causing a significant economic burden (Sachs and Malaney, 2002; Gollin and Zimmermann, 2021).

The first malaria vaccine was approved in 2021, but its efficacy is limited, with protection rates as low as 4% in infants and young children (Olotu *et al.*, 2016). Current strategies to combat malaria are centred around reducing exposure to the mosquito vectors through distribution of bed nets, chemoprophylaxis for vulnerable demographic groups, and fast-acting treatment of active infections (World Health Organisation, 2021). Currently, treatment for malaria relies on artemisinin-based combination therapies (ACT), where fast acting artemisinin-based compounds are administered together with slow-acting partner drugs to clear any remaining parasites that may not have been eliminated by artemisinin (Nosten and White, 2007). Historically, introduction of any front-line therapeutics resulted in – oftentimes rapid – development of parasite resistance, and the same trend can be observed for ACT (Blasco, Leroy and Fidock, 2017; World Health Organisation, 2021). Surveillance of parasite populations and treatment outcomes shows delayed clearance of parasites during treatment with artemisinin-based compounds is occurring in South-East Asia and sub-Saharan Africa (Ndwiga *et al.*, 2021; Siddiqui, Liang and Cui, 2021; World Health Organisation, 2021). Additionally, resistance against many partner drugs is emerging in the same areas (World Health Organisation, 2021). In combination with spreading insecticide resistance among mosquito populations in Africa (World Health Organisation, 2021), this development has contributed to an increase in global malaria cases and deaths for

the first time in two decades (World Health Organisation, 2021; Cohen, Okumu and Moonen, 2022). It is therefore of critical importance to uncover new targets for medical intervention in order to develop new strategies against the spread of *Plasmodium*. The fight against malaria is complicated by the complex biology of the *Plasmodium* parasite, which is divergent to many model organisms. Consequently, many fundamental aspects of *Plasmodium* biology remain unknown.

1.1 History of malaria and *Plasmodium*

Parasites of the genus *Plasmodium* are members of the order Haemosporida, which are ancient unicellular organisms whose ancestors branched off early during the evolution of eukaryotic life (Janouskovec *et al.*, 2019). *Plasmodium* parasites evolved to infect a wide range of vertebrates, including lizards, birds, rodents, ungulates and finally primates (Outlaw and Ricklefs, 2011). Over thousands of years, five of the over 200 of *Plasmodium* species have evolved to infect humans: *Plasmodium falciparum*, *Plasmodium vivax*, *Plasmodium malariae*, *Plasmodium ovale* and *Plasmodium knowlesi* (Sato, 2021). Of these five species, *Plasmodium vivax* (*P. vivax*) and *Plasmodium falciparum* (*P. falciparum*) have had the most impact on human evolution and are still responsible for the majority of the disease burden today, causing an estimated 95% of all malaria cases (World Health Organisation, 2021).

P. falciparum represents the deadliest of the human-infecting *Plasmodium* species, causing over half a million deaths per year today (World Health Organisation, 2021). Although the exact timing of the emergence of *P. falciparum* in human populations is still debated, it is estimated that *P. falciparum* parasites jumped from African great apes to humans sometime between 10,000-60,000 years ago (Liu *et al.*, 2010; Loy *et al.*, 2017). Around 10,000 years ago, *P. falciparum* then experienced a drastic expansion of its population (Tanabe *et al.*, 2010; Rougeron *et al.*, 2022). This timing coincides with the development of warmer climate and agricultural societies following the onset of the Holocene Epoch, which mankind is still experiencing today (Carter and Mendis, 2002). Following the jump to humans, *P. falciparum* rapidly spread across the world, even reaching more temperate regions such as Britain, North America and Northern China (Packard, 2011). The characteristic febrile diseases caused by *Plasmodium* parasites are well-documented among historical texts: in the Han dynasty Chinese physicians talked about recurring paroxysmal fevers in the ancient medical text *Huangdi Neijing* (Cox, 2002) while in ancient Greece Hippocrates already divided fevers according to their periodicity (Pappas, Kiriaze and Falagas, 2008). Later, these diseases eventually came to be known as ‘bad air’ or ‘mala’aria’ in ancient Italian, in reference to theories that they were caused by harmful swamp vapours (Hempelmann and Krafts, 2013).

Early malaria research was characterized by a series of key discoveries (Cox, 2010; Hentzschel and Frischknecht, 2022). In 1880, the French physician Charles Louis Alphonse Laveran first observed *Plasmodium* parasites within the red blood cells of patients suffering from malaria (Laveran, 1881). While his discovery was controversial at first, it gained acceptance in the following years and opened the door for further studies. From 1882 to 1890, using a combination of the recently invented oil immersion objective and eosin staining of blood smears, the Italian

scientists Marchiafava, Bignami and Golgi characterised the parasite blood stages further and assigned different clinical manifestations to different *Plasmodium* species (Grassi, 1900; Cox, 2010). Yet, how the parasites are transmitted from person to person remained a mystery for several years more. Finally, thanks to the efforts of the British military doctor Ross and the Italian scientist Grassi, mosquitoes were implicated as *Plasmodium* vectors. In 1897 Ross demonstrated that mosquitoes of the genus *Culex* can transmit avian malaria parasites, but he was not able to proof the same in humans at the time (Ross, 1897). Instead, in 1898 Grassi and Bignami finally showed that mosquitoes of the genus *Anopheles* transmit human-infecting *Plasmodium* parasites, and over the next two years completed the rudimentary *Plasmodium* life cycle (Grassi, 1900). From then on, a large and still-ongoing effort began to uncover all remaining facets of the *Plasmodium* life cycle.

1.2 The complex life cycle of *P. falciparum*

Today, we know that a *P. falciparum* infection starts with the bite of an infected, female *Anopheles* mosquito (Fig. 1, 1) (Cowman et al., 2016). As the mosquito proboscis is entered into the dermis of the human host in search for a blood vessel, saliva containing motile, extracellular parasite stages called sporozoites is released (Frischknecht and Matuschewski, 2017). Once deposited into the skin, these sporozoites actively move through the epithelium to find a blood vessel (Frischknecht and Matuschewski, 2017). When a sporozoite enters the blood stream, it is transported to the liver, where it adheres to sinusoid liver cells, crosses the sinusoidal barrier and finally invades a suitable hepatocyte (Cowman *et al.*, 2016).

During hepatocyte invasion, the parasite establishes a parasitophorous vacuole, an intracellular membrane-delimited compartment in which the parasite will reside during all of this so-called liver stage development (Fig. 1, 2) (Cowman *et al.*, 2016). Over the next twelve days the parasite grows drastically in size. Liver stage development culminates in the formation of up to 90,000 daughter cells through a process called schizogony (Vaughan *et al.*, 2012; Vaughan and Kappe, 2017). Schizogony is an atypical form of replication, characterized by the occurrence of multiple rounds of nuclear division without cell division, resulting in the development of a multinucleated, polyploid cell (Vaughan and Kappe, 2017). During liver stage schizogony, genome amplification starts as early as two days post invasion and continues until up to tens of thousands new genome copies are produced (Cowman *et al.*, 2016; Vaughan and Kappe, 2017). At the end of the liver stage development, hundreds of daughter cells are formed by cytokinesis and released to the blood stream within large membrane enclosed bags called merosomes (Sturm *et al.*, 2006). Subsequently, merosomes are most likely disrupted by passage through the small blood vessels of the lungs, releasing the infectious daughter cells, called merozoites, into the blood stream (Baer *et al.*, 2007).

This release of merozoites marks the onset of the only clinically relevant stage of the *Plasmodium* life cycle, the so-called blood stage (Fig. 1, 3) (Cowman *et al.*, 2016). Here *P. falciparum* merozoites invade circulating red blood cells, again residing in a parasitophorous vacuole where they develop for approximately 48 hours (Cowman *et al.*, 2016). Again replicating by schizogony, cells initiate nuclear

multiplication towards the last quarter of the blood stage cycle, which culminates in the formation of approximately 20 daughter cells called merozoites (Simon, Stürmer and Guizetti, 2021). At the end of each blood stage cycle, first the parasitophorous membrane and then the red blood cell membrane is lysed, leading to the explosive release of the merozoites (Tan and Blackman, 2021). Thus freed, merozoites then invade new red blood cells, starting the asexual replication cycle anew.

During the blood stage of infection, a low percentage of parasites switch to sexual development (Fig. 1, 4) (Carter *et al.*, 2013). Sexual conversion depends on a combination of environmental and parasite intrinsic factors, with, e.g., high parasitaemia leading to higher sexual conversion rates (Carter *et al.*, 2013; Singh *et al.*, 2021). Sexual development predominantly takes place over a period of approximately fifteen days in the bone marrow, where the morphologically distinct stage I-IV gametocytes are sequestered (Venugopal *et al.*, 2020). At the end of this process, mature stage V gametocytes re-enter the peripheral blood circulation (Venugopal *et al.*, 2020).

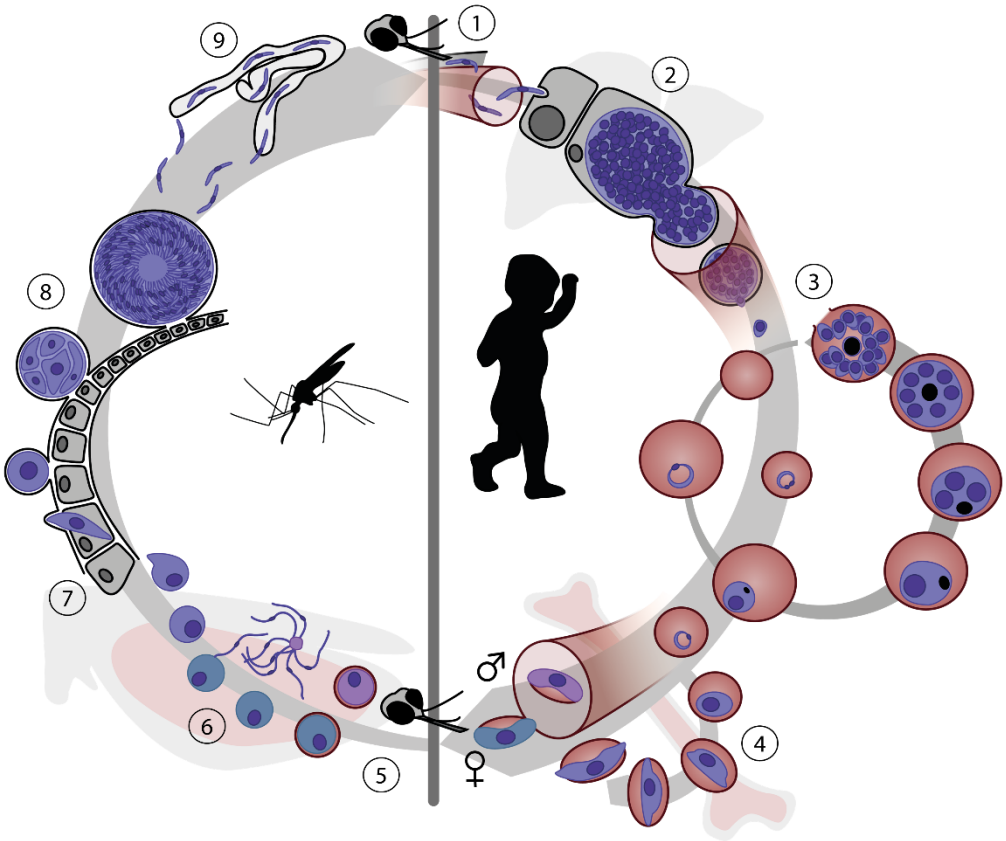

Figure 1 The* P. falciparum *life cycle. *Schematic rendering of the* P. falciparum *life cycle and its stages in the mosquito (left) and human (right) host. 1, mosquito to human transmission; 2, liver stage (liver); 3, blood stage (blood stream); 4, gametocyte development (bone marrow); 5, human to mosquito transmission; 6, gametocyte activation and fertilisation (midgut lumen); 7, ookinete stage; 8, oocyst stage (midgut lining); 9, sporozoite stage (salivary glands).*

Mature male and female gametocytes may be taken up during the blood meal of a female *Anopheles* mosquito (Fig. 1, 5) (Singh *et al.*, 2021). Within the midgut lumen of the mosquito, the change in environmental conditions rapidly causes gametocyte activation, which leads to initiation of DNA replication and formation

of male gametes (Fig. 1, 6) (Singh *et al.*, 2021). Male and female gametes fuse to fertilize, which includes nuclear fusion and meiotic DNA replication, leading to the formation of a tetraploid zygote (Smith and Barillas-Mury, 2016; Singh *et al.*, 2021). Zygotes then further differentiate into motile ookinetes, which are able to penetrate the matrix surrounding the blood bolus and traverse the midgut epithelium (Fig. 1, 7) (Singh *et al.*, 2021). Eventually ookinetes settle between the basal lamina and the midgut epithelium, encysting and transforming into an oocyst (Singh *et al.*, 2021). During the next 1-2 weeks, the oocysts grows and parasite genomes are replicated dozens of times, until hundreds of sporozoites are formed and eventually egress from the oocyst (Fig. 1, 8) (Singh *et al.*, 2021; Hentzschel and Frischknecht, 2022). Freed from the oocyst, sporozoites enter the circulating haemolymph system of the mosquito, eventually passing by and invading the salivary glands (Fig. 1, 9) (Frischknecht and Matuschewski, 2017). There, the sporozoites further mature and become infectious (Matuschewski, 2006). Finally, during the next blood meal of their mosquito host, they will be deposited into the skin of another human host, starting a new *P. falciparum* infection (Matuschewski, 2006; Frischknecht and Matuschewski, 2017).

1.3 *P. falciparum* pathogenesis

"*The malaria infection is produced by a parasite sui generis which invades the red corpuscles, lives within them, and is developed at the expense of their substance, converting their haemoglobin into melanin (now known as haematin), and which multiplies by fission.*"

Russell, 1955 (M.J. Dobson, the malariology centenary, Parassitologia 1999)

Despite its complex live cycle involving many different stages in the human host, only the *Plasmodium* blood stage causes disease symptoms (Fig. 1 and Fig. 2) (Cowman *et al.*, 2016). After the initial invasion of a red blood cell (RBC), *P. falciparum* develops into a so-called ring stage, a small parasite form with a flexible cell shape (Fig. 2) (Grüring *et al.*, 2011). Over time the parasite develops into the trophozoite stage, a transition that is marked by reduced flexibly and the visible appearance of hemozoin – a crystalline degradation product of haemoglobin digestion – at around 24 hpi (Fig. 2) (Grüring *et al.*, 2011).

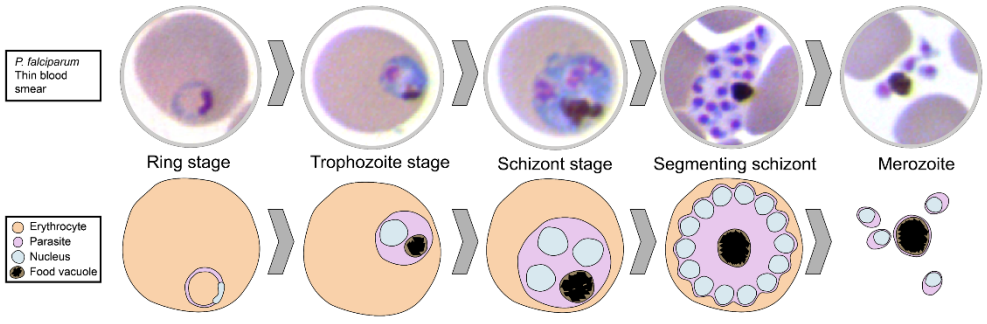

***Figure 2 Blood stage of* P. falciparum.** *Upper panel, single* P. falciparum *parasites infecting circulating red blood cells, as seen via Giemsa staining of thin blood smears. Lower panel, schematic rendering of stages shown in upper panel.*

The last stage of the intra-erythrocytic development is the schizont stage, which is usually considered to start around 30-36 hpi with the first nuclear division and the

appearance of multiple nuclei within the cytoplasm (Fig. 2) (Francia and Striepen, 2014). Intraerythrocytic parasite development is accompanied by an approximately 7-fold increase in parasite size, and culminates in the formation of on average 20±3 daughter cells which are freed by RBC lysis (Fig. 2) (Waldecker *et al.*, 2017; Simon, Stürmer and Guizetti, 2021; Tan and Blackman, 2021).

During the blood stage of infection, the parasite population expands exponentially, leading to significant loss of circulating RBCs (Milner, 2018; Moxon *et al.*, 2020). Loss of RBCs causes anaemia and compromised oxygen delivery, while the release of host cell and parasite material during egress results in an immunological response leading to the characteristic fever patterns observed during malaria (Milner, 2018; Moxon *et al.*, 2020). The key aspects, however, of malaria pathology are related to direct changes of the RBC architecture during infection (Cowman *et al.*, 2016; Milner, 2018; Moxon *et al.*, 2020). Circulating RBCs are subject to a rigorous quality control system that ensures the removal of abnormal RBCs in the spleen (Li *et al.*, 2021). Parasite growth within infected RBCs (iRBCs) causes deformation of the RBC, eventually resulting in the removal of iRBCs from the circulation (Waldecker *et al.*, 2017; Moxon *et al.*, 2020). To avoid clearance in the spleen, *P. falciparum* exports hundreds of proteins to the host RBC, which ultimately form adhesive structures at the RBC surface (Cowman *et al.*, 2016). Adhesion of the iRBC at endothelial cells leads to a sequestration of *P. falciparum* infected RBCs in different tissues such as heart, lung, liver, kidney, subcutaneous tissues, placenta and the brain, depending on which type of adhesion molecules are expressed (Cowman *et al.*, 2016; Milner, 2018; Moxon *et al.*, 2020). Adherence of iRBCs in the vasculature of the brain is especially dangerous and can cause cerebral malaria, where, among other things, a combination of vascular obstruction and inflammation can result in cerebral swelling leading to brainstem herniation and respiratory arrest (Taylor *et al.*, 2004; Seydel *et al.*, 2015).

1.4 *P. falciparum* blood stage replication

"For many years I have held the opinion that the intermittent fevers are produced by parasites which renew the paroxysm by the act of their reproduction, which occurs more or less rapidly according to their different species."

Bassi, 1846 (M.J. Dobson, the malariology centenary, Parassitologia 1999)

During a *P. falciparum* infection, disease outcome is intimately linked with parasite burden, which in turn is dependent on parasite replication (Dondorp *et al.*, 2005; Wassmer *et al.*, 2015). Over the course of its life cycle, *P. falciparum* passes through several bottlenecks, which decrease parasite numbers substantially, requiring a subsequent massive expansion of the parasite population (Fig. 1). These bottlenecks occur during both instances of host switching (Fig. 1) (Smith, Vega-Rodríguez and Jacobs-Lorena, 2014; Graumans *et al.*, 2020). Transmission of gametocytes results in less than ten oocysts on average per mosquito and is followed by a large replication event during sporogony to replenish parasite numbers (Graumans *et al.*, 2020; Singh *et al.*, 2021). Similarly, during transmission from mosquito to human, only very few (on average 10) parasites are transmitted (Graumans *et al.*, 2020). Subsequently, two replicative events take place in the human host (Cowman *et al.*, 2016). The first is in the liver prior to release of

parasites to the circulating blood system (Fig 1) (Vaughan and Kappe, 2017). The second is during the blood stage (Fig. 1 and 2), where repeated asexual replication cycles expand the parasite population exponentially in order to reach parasite densities high enough for gametocytes to be reliably passed to a mosquito during a blood meal (Carter *et al.*, 2013). In the liver and blood stage, *P. falciparum* replicates via schizogony, a divergent form of replication involving repeated rounds of mitosis without cytokinesis (Francia and Striepen, 2014; Vaughan and Kappe, 2017). Only at the end of schizogony cytokinesis is initiated, where nuclei are divided one last time and concomitantly packaged into daughter cells (Rudlaff *et al.*, 2020).

While liver schizogony is not well characterized, blood stage schizogony is comparatively better understood (Leete and Rubin, 1996; Francia and Striepen, 2014). During blood stage schizogony, mitosis is closed, with no breakdown of the nuclear envelope or any observable chromosome condensation (Aikawa and Beaudoin, 1968; Read *et al.*, 1993; Bannister *et al.*, 2000). In addition, nuclear division is asynchronous, despite nuclei sharing the same cytoplasm, which leads to readily observable odd numbers of nuclei in the multinucleated parasite (Read *et al.*, 1993; Leete and Rubin, 1996; Arnot, Ronander and Bengtsson, 2011; Simon *et al.*, 2021). At the end of schizogony, nuclei arrange below the plasma membrane and cytokinesis is initiated, with active daughter cell segmentation starting around 2-3 hours before egress (Kono *et al.*, 2012; Rudlaff *et al.*, 2020). These cytokinesis-associated nuclear divisions were largely considered to occur synchronously (Arnot, Ronander and Bengtsson, 2011; Francia and Striepen, 2014; Gubbels *et al.*, 2020), but more recent data challenges this perception. While membrane invagination and formation of the emerging daughter cells appears synchronous, the last nuclear divisions do not occur completely synchronously (Rudlaff *et al.*, 2020). In schizonts mid-segmentation, different nuclei have been observed to associate with varying numbers of apical complexes, of which there will ultimately be only one per daughter cell, indicating some nuclei are pre-mitosis and some are post-mitosis (Rudlaff *et al.*, 2020).

During the multiplication of nuclei, each nuclear division event is accompanied by a sequence of different intranuclear microtubule structures (Fig. 3) (Simon *et al.*, 2021). These microtubules are organised by the centriolar plaques, the *Plasmodium* mitotic microtubule organization centres (Fig. 3) (Bannister *et al.*, 2000; Simon *et al.*, 2021). Centriolar plaques are membrane-less organelles associated with the nuclear envelope (Aikawa, Huff and Sprinz, 1967; Bannister *et al.*, 2000; Simon *et al.*, 2021). They are distinct from both classical centrosomes and yeast spindle pole bodies and have no discernible structures such as the centrioles or the plaques of the spindle pole body (Bannister *et al.*, 2000; Simon *et al.*, 2021). Instead, the centriolar plaque is comprised of an outer cytoplasmic body connected to an inner nuclear body via a membrane-spanning neck (Simon *et al.*, 2021). The centriolar plaque is exceptionally protein-rich, but few of its components are known. While the outer part houses the conserved centrosomal proteins centrin 1-4, their exact function is unknown (Simon *et al.*, 2021). Within the nucleus, the intranuclear body of the centriolar plaque serves as the microtubule nucleation site and therefore must contain proteins of the microtubule nucleating γ-TuRC complex, such as γ-tubulin

(Zupa *et al.*, 2020). Additionally, the centromeres of *P. falciparum* cluster at the outer border of the intranuclear body of the centriolar plaque for the duration of schizogony, and many cell cycle proteins have been shown to associate with the centriolar plaque during schizogony (Dorin-Semblat *et al.*, 2011; Hoeijmakers *et al.*, 2012; Carvalho, Doerig and Reininger, 2013).

Prior to the first nuclear division, trophozoite nuclei develop large radial microtubule structures known as hemispindles (Fig. 3) (Read *et al.*, 1993; Simon *et al.*, 2021). Hemispindle microtubules are highly dynamic and can range from 0.5 to 2 µm in length, often seemingly exceeding the boundaries of the DNA containing regions, but their function is unknown (Simon *et al.*, 2021). As parasites enter schizogony, centrin starts being detectable at the centriolar plaque and eventually hemispindles collapse into smaller, punctual microtubule structures at the centriolar plaque, possibly already representing mitotic spindles (Fig. 3) (Simon *et al.*, 2021). At around the same time, the centrin signal and, thus, the centriolar plaque duplicates (Simon *et al.*, 2021). Microtubule foci then remain for about 150 minutes until they expand into extended anaphase spindles, separating the two daughter nuclei and their centriolar plaque (Fig. 3) (Simon *et al.*, 2021). Nuclear division is completed with the severing of the nuclear envelope bridge between the two daughter nuclei, which includes the 1-2 large microtubules connecting the centriolar plaques of the daughter nuclei (Fig. 3) (Simon *et al.*, 2021). Severing of the anaphase spindle results in the formation of two new hemispindles, one per nucleus (Simon *et al.*, 2021). Each nucleus then cycles through the next nuclear division seemingly independently, with one sibling dividing before the other (Simon *et al.*, 2021). This causes the characteristic occurrence of different microtubule structures in different nuclei of the same cell and uneven numbers of nuclei (Fig. 2) (Arnot, Ronander and Bengtsson, 2011; Simon *et al.*, 2021).

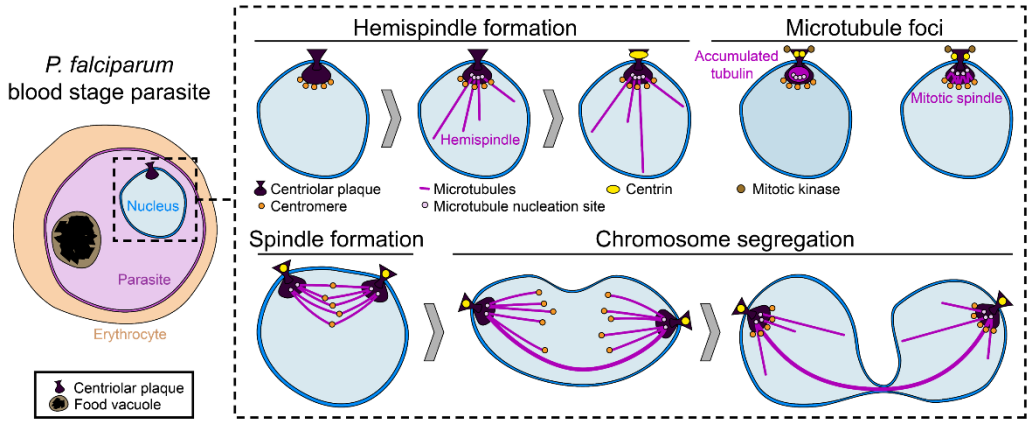

Figure 3 Progression of nuclear division in* P. falciparum *parasites. *Schematic of a mononucleated* P. falciparum *parasite prior to nuclear division. Inlet, schematic showing the first nuclear division and its associated microtubule stages (purple).*

The asynchronous nuclear division of *Plasmodium* nuclei during the blood stage is highly unusual. Multinucleated cells are found on any branch of the eukaryotic tree of life and can either be formed via fusion of mononucleated cells (such as in the muscle myotubes in vertebrates) or by repeated nuclear divisions without cell division (such as in the early *Drosophila* embryo) (Farrell and O'Farrell, 2014; Chal and Pourquié, 2017). Yet, as cell cycle progression is usually mediated by diffusible

cytoplasmic factors, the nuclei of most multinucleated system divide and replicate synchronously (Johnson and Rao, 1971; Westerveld and Freeke, 1971). In comparison, the asynchronous progression of *Plasmodium* nuclei through nuclear division indicates a regulation of the cell cycle at the level of individual nuclei, with nuclei seemingly acting as 'cells-within-cells`. Asynchronous progression of nuclei can also be observed in the very large multinucleated filaments of the fungus *Ashbya gossypii* (*A. gossypii*), which is closely related to yeast (Gladfelter, 2006; Gladfelter, Hungerbuehler and Philippsen, 2006). In *A. gossypii*, asynchrony is caused by compartmentalization of the cytosol, uneven distribution of canonical cell cycle proteins and differences in transcriptional activity in different nuclei (Nair *et al.*, 2010; Lee *et al.*, 2013). However, it is unknown what causes the asynchronous behaviour of nuclei in the *Plasmodium* blood stage of infection and the different dimensions of the cell size makes similar mechanisms as in *A. gossypii* less likely. Research on these topics is complicated by a lack of information on fundamental principles of cell cycle organisation and replication in *Plasmodium* (Francia and Striepen, 2014; Matthews, Duffy and Merrick, 2018).

1.5 *P. falciparum* DNA replication

The cell cycle is commonly divided into four different phases: the G1-phase (cells grow and prepare for DNA replication), the S-phase (DNA replication takes place), the G2-phase (cells prepares for mitosis), and finally the M-phase (mitosis and cytokinesis take place). The assignment of these phases in the blood stage of *P. falciparum* is not immediately obvious and depends on the organisation of events during nuclear multiplication. Although some aspects of nuclear division during blood stage schizogony have recently been elucidated (Simon *et al.*, 2021), little is known about the regulation and organisation of nuclear division and DNA replication. In bulk analysis, the DNA content of *P. falciparum* parasite populations starts increasing between 24-29 hpi (Inselburg and Banyal, 1984; Ganter *et al.*, 2017), which has been suggested to coincide with the first duplication of the centriolar plaque (Arnot, Ronander and Bengtsson, 2011). Yet, the organization of the individual cell cycle events is not well-understood.

One theory suggests that several rounds of DNA replication occur before the resulting genomes are partitioned into nuclei through nuclear division, similar to the endoreplication observed in insect and plant cells (Arnot and Gull, 1998; Gupta, Mehra and Dhar, 2008). This would indicate that parasites undergo a single S-phase where all DNA replication takes place, followed by a single M-phase where nuclear divisions and ultimately cytokinesis occur. Such a cell cycle can be seen in the related apicomplexan parasite *Sarcocystis* spp. (Gubbels *et al.*, 2020). Another theory implies that nuclei undergo alternating rounds of DNA replication and nuclear division (Janse *et al.*, 1986; Leete and Rubin, 1996; Arnot, Ronander and Bengtsson, 2011). In this scenario a DNA replication event always occurs before nuclear division, with the asynchrony of these nuclear cycles potentially being caused by uneven division of the centriolar plaque during mitosis (Arnot, Ronander and Bengtsson, 2011). However, while nuclear divisions can be followed through visualisation of microtubule structures or the nuclear DNA (Simon *et al.*, 2021), there is no live-cell compatible marker for DNA replication that would enable the correlation of these events in living cells.

On a molecular level the picture is somewhat clearer. The minimal machinery necessary for DNA replication is best studied in yeast and therefore in the following paragraphs the names of the yeast proteins are given. S-phase and DNA replication are organised via a cascade of molecular events that can be grouped into three phases: licensing of origin of replication, origin firing, and active DNA replication (Fig. 4 and 5) (Yeeles *et al.*, 2015). During licensing, which takes place in the late M- and the G1-phase, origins of replication are prepared for activation. Licensing involves proteins of the origin recognition complex (ORC 1-6), which bind to the origin of replication (Yeeles *et al.*, 2015). Subsequently, first the cell division cycle 6 (CDC6) protein binds to an origin, followed by the minichromosome maintenance (MCM) proteins and the chromatin licensing and DNA replication factor 1 (cdt1) to form the pre-replication complex (pre-RC) (Fig. 4) (Yeeles *et al.*, 2015). Licensing is a highly regulated process that can only occur in G1 phase and not during S-phase, which ensures that DNA is only replicated once per cycle. This is achieved, e.g., via the cyclin-dependent kinase (CDK) 2 which inhibits licensing of origins by targeting licensing proteins for degradation while simultaneously promoting S-phase (Fig. 4) (Yeeles *et al.*, 2015).

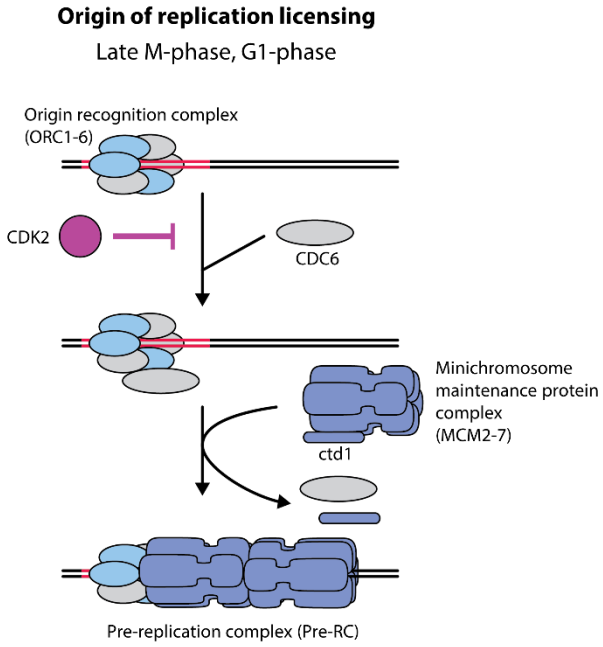

Figure 4 Origin of replication licensing. *Schematic of origin of replication licensing in yeast cells. Red, origin of replication; purple, cell cycle kinases; grey, proteins with no identifiably homologue in* Plasmodium. *Adapted from Yeeles* et al., *2015.*

At the onset of S-phase, origins are fired, which can only occur if an origin has been licensed before (Yeeles *et al.*, 2015; Boos and Ferreira, 2019). During firing, origins of replication are converted into active replication sites, which involves the formation of the transient pre-initiation complex (pre-IC) (Fig. 5) (Yeeles *et al.*, 2015; Boos and Ferreira, 2019). The first components of the pre-IC are recruited after the Dbf4-dependent kinase (DDK) phosphorylates residues of the MCM helicase, which facilitates binding of the firing factors Sld7, Sld3 and CDC45 (Gómez-Escoda and Wu, 2017). Sld7, Sld3 and CDC45 are only available in limited amounts, with copy numbers much lower than the number of origins of replication (Fig. 5) (Tanaka *et al.*, 2011; Boos and Ferreira, 2019). Therefore, the rate of origin

activation is limited by the levels of Sld7, Sld3 and CDC45 within the cell. Recruitment of Sld7, Sld3 and CDC45 is followed by CDK2-dependent phosphorylation of Sld3 among other proteins, and stepwise assembly of the remaining components of the pre-IC complex (MCM10, GINS, Sld2, Dbp 11 and polymerase ε) (Fig. 5) (Yeeles *et al.*, 2015; Boos and Ferreira, 2019). Subsequently, **C**DC45, **M**cm2-7 and **G**INS together form the CMG complex, the active helicase of the replication fork (Fig. 5) (Yeeles *et al.*, 2015; Boos and Ferreira, 2019). Meanwhile, many of the other pre-IC proteins, which only provide a regulatory platform for origin activation, dissociate from the origin to facilitate activation of the next origin of replication (Fig. 5) (Boos and Ferreira, 2019).

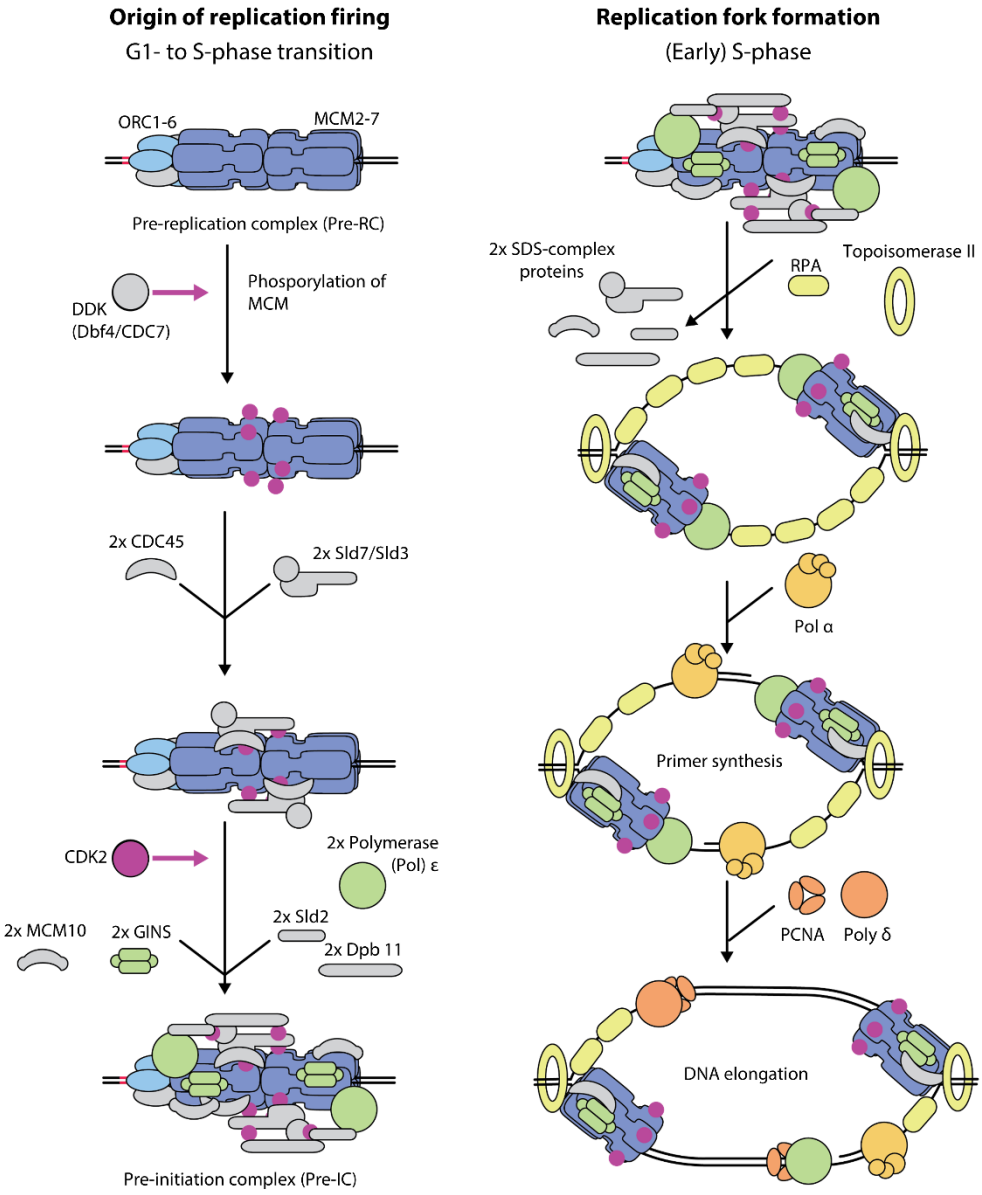

Figure 5 Origin of replication activation. *Schematic of origin of replication firing and replication fork formation in yeast cells. Red, origin of replication; purple, cell cycle kinases and phosphorylation; grey, proteins with no identifiably homologue in* Plasmodium*. Adapted from Yeeles* et al.*, 2015.*

Firing concludes with CMG-dependent rearrangement and opening of the double-stranded DNA at the origin site, which leads to the formation of single-stranded DNA, which is stabilised by the single-strand binding replication protein A (RPA)

proteins (Fig. 5) (Yeeles *et al.*, 2015; Boos and Ferreira, 2019). Additionally, topoisomerase II is recruited to the helicase complex to facilitate detangling and rearrangement of double-stranded DNA during DNA replication (Yeeles *et al.*, 2015). Stand elongation is initiated by polymerase α, which acts as a primase to form the first primer-template junction (Fig. 5) (Waga and Stillman, 1998; Yeeles *et al.*, 2015). Finally, the DNA sliding clamp, proliferating cell nuclear antigen (PCNA) is loaded onto the DNA, which marks the onset of DNA strand elongation via polymerase δ on the leading strand, and via polymerase ε on the lagging strand (Fig. 5) (Waga and Stillman, 1998; Chilkova *et al.*, 2007).

In *P. falciparum*, only some of the core components needed for *in-vitro* licensing and firing are readily identifiable by sequence homology (Fig. 4 and 5) (Matthews, Duffy and Merrick, 2018). The proteins of the DNA replication machinery such as the DNA polymerases, the DNA sliding clamps and the MCM proteins, are comparatively well-conserved and some of the central S-phase proteins have been characterized in different *Plasmodium* parasites. Among them are three identifiable ORC proteins, PfORC1, PfORC2 and PfORC5 (Fig. 4 and 5) (Gupta *et al.*, 2006; Gupta, Mehra and Dhar, 2008; Sharma *et al.*, 2018). In other eukaryotic cells, binding of ORC proteins is the first step of origin licensing and ORC proteins generally remain associated with the DNA until the end of S-phase (Yeeles *et al.*, 2015). The largest subunit of the ORC complex, PfORC1 is expressed in the late trophozoite and early schizont stage and apart from its role in DNA replication has been suggested to be involved in gene silencing (Mehra *et al.*, 2005; Gupta *et al.*, 2006; Deshmukh *et al.*, 2012). Similarly, PfORC2 was shown to be trafficked to the nucleus in late stage parasites and partially co-localises with PfORC1 (Sharma *et al.*, 2018). The last known *P. falciparum* ORC member, PfORC5 also colocalises with PfORC1 starting from the trophozoite stage, but while PfORC1 is degraded towards the end of schizogony, PfORC5 can be detected until cytokinesis (Gupta, Mehra and Dhar, 2008). Both PfORC1 and PfORC5 also colocalize with a *P. falciparum* homologue of PCNA (Gupta, Mehra and Dhar, 2008).

The DNA sliding clamp PCNA is a critical component of the replication fork (Waga and Stillman, 1998). Usually found in a trimeric form that resembles a ring, it is loaded onto the single-stranded DNA once origins are activated and an active replication fork with a primer-template junction has been formed (Fig. 5) (Gulbis *et al.*, 1996; Schrecker *et al.*, 2022). Loading is facilitated by the replication factor C (RFC) complex, a five-subunit complex that is well-conserved in *P. falciparum* (Sheriff *et al.*, 2021; Schrecker *et al.*, 2022). Once loaded to the DNA, PCNA serves as a platform for a range of other replication factors (Maga and Hübscher, 2003; Boehm, Gildenberg and Washington, 2016). This includes the DNA polymerases, whose processivity is 100-fold enhanced by PCNA (Moldovan, Pfander and Jentsch, 2007). Other PCNA-binding proteins include factors involved in active DNA replication, DNA repair, chromatin organisation, cell cycle control and apoptosis, and thus PCNA has been called the “maestro of the replication fork” (Maga and Hübscher, 2003; Moldovan, Pfander and Jentsch, 2007). Active replication forks are often organised into clusters called replication foci or replication factories, where high amounts DNA synthesis take place and DNA replication proteins such as PCNA are concentrated (Meister, Taddei and Gasser,

2006). Hence, replication foci are often identified by visualisation of intra-nuclear areas with a high PCNA concentration, and PCNA has been used to visualize DNA replication in several model organisms (Essers *et al.*, 2005; Meister *et al.*, 2007).

The *Plasmodium* genome harbours two copies of PCNA: PCNA1 and PCNA2 (Kilbey *et al.*, 1993; Patterson *et al.*, 2002). While PCNA1 shares the most homology with the PCNA of other eukaryotic organisms, PCNA2 still shares the overall sequence and structure of DNA sliding clamps and is essential in the rodent malaria parasite *P. berghei* (Patterson *et al.*, 2002; Mitra *et al.*, 2015; Pradhan *et al.*, 2019). PCNA1 has been suggested to be involved mainly in DNA replication, potentially forming structures resembling replication foci in the nuclei of multinucleated parasites (Kilbey *et al.*, 1993; Mitra *et al.*, 2015). In contrast, both PCNA1 and PCNA2 were suggested to act in DNA repair, with overexpression of either protein conferring an increased tolerance to DNA-damaging reagents (Mitra *et al.*, 2015). Function and nuclear localisation of PCNA1 was found to be dependent on tyrosine (Y) 213, the homologous residue to Y211 in human PCNA, which has been shown to be preferentially phosphorylated in cancer cells (Banu *et al.*, 2018; Wang *et al.*, 2022).

Despite our knowledge on several important components of the DNA replication machinery in *P. falciparum*, there are currently no available systems to study DNA replication in living cells. While expression of a thymidine kinase allows the incorporation of nucleoside analogues in nascent DNA that can be detected with specific antibodies, visualisation of these nucleosides requires fixation (Merrick, 2015; Stanojcic *et al.*, 2017; McDonald and Merrick, 2022). While this approach has enabled the profiling of origin sites as well as the speed and organisation of replication forks in *P. falciparum*, the overall organisation of S- and M-phases during schizogony has remained unknown (Stanojcic *et al.*, 2017).

1.6 Cell cycle control in the blood stage of *P. falciparum*

The seemingly independent division of nuclei within *P. falciparum* blood stage parasites suggests a high degree of nuclear autonomy, and a cell cycle control at the level of individual nuclei during schizogony has therefore been proposed. Yet, we know very little about how cell cycle control and thus, nuclear autonomy, is facilitated in *Plasmodium* parasites (Matthews, Duffy and Merrick, 2018).

In most eukaryotic organisms, transition between the four cell cycle stages is achieved through three sequential waves of activation of different cyclin-dependent kinases, the CDKs (Basu *et al.*, 2022). CDKs function as heterodimers with smaller cyclin partners, which are usually required for kinase activity (Malumbres, 2014). While CDKs may be present at any stage of the cell cycle, many cyclins are only present in specific cell cycle phases, leading to time-period specific activation of CDKs (Crosby, 2007). Thus, both CDKs and cyclins are grouped by the cell cycle phase they function in and are commonly divided into G1-, S- and M-phase proteins (Crosby, 2007). Other critical regulators of the eukaryotic cell cycle are the NimA related kinases (Nek), alongside the members of the Aurora and Polo kinase family (Fig. 3) (Smythe and Ayscough, 2003; O'Regan, Blot and Fry, 2007; Lee, Jang and Lee, 2014). Cell cycle progression also includes several defined molecular

checkpoints to buffer against defects occurring during cell growth, DNA replication or chromosome segregation (Barnum and O'Connell, 2014).

Strikingly, to date no canonical cell cycle checkpoints have been identified in any *Plasmodium* species, which appear to lack homologues to many key checkpoint proteins (Matthews, Duffy and Merrick, 2018). Usually a spindle assembly checkpoint monitors the proper attachment of chromosomes to the spindle before genome segregation, ensuring the equal distribution of DNA to the two emerging daughter cells (Barnum and O'Connell, 2014). In *P. falciparum*, genome segregation can be blocked through interference with nuclear division proteins, yet parasites still undergo DNA replication, and attempt cytokinesis and egress towards the end of the intraerythrocytic development (Absalon and Dvorin, 2021). Similarly, while inhibition of DNA replication via depletion of an S-phase promoting kinase stops the occurrence of nuclear divisions, it does not necessarily prevent parasite development, and parasites eventually attempted egress (Ganter *et al.*, 2017).

Plasmodium parasites encode a divergent repertoire of cell cycle proteins (Matthews, Duffy and Merrick, 2018). Only three cyclin homologues have been identified to date, none of which were shown to be expressed cyclically during the blood stage, and none of which are homologues to canonical G1-, S- or M-phase cyclins (Roques *et al.*, 2015; Matthews, Duffy and Merrick, 2018). While *Plasmodium* encodes a larger number of CDKs and CDK-related kinases (CRKs), most share little sequence similarity with canonical CDKs (Matthews, Duffy and Merrick, 2018). In addition, many of the characterized putative cell cycle kinases appear not to function during nuclear multiplication (Matthews, Duffy and Merrick, 2018). The kinase PfPK5 is the closest homologue to canonical CDKs and has been suggested to act in DNA replication based on localisation and unspecific chemical inhibition data, but is not essential in the rodent parasite *P. berghei* (Merckx *et al.*, 2003; Tewari *et al.*, 2010). Additionally, while PfPK5 can be activated by the cyclin H homologue Pfcyclin-1 *in vitro*, immunoprecipitation data suggests that Pfcyclin-1 does not interact with PfPK5 *in vivo* (le Roch *et al.*, 2000; Robbins *et al.*, 2017). Therefore, it is unclear if PfPK5 acts as a CDK during nuclear multiplication.

Similarly, while Pfcyclin-1 is essential for cytokinesis, depletion of Pfcyclin-1 does not affect prior nuclear divisions or DNA replication (Robbins *et al.*, 2017). Of the CRKs, the cdc2-related kinase 5 (PfCRK5) may be a regulator of nuclear multiplication in the blood stage, as the deletion of PfCRK5 resulted in the production of fewer daughter cells (Dorin-Semblat *et al.*, 2012). Other regulators of the cell cycle such as the Nek kinases PfNek-1 and PfNek-3 as well as the Aurora kinases Ark1-3 are essential for blood stage development, but although Nek-1 and Ark1-3 have been suggested to act during mitosis and cytokinesis, their exact molecular functions are not known (Dorin-Semblat *et al.*, 2012; Carvalho, Doerig and Reininger, 2013). Additionally, localisation studies found some kinases such as Ark1 and Nek-4 at the centriolar plaque, which has been suggested to act as a hub for cell cycle control in *P. falciparum* (Fig. 3) (Arnot, Ronander and Bengtsson, 2011; Dorin-Semblat *et al.*, 2012; Carvalho, Doerig and Reininger, 2013).

Currently, the only kinase with a defined roll for cell cycle regulation during nuclear multiplication in *P. falciparum* is the cdc2-related kinase 4 (PfCRK4) (Ganter *et al.*, 2017). The closest homologue to PfCRK4 is CDK2, which facilitates G1-S-phase transition in mammalian and yeast cells (Fig. 4 and 5) (Yeeles *et al.*, 2015; Ganter *et al.*, 2017). In line with this homology, depletion of PfCRK4 results in a reversible arrest of cells prior to S-phase, and phosphoproteomic data indicates that PfCRK4 is involved in licensing and firing of origins (Ganter *et al.*, 2017). This indicates that PfCRK4 could be involved in the regulation of G1-S-phase transition in *P. falciparum* in a similar manner to CDK2 in mammalian and yeast cells. However, while human CDK2 activity is dependent on interaction with cyclins, the cyclin binding motif is not well conserved in PfCRK4, and the kinase carries multiple sequence inserts most likely interfering with a potential cyclin interaction (Ganter *et al.*, 2017). Therefore, in absence of any known cyclin interaction or regulatory partners, it is unclear how regulation of PfCRK4 activity is achieved.

2 Aims of the Thesis

There is a current lack of understanding of fundamental cell biology in *P. falciparum*, which includes the organisation and regulation of the cell cycle during blood stage schizogony (Arnot and Gull, 1998; Francia and Striepen, 2014; Matthews, Duffy and Merrick, 2018). Therefore, the overall aim of my thesis was to establish the basic principles of the organisation of the cell cycle during *P. falciparum* blood stage replication and elucidate mechanisms of cell cycle control and of the apparent autonomy of the nuclei.

The first part of my thesis is centred around understanding the overall organisation of DNA replication and nuclear division during schizogony. To this end I aimed to follow DNA replication and nuclear division in nuclei of single parasites using long-term live-cell imaging. A requisite to this endeavour was the availability of a method to monitor DNA replication in living parasites. The goal of this part of my thesis was therefore twofold: first, I aimed to develop a novel resource to investigate DNA replication *in vivo*; and second, I aimed to clarify the organisation of S- and M-phase within schizogony to provide a model for the cell cycle during the blood stage of infection.

Building on these insights into *P. falciparum* schizogony, the next part of my thesis was focused on the characterisation of the dynamics of schizogony using live cell microscopy. I aimed to achieve this by following parasites as they undergo nuclear multiplication from onset of the first DNA replication event to cytokinesis and egress. Quantification of these parameters would allow further characterization of the *P. falciparum* blood stage cell cycle, but also help to investigate how nuclear asynchrony is introduced during schizogony and if there are patterns to nuclear multiplication hinting at specific regulatory mechanisms.

Lastly, I aimed to investigate the molecular determinants underlying nuclear autonomy during schizogony by exploiting proteins that show a clear cell cycle dependent behaviour. The goal of this part of my thesis was to gain new insights into the mechanistic basis of nuclear autonomy and cell cycle control, leading to a greater understanding of fundamental cell biology principles.

Overall, I aimed to expand our knowledge of *Plasmodium* cell cycle biology and to offer a first model explaining the apparent autonomous behaviour of nuclei during blood stage schizogony.

3 Materials and methods

3.1 Materials

3.1.1 Laboratory equipment

General equipment

Table 1 *Laboratory Equipment.*

Equipment	Name	Company
Agarose gel electrophoresis equipment	EV231	Consort (Turnhout, Belgium)
	E831	Consort (Turnhout, Belgium)
	UV-transilluminator Herolab UVT-28 L	Herolab (Wiesloch, Germany)
	Microwave 900&Grill	SEVERIN Elektrogeräte GmbH (Sundern, Germany)
Balances	Kern EW 600-2M	KERN & SOHN GmbH (Balingen, Germany)
	TE124S-0CE	Sartorius AG (Göttingen, Germany)
Cell culture	BVC professional vacuum pump	VACUUBRAND GMBH + CO KG (Wertheim, Germany)
	Counting Chamber according to Neubauer	neoLab Migge GmbH (Heidelberg, Germany)
	ENVAIReco safe Basic Plus Safety Cabinet	ENVAIR Deutschland GmbH (Emmendingen, Germany)
	Hera Safe KS 15	Thermo Fisher Scientific Inc. (Waltham, USA)
	Isotemp 210 Water Bath	Fisher Scientific International, Inc. (Hampton, USA)
	Labo C201 Incubator	Labotect GmbH (Rosdorf, Germany)
	Sanyo CO2 Incubator MCO-17AI	Sanyo Electric Co., Ltd (Osaka, Japan)
Centrifuges	Heraecus Fresco 21 Centrifuge	Thermo Fisher Scientific Inc. (Waltham, USA)
	Heraeus Pico 21 Centrifuge	Thermo Fisher Scientific Inc. (Waltham, USA)
	Heraeus Multifuge 1 S-R	Thermo Fisher Scientific Inc. (Waltham, USA)
	Heraeus Multifuge 1.0 R	Thermo Fisher Scientific Inc. (Waltham, USA)
	Avanti J-26S XP with rotor JA-10	Beckman Coulter (Brea, USA)
	Mini centrifuge Su 1550	Sunlab GmBH (Aschaffenburg, Germany)
Electroporation devices	Gene Pulser II	Bio-Rad (Hercules, USA)
Fridges and freezers	Liebherr CN 3666	Liebherr-Hausgeräte GmbH (Ochsenhausen, Germany)
	Innova U725 Freezer (-80 °C)	New Brunswick Scientific Co., Inc. (Edison, USA)
	MediLine Freezer (-20 °C)	Liebherr-Hausgeräte GmbH (Ochsenhausen, Germany)
	MediLine Fridge (4 °C)	Liebherr-Hausgeräte GmbH (Ochsenhausen, Germany)
	Liebherr Comfort	Liebherr-Hausgeräte GmbH (Ochsenhausen, Germany)
Heating blocks	neoBlock 1 Heater	neoLab Migge GmbH (Heidelberg, Germany)
	ThermoMixer C	Eppendorf (Hamburg, Germany)
	AccuBlock™ Digital Dry Bath	Labnet (Edison, USA)
Electron microscopy	Leica EM-AFS2	Leica Microsystems GmbH (Wetzlar, Germany)
	Leica EM ICE	Leica Microsystems GmbH (Wetzlar, Germany)
	Leica UC6 ultramicrotome	Leica Microsystems GmbH (Wetzlar, Germany)
Bacterial Incubators	CH-4103	Infors AG (Bottmingen, Switzerland)
	IN75	Memmert (Schwabach, Germany)
Plate reader	Infinite M200 Pro	TECAN (Männedorf, Switzerland)
Pipets	Microliter pipet 0.2-2 µl	Gilson Incorporated (Middelton, USA)
	Microliter pipet 2-20 µl	Gilson Incorporated (Middelton, USA)
	Microliter pipet 20-200 µl	Gilson Incorporated (Middelton, USA)
	Microliter pipet 100-1000 µl	Gilson Incorporated (Middelton, USA)
	12 channel Multipet 2-200 µl	Eppendorf (Hamburg, Germany)
	Microliter pipet 0.5-10 µl	Sunlab GmBH (Aschaffenburg, Germany)
	Microliter pipet 2-20 µl	Sunlab GmBH (Aschaffenburg, Germany)
	Microliter pipet 100-1000 µl	Sunlab GmBH (Aschaffenburg, Germany)

Pipetman	Sunlab digital pipetting aid	Sunlab GmBH (Aschaffenburg, Germany)
	Pipetus	Hirschmann Laborgeräte GmbH & Co. KG (Eberstadt, Germany)
	Accu-jet pro	Brand GMBH + CO. KG (Wertheim, Germany)
Shakers and mixers	Orbital shaker HS 250 basic	IKA-Werke GmbH & CO. KG (Staufen, Germany)
	Orbital shaker Duomax 1030	Heidolph Instruments GmbH & CO. KG (Schwabach, Germany)
	360° Rotator Loopster digital	IKA-Werke GmbH & CO. KG (Staufen, Germany)
	neoLabLine Vortex Mixer	neoLab Migge GmbH (Heidelberg, Germany)
Spectrophotometer	NanoPhotometer NP80	Implen (München, Germany)
Thermal cyclers	FlexCycler2	Analytik Jena (Jena, Germany)
SDS PAGE	Standard Power Pack P25 T	Analytik Jena GmbH (Jena, Germany)
Other	12-Tube Magnetic Separation Rack	New England Biolabs (Ipswich, USA)
	Bioruptor Plus Sonication System	Diagenode, Inc. (Denville, USA)
	Fume Hood	Wesemann GmbH (Syke, Germany)
	Ice Dispenser AF 80	Scotsman Ice Systems (Vernon Hills, USA)
	Pestle	Bel-Art Products (Wayne, USA)
	Heating plate and magnetic stirrer RH basic 2	IKA-Werke GmbH & CO. KG (Staufen, Germany)
	Heat-stir CB162	Stuart Pharmaceutical Company (Pasadena, USA)
	VarioMACS	Miltenyi Biotec (Bergisch Gladbach, Germany)

Microscopes

Table 2 *Microscopes*

Instrument	Specifications	Company
Leica DM IL	**General:** Brightfield microscope with attached Leica DFC320 FireWire Digital Microscope Camera. Equipped with 3 position fluorescence slider. **Objectives**: 2.5x/0.07 HCX FL Plan, 100x/1.25 oil HI Plan, C Plan 40x/0.5 air BE Plan, C Plan 20x/0.03	Leica Microsystems GmbH (Wetzlar, Germany)
Leica SP8 TCS DLS	**General:** Environment control (CO_2, temperature, humidity), resonant scanner, Adaptive Focus Control, spectral detection, acusto-optical beam splitter, HyD detectors, **Objectives**: 63x/1.4 HC PL Apo CS2 Oil, 63x/1.3 HC PL Apo CORR CS2 Gycerol, 20x/0.75 HC PL Apo IMM CORR CS2 H_2O, Glycerol, Oil **Lasers:** UV (50mW) - 405nm, Argon (65mW) - 458, 476, 488, 496, 514nm, DPSS Yellow (20mW) - 561nm, HeNe (10mW) - 633nm	Leica Microsystems GmbH (Wetzlar, Germany)
PerkinElmer UltraVIEW VoX spinning disk vCSU-X1 with Nikon TiE	**General:** Environment control (CO_2, temperature, humidity), FRAP, Perfect Focus System, dual camera (EM-CCD Hamamatsu ImageEM X2, 512px x 512px, 16um x 16um; sCMOS Hamamatsu ORCA Flash 4.0 V2, 2048px x 2048px, 6.5um x 6.5um), Piezo **Objectives**: PLAN Fluor 20x/0.75 MImm (Water, Gycerol, Oil), S Fluor 40x/1.3 Oil DIC H/N2, Apo TIRF 60x1.49 Oil DIC N2, PLAN Apo VC 100x/1.4 Oil, PLAN Apo VC 60x/1.2 Water, PLAN Apo lampda 20x/0.75 **Lasers:** Diode 405nm (50mW), Diode 440nm (40mW), DPSSL 488nm (50mW), DPSSL 515nm (25mW), DPSSL 561nm (50mW), Diode 640nm (40mW)	PerkinElmer Inc. (Waltham, USA) Nikon Corporation (Tokyo, Japan)

JEOL JEM-1400 electron microscope	**General:** 120 kV Transmission electron microscope equipped with a bottom mount 4k by 4k pixel digital camera (TemCam F416, Gauting, Germany).	Jeol (Tokyo, Japan)
Nikon eclipse E100	**General:** Upright, LED illumination brightfield microscope **Objectives**: 10x/0.25 air BE Plan, 100x/1.25 oil BE Plan, 40x/0.65 air BE Plan	Nikon Corporation (Tokyo, Japan)
Zeiss Airyscan 2 LSM900	**General:** Environment control, (CO_2, O_2, temperature, humidity), Variable Dichroics, Definite Focus 2, GaAsP – PMTs, Airyscan 2 with 4xMPLX **Objectives**: Plan-Apochromat 20x/0,8, Plan-Apochromat 40x/1,3 Oil DIC, Plan-Apochromat 63x/1,4 Oil DIC, LD LCI Plan-Apochromat 40x/1,2 Imm Korr DIC, Water, silicon oil or glycerol immersion **Lasers:** Diodenlaser 405nm, 5mW, Diodenlaser 488nm, 10mW, Diodenlaser (SHG) 561nm, 10mW, Diodenlaser 640nm, 5mW	Carl Zeiss AG (Oberkochen, Germany)
Zeiss Axio Observer	**General:** Widefield microscope, Photometric Prime BSI camera **Objectives**: Fluor 10x/0.50 M27, LCI Plan-Neofluoar"25x/0.8, Plan-Apochromat 63x/1.4 Oil DIC M27	Carl Zeiss AG (Oberkochen, Germany)
Zeiss Axiostar plus	**General:** Upright, LED illumination brightfield microscope **Objectives**: CP-Achromat 10x/0.25 air Plan, 100x/1.25 oil A-Plan, CP-Achromat 40x/0.65 air Plan, CP-Achromat 100x/1.25 oil A-Plan	Carl Zeiss AG (Oberkochen, Germany)

3.1.2 Consumables and reagents

Consumables

Table 3 *Consumables*

Name	Company
Cell culture dishes (10 cm, 20 nm)	Greiner Bio-One GmbH (Frickenhausen, Germany)
Cell culture plates (6-well, 24-well, 96-well)	Greiner Bio-One GmbH (Frickenhausen, Germany)
Cryogenic vials (2 ml)	Greiner Bio-One GmbH (Frickenhausen, Germany)
Electroporation cuvettes	Bio-Rad Laboratories, Inc. (Hercules, USA)
Falcon tubes (15 ml, 50 ml)	Greiner Bio-One GmbH (Frickenhausen, Germany)
Filter tips (10 µl, 20 µl, 100 µl, 200 µl, 1000 µl)	Sorenson Bioscience Inc. (Salt Lake City, USA)
Folded filters	Sartorius AG (Goettingen, Germany)
Formvar-coated finder grids	Plano (Wetzlar, Germany)
Formvar-coated slit copper grids	Plano (Wetzlar, Germany)
Glass slides	Thermo Fisher Scientific Inc. (Waltham, USA)
Ibidi microscopy dishes (glass bottom 8-well, 8-well ibidi treat, 35 mm glass bottom round dishes)	Ibidi (Fitchburg, USA)
Mini-PROTEAN TGX Precast Gels	Bio-Rad Laboratories, Inc. (Hercules, USA)
Needles (0.3 mm, 0.4 mm)	BD (Eysins, Switzerland)
Parafilm M	Bemis (Neenah, USA)
PCR tubes (single tubes, 8-strips)	Biozym Scientific GmbH (Hessisch Oldendorf, Germany)
Petri dishes	Greiner Bio-One GmbH (Frickenhausen, Germany)
Pipette tips (unfiltered) (10 µl, 20 µl, 200 µl, 1000 µl)	Steinbrenner Laborsysteme GmbH (Wiesenbach, Germany)
Precision wipes (KIM wipes)	Kimberley-Clark Professional (Irving, USA)
Protein LoBind Tubes (1.5 ml)	Eppendorf AG (Hamburg, Germany)
Reaction tubes (1.5 ml, 2 ml)	SARSTEDT AG & Co. KG (Nümbrecht, Germany)
Serological pipettes (5 ml, 10 ml, 25 ml, 50 ml)	Greiner Bio-One GmbH (Frickenhausen, Germany)
Syringes (1 ml, 50 ml)	BD (Eysins, Switzerland)

Chemicals and reagents

Table 4 *Chemicals and reagents*

Product	Company
2-Mercaptoethanol	Carl Roth GmbH + Co. KG (Karlsruhe, Germany)
Acetone (anhydrous)	Sigma-Aldrich, Inc. (St. Louis, USA)
Agarose NEEO ultra-quality EEO = 0,05-0,13	Carl Roth GmbH + Co. KG (Karlsruhe, Germany)
Albumax II (11021045)	Thermo Fisher Scientific Inc. (Waltham, USA)
Albumin (BSA)	Carl Roth GmbH + Co. KG (Karlsruhe, Germany)
Blasticidin, solution (ant-bl-1)	InvivoGen (San Diego, USA)
$CaCl_2$	Merck KGaA (Darmstadt, Germany)
cOmlpete™, EDTA-free Protease Inhibitor Cocktail	Roche Diagnostics GmbH (Mannheim, Germany)
Concanavalin A C2010	Sigma-Aldrich, Inc. (St. Louis, USA)
Concentrated erythrocytes (O+)	DRK Blutbank Mannheim (Mannheim, Germany)
Cutsmart buffer	New England Biolabs (Ipswich, USA)
DMSO	Honeywell (Seelze, Germany)
D-sorbitol (S1876-500G)	Sigma-Aldrich, Inc. (St. Louis, USA)
DTT	GERBU Biotechnik GmbH (Heidelberg, Germany)
Dulbecco's Phosphate Buffered Saline (DPBS)	Gibco by life technologies (Paisley, UK)
EDTA	Sigma-Aldrich, Inc. (St. Louis, USA)
EGTA	Sigma-Aldrich, Inc. (St. Louis, USA)
Ethanol	Zentralbereich Neuenheimer Feld (Heidelberg, Germany)
Geneticin G-418 Sulphate (11811-031)	Thermo Fisher Scientific Inc. (Waltham, USA)
Gentamycin sulphate solution (HN09.1)	Thermo Fisher Scientific Inc. (Waltham, USA)
GFP-Trap Dynabeads	ChromoTek GmbH (Planegg-Martinsried, Germany)
Glutaraldehyde solution, grade I, 25% in H2O	Sigma-Aldrich, Inc. (St. Louis, USA)
Glycerol	AppliChem GmbH (Darmstadt, Germany)
Glycine	Labochem international (Heidelberg, Germany)
Hemacolor® Rapid staining of blood smear Solution	VWR (Radnor, USA)
Hemacolor® Rapid staining of blood smear Solution 3	VWR (Radnor, USA)
Heparin sodium salt from porcine intestinal mucosa	Sigma-Aldrich, Inc. (St. Louis, USA)
HEPES (H4034)	Sigma-Aldrich, Inc. (St. Louis, USA)
Hypoxanthine (Z-41-M)	c.c.pro GmbH (Oberlorla, Germany)
K_2HPO_4	Merck KGaA (Darmstadt, Germany)
KCl	AppliChem GmbH (Darmstadt, Germany)
KH_2PO_4	Sigma-Aldrich, Inc. (St. Louis, USA)
KOH	Honeywell (Seelze, Germany)
Laemmli Sample Buffer	Bio-Rad Laboratories, Inc. (Hercules, USA)
LB Broth (Lennox)	Carl Roth GmbH + Co. KG (Karlsruhe, Germany)
LR Gold	London Resin Company (London, UK)
Methanol	Zentralbereich Neuenheimer Feld (Heidelberg, Germany)
$MgCl_2$	Honeywell (Seelze, Germany)
Milk, powdered	Carl Roth GmbH + Co. KG (Karlsruhe, Germany)
NaCl	Sigma-Aldrich, Inc. (St. Louis, USA)
Nonidet P-40 (NP-40)	AppliChem GmbH (Darmstadt, Germany)
Paraformaldehyde (PFA) EM-grade	Electron Microscopy Sciences (Hatfield, Pennsylvania)
Phosphate-buffered saline (PBS)	Thermo Fisher Scientific Inc. (Waltham, USA)
Phusion polymerase HF reaction buffer (5x)	New England Biolabs (Ipswich, USA)
Pierce™16% Formaldehyde (w/v), Methanol-free, 28906	Thermo Fisher Scientific Inc. (Waltham, USA)
Purple loading dye	New England Biolabs (Ipswich, USA)
Quick Coomassie Stain	SERVA Electrophoresis GmbH (Heidelberg, Germany)
RPMI 1640 GlutaMAX, phenol-red (61870010)	Gibco by life technologies (Paisley, UK)
RPMI 1640, stable Glutamine, w/o phenol-red, 2 g/l $NaHCO_3$ (P04-16520)	PAN Biotech (Aidenbach, Germany)
Saponin Quillaja sp.	Sigma-Aldrich, Inc. (St. Louis, USA)
SDS	SERVA Electrophoresis GmbH (Heidelberg, Germany)
SOC outgrowth medium	New England Biolabs (Ipswich, USA)
Sodium acetate	Merck KGaA (Darmstadt, Germany)
Sodium borohydrate ($NaBH_4$)	Sigma-Aldrich, Inc. (St. Louis, USA)
Sodium deoxycholate	Sigma-Aldrich, Inc. (St. Louis, USA)

SYBR Green I	Thermo Fisher Scientific Inc. (Waltham, USA)
T4 DNA ligase buffer (10x)	New England Biolabs (Ipswich, USA)
Taq Reaction Buffer	New England Biolabs (Ipswich, USA)
Tris	Carl Roth GmbH + Co. KG (Karlsruhe, Germany)
Triton-X-100	Merck KGaA (Darmstadt, Germany)
Tween-20	Carl Roth GmbH + Co. KG (Karlsruhe, Germany)
WR99210	Jacobus Pharmaceuticals (Plainsboro Township, USA)

Media, buffers and solutions

Table 5 *Media, buffers and solutions*

Name	Composition	Purpose
10x SDS Running buffer	250 mM Tris 1.92 M Glycine 1% SDS	Co-immunoprecipitation (SDS-PAGE)
4x Laemmli buffer	4x Laemmli Sample Buffer 1:10 2-Mercaptoethanol (freshly added)	Co-immunoprecipitation (SDS-PAGE)
Complete Cell culture medium (cRPMI)	RPMI 1640, phenol-red (500 ml bottle) 25 mM HEPES 12.5 µg/ml Gentamycin sulphate solution 0.2 mM Hypoxanthine 0.5% Albumax	Cell culture (Standard culture)
Cytomix	120 mM KCl 0.15 mM $CaCl_2$ 2 mM EGTA 5 mM $MgCl_2$ 10 mM K_2HPO_4/KH_2PO_4 25 mM HEPES	Transfection (Transfection solution)
Freezing solution	28% glycerol 3% D-Sorbitol 0.65% NaCl	Cell culture (Freezing)
Glycine solution	0.125 M Glycine Dulbecco's Phosphate Buffered Saline (DPBS)	Co-immunoprecipitation (Quenching)
Imaging medium	RPMI 1640, w/o phenol-red (500 ml bottle) 25 mM HEPES 12.5 µg/ml Gentamycin sulphate solution 0.2 mM Hypoxanthine 0.5% Albumax	Cell culture (Live-cell imaging)
Incomplete Cell culture medium (iRPMI)	RPMI 1640, phenol-red (500 ml bottle) 25 mM HEPES 12.5 µg/ml Gentamycin sulphate solution	Cell culture (Washing)
RIPA	50 mM Tris/HCl, pH 8 1 % Nonidet P-40 (NP-40) 0.5 % Sodium deoxycholate 0.1 % SDS 1 mM DTT (freshly added) 1x cOmlpete™, EDTA-free Protease Inhibitor Cocktail (freshly added)	Co-immunoprecipitation (Cell lysis)
Sorbitol solution	5 % D-Sorbitol	Cell culture (Synchronisation)
SYBR green solution, pH 7.4	0.16% saponin 20 mM Tris-HCl, pH 7.5 5 mM EDTA, pH 8.0 1.6% Triton X 100 1:1000 SYBR Green I (freshly added)	Cell culture (Growth assay)
TE buffer, pH 7.5	10 mM Tris-HCl, pH 7.5 1 mM EDTA	Transfection (DNA resuspension)
Wash buffer	10 mM Tris/HCl, pH 7.5 150 mM NaCl 0.05 % Nonidet P-40 (NP-40) 0.5 mM EDTA	Co-immunoprecipitation (Washing)

Standard markers

Table 6 *Standard markers*

Name	Company	Product Number
1 kb Ladder	New England Biolabs (Ipswich, USA)	N3232
100 bp Ladder	New England Biolabs (Ipswich, USA)	N3231
Precision Plus Protein Dual Color Standards	Bio-Rad Laboratories, Inc. (Hercules, USA)	1610374

Antibodies and nanobodies

Table 7 *Antibodies and nanobodies*

Name	Species	Application	Dilution	Supplier
α-PfCentrin3, polyclonal	Rabbit	IFA	1:500	AG Guizetti (Yannik Voß) (Center for Infectious Diseases, Heidelberg University Hospital, Heidelberg, Germany)
α-ERC, polyclonal	Rabbit	IFA	1:500	AG Przyborski (Biochemistry and Molecular Biology, Justus Liebig University, Gießen, Germany)
α-Tubulin, B-5-1-2 T5168, monoclonal	Mouse	IFA	1:500	Sigma-Aldrich (St. Louis, USA)
α-GFP, monoclonal	Rabbit	IFA	1:50	Thermo-Fisher Scientific (Waltham, USA)
α-mouse Alexa-Fluor Plus 488	Goat	IFA	1:1000	Thermo-Fisher Scientific (Waltham, USA)
α-mouse-Atto-594	Goat	IFA	1:1000	Thermo-Fisher Scientific (Waltham, USA)
α-rabbit-Atto-647	Goat	IFA	1:1000	Thermo-Fisher Scientific (Waltham, USA)

Dyes

Table 8 *Dyes*

Name	Application	Dilution	Source/Company	Product Number
5'SiR-Hoechst	IFA, live cell imaging	1:8000	(Bucevičius *et al.*, 2019)	-
SPY555-DNA	IFA, live cell imaging	1:2000	Spirochrome (Stein Am Rhein, Switzerland)	SC201
Hoechst 33342	IFA, live cell imaging	1:10 000	Thermo-Fisher Scientific (Waltham, USA)	H3570
SPY650-tubulin	Live cell imaging	1:2000	Spirochrome (Stein Am Rhein, Switzerland)	SC503
SYBR Green I	Growth curves	1:1000	Thermo-Fisher Scientific (Waltham, USA)	S7563

Enzymes

Table 9 *Enzymes*

Name	Company	Product Number
AatII	New England Biolabs (Ipswich, USA)	R0117
AvrII	New England Biolabs (Ipswich, USA)	R0174
BbsI-HF	New England Biolabs (Ipswich, USA)	R3539
EcoRI-HF	New England Biolabs (Ipswich, USA)	R3101
NotI-HF	New England Biolabs (Ipswich, USA)	R3189
Quick CIP	New England Biolabs (Ipswich, USA)	M0525
Phusion Polymerase	New England Biolabs (Ipswich, USA)	M0530
Taq Polymerase	New England Biolabs (Ipswich, USA)	M0273
T4 Ligase	New England Biolabs (Ipswich, USA)	M0202
T4 Polynucleotide Kinase	New England Biolabs (Ipswich, USA)	M0201
Hifi Assembly Master Mix	New England Biolabs (Ipswich, USA)	E2621

Kits

Table 10 *Kits*

Name	Company	Product Number
GenEluteTM HP Plasmid Miniprep Kit	Sigma-Aldrich (St. Louis, USA)	NA0150
NucleoBond Xtra Midi Plus	Macherey-Nagel (Düren, Germany)	740412.50
High Pure PCR Product Purification Kit	Roche (Mannheim, Germany)	11732676001
DNeasy Blood & Tissue Kit (50)	Qiagen (Hilden, Germany)	69504

3.1.3 Cell lines

Plasmodium falciparum cell lines

Table 11 *P. falciparum cell lines*

Name	Description	Source
3D7	*P. falciparum* cell lined derived from clonal dilution from NF54	(Ponnudurai, Leeuwenberg and Meuwissen, 1981)

Bacteria

Table 12 *Bacteria*

Name	Description	Source	Product number
NEB® 5-alpha F'Iq Competent *E. coli*	Chemically competent *E. coli* cells derived from DH5α	New England Biolabs (Ipswich, USA)	C2992

3.1.4 DNA

Oligonucleotides

Table 13 *Oligonucleotides. Magenta indicates gRNA sequences.*

Sequencing primers		
Name	**Sequence (5'→3')**	**Purpose**
216_AmpR_Seq_Rev	GGGCGACACGGAAATGTTG	Sequencing from ampicillin
230_GFP_AvrII_FP	GATCCTAGGGGAGGTGG	Sequencing from GFP
pARL_5-crt-fw_seq	ATCGACATTCCGATATATTATA	Sequencing pArl
pARL_3-hsp_rev_seq	ATGCACACAACATACAC	
pDC2_donorcassette_fw_seq	aacatatgttaaatatttatttctc	Sequencing pDC2
pUC-R	TGCCTGCAGGTCGACTCTAG	
Endogenous PCNA1 tagging via CRISPR-Cas9 editing		
Name	**Sequence (5'→3')**	**Purpose**
0347_PCNA1_FP	GAGGTACCGAGCTCGAATTCATGTTAGAGGCCAAATTAAATAA	Homology region cloning
0348_PCNA1_g624_RP	GTTTGATTTAGAAAACAAGTTTAAATACTTGATCGCAAACGATTG	
0349_PCNA1_g624_FP	ACTTGTTTTCTAAATCAAACATTTT	
0350_PCNA1_g738_RP	CCAATTTTTAAGGTGTCTGAATCCGGGGACGTATCTTTA	
0351_PCNA1_g738_FP	TCAGATACCTTAAAAATTGGATTTG	
0352_PCNA1-EGFP_RP	TATATAATATTTTATTGAGATTATTTATAAAGCTCATCCATTCC	
0353_PCNA1_3UTR_FP	TGGATGAGCTTTATAAATAATCTCAATAAAATATTATATATATATATATGTACATATTTTCATAT	
0354_PCNA1_3UTR_RP	GAAAAGTGCCACCTGACGTCGTGTGTGTGTGAACAAATATGG	
0355_gRNA_738_F	TATTTAAGGTATCTGAATCAGGGG	gRNA
0356_gRNA_738_R	AAACCCCCTGATTCAGATACCTTA	
0357_gRNA_624_F	TATTTGTTTAAATATTTGATGGCAA	

0358_gRNA_624_R	AAACTTGCCATCAAATATTTAAAC	
0365_PCNA1_IntPrimer_5UTR_Fwd	TGCTATTAGAAAATTGTCAGCCAA	Integration PCR
0366_PCNA1_IntPrimer_3UTR_Rev	ACGACGATTATTTTGTTGTGTT	
Episomal expression of PCNA1 mutants		
Name	**Sequence (5'→3')**	**Purpose**
0281_NES_11deletion23_FP	AATGATGCCAATGTGGATGC	PCNA1 mutation
0282_NES_11deletion23_RP	TGATGCATTATTTAATTTGGCCTC	
0283_NLS_101deletion120_FP	ATTGAATTGGACTCTTTAAATATACCAGATTG	
0284_NLS_101deletion120_RP	ATTTAAATTATCTTCATCATCTTTACTAGATATAACTAC	
0285_NLS_F114A_FP	AGTTACTAACGCTTCTTTAAAATTAATGTCTATTGAATTGG	
0286_NLS_F114A_RP	TTATCTTCTTTGTTGTTTTCAAAAACAAAATT	
0287_Y213F_FP	GCCATCAAATTTTTAAACTTGTTTTCTAAATC	
0288_Y213F_RP	AAAGGATTGTTTAATTTTTTTTTTGGATTTAATTG	
0289_247deletion254_FP	ATTGGATTTGTTAAATTTTTCTTAGCTCC	
0290_247deletion254_RP	GGTATCTTTAATTTCATATTTGAATTCGATTG	
0321_NEStoGSlinker_FP	GGAGGTGGATCTGGAGGTGGAGGTTCTGGAGGTGGATCTAATGATGCCAATGTGGATGC	
0322_NEStoGSlinker_RP	TGATGCATTATTTAATTTGGCCTCTA	
0323_NES_KKKtoAAA_FP	GCATCAATTTTAGCAGCACTTTTTGAATGTATCGCAGATTTAGTAAATGATGCCAATG	
0324_NES_KKKtoAAA_RP	ATTATTTAATTTGGCCTCTAACAT	
0325_NLStoGSlinker_FP	GGAGGTGGAGGTTCTGGAGGTGGAGGTGGAGGTATTGAATTGGACTCTTTAAATATACCAGATTG	
0326_NLStoGSlinker_RP	AGAACCTCCACCTCCAGAACCTCCACCTCCATTTAAATTATCTTCATCATCTTTACTAGATATAACTACT	
0327_NLS_FKKtoAAA_FP	TTTAAATTTTGTTGCTGAAAACAACAAAGAAGATGCAGTTACTAACTTTTCTTTAGCATTAATGTCTATTG	
0328_NLS_FKKtoAAA_RP	TTATCTTCATCATCTTTACTAGATATAACTACTGAT	
0329_NES_GSoverhang_RP	AGAACCTCCACCTCCAGAACCTCCACCTCCTACTAAATCTTTGATACATTCAAAAAGTTTTTTTAAAAT	
0330_GSoverhang_NLS_FP	GGAGGTGGAGGTTCTGGAGGTGGAGGTTCTTTTGTTTTTGAAAACAACAAAGAAGAT	
0331_NLS_AvrII_RP	CAGcctaggAGACATTAATTTTAAAGAAAAGTTAGTAACT	
0332_GSlinker_GFP_FP	GGAGGTGGAGGTTCTGGAGGTGGAGGTTCTATGA	
0333_GFP_NoSTOP_GSoverhang_RP	GAACCTCCACCTCCAGAACCTCCACCTCCTTTATAAAGCTCATCCATTCCGTGA	
0334_NLS_Stop_KpnI_RP	CTGggtaccCTAAGACATTAATTTTAAAGAAAAGTTAGTAACTTTATCT	
Episomal expression of PCNA1-derived peptides		
Name	**Sequence (5'→3')**	**Purpose**
0373_PCNA1_NES1_Fwd	tcgagatgAAATTAAATAATGCATCAATTTTAAAAAAACTTTTTGAATGTATCc	PCNA1-derived peptide cloning
0374_PCNA1_NES1_Rev	ctaggGATACATTCAAAAAGTTTTTTTAAAATTGATGCATTATTTAATTTcatc	
0375_PCNA1_NLS1_Fwd	TAActcgagatgTCAATTTTAAAAAAACTTTTTGAATGTA	
0376_PCNA1_NLS1_Rev	TCCcctaggATCTAATGCTTGTAATTTTAATCCA	
0377_PCNA1_NLS/NES1_Fwd	TAActcgagatgAAATTAAATAATGCATCAATTTT	
0378_PCNA1_NLS/NES1_Rev	TCCcctaggATCTAATGCTTGTAATTTTAATCCA	
0379_PCNA1_NES2_Fwd	tcgagatgTTTTCTTTAAAATTAATGTCTATTGAATTGGACTCTTTAAATATAc	
0380_PCNA1_NES2_Rev	ctaggTATATTTAAAGAGTCCAATTCAATAGACATTAATTTTAAAGAAAAcatc	
0381_PCNA1_NLS2_Fwd	tcgagatgAAATCCAAAAAAAAAATTAAACAATCCTTTc	
0382_PCNA1_NLS2_Rev	ctaggAAAGGATTGTTTAATTTTTTTTTTGGATTTcatc	
Point mutation within exportin-1 via CRISPR-Cas9 editing		
Name	**Sequence (5'→3')**	**Purpose**
0297_Gibson_outer_guide64_FP	GAGGTACCGAGCTCGAATTCCATCATCTTTAACAAATAGAAAATCATATAGTTTTG	Homology region cloning
0298_Gibson_outer_guide49_FP	GAGGTACCGAGCTCGAATTCTCAGATATTAAGAAAATGTGCCCACG	

0299_guide64_FP	CCATCAGACATAAAGAAGATGTGCCCACGTATAAAATTATATG	
0300_guide64_RP	GGCACATCTTCTTTATGTCTGATGGATTTAAATCAATT	
0303_ItoC_guide64_FP	AGAATATATTTACATATGTGTGAAGTTAAAAATGGCGAAG	
0304_ItoC_guide64_RP	CCATTTTTAACTTCAcaCATATGTAAATATATTCTGAGAATGTACATTAAAAAGTCTTG	
0305_ItoC_guide49_FP	TTTACACATGTGTGAAGTTAAGAATGGCGAAGAAAATAGAGCCATTCTAG	
0306_ItoC_guide49_RP	CCATTCTTAACTTCACACATGTGTAAATATATTCTGAGAATGTACATTAAAAAGTCTTG	
0307_guide49_FP	TTACACATGATTGAAGTTAAGAATGGCGAAG	
0308_guide49RP	CCATTCTTAACTTCAATCATGTGTAAATATATTCTG	
0309_outer_Gibson_RP	CGAAAAGTGCCACCTGACGTCATCTTGTACCTTTTCATTCTCAGC	
0310_guide49_Top_FP	TATTCATATGATTGAAGTTAAAAA	gRNA
0311_guide49_Bottom_RP	AAACTTTTTAACTTCAATCATATG	
0312_guide64_Top_FP	TATTCACATTTTCTTAATATCTGA	
0313_guide64_Bottom_RP	AAACTCAGATATTAAGAAAATGTG	
0335_XPO1_b4_CRISPR_site_FP	CTTCATCTCTTGATATGAAAAATACATTAACGAC	Integration PCR

Plasmids

Table 14 *Plasmids*

Parental plasmids		
Name	**Description**	**Source**
pArl_WR_PCNA1_GS_eGFP	Constitutive episomal expression of *P. falciparum* PCNA1 tagged with eGFP via a short glycine linker; expression of hDHFR to facilitate resistance against WR99210	Julien Guizetti (Center for Infectious Diseases, Heidelberg University Hospital, Heidelberg, Germany)
p3xNLS-2L-mCherry with hsp86-Promoter BSD (3xNLS::mCherry)	Constitutive episomal expression of mCherry tagged with three nuclear localisation signals; expression of blasticidin S deaminase to facilitate resistance against blasticidin S	Darius Klaschka, Marta Machado (Center for Infectious Diseases, Heidelberg University Hospital, Heidelberg, Germany)
pDC2-cam-coCas9-U6.2-hDHFR (pDC2)	Carries insertion site for a homology directed repair template; episomal expression of Cas9, a gRNA and hDHFR to facilitate resistance against WR99210	Markus Lee (Parasites and Microbes Programme, Wellcome Sanger Institute, Hinxton, UK)
New pArl based episomal expression plasmids		
Name	**Description**	**Source**
Note: All plasmids cause expression of hDHFR to facilitate resistance against WR99210		
pARL_WR_PCNA1_F114A_eGFP	Constitutive episomal expression of mutant *P. falciparum* PCNA1 tagged with eGFP via a short glycine linker	This thesis
pARL_WR_PCNA1_ΔNES_eGFP		This thesis
pARL_WR_PCNA1_ΔNLS_eGFP		This thesis
pARL_WR_PCNA1_ΔC_term_eGFP		This thesis
pARL_WR_PCNA1_Y213F_eGFP		This thesis
pARL_WR_PCNA1_ΔNES_Linker_eGFP		This thesis
pARL_WR_PCNA1_ΔNLS_Linker_eGFP		This thesis
pARL_WR_PCNA1_KKKMut_eGFP		This thesis
pARL_WR_PCNA1_FKKMut_eGFP		This thesis
pARL_WR_PCNA1peptide1_eGFP	Constitutive episomal expression of a *P. falciparum* PCNA1-dervied peptide tagged with eGFP via a short glycine linker	This thesis
pARL_WR_PCNA1peptide2_eGFP		This thesis
pARL_WR_PCNA1peptide3_eGFP		This thesis
pARL_WR_PCNA1peptide4_eGFP		This thesis
pARL_WR_PCNA1peptide5_eGFP		This thesis
New pDC2 based CRISPR-Cas9 gene editing plasmids		
Name	**Description**	**Source**
Note: All plasmids cause expression of hDHFR to facilitate resistance against WR99210		
pDC2_WR_PCNA1-GFP_guide624		This thesis

pDC2_WR_PCNA1-GFP_guide738	Endogenous GFP tagging of *P. falciparum* PCNA1	This thesis
pDC2_WR_exportin1_ItoC_guide49	Point mutation of isoleucine 637 to cysteine in endogenous *P. falciparum* exportin-1	This thesis
pDC2_WR_exportin1_ItoC_guide64		This thesis

3.1.5 Computer systems

Workstations and computers

Table 15 *Workstations and computers*

Name	Specifications	Company
HIVE Server	**Storage:** 156TB RAID6 with 2.4GB/s + 10TB RAID5 with 600MB/s writing speed **Processor:** Intel Xeon E5-2683 V4 @2.1GHz (16 cores) **Graphics card**: 1GB NVidia Quadro M5000 **RAM**: 256GB **Network**: 10Gbit/s Netgear M4300-12x12F switch, 240Gbit/s backbone **OS:** Windows Server 2012R	ACQUIFER Imaging (Heidelberg, Germany)
Idip workstation 1	**Processor:** Intel Core i9-7900X CPU @ 3.30Ghz **RAM**: 128GB **OS:** Windows 10 64x	EXTRA Computer GmbH (Giengen an der Brenz, Germany)
Idip workstation 2	**Processor:** Intel Core i9-9940X CPU @ 3.30Ghz **RAM**: 128GB **OS:** Windows 10 64x	EXTRA Computer GmbH (Giengen an der Brenz, Germany)

Software

Table 16 *Software*

Name	Description	Source/reference
Fiji	Open source image processing package based on the ImageJ2 distribution of ImageJ	(Schindelin *et al.*, 2012)
Graphpad Prism	2D graphing and statistics software	GraphPad Software (San Diego, USA)
Leica Application Suite (LAS) X	Leica microscopy user interface	Leica Microsystems GmbH (Wetzlar, Germany)
SerialEM	Electron microscopy tilt series acquisition software	(Mastronarde, 2005)
Snapgene	Molecular biology software used to do in-silico cloning of vectors and inspection and alignment of Sanger-sequencing results	Snapgene (Chicago, USA)
Snapgene Viewer	Free version of Snapgene molecular biology software used to visualize and annotate plasmids and DNA sequences	Snapgene (Chicago, USA)
Volocity	Perkin Elmer microscopy user interface	Perkin Elmer (Waltham, USA)
Zen Blue	Zeiss microscopy user interface and image processing software	Carl Zeiss AG (Oberkochen, Germany)

3.2 Methods

3.2.1 Nucleotide based molecular biology methods

Cloning strategy: Episomal overexpression

To investigate the localisation of proteins and peptides of interest, I expressed selected genes from episomally maintained overexpression vectors. These bacterial plasmids can be introduced into the parasite via electroporation and are replicated alongside genomic DNA during parasite replication (Crabb *et al.*, 1997; O'Donnell *et al.*, 2001). Plasmids are distributed asymmetrically during schizogony, resulting in a heterogenous distribution of plasmids in the parasite population (van Dijk *et al.*, 1997; O'Donnell *et al.*, 2001). Presence of plasmids is enforced by expression of a drug resistance marker from the plasmid and continuous selection against the

corresponding drug during routine cell culture. In absence of drug selection, episomal plasmids are usually lost rapidly, but formation of more stable replicating forms comprised of large concatamers has also been observed (O'Donnell *et al.*, 2001).

All vectors for episomal overexpression of proteins were based on the vector pArl-PCNA1-GS-mEGFP, which was kindly gifted by Julien Guizetti (Center for Infectious Diseases, Heidelberg University Hospital, Heidelberg, Germany). This plasmid carries two *Plasmodium* expression cassettes – one for selection in *P. falciparum* and one for expression of a protein of interest (POI) connected with another protein via a glycine-serine (GS) linker. Here, the POI was the *P. falciparum* replication protein PCNA1, which was tagged with mEGFP and expressed from the constitutively active chloroquine resistance transporter promoter. Additionally, this plasmid carries a bacterial ampicillin resistance cassette for selection in *E. coli*. The original pArl vector expresses the human dihydrofolate reductase (hDHFR) for selection against WR99210 in *P. falciparum* (Hekmat-Nejad and Rathod, 1997; de Koning-Ward *et al.*, 2000).

To introduce alternative sequences into the open reading frame (ORF) before the GS-linker, the restriction enzymes XhoI and AvrII were used. To generate the same pArl plasmids expressing mutated PCNA1 tagged with GFP, cloning was done via an intermediate smaller vector. This minimal PCNA1 vector was created by digestion of the original PCNA1-GS-mEGFP plasmid with NotI and AatII, resulting in removal of all features except the bacterial resistance gene. The minimal vector backbone of approximately 2200 bp was then ligated with a PCNA1 WT fragment. This WT PfPCNA1 fragment was generated through a PCR reaction using primers with long overhangs containing a NotI or an AatII and AvrII restriction site, and was isolated and digested with NotI and AatII prior to ligation. From the approximately 3000 bp long minimal vector containing only a WT PCNA1 sequence flanked by a NotI and AvrII site, all mutants were created by PCR. Mutations were created by generating primers encoding the desired mutations in the 3' end, with primers binding tail-to-tail within the PCNA1 sequence. During PCR with these primers, a single fragment was produced spanning the whole vector, with the desired mutations at each end of the fragment. The 3000 bp long linearized vector carrying the mutations in the PCNA1 sequence was subsequently re-circularized via blunt end ligation. Finally, the mutated PCNA1 sequence was removed from the minimal vector and reintroduced into the pArl overexpression vector in place of WT PCNA1 by restriction digest using the NotI and AvrII enzymes.

For assembly of the sequences encoding for the small PCNA1 derived peptides PCNA1_NES1, PCNA1_NES2 and PCNA1_NLS2, complementary oligos with overhangs corresponding to the regions flanking the NotI and AvrII restriction sites were ordered, annealed and inserted into the linearized plasmid. The sequences for the longer peptides PCNA1_NLS1 and PCNA1_NLS/NES were amplified via PCR using primers with NotI and AvrII cut sites and the original pArl-PCNA1-GS-mEGFP plasmid as a template.

In addition, I used the vector p3xNLS::mCherry (3xNLS::mCherry) (D. Klaschka, M. Machado) which expresses mCherry coupled to three nuclear localisation signals (NLS) from a constitutively active Pfhsp86 promoter. This plasmid also carries a blasticidin resistance cassette for selection in *P. falciparum* and a bacterial ampicillin resistance cassette for selection in *E. coli* (Mamoun *et al.*, 1999). The 3xNLS::mCherry plasmid was based on the p3×NLS-FRB-mCherry nuclear mislocalizer plasmid used in the knock sideways system by Birnbaum *et. al.,* (Birnbaum *et al.*, 2017), and was kindly provided by T. Spielmann (Bernhard Nocht Institute for Tropical Medicine, Parasitology Section, Hamburg, Germany).

An overview of all proteins and peptides expressed from these vectors and their associated reporters and resistances can be found in Tab. 17.

Table 17 *pArl based episomal expression constructs*

Protein/peptide expressed	Other name	Mutation	Tag	Resistance
Proliferating cell nuclear antigen 1 (PF3D7_1361900)	PCNA1	WT	eGFP	WR
Proliferating cell nuclear antigen 1 – single point mutations and deletions	Trimerization mutant	F114A	eGFP	WR
	Phosphorylation mutant	Y213F		
	ΔPf-specific insertion	ΔT246-K254		
	ΔhNES	ΔI11-L22		
	ΔhNES linker replacement	ΔI11-L22-2xGGGGS		
	Triple lysine mutation	KKK13,14,20AAA		
	ΔhNLS	ΔF100-S210		
	ΔhNLS linker replacement	ΔF100-S210-3xGGGGS-1xG_6		
	Triple mutation	FKK103,110,117AAA		
Proliferating cell nuclear antigen 1- derived peptides	NES1	synthetic	eGFP	WR
	NLS1	synthetic		
	NES1/NLS1	synthetic		
	NES2	synthetic		
	NLS2	synthetic		
3x nuclear localisation signal	3xNLS	synthetic	mCherry	BSD

Cloning strategy: CRISPR-Cas9 mediated gene editing

To interrogate protein function on the level of endogenous gene expression, modification of the original genomic sequence is necessary. Traditional methods for gene disruption or editing in *P. falciparum* are based on long-term culture of parasites in presence of episomal templates for homologous recombination upon a stochastic double strand break at the region of interest and until either a single or double crossover event is observed. However, long waiting times and low efficiency make these approaches cumbersome. Therefore, I decided to use the Clustered Regularly Interspaced Short Palindromic Repeats-CRISPR-Associated 9 (CRISPR-Cas9) gene editing system to modify endogenous genome sequences.

Originally discovered in *E. coli* as a defence mechanism against bacteriophages (Jiang & Douda 2017), the CRISPR-Cas9 system can be used to modify genomic DNA in a wide range of organisms, including *P. falciparum* (Ghorbal *et al.*, 2014; Lee and Fidock, 2014). Short guide RNAs (gRNA) are used to target the Cas9 endonuclease to specific, complementary genomic sequences. At the target site, the presence of a protospacer adjacent motif (PAM) with the sequence NGG is critical to allow the Cas9 to induce a double strand break. Therefore, selected genomic target site must have a N20-NGG structure to allow cleavage. Following cleavage, DNA repair mechanisms are initiated by the cell to avoid death. While a non-homologous end joining like repair mechanism has been shown to exist in *P. falciparum* (Kirkman, Lawrence and Deitsch, 2014), other studies indicate that it is likely inefficient and infrequent (Wagner *et al.*, 2014). Consequently, repair is usually mediated by homology directed repair. As *Plasmodium* is haploid during the blood stage this can be exploited by presenting the cell with an episomal repair template carrying the desired mutations.

Thus, for successful CRISPR-Cas9 mediated gene editing three components are essential: expression of the Cas9 nuclease, expression of a 20 bp gRNA to direct the Cas9 endonuclease to the PAM adjacent target site in the genome, and a repair template encompassing homology regions around the target mutation site.

Here, all vectors for CRISPR-Cas9 mediated gene manipulation were based on the vector pDC2-cam-coCas9-U6.2-hDHFR (Fig. 6A) generously gifted by Markus Lee (Parasites and Microbes Programme, Wellcome Sanger Institute, Hinxton, UK) (Lim *et al.*, 2016; Lee *et al.*, 2019). This vector expresses the Cas9 protein fused to three NLS and three hemagglutinin (HA) tags using the PfCalmodulin (cam) promotor and a gRNA from a U6 cassette (Fig. 6A). It additionally encodes a WR99210 resistance cassette expressing hDHFR for selection in *P. falciparum* (Fig. 6A) as well as an ampicillin resistance cassette for selection in *E. coli*. In this vector, gRNA sequences can be inserted into the U6 cassette by digestion of the plasmid using the restriction enzyme BbsI, annealing two overlapping oligos carrying overhangs complementary to the BbsI cut sites and fusion of the annealed oligo with the linearized plasmid. Donor template sequences for homology directed repair can be introduced between the EcoRI and AatII restriction sites by inserting sequences amplified using outer primers with 20+ bp long overhangs at the 5' end that corresponded to the intact sequences adjacent to the cut sites (Fig. 6B).

The 20 bp gRNA target sites were selected to be a maximum of 500 bp up- or down-stream of the desired mutation sites to achieve effective mutation. To this end about 1000 bp of the genomic sequence around the target mutation site was sourced from the data bank PlasmoDB using the *P. falciparum* 3D7 reference sequence (Gardner *et al.*, 2002; Böhme *et al.*, 2019). gRNA sites within this region were compiled using either the protospacer program (MacPherson and Scherf, 2015) or the Eukaryotic Pathogen CRISPR guide RNA/DNA Design Tool (Peng and Tarleton, 2015). Selection of guides was done by comparing distance to target mutation site, efficiency scores (Doench-Root score (Doench *et al.*, 2014)) and uniqueness by comparing to the *P. falciparum* 3D7 PlasmoDB-26 reference genome. Whenever possible, gRNA sequences which overlapped with the mutation target site were chosen, as mutation would then automatically lead to protection against re-cutting

(Fig. 6B). When the selected gRNA did not start with guanine (G) or adenosine (A), a leading G or A was manually added to the oligo sequence before the BbsI compatible overhang. gRNA sequences without the PAM site and with BbsI compatible overhangs were ordered as non-phosphorylated oligos and aligned and inserted into the linearized plasmid as detailed below (Fig. 6B).

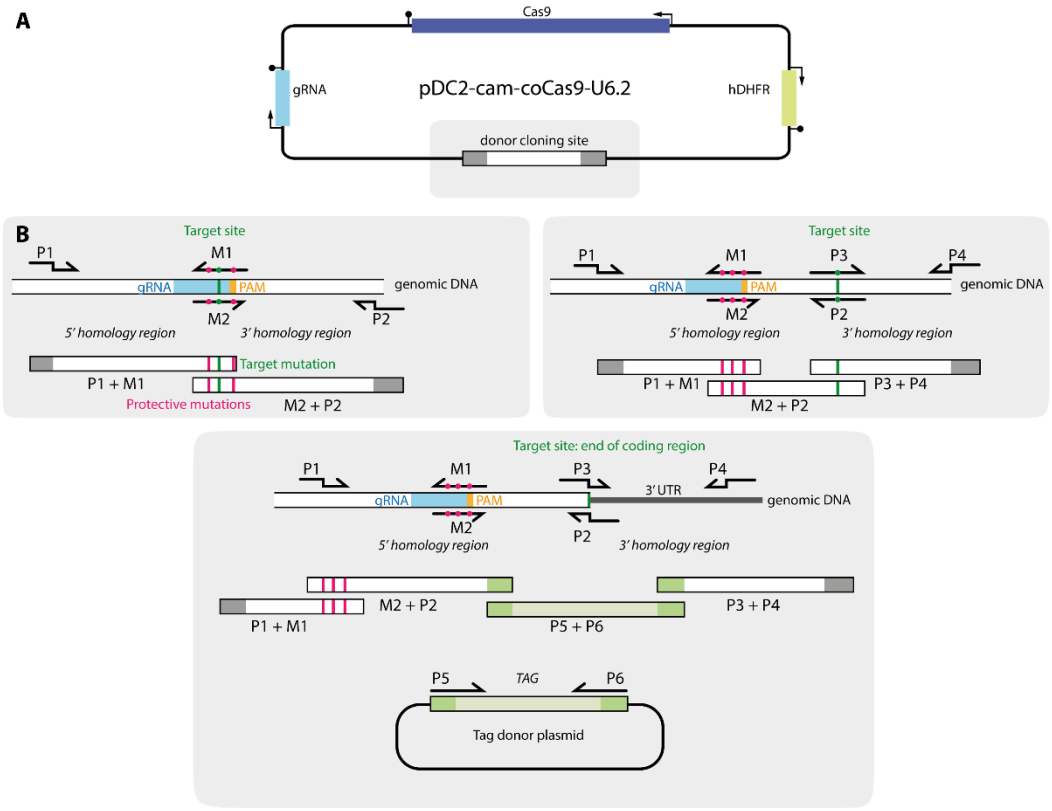

Figure 6 Schematic overview of CRISPR-Cas9 editing plasmid and cloning strategy. *(A) CRISPR-Cas9 editing plasmid. Dark blue, Cas9 expression cassette; light blue, gRNA expression cassette; grey/white, donor cloning site; green, WR99210 resistance cassette. (B) Strategies for cloning of repair donor sequence. Dark green, target site and mutations; magenta, protective mutations; blue, gRNA; orange, PAM; light green, tag; P and M, primers.*

For donor template design, 5' and 3' homology regions around 400 bp and up to 800 bp around the target mutation site were chosen. If the gRNA sequence overlapped with the target mutation site, target mutations as well as protective silent mutations were introduced using overlapping primers with the desired mutations to amplify the donor template as two overlapping fragments (Fig. 6B). Here, the sequence upstream of the target site served as the 5' homology region and the sequence downstream of the target site served as the 3' homology region during homology directed repair (Fig. 6B).

If the gRNA sequence did not overlap with the target mutation site, the donor template had to be designed to include both the target mutation as well as protective mutations in the gRNA sequence to avoid recutting of the edited sequence. Whenever possible, protection against recutting was achieved by introducing silent mutations destroying the gRNA adjacent PAM (Fig. 6B). Alternatively, three silent mutations were introduced in the seed region (Fig. 6B) of the gRNA. Both target mutations and protective mutations were introduced via PCR by using overlapping

primers containing the desired mutations, resulting in the creation of three overlapping fragments (Fig. 6B).

For tagging of endogenous proteins, gRNA sites were chosen close to the stop codon of the target gene (Fig. 6B). In all cases, this resulted in the selection of gRNA sites within the coding region as the 3'UTR is habitually too AT-rich to contain gRNA sequences with a high predicted efficiency. Similarly, all gRNA sequences were at least 100 bp upstream of the stop codon, so that protective mutations had to be introduced independently of the tag. In total four overlapping fragments were amplified: the two parts of the coding region representing the 5'homology region including the protective mutations but without the stop codon, a fragment of the 3'UTR which acts as the 3'homology region, as well as the tag sequence with a stop codon (Fig. 6B). These fragments were either directly inserted into the linearised plasmid at the donor cloning site via Gibson Assembly or – in case assembly was inefficient – first partly fused via overlap extension PCR and/or assembled into a smaller pArl based intermediate plasmid.

An overview of all proteins that were targeted via CRISPR-Cas9 editing as well as the intended genomic change and resistance cassette of the vector can be found in Tab.18.

Table 18 *pDC2 based CRISPR-Cas9 editing targets*

Full name	Abbrev.	Gene ID	Mutation	Guide nr.	Resistance
Proliferating cell nuclear antigen 1	PCNA1	PF3D7_1361900	eGFP tag	624 738	WR
Exportin-1	XPO-1	PF3D7_0302900	I637C	49 64	WR

Isolation of genomic DNA from parasites

Genomic DNA was isolated from blood stage parasites using the DNeasy Blood & Tissue Kit as detailed in the manufacturer's instructions for non-nucleated blood. 200 µl of infected RBCs with a parasitaemia between 1-5% and a majority of multinucleated parasites were used. When DNA could not be extracted on the same day as RBCs were collected, RBCs pellets were stored at -20°C until isolation could be performed. Elution was carried out using a volume of 30-50 µl.

Polymerase chain reaction (PCR)

DNA fragments were amplified via PCR using the Phusion® High-Fidelity DNA Polymerase according to the provided NEB Phusion reaction protocol without DMSO. When DNA fragments had to be isolated post-PCR, 50 µl reactions were used. When PCR was performed for integration checks or to profile bacterial colonies during cloning, the reaction was carried out in a final volume of 25 µl. Generally, 0.5-1 µl of template DNA was used, which contained below 250 ng of DNA. Primers were designed using the SnapGene software, with melting temperatures between 50-55°C. Primers were ordered as an unmodified and desalted lyophilizate and reconstituted in ddH_2O for a stock solution of 100 µM. Stock solutions were stored at -20°C and diluted 1:10 for a final working solution of 10 µM. Pipetting was done on ice and reactions were mixed and briefly pelleted

by centrifugation before amplification was carried out using the cycling conditions listed below. Here, due to the AT-richness of the *P. falciparum* genome, the extension temperature of the PCR reaction was lowered to 68°C or 62°C to reduce processivity errors.

Table 19 *Standard PCR reaction mixture*

Component	25 µl reaction	50 µl reaction	Final concentration
ddH2O	to 25 µl	to 50 µl	
5X Phusion HF Buffer	5 µl	10 µl	1X
10 mM dNTPs	0.5 µl	1 µl	200 µM
10 µM Forward Primer	1.25 µl	2.5 µl	0.5 µM
10 µM Reverse Primer	1.25 µl	2.5 µl	0.5 µM
Template DNA	variable	variable	variable
Phusion Polymerase	0.25 µl	0.5 µl	1.0 units/50 µl PCR

Table 20 *Standard PCR reaction settings*

Step	Temp	Time
Initial Denaturation	98°C	30 seconds
30 Cycles	98°C 50-55°C 62 or 68°C	10 seconds 30 seconds 15-30 seconds per kb
Final Extension	62 or 68°C	10 minutes
Hold	4°C	-

Overlap-extension PCR

Overlap-extension PCR, also called PCR-sewing, was used to fuse overlapping DNA fragments. Homologous regions were generally between 16-32 bp long. First, the individual fragments were synthetized using standard PCR conditions. Then, overlap PCR was performed. For this, PCR was carried out without primers using the reaction and cycling conditions listed below. Here, the overlapping DNA segments act as the initiation point for DNA elongation. DNA fragments were used in an equimolar ratio, which was calculated using the online tool NEBioCalculator (NEBioCalculator v1.15.0). Whenever possible, 50 ng of the largest fragment were used and all other fragments adjusted accordingly. The melting temperature of the homologous regions was used in the annealing step.

Table 21 *Overlap-extension PCR reaction mixture*

Component	25 µl reaction	50 µl reaction	Final concentration
ddH2O	to 25 µl	to 50 µl	
5X Phusion HF Buffer	5 µl	10 µl	1X
10 mM dNTPs	0.5 µl	1 µl	200 µM
Template DNA	variable	variable	variable
Phusion Polymerase	0.25 µl	0.5 µl	1.0 units/50 µl PCR

Table 22 *Overlap-extension PCR reaction settings*

Step	Temp	Time
Initial Denaturation	98°C	30 seconds
15 Cycles	98°C 50-72°C 62 or 68°C	10 seconds 30 seconds 15-30 seconds per kb
Final Extension	62 or 68°C	10 minutes
Hold	4°C	-

After the overlap PCR, the primers flanking the fused fragment were added to the mixture at a final concentration of 0.5 µM and extension PCR was performed using standard PCR conditions with an annealing temperature matching that of the flanking primers. As this method yields multiple bands, the fragment of the correct size was excised after the following agarose gel electrophoresis and purified as specified below.

Restriction digest

Enzymatic restriction digest of DNA was carried out using 1-3 commercially available enzymes from NEB per reaction. For preparatory digest 1 µg of DNA were used in a final volume of 50 µl while 200-500 ng DNA in a final volume of 25 µl were used for characterization of plasmids and colonies during cloning. Whenever possible, digest was done using high-fidelity (HF) enzymes. Incubation was carried out at 37°C for 15 min to several hours depending on reaction efficiency and Time-Saver qualification of the enzymes used. If necessary, 1 µl of Quick CIP (NEB) was added for the last 10 minutes of digestion to dephosphorylate DNA ends, e.g., when linearizing vectors during cloning.

Table 23 *Restriction digest reaction mixture*

Component	25 µl reaction	50 µl reaction
ddH_2O	to 25 µl	to 50 µl
10x Cutsmart Buffer	2.5 µl	5 µl
DNA	variable	variable
Enzyme	0.25 µl (5 units)	0.5 µl (10 units)

Agarose gel electrophoresis

To separate DNA fragments by size, agarose gel electrophoresis (AGE) was performed using 0.8% agarose (w/v in TAE buffer) gels in TAE buffer. DNA was mixed with 6x loading dye supplemented with Midori green and run for 20-30 minutes at 130 V alongside either 5 µl 1 kb or 100 bp ladder. Visualisation of DNA fragments was performed using a UV-transilluminator. If necessary, gel pieces containing specific DNA fragments were excised using a scalpel for subsequent purification.

DNA purification

DNA fragments were recovered from reaction mixtures after PCR or restriction digest using the High Pure PCR Product Purification Kit according to the manufacturer's instructions. Similarly, DNA was recovered from agarose gels following electrophoresis by excision of the target bands from the gel and purification according to manufacturer's instructions in the High Pure PCR Product Purification Kit. In all cases elution was carried out using 35 µl of the included elution buffer.

Oligo annealing

DNA oligonucleotides, e.g., gRNA oligos, were phosphorylated and annealed before insertion into linearized vectors. For this oligos were mixed and annealed using a thermocycler with the reaction parameters listed below.

Table 24 *Oligo annealing reaction mixture*

Component	Volume
ddH_2O	6.5 µl
100 µM oligo 1	1 µl
100 µM oligo 1	1 µl
10x T4 ligation buffer	1 µl
T4 Polynucleotide Kinase	0.5 µl

Table 25 *Oligo annealing reaction settings*

Step	Temp	Time
Phosphorylation	37°C	30 min
Denaturation	94°C	5 min
Annealing	94° → 25°C	6°C/min

The phosphorylated and annealed oligos were subsequently diluted 1:200 in ddH_2O before ligation into the linearised plasmid.

DNA ligation

To ligate DNA fragments with compatible sticky ends, such as annealed gRNA oligos with a linearised vector, T4 DNA ligation was performed. When annealed oligos were ligated, 1 µl of the previously diluted oligos were mixed with 50 ng of linearised vector in a 10 µl reaction volume as detailed below and incubated for 10 minutes at room temperature before transformation into competent bacteria.

Table 26 *Oligo ligation reaction mixture*

Component	Volume
ddH_2O	to 10 µl
Linearised vector (~50 ng)	variable
Annealed oligos (1:200)	1 µl
10x T4 DNA ligase buffer	1 µl
T4 DNA ligase	1 µl

When DNA fragments with compatible sticky ends were ligated, a linearized vector and the digested insert were mixed in a pre-defined ratio in a 10 µl or a 20 µl reaction volume. Generally, an excess of insert (~ molar ratio of 1:3 vector to insert) was used, which was calculated using the online tool NEBioCalculator. For small inserts, the ratio was increased to 1:5 vector to insert. Whenever possible, 50 ng of vector was used, and the insert mass adjusted accordingly. If DNA concentrations were low and the required volumes for 50 ng of vector DNA and the corresponding insert volume exceeded the reaction volume, the amount of vector DNA was decreased to as few as 10 ng. The reaction volume was pipetted on ice as detailed below and left to incubate either overnight at 16°C or at room temperature for 10 minutes. Subsequently, 2 µl of the reaction volume were transformed into competent bacteria.

Table 27 *Standard DNA ligation mixture*

Component	10 µl reaction	20 µl reaction
ddH_2O	to 10 µl	to 20 µl
Linearised vector (~50 ng)	variable	variable
Digested insert	variable	variable
10x T4 DNA ligase buffer	1 µl	2 µl
T4 DNA ligase	0.5 µl	1 µl

Gibson cloning

DNA fragments with overlapping homologous ends were fused using the NEBuilder Hifi DNA assembly reaction. Whenever possible 50 ng of vector were used and inserts were added in pre-determined molar ratios – for reactions involving 2-3 fragments (including the vector) inserts were added in a 1:2 vector to insert molar ratio and for reactions involving 4-6 fragments (including the vector) fragments were added in an equimolar ratio. Fragment volumes were calculated using the online tool NEBioCalculator. The reaction was carried out in a 10 µl reaction volume unless low DNA concentrations necessitated upscaling to a 20 µl reaction. Fragments were assembled in a thermocycler at 50°C for either 15 min (2-3 fragments and reactions involving short fragments below 100 bp) or up to 60 min (4-6 fragments). When 4-6 fragments were fused and assembly proved to be inefficient, insert fragments were pre-assembled for 15 min at 50°C before addition of the vector fragment (and the corresponding amount of Assembly Master Mix) and further assembly for 45 min at 50°C. Subsequently, 2 µl of the reaction volume were transformed into competent bacteria.

Table 28 *Gibson assembly reaction mixture*

Component	10 µl reaction	20 µl reaction
ddH_2O	to 5 µl	to 10 µl
Linearised vector (~50 ng)	variable	variable
Digested insert(s)	variable	variable
NEBuilder HiFi DNA Assembly Master Mix	5 µl	10 µl

Transformation

Plasmid DNA was introduced into commercially available chemically competent *E. coli* via heat shock. *E. coli* cells were thawed and 50 µl of cell suspension added to pre-prepared DNA mixtures without pipetting up and down. The transformation mixture was incubated for 30 minutes on ice, before heat shock was applied for 30 sec at 42°C. Bacteria were left to recover for 5 min on ice, before addition of 950 µl of SOC outgrowth medium and pre-culture for 1 h at 37°C and 600 rpm on a benchtop incubator.

Plasmid amplification and purification

Plasmids were cloned and amplified after transformation of ligation mixtures by plating the transformed bacteria onto LB agar plates containing 50 µg/ml ampicillin. For this, the pre-cultured transformation mixture was spun down for 3 min at 1000 g, the supernatant decanted, and the bacteria pellet resuspended in the remaining supernatant before transferring it to a pre-warmed LB agar plate. The bacteria were spread on the LB plate using either a pipet tip or an inoculation loop and incubated overnight at 37°C until white bacterial colonies were visible. Subsequently, individual colonies were picked and amplified in 2-3 ml of LB broth containing 50 µg/ml ampicillin by incubation overnight at 37°C and 135 rpm in a bacterial shaker (miniprep). Plasmid DNA was isolated from the bacterial mixtures using the GenEluteTM HP Plasmid Miniprep Kit according to manufacturer's instructions. Elution was carried out using 35 µl of the provided elution buffer.

For long term storage, some of the bacterial solution was mixed 1:1 with 50% glycerol in ddH_2O, transferred to a cryotube and stored at -20 or -80°C.

When plasmid DNA was prepared in larger quantities, e.g., for transfection of *P. falciparum* asexual blood stages, 200 ml of LB medium with 50 µg/ml ampicillin were inoculated with bacterial solution, either from leftover solution after miniprep, glycerol stocks or from pre-culture after retransformation of a plasmid. Bacteria were grown overnight at 37°C and 135 rpm in a bacterial shaker (midiprep). Plasmid DNA was isolated from the bacterial mixtures using the NucleoBond Xtra Midi Plus Kit with a finalizer according to manufacturer's instructions. Elution was carried out using 400-600 µl of the provided elution buffer.

DNA sequencing

DNA was sequenced using the SupremeRun Tube Sanger Sequencing service of eurofins genomics (previously GATC). For this, samples and primers were prepared according to the sample submission guidelines provided online and sent for sequencing in standard Eppendorf tubes at room temperature. Results were usually received within 1-3 days post sample submission and examined and aligned to in-silico created reference constructs using the SnapGene software. Sequencing was examined for quality by inspecting base calling files for double peaks, signal-to-noise ratio as well as sequence length before degradation of base calling peaks.

Preparation of DNA for transfection

DNA was purified for transfection into *P. falciparum* blood stages via DNA precipitation. For each transfection 100 µg of DNA were used in total. When multiple plasmids were transfected at the same time, the DNA amount was equally divided between the plasmids, e.g., 50 µg plasmids 1 and 50 µg plasmid 2. DNA was precipitated by adding 0.1 volumes 3M NaAcetate and 2.5 volumes 100% ethanol, briefly agitating and incubating the precipitation mixture at -80°C for at least 30 min and up to overnight. After precipitation the sample was pelleted at 4°C for 15 min at maximum speed (usually 21000 g). From this point onward, the sample was treated under sterile conditions in the cell culture hood. The DNA pellet was washed twice with 500 µl 70% ethanol, all liquid removed, and the pellet air-dried in the hood until it changed appearance from white to completely transparent. The DNA was then fully resuspended in 30 µl of sterile TE buffer and stored at -20°C until transfection.

3.2.2 Cell biology methods

Maintenance of parasite lines

Parasites were routinely cultured in complete RPMI (cRPMI; see Media, Buffers and Solutions) at 4% haematocrit in unwashed peripheral human 0+ red blood cells (RBCs) using standard 10 cm cell culture dishes in an incubator maintaining 90% humidity, 3% CO_2 and 5% O_2 (Trager and Jensen, 1976). Parasitaemia was monitored via microscopic inspection of thin blood smears fixed in 100% methanol and stained using Hemacolor rapid staining of blood smear solutions II and III. Parasites were observed using the 100x oil objective on a Zeiss Axiostar Plus or a Nikon Eclipse E100 microscope. Parasitaemia was calculated as the percentage of

iRBCs to total RBCs in 3-10 counting grids included in the microscope ocular. During standard cell culture conditions, a parasitaemia between 0.1-3% was maintained by passaging cultures 2-3 times a week. When a high parasitaemia (over 3%) was required for longer periods, the haematocrit was decreased to 1-2% to avoid cell death due to nutrient depletion of media.

Freezing of parasite line

P. falciparum blood stages may be cryopreserved by stepwise addition of a glycerol-containing freezing solution (Tab. 29) to pelleted iRBCs before storage at -80°C or in liquid nitrogen. Parasite survival during cryopreservation is dependent on the parasite stage, with chance of survival decreasing with parasite age. Therefore, cultures should contain microscopically detectable ring stage parasites in a thin blood smear on the day of freezing.

For freezing, iRBCs were pelleted in a 50 ml falcon tube for 5 min at 800 g and the supernatant discarded. Subsequently, 40% (v/v) of freezing solution was added. The solution was incubated for 5 minutes at RT before addition of another 120% (v/v) of freezing solution under constant agitation in a drop-wise fashion. After incubation for another 5 min at RT, a final volume of 240% (v/v) freezing solution was added, again under constant shaking in a drop-wise fashion. The solution was then partitioned into cryotubes at around 800-1000 µl per tube and rapidly transferred to storage at -80°C. Vials containing frozen iRBCs may be transferred to liquid nitrogen for long term storage.

Table 29 *Freezing of asexual blood stages solution volumes*

Component	Volumes
iRBCs pellet	400 µl
40% (v/v) freezing solution	160 µl
120% (v/v) freezing solution	480 µl
240% (v/v) freezing solution	960 µl
Final mixture	2000 µl

Thawing of parasite lines

Cryopreserved iRBCs can be thawed by stepwise addition of salt solutions with different molarities (Tab. 30). Specifically, frozen iRBCs were warmed by hand until the solution turned fully liquid. The solution was then transferred to a 50 ml falcon before dropwise addition of 0.2% (v/v) of a 12% NaCl (w/v) solution under constant agitation.

Table 30 *Thawing of asexual blood stages solution volumes*

Component	Volumes
Frozen iRBCs solution	800 µl
0.2% (v/v) 12% NaCl (w/v)	160 µl
9% (v/v) 1.6% NaCl (w/v)	7200 µl

After 5 min of incubation at RT, another 9% (v/v) of a 1.6% NaCl (w/v) solution were added in a dropwise fashion under constant agitation. The thawed iRBCs were then pelleted by centrifugation at 800g for 2 min, the supernatant removed, and the pellet resuspended in 10 ml cRPMI. The mixture was transferred to a fresh 10 cm dish and 200 µl of fresh RBCs were added before transferring to the incubator. A

more accurate 4% haematocrit was established during subsequent passaging. For cell lines requiring constant selection pressure, the corresponding drugs were added 24 h after thawing.

Parasite synchronisation

Parasites were synchronized either by enriching hemozoin-containing stages via magnetic purification, osmotic lysis of late-stage parasites or by stopping invasion for specific time periods through heparin treatment. To obtain tightly synchronized stages, several methods were usually combined, e.g., parasites were cultured in the presence of heparin until a time when a high number of segmenters were present, before heparin was removed, hemozoin-containing parasites isolated and invasion was allowed for a pre-defined time period. Osmotic lysis was then applied to the culture to remove the remaining late stages and obtain a highly synchronized culture.

Magnetic purification was done using a magnetic activated cell sorting (MACS) system, specifically the VarioMACS system from Miltenyi Biotec. Late-stage hemozoin-containing *P. falciparum* parasites are weakly magnetic due to the presence of Fe(III) paramagnetic complexes in hemozoin (Ribaut *et al.*, 2008; Coronado, Nadovich and Spadafora, 2014). When the MACS column is placed into the strong, magnetic field of the MACS separator, the presence of ferromagnetic spheres in the column amplifies the magnetic field by 10,000, which allows for the retention of hemozoin-containing cells (Paul *et al.*, 1981; Ribaut *et al.*, 2008). Prior to loading of parasites, the MACS column was washed twice with prewarmed MACS buffer. Cultures were then slowly passed through magnetic MACs columns at an elution speed of one drop per 3 seconds. After washing with prewarmed MACS buffer until the elution solution ran clear in order to remove uninfected RBCs and early-stage parasites, the late-stage parasites can be collected by removing the column from the separator and eluting in 10 ml of prewarmed MACS buffer, thereby concentrating the late-stage parasites into a parasitaemia of almost 100%. The collected iRBCs were then pelleted by centrifugation, the supernatant discarded, and the pellet resuspended in the appropriate solution for the following experiment.

Late-stage parasites can be selectively removed from cultures through osmotic lysis via sorbitol treatment (Lambros and Vanderberg, 1979). Lysis is dependent on the presence of new permeation pathways (NPPs) in the membranes of both host and parasite cell, which increases from the early trophozoite stage onward. To achieve lysis, iRBCs were pelleted from culture by centrifugation at 800 g for 2 min. The iRBCs were then resuspended in 8-10 ml 5% D-sorbitol solution per 400 µl of iRBC pellet. The mixture was incubated 10-12 min at 37°C in a water bath and inverted several times every 2-3 min. Subsequently, the mixture was pelleted again at 800g for 2 min, the pellet washed 1-2 times with 8-10 ml cRPMI per 400 µl of iRBC pellet, before the synchronized iRBC pellet was resuspended in an appropriate amount of cRPMI supplemented with selection drugs when required.

Heparin and heparin-like molecules can inhibit the growth of asexual *P. falciparum* parasites by interfering with invasion (Boyle *et al.*, 2010). Therefore, parasites can be synchronized by incubation of cultures with heparin to stop invasion until a

predetermined time point, when heparin can be removed by washing, allowing parasites to invade from this point onward. For this heparin was added to the cell culture medium at 50 U/ml during continuous culture. To allow invasion, heparin was removed by pelleting the iRBCs from culture at 800 g for 2 min and washing twice with cRPMI.

Transfection of parasites

Transfection of blood stage *P. falciparum* parasites with plasmid DNA was carried out using two different protocols, which both require a total of 100 µg of DNA per transfection and young, synchronized ring stage parasites with a parasitaemia between upwards of 4% (Wu *et al.*, 1995). Young, synchronized parasites were generated by several rounds of sorbitol synchronisation (Lambros and Vanderberg, 1979).

Protocol one was carried out in 10 cm dishes using 200 µl iRBCs and required daily actions for one week after transfection before transitioning to maintenance actions twice per week. As this was both time and material intensive, some of the later transfections were carried out using an alternative protocol, where transfection is done in a 6-well plate using 150 µl iRBCs per transfection. This second protocol additionally requires only 4 steps in the week directly after the transfection before it transitions into maintenance actions trice a week.

For protocol one, 200 µl iRBCs per transfection were pelleted from culture by centrifugation at 800 g for 2 min. iRBCs pellets covered with supernatants were kept in the water bath at 37°C while one 10 cm dish containing 10 ml cRPMI and 200 µl fresh RBCs per transfection were prepared.

Transfections were carried out one at a time. First, the supernatant was removed from one prepared iRBCs pellet. Then, while using the same pipet tip, 30 µl DNA in TE buffer were first mixed with 370 µl prewarmed cytomix and the pre-prepared 200 µl iRBCs (van den Hoff, Moorman and Lamers, 1992). The transfection mixture was transferred bubble-free to a 2 mm electroporation cuvette and electroporated at 0.31 kV and 950 µF (Wu *et al.*, 1995). The electroporated mixture was then rapidly transferred to the prepared 10 cm dish by decanting and washing with cRPMI from the culture dish. Transfected cultures were then immediately returned to the incubator for recovery.

Parasites were left to recover for 6-12 h before medium change and addition of the selection drug(s) corresponding to the resistance cassette of the transfected plasmid. Over the following week media was changed and parasite death was monitored with thin blood smears. On day 3 and 5 post transfection 50 µl fresh RBCs was added to each dish; on day 8 post transfection the culture was split 1:2. From this point onwards the media was changed twice a week. Additionally, once a week in an alternating schedule 50 µl of fresh RBCs was added or the culture was split 1:2 until parasites could be observed in a thin blood smear. If no parasites were observed at 80 days post transfection, the transfection was considered a failure and the culture was discarded.

For protocol two, one well of a 6-well plate per transfection was prepared with 7 ml cRPMI and 120 µl fresh RBCs. Only alternate wells were filled to avoid cross-

contamination and the plate(s) were then pre-incubated until needed. In addition, 1 15 ml-falcon per transfection containing 5 ml cRPMI was prewarmed to 37°C and one 2 mm electroporated cuvette per transfection was cooled to 4°C for at least 30 min prior to transfection.

Transfection was carried out 1-3 reactions at a time to avoid long waiting times between the different steps. 150 µl of iRBCs were pelleted by centrifugation at 800 g for 2 min and washed once with 2.25 ml prewarmed cytomix per 150 µl iRBCs before all supernatant was removed. The iRBC pellet was pipetted into the Eppendorf tube containing the thawed plasmid and mixed slowly by pipetting up and down 10 times. Then, 300 µl of prewarmed cytomix were added to the blood/plasmid mixture and again mixed by slowly pipetting up and down 10 times. Each batch of transfections was prepared to this point.

The transfection mixture was then transferred air bubble-free to a 2 mm wide electroporation cuvette and electroporated at 0.31 kV and 950 µF. The electroporated solution was resuspended without pipetting up or down in 1 ml prewarmed cRPMI of the previously prepared 15 ml-falcon and gently transferred back to the 15 ml-falcon with the remaining 4 ml of medium. The remaining electroporated mixture was removed from the cuvette by tilting the cuvette and transferring the solution with the same pipet tip. The transfected culture was then left to recover in the 15 ml-falcon for 30 min in the incubator.

After recovery, all transfected cultures were pelleted by centrifugation for 2 min at 800 g. The supernatant containing lysed red blood cells and cell debris after transfection was removed by aspiration and the pellet gently resuspended in 3 ml of cRPMI from one well of the previously prepared 6-well plate and transferred to the well.

On the day after transfection the medium of the culture was changed to 5 ml of cRPMI containing the appropriate selection drug(s). Parasites were monitored via thin blood smear and should be late stages. On day 2 post transfection the medium was changed again, and parasites observed via thin blood smear – parasites should be arrested at the trophozoite/schizont stage and no new ring stages should be visible. On day 3 post transfection the transfected cultures were split 1:5. Subsequently, from day 6 or 7 post transfection the cultures were maintained by exchanging medium twice a week and splitting once per week 2:3. Parasitaemia was monitored via thin blood smears once per week until parasites could be detected. If no parasites were observed at 80 days post transfection, the transfection was considered a failure and the culture was discarded.

Cloning of parasite lines

Parasite lines were cloned using limited dilution. For this, a 2% haematocrit solution was cultured at 200 µl per well in a 96-well plate format at a starting density of 0.3 parasites per well. The initial dilution required to reach the starting density of 0.3 parasites per 200 µl (corresponding to 30 parasites in 20 ml) was calculated based on the starting parasitaemia calculated from counting 3 times 10 fields of a thin blood smear.

For this an initial dilution to a 0.1% parasitaemia was performed according to the following formulas:

X = initial parasitaemia
0.1 = target parasitaemia
X/0.1 = dilution factor

From this initial dilution the culture was further diluted 1:1000, resulting in a culture with a parasitaemia of 0.0001%. A culture with a 0.0001% parasitaemia contains 1 parasite in 1,000,000 RBCs. At a volume of 150 fl per RBC, this corresponds to 1 parasite in 0.15 µl of iRBCs and 30 parasites in 4.5 µl of iRBCs. Therefore, to achieve the final concentration of 30 parasites/20 ml, a volume corresponding to 4.5 µl of blood (112,5 µl in case of a 4% haematocrit culture with a 0.0001% parasitaemia) was transferred to 10 ml of a 2% haematocrit mixture.

The solution was pipetted into all wells of a 96-well U-bottom plate except the border wells. Instead, the border wells were filled with 200 µl PBS to prevent evaporation. The cells were kept undisturbed at standard culture conditions for 2 weeks before individual wells were examined. Either wells were examined for plaques using a 40 x air objective on an inverted Leica DM IL microscope or thin blood smears from a subset of wells were examined. For those samples showing no parasites, medium was exchanged once per week without agitating the RBC layer and monitoring continued once a week until either parasites were apparent, or 6 weeks had passed.

The content of those wells showing either a single plaque or parasites in thin blood smears were resuspended und transferred into 1 ml fresh medium on a 24 well plate. Clonal cultures were monitored for parasitaemia and sequentially passaged into bigger volumes until reaching high enough volumes and parasitaemia for cryogenic preservation. Cells were frozen at least on two different occasions and gDNA was extracted for genomic profiling via PCR.

P. falciparum SYBR green growth assay

P. falciparum blood stage growth assays were performed over two asexual growth cycles. Cells were seeded in 100 µl in a well of a 96-well plate at 0.15% parasitaemia and a 2% haematocrit in triplicate with drug or carrier concentrations corresponding to the desired concentrations, excluding the outer wells, which were filled with PBS to avoid evaporation effects. Subsequently, cells were cultured for 96 h at standard culturing conditions. After 96 h, 20 µl of SYBR green solution was per well, the plate was covered and incubated for 24-48 h in the dark at RT. Subsequently, fluorescence in the individual well was read out using a plate reader with excitation at 494 nm and emission at 530 nm. Values were normalised to the mean fluorescence intensity of the triplicates of 3D7 wild type parasites treated with the lowest concentration of the carrier control.

3.2.3 Protein based molecular biology methods

Parasite harvesting, co-immunoprecipitation and western blot analysis was performed by and according to a protocol developed by W. Straßburger during her Master's thesis. This protocol was adapted from a protocol provided by M. Brochet

(Department of Microbiology and Molecular Medicine, Faculty of Medicine, University of Geneva, Geneva, Switzerland) which has previously been successfully used to profile parasite protein interaction partners (Balestra *et al.*, 2021).

Co-immunoprecipitation

For co-immunoprecipitation, 6 ml of iRBCs with a parasitaemia of more than 4 % and at least 40% multinucleated stages were used. Samples were processed in batches of 2 ml iRBCs. Prior to harvesting, 10 µl of each culture containing 2 ml iRBCs was diluted 1:500 in PBS to determine the number of RBCs per ml using a Neubauer counting chamber according to the following formula.

2 ml of iRBCs were pelleted by centrifugation at 340 g for 5 min with acceleration set to 9 and braking set to 4. The supernatant was removed, and RBCs lysed by incubation with 10 ml pre-warmed cRPMI containing 0.1 % Saponin and 1x cOmlpete™, EDTA-free Protease Inhibitor Cocktail per 2 ml of iRBC pellet. Lysis solutions were directly transferred to 15 ml Falcon tubes and pelleted at 3000 g for 6 min. Supernatants containing visible amounts of parasites were reserved. Pellets were resuspended again in 10 ml pre-warmed RPMI containing 0.1 % Saponin and 1x cOmlpete™, EDTA-free Protease Inhibitor Cocktail and pelleted again at 3000 g for 6 min together with the previously reserved supernatants. All supernatants were removed and all pellets belonging to the same 2 ml iRBC batch were merged and resuspended in 500 µl RPMI in a 1.5 ml reaction tube.

For crosslinking of proteins, fresh 16 % formaldehyde was added to each resuspended parasite pellet to a final concentration of 1 %. Crosslinking was carried out for 10 min at RT under constant gentle agitation in a fume hood. Parasites were then pelleted by centrifugation for 6 min at 1000 g, the supernatants removed, and the cross-linking reaction quenched by sequential addition of first 1 ml and then 9 ml of a 0.125 M glycine solution in PBS per pellet. Quenching was carried out for 5 min at RT under gentle agitation. Samples were then pelleted for 10 min at 1000 g, the supernatant discarded, and parasite pellets stored at -80 °C.

To ensure sample integrity, cross-linked samples were slowly thawed on ice prior to lysis. For lysis 1 ml of RIPA buffer supplemented with freshly added DTT and cOmlpete™, EDTA-free Protease Inhibitor Cocktail was added per 1 x 10^9 parasites. Lysis was carried out for at least 30 min on ice, while passaging the solution through a 0.3 mm needle around 10 times or until the sample turned viscous. 30 µl of sample (whole cell lysate) was mixed with 10 µl of 4 x Laemmli buffer and stored at -20°C. To ensure complete lysis and breakdown of hemozoin, the whole cell lysate was sonicated for 13 min (30 sec on/off) at 4 °C. Cell debris was pelleted by centrifugation at 4 °C at 21,000 g for 30 min. The protein-containing supernatant (input) was transferred to a new Protein LoBind tube and stored at -20°C until co-immunoprecipitation. 30 µl of input samples was mixed with 10 µl of 4 x Laemmli buffer and stored at -20°C.

Immunoprecipitation of proteins using GFP-Trap Dynabeads was performed according to the manufacturer's protocol with minor modifications. Briefly, all steps were carried out as described but cOmlpete™, EDTA-free Protease Inhibitor

Cocktail was added freshly to the Wash buffer during the washing step. Proteins were eluted using 40 µl of 4 x Laemmli buffer.

SDS-PAGE

Samples were boiled for 5-10 min at 95°C and remaining hemozoin pelleted by centrifugation at 21,000 g for 5 min before gel electrophoresis. Samples were loaded on a pre-cast gel with chambers holding a maximum of 35 µl (Mini-PROTEAN TGX Precast Gels). For reference, 5 µl of a stained protein ruler (Precision Plus Protein Dual Color Standards) was loaded in one lane. Electrophoresis was performed at 140 V for approximately 40 min in a 1x SDS Running buffer freshly diluted from the 10 x stock.

Mass spectrometry (MS)

Liquid Chromatography (LC)-MS was performed at the Core Facility for Mass Spectrometry & Proteomics (CFMP) at the Zentrum für Molekulare Biologie der Universität Heidelberg (ZMBH). Within the facility, samples were separated via SDS-PAGE for 1 cm on a pre-cast gel and stained with a Coomassie stain. Each lane corresponding to one sample was cut in two and analysed separately. Proteins were digested in-gel before analysis via LC-MS with a separation of 25 min. Gene ontology enrichment analysis was performed with PlasmoDB.

3.2.4 Microscopy methods

Life-cell imaging: short-term

For short-term observation of live parasites to evaluate expression of fluorescent proteins, 10 µl of resuspended culture was pipetted onto a microscopy glass slide and covered with a square 22 x 22 mm glass coverslip. The edges of the coverslip were sealed using a 1:1:1 wool fat, paraffin, Vaseline mixture heated to just below 100°C that immediately solidifies upon application to the slide. Cells were immediately observed using either a Leica SP8 TCS DLS microscope in the confocal mode using a 63 x/1.4 HC PL APO CS2 oil objective or Zeiss Axio Observer microscope using a 63 x oil objective. When appropriate, parasite nuclei were stained using Hoechst 33342 (Hoechst) by incubating 100 µl of a resuspended culture at 1:1000 for 10 min at 37°C in an Eppendorf tube before application to the microscopy slide.

Preparation of imaging dishes

When parasites were imaged for longer time periods or prepared for immune fluorescence assays (IFAs), iRBCs were seeded as monolayers in glass bottom microscopy dished according to Grüring et al (Grüring and Spielmann, 2012) with minor modification. Parasites were seeded and, when needed, imaging medium was prepared at least 4h prior to microscopy to allow parasites time to recover from seeding and to allow imaging medium to equilibrate to incubator gas conditions. Cells were either seeded into concanavalin A coated wells of 8-well glass bottom ibidi dishes, concanavalin A coated 3.5 mm round glass bottom dishes or directly into PBS-washed ibidi-treat 8 well dishes. Volumes used during seeding can be found in Tab. 31.

Dishes were coated by applying 5 mg/ml concanavalin A and incubating for 20-30 min at 37°C. Concanavalin A was removed and the dish washed 3 times with prewarmed PBS before cell suspensions were applied. To prepare cell suspensions, resuspended parasites were taken from culture, spun down for 30s at 800g, the supernatant removed, and the pellet washed twice with iRPMI. Subsequently, iRBC pellets were resuspended in iRPMI and applied to the prepared imaging dish. Cells were left to settle for 10 min at 37°C in the incubator before unattached iRBCs were removed by washing with cRPMI. When only a thin golden layer of RBCs remained, cells were covered with cRPMI and cultured with an open lid at standard conditions until imaging was started or cells were fixed.

Table 31 *Imaging dish preparation solution volumes. Asterisk, resuspension in 1000 µl, of which 300 µl are used for seeding.*

Solution	Vol./well in 8-well ibidi-treat dish	Vol./well in 8-well glass bottom dish	Vol./dish in 35 mm glass bottom dish
5 mg/ml Concanavalin A	-	80 – 100 µl	200 µl
PBS	250 µl	250 µl	500 µl
Resuspended culture	150 µl	150 µl	500 µl
iRPMI - washing	250 µl	250 µl	500 µl
iRPMI - seeding	250 µl	250 µl	300 µl (of 1000 µl)*
cRPMI - recovery	500 µl	500 µl	5 ml

Immune fluorescence assays

Generally, immune fluorescence assays were performed in either ibidi-treat or glass bottom 8-well dishes according to Mehnert *et. al.,* (Mehnert, Simon and Guizetti, 2019). Briefly, cells were quickly rinsed with PBS before fixation with either freshly prepared, prewarmed 4% PFA in PBS or freshly prepared, prewarmed 4% PFA/0.0075% GA in PBS for 20 min at 37°C. Cells were rinsed once with 250 µl PBS per well, before permeabilization with 0.1% Triton X-100 in PBS for 15 min at RT. Cells were washed three times with PBS, quenched with 0.1 mg/ml NaBH4 in PBS for 10 min at RT, again washed three times with PBS and blocked for 30 min to 1h at RT with 3% BSA in PBS. Incubation with primary antibodies was carried out for 1-2 h on a rocking platform at RT in 3% BSA in PBS. Cells were washed 3 times for 5-10 minutes with 0.5% Tween-20 in PBS on a rocking platform before incubation with secondary antibodies and/or Hoechst in 3% BSA in PBS for 30 min to 1h at RT in darkness on a rocking platform. Finally, cells were washed two times for 5-10 minutes with 0.5% Tween-20 in PBS and once with PBS on a rocking platform before imaging.

Generally, PFA only fixation was performed when using antibodies due to the improved specificity and effectivity of staining, while PFA/GA fixation was used when observing fluorescent proteins directly. All used antibodies and their dilutions can be found in Tab. 7. Microscopy dishes with cells covered by PBS could be stored at 4°C for several days after fixation or up to several weeks/months after staining.

Images were acquired at a Leica SP8 TCS DLS microscope in the confocal mode using a 63 x/1.4 HC PL APO CS2 oil objective. Depending on the fluorophores, four different lasers were used: a 50 mW 405 nm UV laser, a 65 mW Argon 488 nm laser, a 20 mW diode-pumped solid-state (DPSS) Yellow 561 nm laser and a

10 mW Helium-Neon (HeNe) 633 nm laser. Pictures were acquired with the pinhole set to 1 AU at a pixel size of 28-66 nm, scanning bidirectionally at a scan speed of 700 lines per second. 6.5 µm image stacks were acquired with a z-spacing of 130-300 nm. Depending on the purpose of the imaging and the number of fluorophores imaged, multichannel images were acquired sequentially using HyD or PMT detectors in the standard mode, with detector ranges and sequences as proposed by the LAS X Dye Assistant at the setting with minimal bleed-through. When sequential acquisition of fluorophores was done, stack sequential acquisition was selected. For PMT detectors, the gain was adjusted to 800-900 V while offset was minimally adjusted to ≤1%. Laser intensity settings were adjusted depending on signal intensity but never exceeded 20%. Brightfield images were acquired from a transmitted light PMT detector with a variable gain adjusted to the available photons from excitation. When appropriate, images were processed with the Lightning algorithm in the adaptive mode using default settings.

Table 32 *IFA microscope settings*

Light range	Fluorophore	Laser	Comment
Blue	Hoechst 33342	405 nm	Due to the long emission tail of Hoechst, its signal was never acquired in the same acquisition sequence as green light emitters
Green	eGFP Alexa488+	488 nm	GFP and far-red fluorophores were usually imaged together as their absorption and emission spectra are well separated
Red	mCherry Spy555 DNA Atto594	561 nm	Red fluorophores were usually imaged together with either Hoechst or GFP as their absorption and emission spectra are generally well separated
Far-red	5-SiR-Hoechst Atto647(N)	633 nm	GFP and far-red fluorophores were usually imaged together as their absorption and emission spectra are well separated

Life-cell imaging: long-term

Prior to imaging, the culture medium of the prepared imaging dish was exchanged to phenol-red free imaging medium (750-800 µl per well for 8-well dishes and 8-9 ml for 35mm round dishes) filling as much of the well/imaging dish as possible. When parasites were stained using DNA or tubulin dyes, imaging medium supplemented with the appropriate concentration of dyes was added 2-3 hours before start of imaging. Directly before imaging, the dishes were closed tightly and sealed with parafilm before transportation to the microscope in a prewarmed metal transport box.

Imaging parameters were dependent on the instrument as well as the intent of the experiment. Generally, three microscopes were routinely used for long-term live cell imaging: a Leica SP8 TCS DLS microscope, a PerkinElmer UltraVIEW VoX spinning disk microscope with a CSU-X1 spinning disk head and a Nikon TiE microscope body or a Zeiss Airyscan 2 LSM900 microscope. An overview of the microscopy settings used for the different microscopes and experiments can be found below.

The PerkinElmer UltraVIEW VoX spinning disk microscope was used at 37°C using an Apo TIRF 60 x/1.49 N.A. oil immersion objective (pixel size 220 nm) or

a Plan Apo VC 100x/1.4 N.A. oil immersion objective in combination with a 1.5 manual zoom (pixel size 88 nm). Depending on the application, 2 or 3 solid state lasers with excitation at 488, 561 or 640 nm and matching emission filters were used. Image stacks ranging from 17 x 0.5 µm to 13 x 0.5 µm were acquired. Images were acquired with a Hamamatsu sensitivity C9100-23B EM-CCD camera at multiple positions using an automated stage and the Perfect Focus System for focus stabilization with a time-resolution of 5 min/stack. Brightfield images were acquired from a transmitted light source in parallel.

Table 33 *PerkinElmer UltraVIEW VoX spinning disk live-cell imaging microscope settings*

Fluorophore	Laser	Exposure time	Laserpower
eGFP	488 nm	100 ms	4% (60x), 6% (100x)
mCherry	561 nm	100 ms	4% (60x), 6% (100x)
SiR-coupled dyes	640 nm	100 ms	6% (60x), 10% (100x)

The Leica SP8 TCS DLS microscope was used in the confocal mode at 37°C using the 63 x/1.4 N.A. HC PL APO CS2 oil immersion objective. Generally, for live-cell imaging, 3 different lasers were used: a 65 mW Argon laser for excitation at 488 nm, a 20 mW diode-pumped solid-state (DPSS) Yellow laser for excitation at 561 nm and a 10 mW Helium-Neon (HeNe) laser for excitation at 633 nm. Pictures were acquired with the pinhole set to 1AU at a pixel size of 103.17 nm, scanning bidirectionally at a scan speed of 700 lines per second. Image stacks of either 9 x 0.5 µm (3xNLS::mCherry only) or 4 x 0.75 µm (3xNLS::mCherry, PCNA1::GFP and 5'SiR-Hoechst) were acquired. Images were acquired at multiple positions using an automated stage and the Adaptive Focus Control (AFC) in the best focus mode for focus stabilization with a time-resolution of 5 min/stack. Depending on the purpose of the imaging and the number of fluorophores imaged, multichannel images were acquired sequentially using HyD or PMT detectors in the standard mode. Detector ranges were adjusted for optimal acquisition without bleed through and channels acquired in stack sequential mode. For PMT detectors, the gain was adjusted to 800V while offset was not adjusted. Brightfield images were acquired from a transmitted light PMT detector with a variable gain adjusted to the available photons from excitation.

Table 34 *Leica Sp8 TCS DLS live-cell imaging microscope settings*

Fluorophore	Laser	Detector	Laserpower
eGFP	488 nm	HyD	1.4%
mCherry	561 nm	PMT	3.8%
SiR-coupled dyes	633 nm	HyD	4%

The Zeiss Airyscan 2 LSM900 microscope was used in the super resolution (SR) mode at 37°C using a Plan-Apochromat 63 x/1.4 N.A. DIC oil immersion objective. Depending on the application 2-3 different diode lasers were used: a 10 mW 488 nm laser, a 10 mW 561 nm laser and a 5 mW 640 nm laser. Emission detection with the Airyscan detector was configured according to the used fluorophores using variable dichroic mirrors at a gain of at a gain of 700-900 V. Images were acquired at multiple positions using an automated stage and the Definite Focus module with a time-resolution of 10 min/stack. Pictures were acquired sequentially in the line-scanning mode using Nyquist optimised setting in xy (pixel size ~50 nm), scanning

bidirectionally with a pixel dwell time of 0.73 µs. Image stacks of 6 µm were acquired with a z-spacing of 600 nm. Brightfield images were acquired from a transmitted light PMT detector after excitation using the 640 nm laser at a gain of 700-900 V. Images were subsequently processed using 2D Airyscan processing with automatically determined default Airyscan Filtering strength with the Zen Blue 3.1 software.

Table 35 *Zeiss Airyscan 2 LSM900 live-cell imaging microscope settings*

Fluorophore	Laser	Detector	Detector range	Laserpower
eGFP	488 nm	Airyscan 2	490-650 nm	0.5%
mCherry	561 nm	Airyscan 2	490-650 nm	0.5%
SiR-coupled dyes	640 nm	Airyscan 2	490-700 nm	0.2%
[DIC]	640 nm	GaAsP PMT	400-490 nm; 650-700 nm	0.02 %

Electron microscopy (EM)

While I synchronized and purified parasites samples, sample preparation (specifically high-pressure freezing, freeze substitution and sectioning for correlative light and electron microscopy (CLEM)) was carried out by C. Funaya of the Heidelberg University EMCF (Electron Microscopy Core Facility, Heidelberg University, Heidelberg, Germany), who also imaged and correlated cells during CLEM. Additionally, J. Kim, a master student of the Frischknecht research group (Center for Infectious Diseases, Heidelberg University Hospital, Heidelberg, Germany) sectioned, imaged and analysed cells from the same sample for serial section tomography under the supervision of M. Cyrklaff of the Frischknecht group.

Sample preparation for EM

P. falciparum 3D7 parasites expressing 3xNLS::mCherry and PCNA1::GFP were synchronized via multiple sorbitol treatments and RBCs infected with late-stage multinucleated parasites isolated via VarioMACS. Parasites were washed once with PBS and resuspended in iRPMI. Hight pressure freezing was carried out immediately. Pelleted iRBCs were filled into 0.2-mm-deep aluminium carriers and cryo-immobilized by high-pressure freezing using the Leica EM ICE.

Vitrified water was freeze substituted with 0.3% (w/v) uranyl acetate in anhydrous acetone for 14 h at -90°C using the Leica EM-AFS2. Subsequently, the sample was transferred to -45°C by raising temperature at 5°C/hour. Samples were incubated for 2 h at -45°C and rinsed with 100% anhydrous ethanol for 1h before infiltration with LR Gold. Infiltration was carried out at -25°C in consecutive 2 h steps with increasing concentrations of LR Gold - 25%, 50% and then 75% -dissolved in ethanol. Samples were then incubated with 100% LR Gold for 16h before UV polymerization for 24 h at -25°C. Subsequently, samples were returned to 20°C under continuous UV exposure with a temperature increase at a rate of 5°C per hour. Lastly, UV polymerization was continued for 24 h at RT.

Sectioning into 200 nm thick sections was done on a Leica UC6 ultramicrotome, and sections were collected either on formvar-coated finder grids for CLEM or on formvar-coated slot copper grids for serial section tomography.

Correlative light and electron microscopy (CLEM)

Finder grids with sections were immersed in PBS and sandwiched between two cover glasses. Cells were imaged in the mCherry and GFP channel using a Zeiss observer ZI fluorescence microscope. Using finder marks of the grid, the same cells were subsequently imaged on a JEOL JEM-1400 electron microscope operating at 80 kV and equipped with a 4K TemCam F416 camera. Image correlation of fluorescent and EM images was carried out based on cell morphology using the eC-CLEM software.

Serial Section tomography

Consecutive sections collected on individual formvar-coated slot copper grids were imaged using a Tecnai F30 transmission electron microscope operating at 300 keV. Tilt series were acquired using the SerialEM software at an angle ranging from −60° to 60° with 2° increments and Gatan OneView 4k camera with a nominal magnification of 12,000.

3.2.5 Image analysis

Image analysis was done using the Fiji distribution of ImageJ (Schindelin *et al.*, 2012). Quantitative results were exported as comma-separated value (csv) files, analysed, and plotted using Microsoft Excel or GraphPad Prism version 5.0.0 for Windows. In many cases image analysis was automated using the macro function of ImageJ. Generally, macros were created by recording workflows via the record macro window and then adjusting the code until the desired output was achieved. Markos were written in the Java-based ImageJ language and saved as .ijm files.

Image segmentation

Segmentation of images was carried out based on fluorescence signals in the cellular compartments of interest. Here, most image segmentation was applied to create masks of the nuclear compartment based on the expression of the 3xNLS::mCherry marker. Other reference signals included DNA dyes (to segment the nuclear compartments) or background GFP fluorescence signals (to segment the parasite compartment excluding the food vacuole). As signal noise can impeded accurate threshold-based segmentation due to its sensitivity to outlier values, reference signals were routinely homogenized by application of filters before thresholding. Filters included median filters and gaussian blurs. Thresholding was done using the default threshold option in ImageJ with threshold values depending on the settings and instruments used during acquisition. In some cases, background subtraction was applied before image homogenisation. An overview of different segmentation parameters can be found in Tab. 36.

Table 36 *Image segmentation parameters. Asterix, threshold values depending on replicate.*

Purpose	Reference signal	Microscope	Type	Background subtraction	Filter	Threshold values	Comment
DNA quantification	5-SiR-Hoechst	SP8	16-bit	-	-	300 - 65536	Lightning-processed
DNA quantification	mCherry	SP8	8-bit	-	Median (2 px)	20,35 - 255*	Cells with two nuclei
DNA quantification	mCherry	Spinning disk	16-bit	2020	Median (1px)	170 - 65536	Cells with one nucleus
DNA quantification	mCherry	SP8	8-bit	-	Median (1px)	15 - 255	Cells with one nucleus

Thresholding results in images containing only pixels with either a minimum value (0) or a maximum value (255) (Fig. 7A). Binary compartment masks were created from these images by division with 255, resulting in images containing pixels with only the values 0 and 1, with compartments of interest being marked by pixels with the value 1 (Fig. 7A).

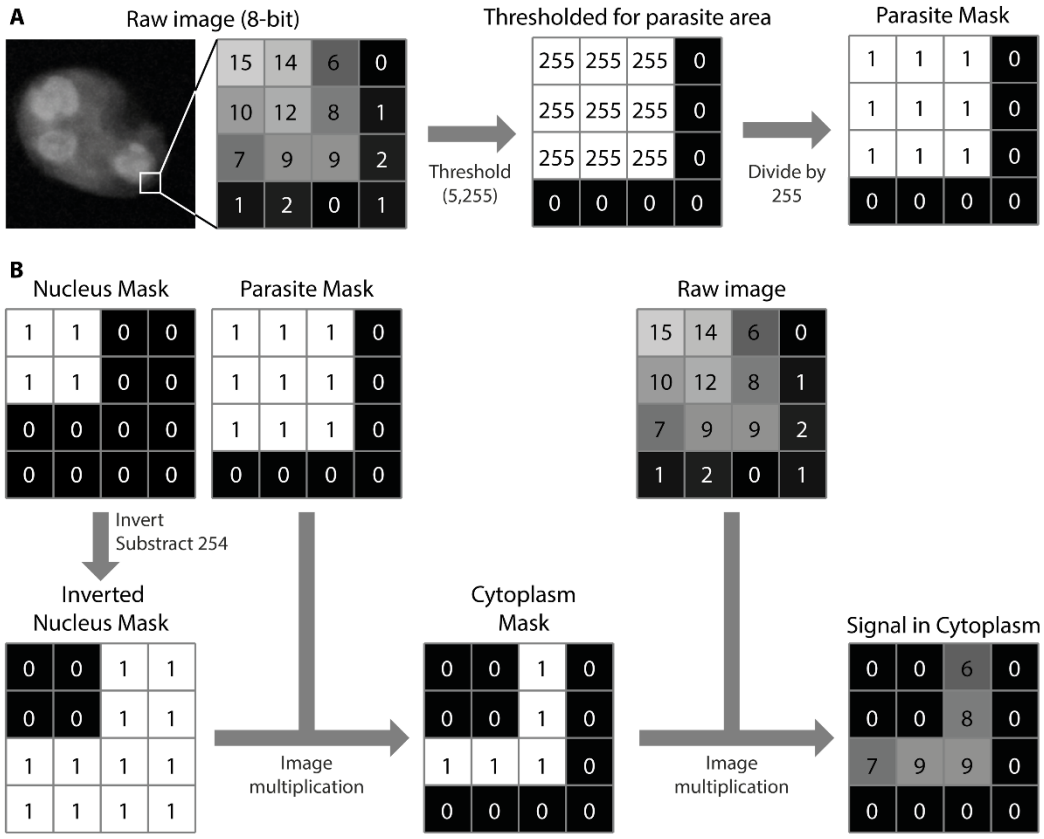

Figure 7 Schematic overview of image segmentation and quantification analysis*. (A) Image segmentation pipeline; fictional image example and pixel values. (B) Image analysis strategies for segmentation of cytoplasm and quantification of pixel values in cytoplasm; fictional image example and pixel values as in (A).*

Sub-compartmentalisation of segmented areas was achieved by using the image calculator function of ImageJ. This was done when signal intensities within the parasite cytoplasm were compared with signal intensities in the nuclear compartments. To start, a compartment mask of the nuclear area was created using the 3xNLS::mCherry signal as reference and a parasite mask was created using the background PCNA1::GFP signal as reference. Subsequently, the nuclear area was removed from the parasite mask to create a parasite cytoplasm mask (Fig. 7B). This was achieved by first inverting the nuclear mask through the ImageJ invert function and subtracting 254, and then using the image calculator function to multiply the inverted nuclear mask and the parasite mask with each other (Fig. 7B). In positions where either one or both masks have a pixel with the value 0, this generates a pixel with a value of 0 in the resulting image (Fig. 7B). Only when both masks have a pixel with the value 1 in the same position will multiplication generate a pixel with the value 1 in the resulting image (Fig. 7B). This creates a mask that only has pixels with a value 1 in the area of the parasites that does not include the nuclei, i.e., the cytoplasm (Fig. 7B).

In cases where compartments could not automatically be separated, such as when quantifying signals in individual nuclei of parasites with multiple nuclei in close proximity, compartments were segmented manually by drawing selections around the compartment of interest, either in the mask or the raw image, and duplicating only the selection with the compartment of interest.

Fluorescence quantification

In fluorescence microscopy, signal intensities correlate with the amount of intact fluorescent protein expressed by the cells. In the absence of significant photobleaching, measuring signal intensities therefore allows us to obtain quantitative information on protein levels, in some cases over time, e.g., during live-cell microscopy. Signal intensities are usually read out as pixel values, which range from 0-255 in case of 8-bit images and from 0-65536 in case of 16-bit images. In the context of this thesis, I used ImageJ to measure signal intensities as raw integrated density, which is the sum of all pixel values in an analysed image. Fluorescence quantification included quantification of GFP signal intensities in the cytoplasm compared to the nucleus over time and quantification of DNA in fixed and live cells based on signal intensities of DNA binding dyes. Here, the raw integrated density of pixels within the compartments of interest was measured.

Images were cropped to square images containing single iRBCs and the background was subtracted if necessary (Tab. 36). Then, binary masks of the compartment of interest, e.g., the nuclear area (Tab. 36), were multiplied with the raw or background subtracted image using the ImageJ image calculator tool (Fig. 7B). The resulting image contains only the signal within the area of interest (Fig. 7B), which can be measured using the multi measure tool of the ImageJ ROI manager, either directly on all individual z-slices of the image, or on a z-projection summing all pixel intensities (Tab. 37).

Table 37 *Fluorescence quantification parameters*

Purpose	Microscope	Image type	Fluorophore /dye	Background subtraction	Type
DNA quantification in one nucleus cell	Spinning disk	16-bit	5'SiR-Hoechst	Yes (2300)	Camera background
Fluorescence intensity in nucleus vs cytoplasm	Spinning disk	16-bit	eGFP	Yes, individually for each cell	Camera background

Area quantification

To quantify fluorophore concentration and therefore protein concentration within certain areas, the amount of fluorophores in a given area has to be divided by the size of that area. To this end, the area has to be quantified. I measured areas from binary segmentation masks in 3D by applying the multimeasure function on thresholded (1, 255) masks. To calculate the total area per time point, the areas from the individual z-slices were then summed.

Visualisation of nuclear accumulation of PCNA1::GFP

During nuclear accumulation, due to the concentration of GFP signal, the largest GFP pixel value seen within the image increases drastically in comparison to timepoints where no PCNA1::GFP accumulation is present. Therefore, periods of

nuclear accumulation, i.e., DNA replication, can be visualized by peaks in the maximum GFP signal over time. To this end, normalized maximal GFP pixel intensity values over time were plotted as a heatmap. Average intensity z-projections were created from long-term time lapse images and maximal GFP pixel values per time point were measured. Subsequently, these values were normalized to maximal and minimal values within each cell. Value sequences from individual cells were then aligned by occurrence of the first, most prominent, PCNA1::GFP nuclear accumulation and ordered by occurrence of second PCNA1::GFP accumulation. From these values, a heatmap was created by renormalizing values to the eight-bit value range (0 to 255) importing values as a text image in ImageJ.

Image registration

During Airyscan microscopy, due to the imprecision of the stage in xy during multiposition imaging, individual positions often experienced strong, non-linear xy drift. To facilitate image analysis as well as image visualisation, individual positions were stabilised by image registration. Registration was carried out with the plugin 'Register Virtual Stack Slices' version 3.0.8. and the complementary plugin 'Transform Virtual Stack Slices'. To this end, first a timelapse of a single z-plane of the DIC channel was registered using the plugin 'Register Virtual Stack Slices' in standard settings and all transformation matrixes were saved. Then, these reference transformation matrixes were applied to all other single z-planes and channels via the 'Transform Virtual Stack Slices' plugin. The resulting image sequences were loaded into ImageJ and reordered using the Stack to Hyperstack function to reconstruct the stabilised 3D time-lapse images of the individual channels.

3.2.6 Mathematical modelling

Mathematical modelling was carried out by P. Binder of the Heidelberg research groups of T. Höfer (Theoretical Systems Biology, German Cancer Research Center (DKFZ), Heidelberg, Germany) and U. Schwarz (Institute for Theoretical Physics and BioQuant, Heidelberg University, Heidelberg, Germany) with support from N. Becker (Theoretical Systems Biology, German Cancer Research Center (DKFZ), Heidelberg, Germany). P. Binder modelled schizogony as a simple branching process after I provided single cell DNA replication, cell division and egress timings. A detailed account of the modelling process is published in Klaus *et. al.,* 2022 and can be found in the supplementary text (Klaus *et al.*, 2022). It is paraphrased below.

As the first reliably determined nuclear event was the onset of the first DNA replication event, we defined a nuclear cycle as the time between the onset of an S-phase and the onset of one of the following S-phases. P. Binder then divided the cycle into two phases: the S-phase (time period of nuclear PCNA1::GFP accumulation in a given nucleus) followed by two parallel D-phases, one for each emerging daughter nucleus (time from the end of nuclear PCNA1::GFP accumulation to the start of the next PCNA1::GFP accumulation in one of the daughter nuclei). Accordingly, the timing of nuclear division is not relevant in this model, which is based exclusively on DNA-replication events. As the length of the

nuclear cycles was not correlated over the first and second generation, all correlations between individual S- or D-phases were neglected.

The experimental data on the DNA replication and nuclear division timings of the first two generation of nuclei was used to generate gamma distributions for the first and second generation of S- and D-phases with a density of $f(x; \alpha,\beta) = \beta^{\alpha}x^{\alpha-1}e^{-\beta x}/\Gamma(\alpha)$ (Tab. 38). This process resulted in four gamma distributions: S_1 for the first S-phase, D_1 for the two first-generation S-phases, S_{2+} for the two second-generation S-phases and D_{2+} for the four second-generation D-phases.

Table 38 *Gamma distribution parameters for mathematical modelling of P. falciparum schizogony*

	First nuclear cycle		Second and higher nuclear cycle	
Nuclear cycle phase	S_1	D_1	S_{2+}	D_{2+}
Input data	S_1	$SD_1 + DS_{2,1}$, $SD_1 + DS_{2,2}$	$S_{2,1}$, $S_{2,2}$	$SD_{2,1} + DS_{3,1}$, $SD_{2,1} + DS_{3,2}$, $SD_{2,2} + DS_{3,3}$, $SD_{2,2} + DS_{3,4}$
α	8.14	18.77	12.49	25.85
β	0.15	0.15	0.30	0.32
KS test p	0.24	0.033	0.013	0.17

Simulations started with a single nucleus entering an S-phase at t = 0. At this point the S-phase duration was sampled from S_1. Subsequently, the following two D-phases were independently drawn from D_1, with the following two S-phases and four D-phases drawn from S_{2+} and D_{2+} following the same pattern. Initially, the timing of S- and D-phases after the second generation of nuclei were also sampled from S_{2+} and D_{2+} to keep nuclear multiplication dynamics constant from the second generation onward. Later, the slow-down factor γ was introduced to investigate different nuclear multiplication dynamics from the third generation onwards. γ was used to change the rate parameter β to $\beta_\gamma = \beta/\gamma^{i-2}$ starting from the third generation of S-phases onwards, with i being the nuclear cycle number.

To stop the simulation, two different stopping mechanisms proposed in the context of *Plasmodium* schizogony (Simon, Stürmer and Guizetti, 2021) were considered. A timer would stop growth, i.e., the simulation, when a certain time is reached and predicts no correlation between the duration of the first nuclear cycle and the total time from the start of the first S-phase until the end of nuclear multiplication (determined either by the end of the last S-phase or egress). A counter – an adapted form of the sizer mechanisms – would stop the simulation after a certain number of nuclei is reached. A counter posits a positive correlation between the duration of the first nuclear cycle and the total time from the start of the first S-phase until the end of nuclear multiplication as delays in the initial cycles prolong the overall duration of nuclear multiplication. In an ideal synchronous system, the slope of this correlation would be 1 as the delay of the initial cycle would be translated into exactly the same delay of the completion of nuclear multiplication. In an asynchronous branching process such as is the case here however, a slope of less than 1 would be expected due to different branches of the process being partially able to compensate for the delay.

As my data showed a significant positive correlation with a slope of less than 1 for the correlation between the duration of the first nuclear cycle and the total time from

the start of the first S-phase until the end of nuclear multiplication, P. Binder adopted a counter mechanism to stop the simulation. This was realized by stopping the simulation when a given number of nuclei n_{stop} is reached. To recreate the distribution of daughter cells observed in the experimental data, all running S-phases $n_{running}$ were allowed to complete after n_{stop} was reached, resulting in a varying number of final nuclei (i.e., daughter cells) $n_{final} = n_{stop} + n_{running}$ for each run of the simulation. To create realistic simulations matching the experimental data, n_{stop} was adjusted so that the simulations recreated the experimentally observed distribution for the total time of replication.

3.2.7 Statistical analysis

Quantitative results were plotted using Microsoft Excel, GraphPad Prism version 5.0.0 or 9.4.0 for Windows, or Python with Matplotlib 3.2.2, NumPy 1.19.2, pandas 1.2.0, and SciPy 1.6.0. All statistical analysis was either done with Python with Matplotlib 3.2.2, NumPy 1.19.2, pandas 1.2.0, and SciPy 1.6.0 or GraphPad Prism version 5.0.0 or 9.4.0 for Windows, using the test indicated in the corresponding figure legends. Generally, correlation was analysed via bootstrapped spearman correlation while analysis of the significance of the difference between sample population was done via two-sided Mann-Whitney *U* test.

4 Results

4.1 Characterizing the spatiotemporal organisation of *P. falciparum* blood stage schizogony

During *Plasmodium* blood stage schizogony, the parasite nuclei divide through asynchronous closed mitosis, leading to the formation of a multinucleated cell often containing odd numbers of nuclei (Janse *et al.*, 1986; Read *et al.*, 1993). However, previous data on schizogony was largely limited to snapshots and bulk data (Janse *et al.*, 1986; Arnot, Ronander and Bengtsson, 2011), lacking information on single cells and on the dynamics of nuclear multiplication. Additionally, little was known about the organization of DNA replication during schizogony. In the first part of this thesis, I therefore aimed to develop tools to investigate and characterize basic features and organisation of *P. falciparum* schizogony, focussing on the dynamics and organisation of DNA replication.

[Part 4.1 was published in Science Advances (Klaus et al., 2022). Figures and tables were adapted and modified when necessary from this publication. As this project was highly collaborative, all people that were involved in data generation, visualisation and analysis will be mentioned at the end of the respective section.]

4.1.1 Organisation of *P. falciparum* genome duplication and nuclear division during blood stage schizogony

One of the first studies on *Plasmodium* blood stage schizogony in the rodent malaria parasite *P. berghei* indicated that parasite nuclei undergo consecutive rounds of DNA replication and nuclear division (Janse *et al.*, 1986; Leete and Rubin, 1996; Arnot, Ronander and Bengtsson, 2011) (Fig. 8A, model 1). This suggests a positive correlation of the number of nuclei and DNA content (Fig. 8A, model 1). Besides this hypothesis, another model of *Plasmodium* proliferation was put forward. This second model assumed several rounds of DNA replication at the onset of schizogony, resulting in the production of multiple genomes contained within a single polyploid nucleus (Arnot and Gull, 1998; Gupta, Mehra and Dhar, 2008). DNA replication was suggested to then be followed by multiple rounds of nuclear division to partition the genomes (Fig. 8A, model 2). In this model, a cell with a single nucleus would contain a variable number of genomes, while the average genome content in cells with multiple nuclei would remain largely constant (Fig. 8A, model 2).

To test both models, I adapted the experiment by Janse *et. al.,* using *P. falciparum* schizonts in 3D high resolution fluorescence microscopy and quantified both the number of nuclei and the DNA content. For this, I fixed and permeabilized three samples of asynchronous *P. falciparum* parasites and stained them with the quantitative DNA binding dye 5-SiR-Hoechst (Bucevičius *et al.*, 2019). The samples were then imaged in 3D at a Leica confocal microscope SP8 using the Lightning mode, which allows imaging at super-resolution (Leica Microsystems GmbH). As it was not possible to reliably segment individual nuclei, the total number of genomes in each schizont was quantified and compared to the number of nuclei in the same schizont, as determined by three independent researchers (Fig. 8B and C). For the quantification of nuclei numbers, individual foci of high Hoechst

signal, previously called ‘DNA packets’, served as a proxy for nuclei (Janse *et al.*, 1986). The mean DNA signal intensity within haploid ring-stage parasites served as a reference for one genome (1*C*) in each sample (Fig. 8C).

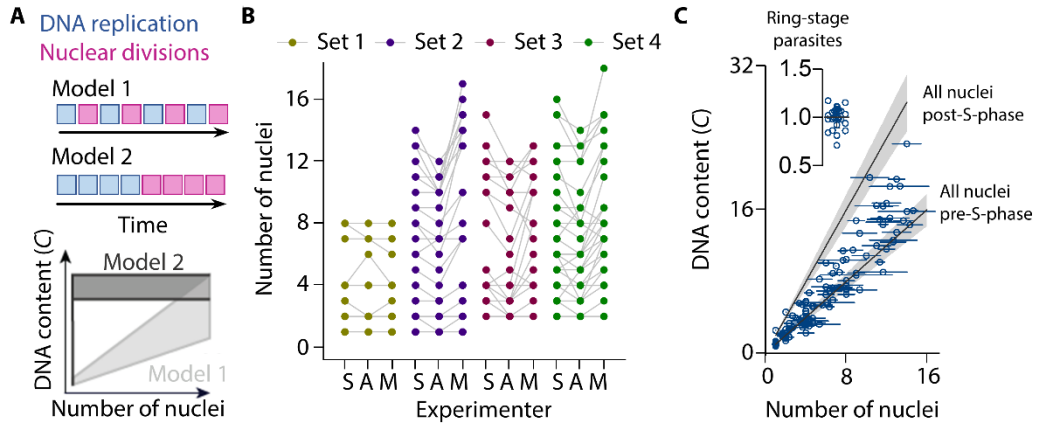

Figure 8* P. falciparum *proliferates via alternating rounds of DNA replication and nuclear division. *(A) Schematic and predictions on the relation of DNA content and number of nuclei of two models proposed for the mode of* P. falciparum *proliferation in the blood stage of infection. (B) Quantification of* P. falciparum *nuclei for (C) by three independents experimenters (S, A, and M). Each set of parasites represents an independent biological replicate. Connected data points represent the same cell analysed by three experimenters. (C) Quantification of total DNA content and the number of nuclei of* P. falciparum *schizonts. DNA content was normalized to haploid ring-stage parasites (insert), defined as 1C. Horizontal bars, SD; grey lines, expected DNA contents of parasites with all nuclei before or after S-phase; grey bands, propagated error (SD) of ring-stage measurements. (A)-(C) Modified from Klaus et al., 2022.*

The resulting distribution showed that the genome content of schizonts increased proportionally to the number of nuclei and did not exceed a total value of 2*C* per nucleus (Fig. 8C). This finding was consistent with model 1 and the study of Janse *et. al.,* in *P. berghei*, providing strong evidence that *P. falciparum* proliferates through alternating rounds of DNA replication and nuclear division (Fig. 8A).

While we assumed that each Hoechst-stained focus represents an individual nucleus, it could not be excluded that these foci were still connected via membranous structures not filled with DNA. As there is no marker available that specifically stains the nuclear envelope, I prepared samples of multinucleated schizonts, which were high-pressure frozen and used in serial-section electron tomography to image cell parts containing multiple, whole nuclei in close proximity (Fig. 9A-D). From these tomograms the inner leaflet of the nuclear envelope was traced and reconstructed (Fig. 9A and B). In the eight analysed cells we only found a single pair of nuclei exhibiting a thin membranous connection (Fig. 9C), although nuclei were sometimes only separated by a single line of ribosomes, with as few as 75 nm separating their inner nuclear envelope leaflets (Fig. 9D and E). This observation indicates that, apart from the duration of nuclear division, nuclei are independent compartments, with unconnected nucleoplasm (Klaus *et al.*, 2022).

[Samples for electron microscopy were prepared by C. Funaya. Serial sectioning, electron tomography and reconstruction of nuclear envelopes was performed by J. Kim, working together with M. Cyrklaff, for his Master thesis in the Frischknecht lab, which I partially supervised. M. Ganter and A. Kudulyte, an Erasmus+ student helped with analysis of nuclei numbers.]

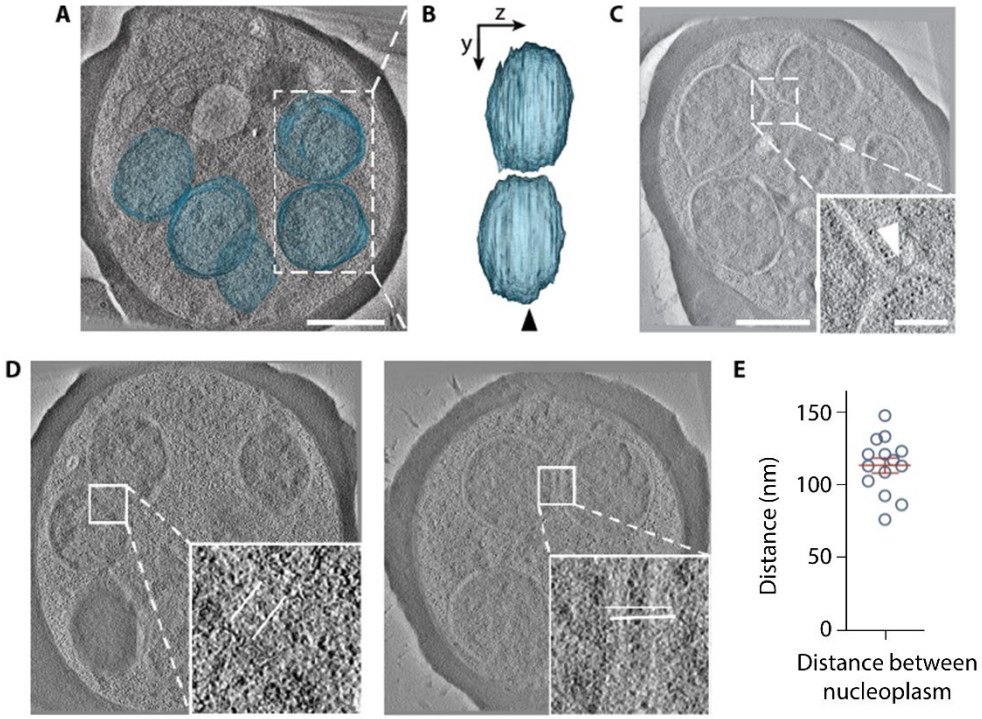

Figure 9* P. falciparum *nuclei during schizogony are individual compartments residing in close proximity. *(A) Electron tomogram of a high-pressure frozen RBC infected with a* P. falciparum *schizont, overlayed with 3D-segmented inner nuclear membranes (blue); scale bar, 1 µm. (B) Side view of the same nuclear volumes as shown in (A) with 90° rotation around the y axis; arrowhead, tomogram plane shown in (A). (C) Electron tomogram of a* P. falciparum *schizont containing two connected nuclei; scale bar, 1 µm; inset highlights the connection (arrowhead); scale bar, 250 nm. (D) Representative examples of measurements of the minimal distance between the nucleoplasm of adjacent nuclei; white lines in inserts represent quantified distances; note, ribosomes were detectable in the space between nuclei. (E) Minimal distance between nucleoplasm of adjacent nuclei; red line, average (± standard deviation.). (A)-(D) Electron tomogram slices and nuclear envelope rendering by J. Kim. (A)-(E) Modified from Klaus et al., 2022.*

4.1.2 *P. falciparum* blood stage DNA replication is asynchronous

The asynchrony of nuclear division during schizogony is well documented and starts as early as the second nuclear division, with one of the sister nuclei completing nuclear division earlier than the other (Read *et al.*, 1993; Arnot, Ronander and Bengtsson, 2011; Simon *et al.*, 2021). However, prior to nuclear division, DNA replication must take place in both sister nuclei. It is unknown if DNA replication is already asynchronous in these sisters or if asynchrony is introduced after DNA replication.

As no live-cell compatible marker for DNA replication was available, I aimed to quantify the DNA content within individual nuclei in single cells over time to compare the DNA replication dynamics between sister nuclei. To do so I used a reporter parasite line with a nuclear marker to visualize nuclei and nuclear division. This 3D7 *P. falciparum* cell line episomally expresses the red fluorescent protein mCherry N-terminally coupled to three nuclear localisation signals (3xNLS::mCherry), which results in an exclusively nuclear localisation of mCherry (Fig. 10A). Using this cell line, I was able to observe nuclear morphology and nuclear division in live cells over extended periods of time (Fig. 10A). I then stained the DNA of these parasites using the live-cell compatible quantitative DNA dye 5-SiR-Hoechst (Bucevičius *et al.*, 2019) and imaged parasites containing two nuclei

for several hours in 3D at a temporal resolution of 5 min (Fig. 10B). The DNA content of individual nuclei was quantified and normalized to the DNA content present in the respective nucleus at the start of imaging (Fig. 10C). Analysing the DNA content over time in the sister nuclei of several parasites revealed three different DNA replication patterns: (i) neither of the nuclei showed an increase in the DNA content (no DNA replication, 2/7 cells), (ii) both sister nuclei approximately doubled their DNA content at the same time (synchronous DNA replication, 2/7 cells), or (iii) one of the sister nuclei increased its DNA content at a different time than the other (asynchronous DNA replication, 3/7 cells) (Fig. 10C).

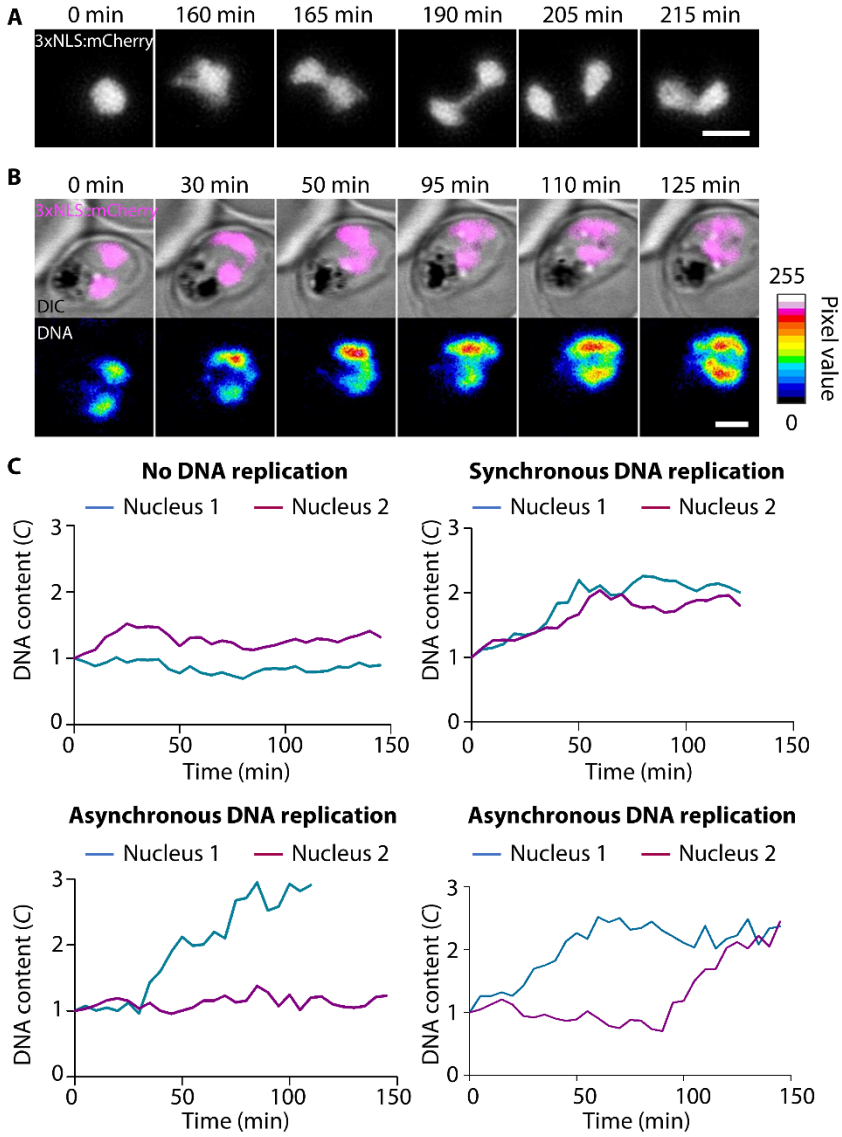

Figure 10 DNA replication can occur asynchronously in* P. falciparum *sister nuclei. *(A) High-resolution time-lapse microscopy of a nuclear division event in a* P. falciparum *3D7 cell expressing the nuclear reporter 3xNLS::mCherry; bar, 1 µm. (B) Time-lapse microscopy of the 3xNLS::mCherry (magenta, top row) expressing reporter parasite with two nuclei stained with the DNA dye 5-SiR-Hoechst (multicolour, bottom row); scale bar, 2 µm. (C) Quantification of the nuclear DNA content in representative sister nuclei during time-lapse microscopy of the 3xNLS::mCherry reporter parasite stained with the quantitative DNA dye 5-SiR-Hoechst. (A)-(C) Modified from Klaus et al., 2022.*

These findings indicate not only that the asynchrony of cell cycle processes may be introduced before nuclear division, but also that DNA replication and nuclear division events may not follow a conserved temporal pattern. These observations

prompted me to investigate the dynamics of DNA replication and its interplay with nuclear division in detail over the whole course of schizogony (Klaus *et al.*, 2022).

[The plasmid for visualisation of the parasite nuclei was created by D. Klaschka over the course of his medical doctorate thesis, while the 3D7 cell line episomally expressing 3xNLS::mCherry from this plasmid was created by M. Machado. 5-SiR-Hoechst was a kind gift from J. Bucevičius and G. Lukinavičius (Department of NanoBiophotonics, Max Planck Institute for Biophysical Chemistry, Göttingen, Germany.]

4.1.3 A novel nuclear cycle sensor system for *Plasmodium* parasites

While DNA replication can be visualized using DNA-binding dyes in the short term, long-term incubation results in abnormal cell cycle progression (Sen, Saurin and Higgins, 2018) and in combination with phototoxic stress leads to low viability during imaging (personal observation). In addition, although the 3xNLS::mCherry reporter line alone allows for long-term observation of nuclei, it is increasingly difficult to track individual nuclei from the three-nuclei-stage onward due to crowding of the nuclei. We therefore aimed to develop a parasite reporter line which allows the visualisation of both nuclear division as well as DNA replication. The DNA sliding clamp protein proliferating cell nuclear antigen (PCNA) is an essential component of the replication machinery and forms a trimeric complex, which is loaded onto single stranded DNA during replication (Moldovan, Pfander and Jentsch, 2007). In other organisms, tagged PCNA can serve as a marker for replication due to the formation of characteristic replication foci patterns during S-phase (Essers *et al.*, 2005; Meister *et al.*, 2007). While *P. falciparum* has two PCNA homologues, previous studies indicated that only PCNA1 is involved in DNA replication (Kilbey *et al.*, 1993; Patterson *et al.*, 2002; Mitra *et al.*, 2015). We therefore hypothesized that by tagging PCNA1 in addition to expressing 3xNLS::mCherry we would be able to track DNA replication events due to the formation of replication foci in nuclei undergoing S-phase. We first attempted to endogenously tag PCNA1 with GFP via CRISPR-Cas9 editing (Fig. 11A).

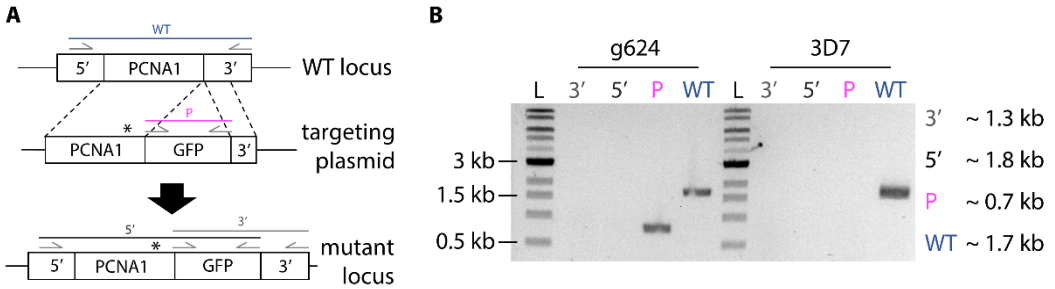

Figure 11 Endogenous fusion of* P. falciparum *PCNA1 with GFP via CRISPR-Cas9 genome editing was not possible. *(A) Scheme illustrating the CRISPR-based genome editing strategy to fuse endogenous* P. falciparum *PCNA1 with GFP; arrows, primer binding sites; lines, expected PCR-amplicons of diagnostic PCR reactions (blue, wild type band; grey, integration products; magenta, plasmid product); asterisk, position of mutated PAM-site; not drawn to scale. (B) Agarose gel of different PCR products of diagnostic integration PCR using genomic DNA extracted from* P. falciparum *3D7 cells transfected with g624-containing CRISPR-Cas9 vector and wild type 3D7. g624, transfectant genomic DNA; 3D7, parental wild type* P. falciparum *genomic DNA; L, 1 kb ladder; 3', 3' test PCR; 5', 5' test PCR; P, plasmid test PCR; WT, wild type test PCR. (A, B) Modified from Klaus et al., 2022.*

Two guide RNAs (g624 and g738) with high predicted efficiency scores were selected and the corresponding CRISPR-Cas9 editing plasmids cloned and transfected into WT *P. falciparum* 3D7 parasites. While parasites transfected with g738 did not recover, parasites transfected with g624 recovered, but showed no integration and only unspecific, evenly distributed GFP fluorescence (Fig. 11B, data on fluorescence not shown).

These results as well as the previously reported essentiality of PCNA1 (Pradhan *et al.*, 2019) indicated that endogenous PCNA1 does not tolerate GFP fusion. Therefore, I instead introduced an additional copy of tagged PCNA1 by transfecting the 3xNLS::mCherry expressing cell line with a plasmid for episomal expression of PCNA1 tagged with GFP via a glycine-serine linker (PCNA1::GFP) from a constitutively active strong promoter. The resulting cell line showed a robust expression of GFP, which localised to the whole parasite except the food vacuole and generally showed a slightly higher signal in the nuclei (Fig. 12A and B). Correlative light and electron microscopy (CLEM) analysis of high pressure-frozen parasites revealed that in contrast to previous reports (Mitra *et al.*, 2015), PCNA1::GFP was unevenly distributed in nuclei of a schizont (Fig. 12C-F). In a subset of parasites, GFP foci with a high signal intensity were only present in some nuclei of multinucleated parasites, indicating a possibly asymmetric distribution of replication factories (Fig. 12C-F).

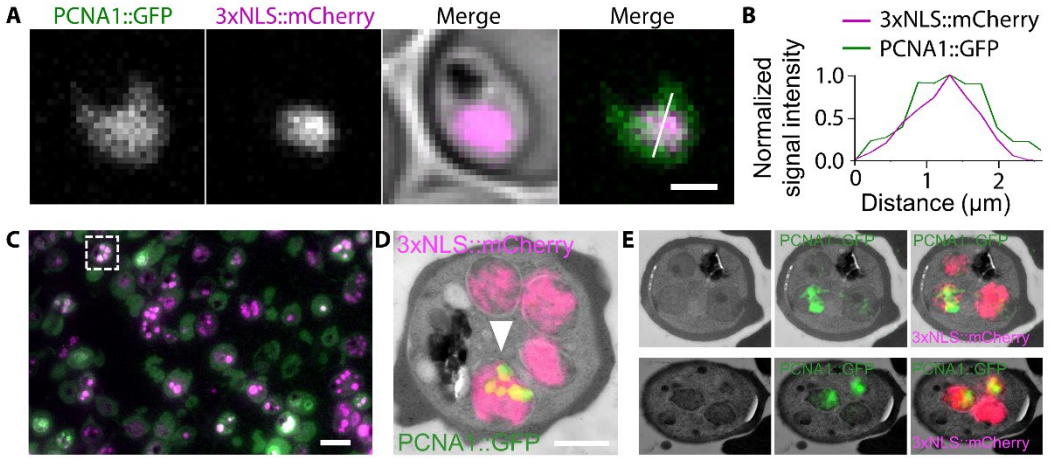

Figure 12 Localisation of episomally expressed PCNA1::GFP*. (A) Live-cell imaging of a 3D7* P. falciparum *cell episomally expressing PCNA1::GFP (green) and 3xNLS::mCherry (magenta); white line represents quantified profile in (B). Scale bar, 2 µm. (B) Normalized pixel intensity values for GFP (green) and mCherry (magenta) across the line profile shown in (A). (C) Overview of fluorescence image during correlative light and electron microscopy shows multinucleated parasites expressing both PCNA1::GFP (green) and 3xNLS::mCherry (magenta); insert, parasite shown in (D). Scale bar, 5 µm. (D) Correlative light and electron microscopy of a single 200 nm slice of a parasite expressing PCNA1::GFP (green) and 3xNLS::mCherry (magenta); scale bar, 1 µm; arrowhead, PCNA1::GFP focus. (E) Correlative light and electron microscopy of two* P. falciparum *schizonts expressing PCNA1::GFP (green) and 3xNLS::mCherry (magenta); left panel, transmission electron micrograph; middle panel, transmission electron micrograph overlayed with GFP signal; right panel, transmission electron micrograph overlayed with GFP and mCherry signal. (C)-(F) Images generated by C. Funaya. (D, E) Modified from Klaus et al., 2022.*

I then performed live-cell imaging on the 3xNLS::mCherry and PCNA1::GFP expressing cell line in 3D and at a time resolution of 5 minutes using a Perkin Elmer spinning-disk confocal microscope. Imaging was carried out for several hours and revealed that PCNA1::GFP periodically and transiently accumulates in a changing subset of nuclei (Fig. 13A). Transient GFP accumulation within a nucleus was

accompanied by a corresponding, reversible decrease in the cytoplasmic signal, indicating that nuclei access a common pool of PCNA1::GFP (Fig. 13B). Next, I tested if these accumulations represented DNA replication events and quantified the DNA content of nuclei during PCNA1::GFP accumulation. For this I stained parasites with single nuclei using 5-SiR-Hoechst and imaged them in high resolution using different live-cell microscopy systems. This showed that nuclear accumulation exactly coincides with a doubling of the DNA content, rendering PCNA1::GFP accumulation as a reporter for DNA replication and consequently S-phase (Fig. 13C and D). In combination with expression of 3xNLS::mCherry, which allowed us to track individual nuclei and nuclear division events, this established a novel nuclear cycle sensor system for *Plasmodium* parasites in analogy to the widely used cell cycle sensor system FUCCI for mammalian cells (Sakaue-Sawano *et al.*, 2008; Klaus *et al.*, 2022) (Fig. 13E).

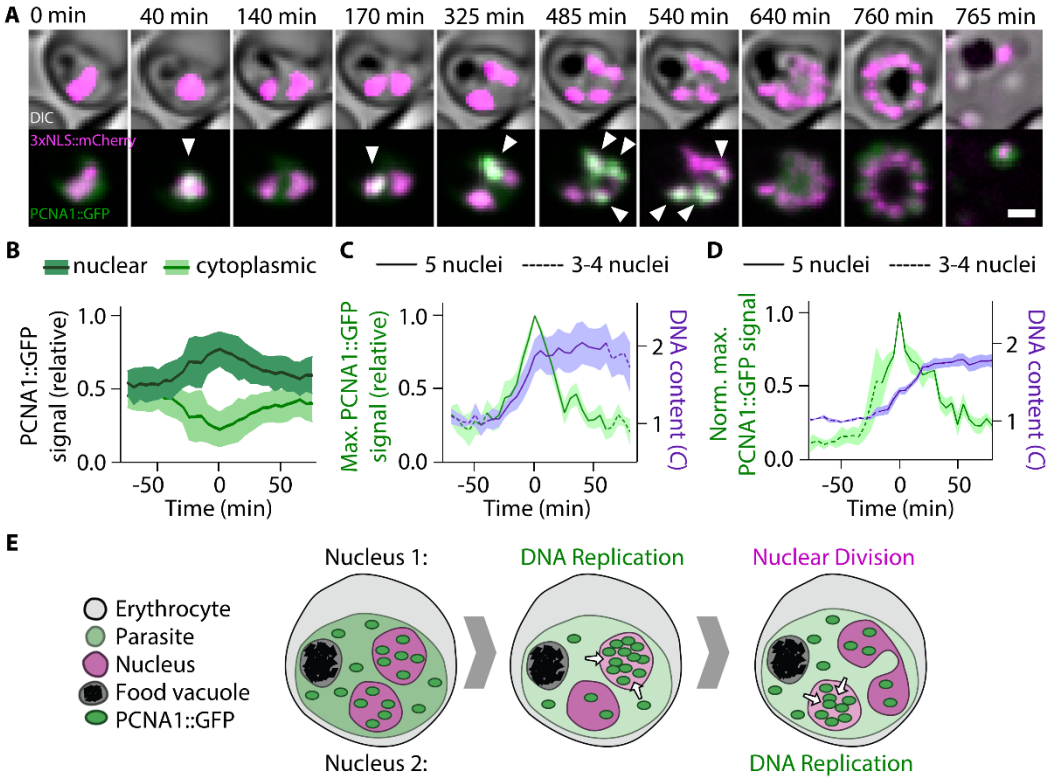

Figure 13 PCNA1::GFP transiently accumulates within nuclei undergoing DNA replication. *(A) Time-lapse microscopy of a 3D7 reporter line episomally expressing PCNA1::GFP (green) and 3xNLS::mCherry (magenta); scale bar 2 µm; arrowheads, nuclear PCNA1::GFP accumulation. (B) Quantification of cytoplasmic (light green) and nuclear (dark green) GFP during nuclear PCNA1::GFP accumulation; lines, mean (n = 4); bands, SD. (C and D) Quantification of DNA content (purple) during nuclear PCNA1::GFP accumulation (green). DNA content was normalized to the average of 10 or all available values before the nuclear accumulation of PCNA1::GFP, defined as 1C; solid lines, mean; bands, SD; (C) quantification of videos acquired on Perkin Elmer spinning disk system at 100x; (D) quantification of videos acquired on Leica Sp8 confocal line scanning system at 63x. (E) Schematic of nuclear cycle sensor system for* P. falciparum*. 3xNLS::mCherry allows visualisation of nuclei and nuclear division while nuclear accumulation of PCNA1::GFP shows DNA replication events. (A)-(D) Modified from Klaus et al., 2022.*

[C. Funaya prepared and imaged all CLEM samples. V. Schaaf attempted endogenous tagging of PCNA1 during her bachelor thesis, which I helped supervise, while J. Guizetti prepared and provided the plasmid for episomal expression of GFP-tagged PCNA1.]

4.1.4 Dynamics of blood stage DNA replication and nuclear division in *P. falciparum*

I then recorded 3D time-lapsed videos of *P. falciparum* cells undergoing schizogony at a 5 min time resolution using a confocal spinning disk microscope to investigate the dynamics and organisation of DNA replication and nuclear division events. In total, I acquired data from over 170 cells in 8 independent experiments. Maximum projections of the time-lapse videos were examined for the following parameters: parasite death (seen as lysis of cell or loss of nuclear mCherry signal), number of nuclei at start of imaging, occurrence of egress, and observability of DNA replication. Parasites that showed at least one DNA replication event, or the last DNA replication events as well as egress (n = 106) were then analysed for different aspects of nuclear multiplication dynamics. The onset of nuclear multiplication was defined as the first timepoint of PCNA1::GFP accumulation in a parasite containing a single nucleus (i.e., start of the first S-phase). Subsequently, the time from the start of the first S-phase, defined as the onset of the schizont stage, to the end of the last visible GFP accumulation, or to parasite egress was determined (Fig. 14A). On average 849 ± 54 min (~14 ± 1 hour) elapsed from the onset of nuclear multiplication to parasite egress (Fig. 14A). The average time from the end of the last S-phase to egress was 163 ± 33 min (Fig. 14A). In comparison, 694 ± 58 min (~11.5 ± 1 hours) elapsed from the onset of nuclear multiplication to the end of the last S-phase (Fig. 14A, Tab. S1).

The last round of S-phases has long been assumed to be synchronous due to the (presumably) synchronous last nuclear division, which coincides with daughter cell formation, but there is only circumstantial evidence in the literature to support this notion. While segmentation of individual nuclei was not possible during late schizogony, I was able to analyse the synchrony of the final DNA replication events by assessing if the last PCNA1::GFP accumulations before egress disappeared simultaneously in all nuclei. In most parasites (37/39 of cells) which I analysed for the synchrony of PCNA1::GFP accumulation disappearance, PCNA1::GFP disappearance occurred asynchronously, i.e., some nuclei lost the high PCNA1::GFP signal before others (Fig. 14B).

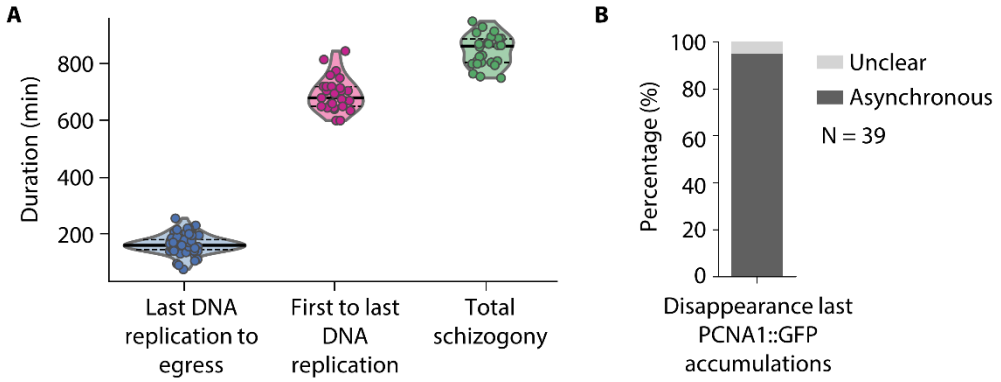

Figure 14 The schizont stage is around 14 hours long and concludes with an asynchronous last round of DNA replication events. *(A) Quantification of overall schizogony parameters of* P. falciparum *via long-term time-lapse microscopy; last DNA replication was defined as last detectable nuclear accumulation of PCNA1::GFP; solid lines, median; dashed lines, quartiles. Graph generated by P. Binder. Modified from Klaus et al., 2022. (B) Percentage of asynchronously disappearing PCNA1::GFP foci in parasites, where last PCNA1::GFP accumulations and egress could be observed.*

In those cells where I could reliably identify and quantify the number of nuclei at the onset of imaging (usually parasites containing 1-3 nuclei), I tracked nuclei as they underwent nuclear multiplication. In early schizonts, three distinct events could be observed, which repeated for every generation of nuclei: onset of S-phase (i.e., first timepoint of PCNA1::GFP accumulation) in a given nucleus, end of S-phase (i.e., last timepoint of PCNA1::GFP accumulation) in a given nucleus, and completion of nuclear division (i.e., the first time two completely separate nuclei originating from the same parent nuclei were visible) (Fig. 15A). As the onset of the first S-phase was the first event that could be reliably observed at the onset of nuclear multiplication, I defined a nuclear cycle as the time between the onset of an S-phase and the onset of the following S-phase in either of the two daughter nuclei (Fig. 15B). I then divided the nuclear cycle further into three distinct nuclear cycle stages: S-phase (start to end of PCNA1::GFP accumulation), SD-phase (end of S-phase to completed nuclear division) and DS-phase (completion of nuclear division to the onset of a new S-phase) (Fig. 15B). The DS-phase can be considered as analogous to a G1 phase, although acting on the level of an individual nucleus. Correspondingly, the SD-phase could be analogous to the combination of the G2- and M-phase. In each time-lapse video of a single cell, these events were numbered by the generation of nuclei and in the order of S-phase occurrence (Fig. 15B). Therefore $S_{1,1}$ corresponds to the first S-phase, which occurs in a parasite containing one nucleus. Nuclear division results in two nuclei of the second generation, where the events in the nucleus initiating S-phase first are labelled 2,1 and the events in the nucleus initiating S-phase later are labelled 2,2 (Fig. 15B). In the case of simultaneous initiation of S-phase, events were ordered and labelled according to the next symmetry breaking event, e.g., in synchronously replicating nuclei of the second generation, the nucleus ending S-phase or initiating nuclear division earlier was labelled 2,1.

I then quantified the duration of these phases in the first three generation of nuclei. As the number of nuclei increased over time, it became increasingly difficult to separate and track, thus, no reliable data could be acquired for nuclei after the third generation. Analysis showed that all phases of the first nuclear cycle were longer in comparison to the phases of the second nuclear cycle (Fig. 15C-E, Tab. S1). While S-phase took an average of 54 ± 19 min in the first generation of nuclei, the nuclei of the second and third generation showed shorter S-phases of around 40 min (Fig. 15C, Tab. S1). Similarly, while it took an average of 80 ± 25 min for first generation nuclei to complete the SD-phase and therefore nuclear division, the SD-phases of the nuclei in the following generations were much shorter ($SD_{2,1}$ = 50 ± 12; $SD_{2,2}$ = 54 ± 8) (Fig. 15D, Tab. S1). Finally, while sister nuclei stemming from the first division needed 33 ± 18 and 59 ± 33 min to complete the subsequent DS-phases and initiate the next round of S-phases, the duration of the DS-phases was reduced in the next generations ($DS_{3,1}$ = 22 ± 9; $DS_{3,2}$ = 33 ± 16; $DS_{3,3}$ = 29 ± 18; $DS_{3,4}$ = 42 ± 19) (Fig. 15E, Tab. S1). Between sister nuclei the duration of the S- and SD-phase was comparable, but the duration of the DS-phase showed a high variability between siblings (Fig. 15F), indicating that asynchrony of nuclear multiplication is introduced mainly after nuclear division and before the next S-phase.

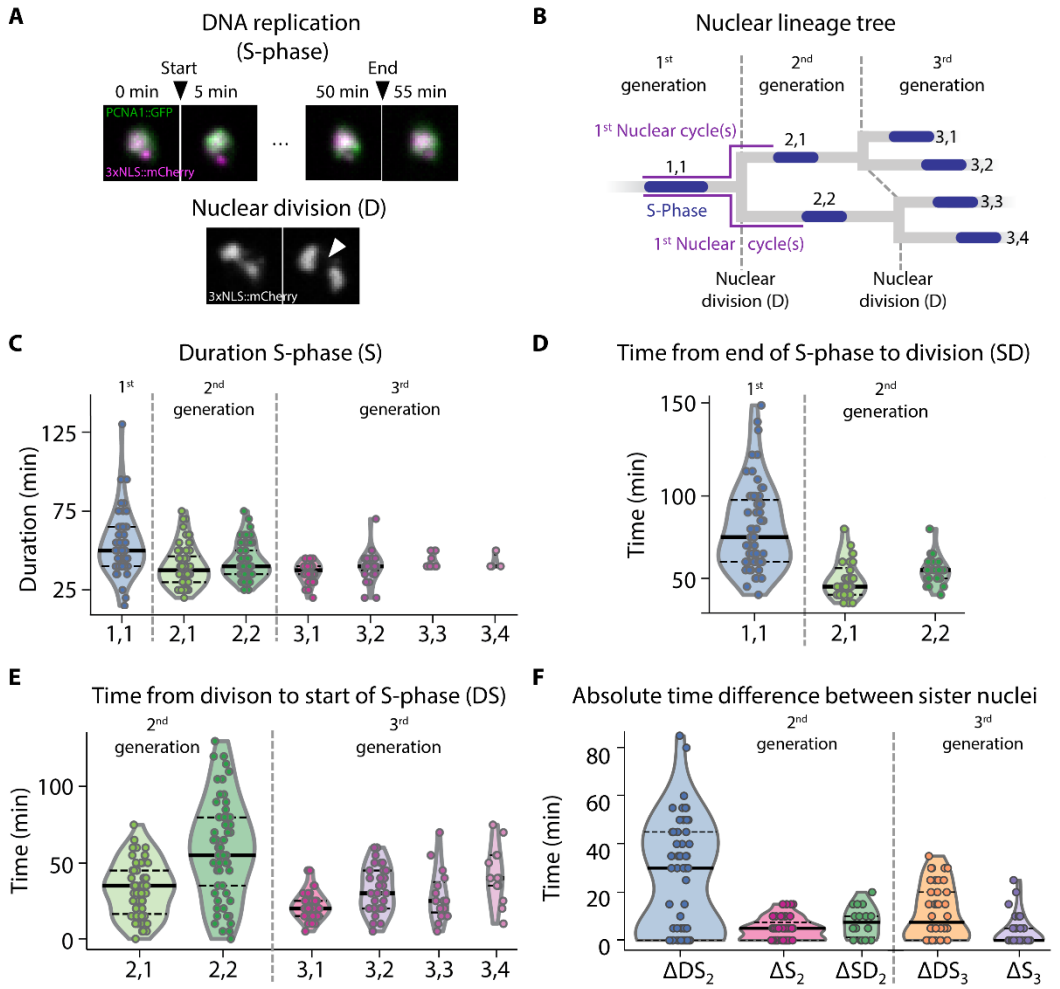

Figure 15 Dynamics of DNA replication and nuclear division during schizogony. *(A) Definitions of onset and end of DNA-replication (S-phase) as well as concluded nuclear division, D, during inspection of time-lapse data of 3D7* P. falciparum *cells expressing 3xNLS::mCherry and PCNA1::GFP. (B) Nuclear lineage tree illustrating the three consecutive generations of nuclei quantified in (C) to (E). Dashed lines, nuclear divisions D demarcating generations; blue, S-phases; purple, 1st nuclear cycle; nuclei are numbered by generation and in order of S-phase occurrence. (C) S-phase durations of three generations of nuclei. $S_{1,1}$-phases were longer than the pooled second-generation S-phases $S_{2,1/2}$ (two-sided Mann-Whitney U test effect size $f = 0.72$, $n_1 = 54$, $n_2 = 117$, $P = 3.2 \times 10^{-6}$), and $S_{2,1/2}$ was the same as $S_{3,1/2/3/4}$ ($f = 0.51$, $n_1 = 117$, $n_2 = 75$, $P = 0.85$). (D) Time from end of S-phase to nuclear division (S-D) of two generations of nuclei. $(S\text{-}D)_{1,1}$ was longer than $(S\text{-}D)_{2,1/2}$ ($f = 0.87$, $n_1 = 63$, $n_2 = 60$, $P = 8.1 \times 10^{-13}$). (E) Time from nuclear division to start of S-phase (D-S) of two generations of nuclei. $(D\text{-}S)_{2,1/2}$ was longer than $(D\text{-}S)_{3,1/2/3/4}$ ($f = 0.66$, $n_1 = 119$, $n_2 = 91$, $P = 4.2 \times 10^{-5}$). Each dot represents an event occurring in a single nucleus of a single parasite of 70 parasites analysed; solid lines, median; horizontal dashed lines, quartiles. (F) Absolute time difference of nuclear cycle phases between sister nuclei; solid lines, median; dashed lines, quartiles. (C)-(F) Visualisation and statistical analysis by P. Binder. (B)-(F) Modified from Klaus et al., 2022.*

Tracking of nuclear cycle events within single cells resulted in unique nuclear lineage trees for each parasite with no discernible conserved pattern overall (Fig. 16). This was already apparent in cell with two nuclei; in agreement with my earlier observations on the sequence of genome duplications in parasites with two nuclei (Fig 10C), I observed that S_2-phases can occur either completely synchronously, have a temporal overlap or not overlap at all. Occurrence of synchronous S_2-phases was often associated with a subsequent synchronous nuclear division, but not in all cases (Fig. 16)(Klaus *et al.*, 2022).

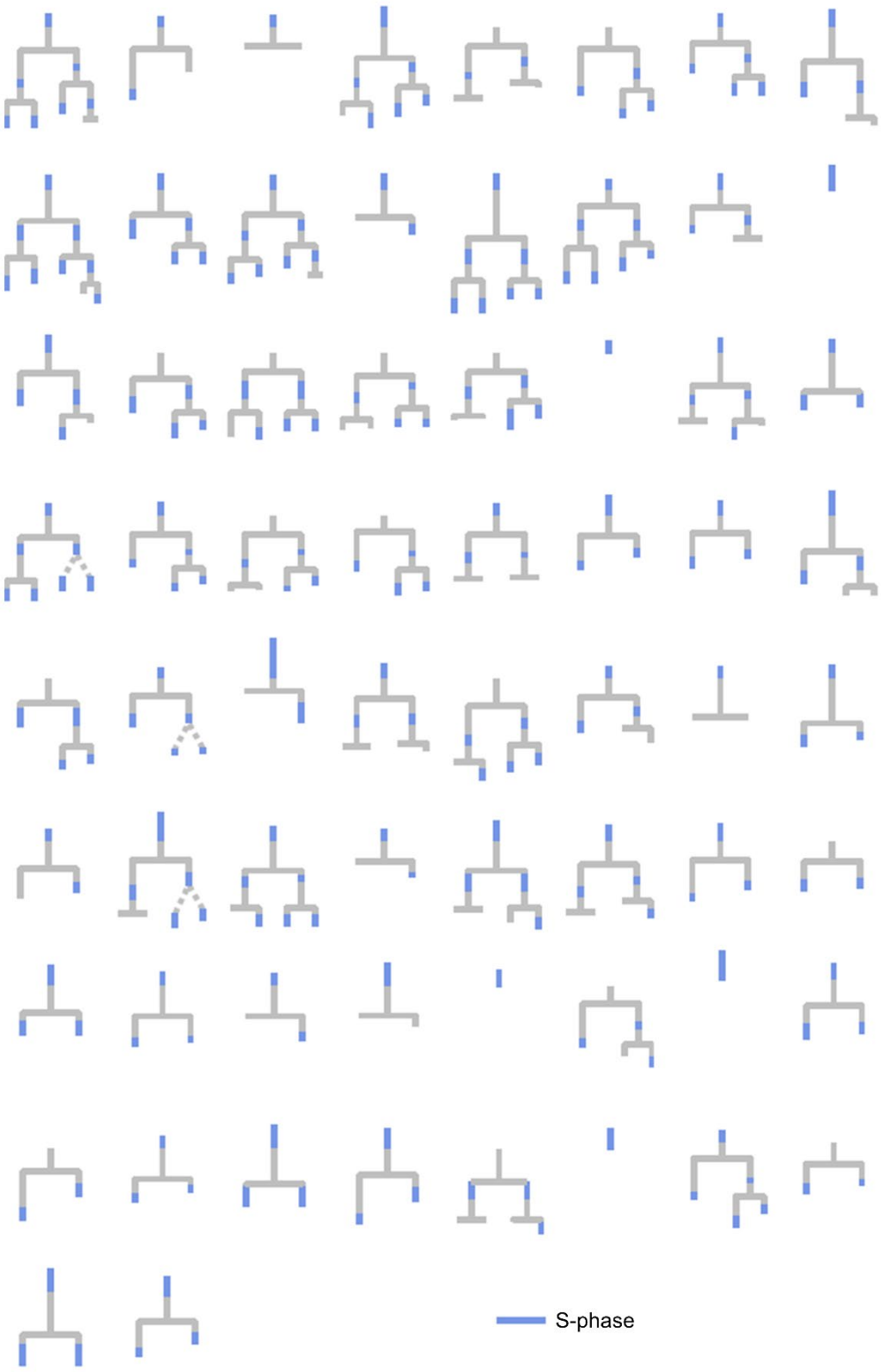

Figure 16 DNA replication and nuclear division events do not follow a conserved pattern during schizogony. *Summary of all nuclear lineage trees that were analysed for this thesis; dashed lines, timing of nuclear division event could not be determined with confidence; timing drawn to scale. Figure generated by P. Binder. Modified from Klaus et al., 2022.*

[Visualisation of data and data analysis was done in collaboration with P. Binder of the Heidelberg Research groups of U. Schwarz and T. Höfer with support from N. Becker.]

4.1.5 *P. falciparum* blood stage nuclear multiplication slows as schizogony progresses

As crowding of nuclei during the latter half of the schizont stage made confident tracking of late nuclear cycle dynamics impossible (Fig. 17A), I collaborated with P. Binder and N. Becker of the Schwarz and Höfer research groups to investigate nuclear multiplication dynamics by modelling it as a branching process. To construct this model, we further simplified the nuclear cycle by merging the SD- and DS-phases into a single-phase termed D, in which nuclear division takes place. We then used the experimentally determined nuclear cycle dynamics of the first and second nuclear cycle (Fig. 15C-E) to parameterize the model. While comparison of the S- and D-phase durations within single parasites showed a significant correlation between the length of the first S-phase S_1 and the length of the following S-phases S_2 and S_3 (Fig. 17B and C), there was no correlation between the duration of the first nuclear division phase D_2 and the second nuclear division phase D_3 nor between any S- or D -phases (Fig. 17B). In addition, when considering the entire nuclear cycle, we did not observe any correlation between the length of two consecutive nuclear cycles (Fig. 17D). Therefore, inheritance of factors was not factored into the model.

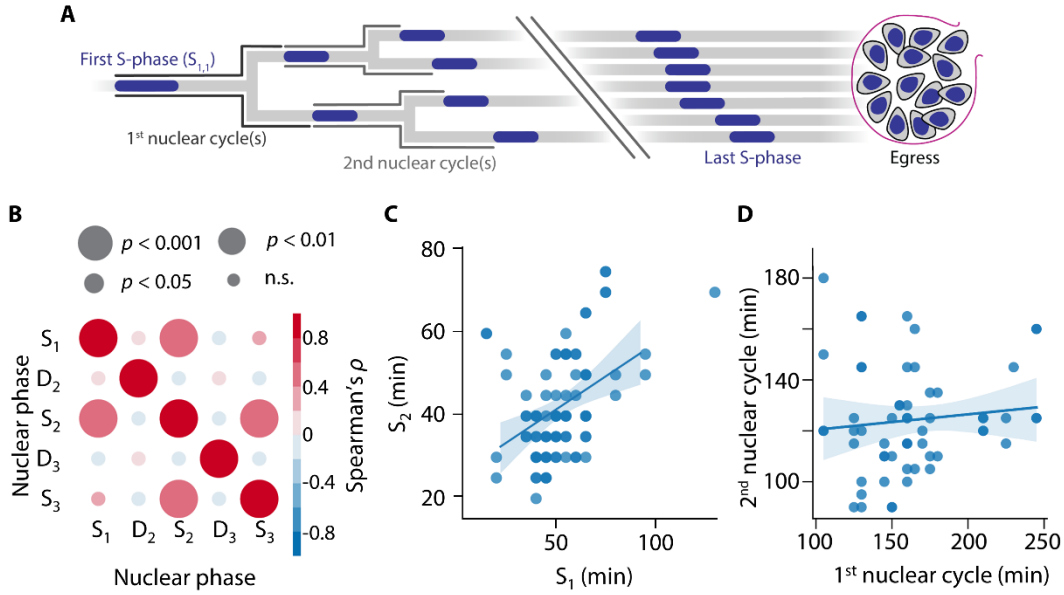

Figure 17 Replication dynamics are not inherited over multiple generations of nuclei. *(A) Nuclear lineage tree illustrating events of* P. falciparum *proliferation that were quantified in single parasites. S-phases depicted blue; nuclear cycles in grey. Break indicates events that could not be individually resolved in the experiments. (B) Spearman rank correlation of the phases of the simplified two-phase tree consisting of S-phase where DNA replication takes place, and D-phase where nuclear division takes place. (C) Duration of the first S-phase (S_1) correlated with the duration of the second S-phase ($S_{2,1}$ and $S_{2,1}$). Solid line, linear regression; band, bootstrapped 95% confidence interval; Spearman's ρ = 0.44, n=85, P = 2.8 x 10^{-05}. (D) Duration of the first nuclear cycle correlated with the duration of the second nuclear cycles (Spearman's ρ = 0.14, n = 58, P = 0.28); solid line, linear regression; band, bootstrapped 95% confidence interval. (B)-(D) Visualisation and statistical analysis by P. Binder. (A)-(D) Modified from Klaus et al., 2022.*

Furthermore, to introduce a biologically informed stopping criterion into the model, we investigated how a well-defined endpoint of nuclear multiplication is achieved to allow for timely formation of daughter cells. Here, we compared two mechanism that had been proposed in context of *Plasmodium* proliferation (Simon, Stürmer and

Guizetti, 2021): a timer mechanism, where nuclear multiplication is stopped after a set time (Fig. 18A), and a counter mechanism, a form of a sizer mechanism, which stops schizogony after a set system size is reached – here a certain number of nuclei (Fig. 18B).

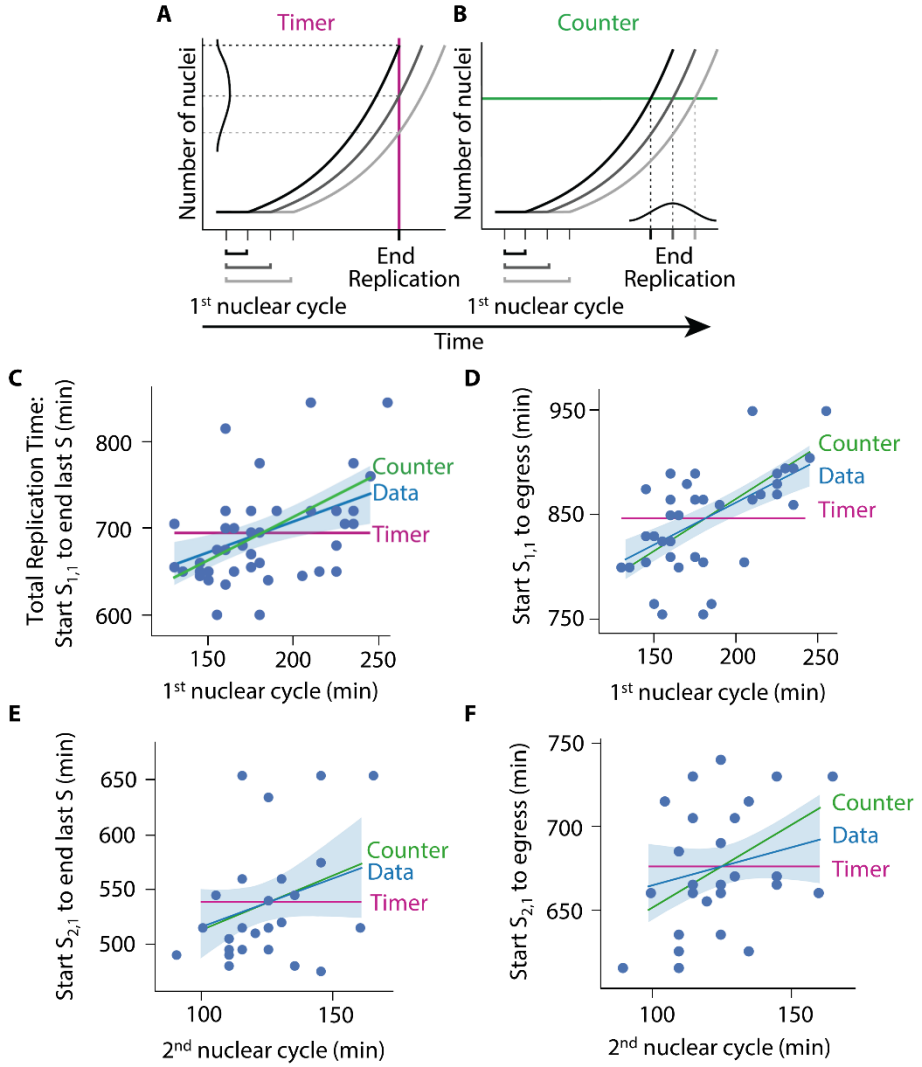

Figure 18 Schizogony is stopped by a counter-type stopping mechanism. *(A and B) Schematic illustrating how the duration of the first nuclear cycle affects the time needed to complete nuclear multiplication. (A) Timer mechanism with a set total time (magenta line) predicts no correlation between duration of the first nuclear cycle and the overall time needed for schizogony. (B) Counter mechanism with a set total number of nuclei (green line) predicts a positive correlation between duration of the first nuclear cycle and the overall time needed for schizogony. (C) Correlation between duration of first nuclear cycle and total time needed, i.e., time from start $S_{1,1}$ to end of last S-phase (Spearman's $\rho = 0.42$, $n = 46$, $P = 0.0034$). (D) Correlation of the duration from the start of S_1 to egress, i.e., parasite exit from the host erythrocyte (Spearman's $\rho = 0.55$, $n = 42$, $P = 1.9 \times 10^{-4}$). (E) Correlation of the duration from the start of S_2 to egress with the duration of the second nuclear cycle is consistent with a counter mechanism (Spearman's $\rho = 0.23$, $n = 35$, $P = 0.18$). (F) Correlation of the duration from the start of $S_{2,1}$ to last S-phase with the duration of the second nuclear cycle is consistent with a counter mechanism (Spearman's $\rho = 0.33$, $n = 35$, $P = 0.054$). (C) – (F) Data obtained from time lapse imaging. blue solid line and band, linear regression and bootstrapped 95% confidence interval; magenta solid line, timer prediction; green solid line, counter prediction if all events were synchronous. (A)-(F) Visualisation, modelling and statistical analysis by P. Binder. (A)-(F) Modified from Klaus et al., 2022.*

If nuclear multiplication is controlled by a timer mechanism, it will end at a set time, no matter how long the initial nuclear cycles took or how many nuclei were made. In a timer scenario, the duration of the first or second nuclear cycle should therefore not correlate with the overall duration of nuclear multiplication. Thus, in

a timer scenario, when the duration of the nuclear cycles is plotted against the length of nuclear multiplication, we would expect no correlation, i.e., a correlation with a slope of 0 (Fig. 18A).

If nuclear multiplication is controlled by a counter mechanism however, nuclear multiplication will only stop after a set number of nuclei has been reached. A longer first or second nuclear cycle would introduce a delay in the following cycles and lead to a longer overall duration of nuclear multiplication as it would take longer to reach the required number of nuclei. Therefore, in a counter scenario, the duration of the first and second nuclear cycle would positively correlate with the overall duration of schizogony (Fig. 18B). In a scenario with perfectly synchronous nuclei, the slope of such a correlation would be 1, as any delay in the initial cycles would directly translate into the same delay in the overall duration of nuclear multiplication. However, as *Plasmodium* nuclear multiplication is highly asynchronous however, the slope of the correlation would be expected to be below 1. Thus, for a counter scenario we would expect a positive correlation with a slope of less than 1.

When we compared the duration of the first nuclear cycle to the time from the onset of the first S-phase to either the end of the last S-phase or egress, we indeed found a positive correlation of both values with a slope of less than 1, which was significantly different from the slope expected for a timer (Fig. 18C and D). Similarly, when we compared the duration of the second nuclear cycle to the time from the onset of the second S-phase to either the end of the last S-phase or egress, we found a trend towards a positive correlation with a slope of less than 1, although it was not significantly different to the expected slope of a timer (Fig. 18C and D). Hence, these data are compatible with a counter but not a timer mechanism, and suggest that *Plasmodium* nuclear multiplication is controlled by a mechanism that stops multiplication once a certain number of nuclei is reached.

Based on this experimental data, P. Binder then integrated a counter criterion into the model by stopping the simulation once a certain number of nuclei is reached. As all ongoing S-phases at this stop point are allowed to finish, the implementation of this stopping criterium results in a different number of final daughter cells for each parasite, as is the case in experimental data (Reilly *et al.*, 2007; Simon, Stürmer and Guizetti, 2021). We then used the model to simulate nuclear multiplication while adjusting the stopping parameters to reproduce the experimentally determined overall duration of the total replication time (Fig. 19A). These simulations also reproduced the slope of the correlation between the duration of first nuclear cycle and the interval from the start of S_1 to last S-phase (Fig. 19B). We then used the model and compared the daughter cell number generated by the simulation with experimental data.

For this, I first quantified the number of nuclei in segmented schizonts of our PCNA1::GFP and 3xNLS::mCherry expressing line, which represents the final number of daughter cells. To do so, I incubated late schizonts with the protease inhibitor E64, which arrests parasites after daughter cell formation but before egress. I stained the DNA of fixed cells, and imaged schizonts in 3D using a Sp8 confocal microscope with the Lightning Module. Subsequently, I quantified the

number of daughter cells per schizont from these images and found that our parasite line produced approximately 23 daughter cells (Fig. 19C), which fits previous results in other studies (Reilly *et al.*, 2007; Simon, Stürmer and Guizetti, 2021).

Comparing the results of simulation and experimental data, we found that when leaving the speed of nuclear multiplication constant from the second generation of nuclei onward, the simulation produced numbers of nuclei far exceeding those observed in an experimental setting (Fig. 19C). We then introduced a slow-down factor, which decreased the speed of nuclear multiplication from the third generation onward. Slowing down nuclear multiplication by a factor of 17% in every generation of nuclei fitted our experimental data best (Fig. 19A-C), suggesting that the speed of nuclear multiplication decreases over time (Klaus *et al.*, 2022).

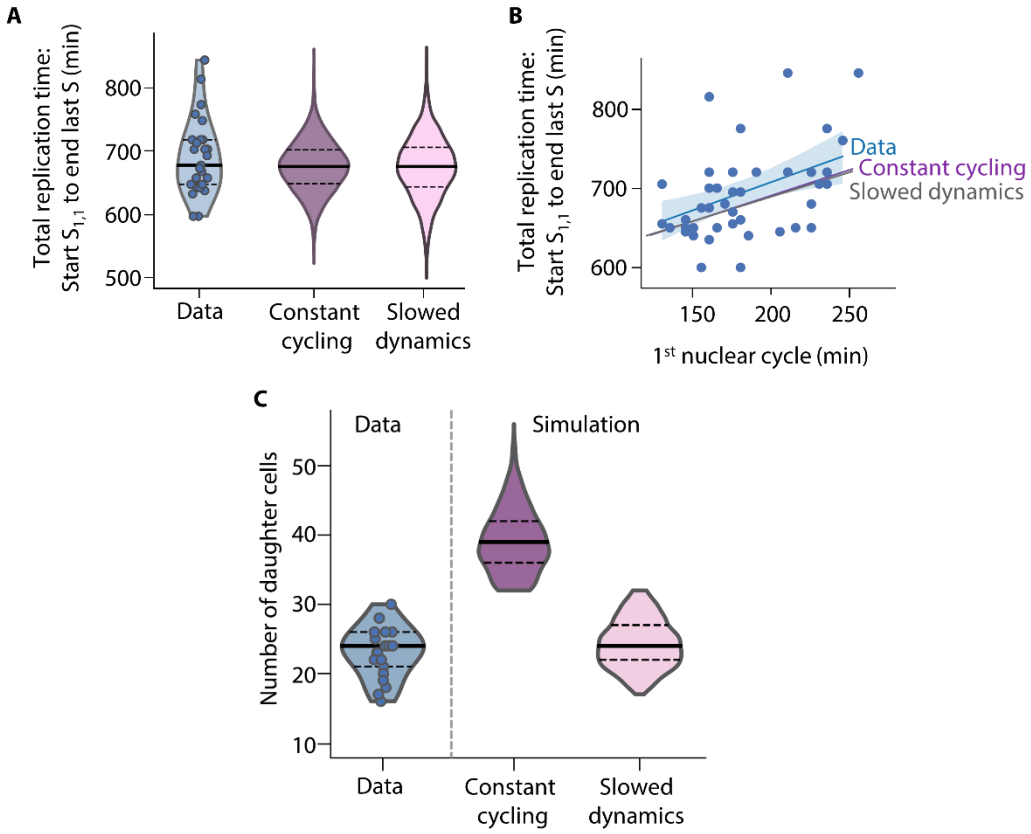

Figure 19 Nuclear multiplication slows down as schizogony progresses. *(A) Time needed to complete nuclear multiplication as measured (blue) or computationally modelled (with constant cycling-speed (dark purple) or 17% slowdown per nuclear cycle (light purple), respectively); solid lines, median; dashed lines, quartiles. (B) Correlation between length of first nuclear cycle and total replication time. Data points same as in Fig 18C. Blue line, linear regression of data ρ = 0.42 [0.15, 0.64], m = 0.71 [0.26, 1.17]), Violet line, linear regression from simulation with constant cycling-speed (ρ = 0.55, m = 0.65); grey line, linear regression from simulation with 17% slowdown per nuclear cycle (ρ = 0.44, m = 0.60); shaded bands and square brackets for m,ρ: bootstrapped 95% confidence intervals. (C) Number of daughter cells as determined by manual counting of fixed* P. falciparum *segmenters treated with the egress inhibitor E64 or generated by mathematical modelling with constant cycling dynamics from the second nuclear generation (dark purple) or slowing nuclear cycling dynamics (17% per cycle; light purple); solid lines, median; dashed lines, quartiles. (A)-(C) Visualisation, modelling and statistical analysis by P. Binder. (A)-(C) Modified from Klaus et al., 2022.*

[P. Binder modelled nuclear multiplication with advice from N. Becker of the Höfer group. Visualisation of data and data analysis was also done in collaboration with P. Binder.]

4.1.6 *P. falciparum* blood stage DNA replication is a rate limited process

As nuclear multiplication continues, the number of nuclei increases. This increases the chance that several nuclei are in the same nuclear cycle phase. Because nuclei in the same nuclear cycle phase require the same resources, we hypothesized that limited resources could cause nuclear multiplication to slow down over time. To test this hypothesis, we compared the duration of the different nuclear cycle phases in parasites with two nuclei that started and ended S_2-phases either at the same time (Fig. 20A; synchronous S_2) or at different times (Fig. 13A; asynchronous S_2).

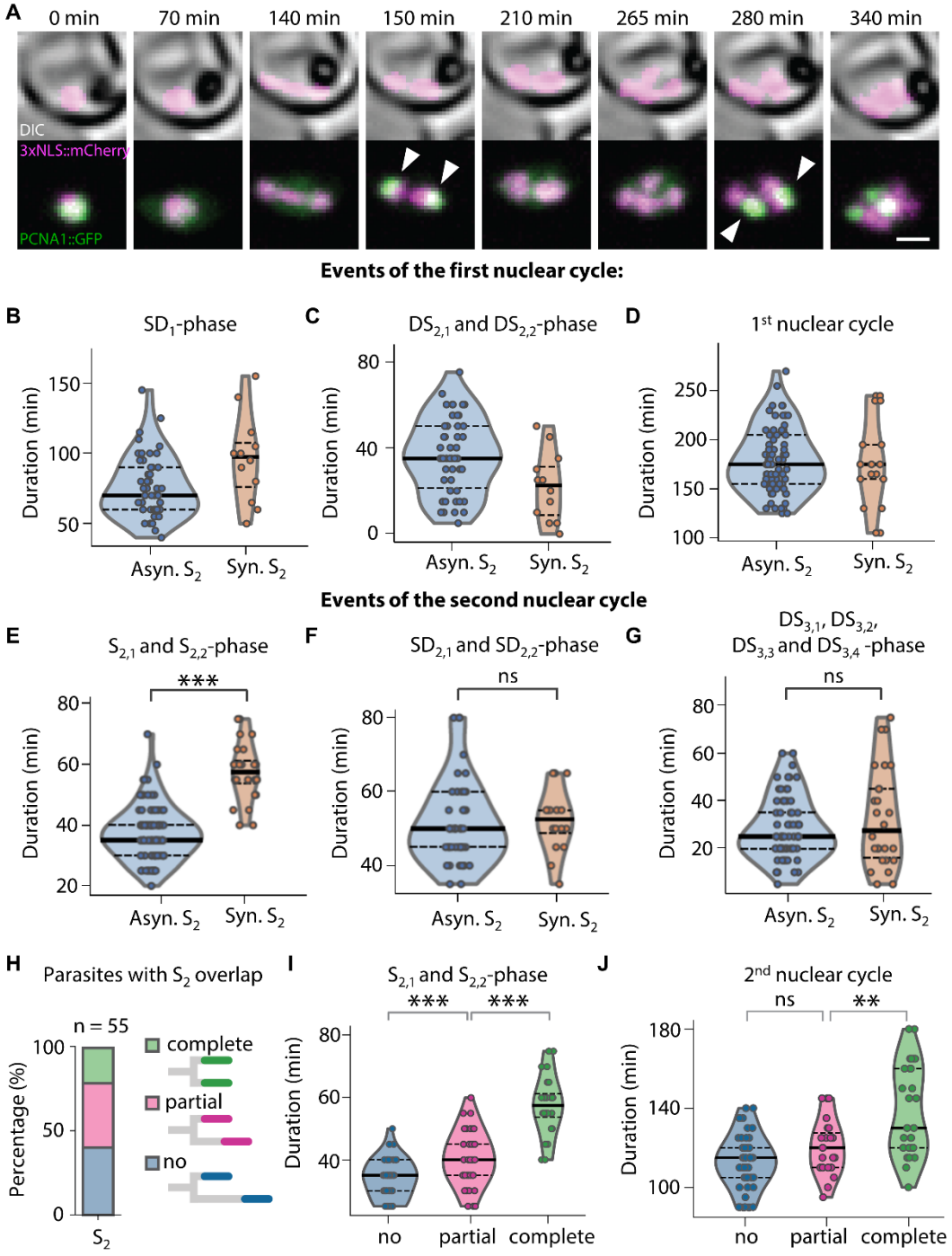

Figure 20 DNA replication is a rate limited process and synchronous S-phases increase nuclear cycle duration. *(A) Time-lapse microscopy of a parasite expressing 3xNLS::mCherry (magenta) and PCNA1::GFP (green) with synchronous DNA replication events (arrowheads); scale bar, 2 µm. (B) SD_1-phase duration of parasites undergoing synchronous or asynchronous S_2-phases. Solid lines, median; dashed lines, quartiles. (C)*

*DS_2-phase durations of parasites undergoing synchronous or asynchronous S_2-phases. Solid lines, median; dashed lines, quartiles. (D) Comparison of first nuclear cycle duration of parasites undergoing synchronous or asynchronous S_2-phases. Solid lines, median; dashed lines, quartiles. (E) Comparison of S_2-phase duration of parasites undergoing synchronous or asynchronous S_2-phases; two-sided Mann-Whitney U-test, effective size $f = 0.065$, $n_1 = 93$, $n_2 = 24$, $p = 3.4 \times 10^{-11}$; solid lines, median; dashed lines, quartiles. (F) Comparison of SD_2-phase duration of parasites undergoing synchronous or asynchronous S_2-phases; two-sided Mann-Whitney U-test, effective size $f = 0.44$, $n_1 = 44$, $n_2 = 16$, $p = 0.47$; solid lines, median; dashed lines, quartiles. (G) Comparison of DS_2-phase duration of parasites undergoing synchronous or asynchronous S_2-phases; two-sided Mann-Whitney U-test, effective size $f = 0.44$, $n_1 = 65$, $n_2 = 26$, $p = 0.68$; solid lines, median; dashed lines, quartiles. (H) Fraction of parasites with completely, partially, and not overlapping $S_{2.1}$ and $S_{2.2}$. (I) Comparison of S_2-phase duration of parasites undergoing non-overlapping, overlapping or temporally separated S_2-phases; solid lines, median; dashed lines, quartiles; two-sided Mann-Whitney U test, no versus partial overlap, $f = 0.28$, $n_1 = 44$, $n_2 = 42$, $P = 2.7 \times 10^{-4}$; partial versus complete overlap, $f = 0.10$, $n_1 = 42$, $n_2 = 24$, $P = 5.9 \times 10^{-8}$. (J) Comparison of second nuclear cycle duration of parasites undergoing non-overlapping, overlapping or temporally separated S_2-phases; solid lines, median; dashed lines, quartiles; no versus partial overlap, $f = 0.36$, $n_1 = 41$, $n_2 = 23$, $P = 0.07$; partial versus complete overlap, $f = 0.27$, $n_1 = 23$, $n_2 = 26$, $P = 0.0067$. ns, not significant; **P < 0.01; ***P < 0.001. (B)-(J) Visualisation and statistical analysis by P. Binder. (A) and (E)-(J) Modified from Klaus et al., 2022.*

In parasites with synchronous S_2-phases, the preceding DS_2 phases were shorter and succeeding SD_1 phases were longer, i.e., synchronous S_2 phases occurred closer to the preceding nuclear division than asynchronous S_2 phases. However, the overall duration of the first nuclear cycle did not differ between parasites with synchronous or asynchronous S_2-phases in the second nuclear cycle (Fig. 20B-D). In the second nuclear cycle, we found no significant difference in the duration of the SD_2- or DS_3-phases, but the duration of S_2-phases of parasites undergoing synchronous S_2-phases was significantly prolonged (Fig. 20E-G).

We then further stratified S_2-phases into three categories: S_2-phases that started and ended at the same time (complete temporal overlap), S_2-phases that partially overlapped or S_2-phases that occurred sequentially (no overlap) (Fig. 20H). When S_2-phases overlapped, their duration was significantly longer than the S_2-phases of nuclei that replicated their DNA sequentially (Fig. 20I). Similarly, S_2-phases that occurred completely synchronously took significantly longer than partially overlapping S_2-phases (Fig. 20I). Synchronous S_2-phases also translated into longer nuclear cycles: while the duration of the second nuclear cycle in parasite with non-overlapping and partially overlapping S_2-phases did not differ significantly, the length of the second nuclear cycle in parasites which underwent synchronous S_2-phases was significantly prolonged (Fig. 20J). This observation indicates that DNA-replication is a rate limited process influenced by a factor that is shared between nuclei, and that strong delays in S-phase translate into overall delays in the entire nuclear cycle (Klaus *et al.*, 2022).

[Visualisation of data and data analysis was done in collaboration with P. Binder.]

4.2 Investigating the molecular determinants of nuclear autonomy in *P. falciparum* blood stages

Although the nuclear cycle events during blood stage schizogony may be linked through shared factors influencing their dynamics, nuclei appear to act largely independently during nuclear multiplication. This apparent autonomy is particularly conspicuous in the behaviour of the DNA replication marker protein PCNA1::GFP. PCNA1::GFP is distributed evenly through the whole parasite and appears equally accessible to every nucleus. Yet, it accumulates only in those nuclei undergoing DNA replication. To investigate how nuclei can control the targeted

nuclear accumulation of PCNA1::GFP, I characterized a range of protein features of PCNA1.

4.2.1 Conserved amino acids are essential for PCNA1::GFP accumulation

Conceptually, PCNA1::GFP accumulation could be accomplished by different mechanisms. Studies of mammalian cells, where PCNA is often exclusively nuclear and only exported from the nucleus in specific scenarios, have shown that mammalian PCNA does not passively diffuse to the nucleus but is actively imported via importin-β and can be exported from the nucleus via exportin-1 (Byung and Lee, 2006; Kim and Lee, 2008; Bouayad *et al.*, 2012). Consequently, PCNA1::GFP accumulation could be achieved by regulated nucleo-cytoplasmic transport, either through decrease of nuclear export, increase of nuclear import, or a combination of both (Fig. 21, left panel). On the other hand, PCNA1::GFP accumulation could also be caused by sequestration of PCNA1::GFP in replicating nuclei via binding to intranuclear targets such as nuclear proteins or DNA (Fig. 21, right panel). In both cases, regulation could be facilitated through reversible modification of PCNA1 residues.

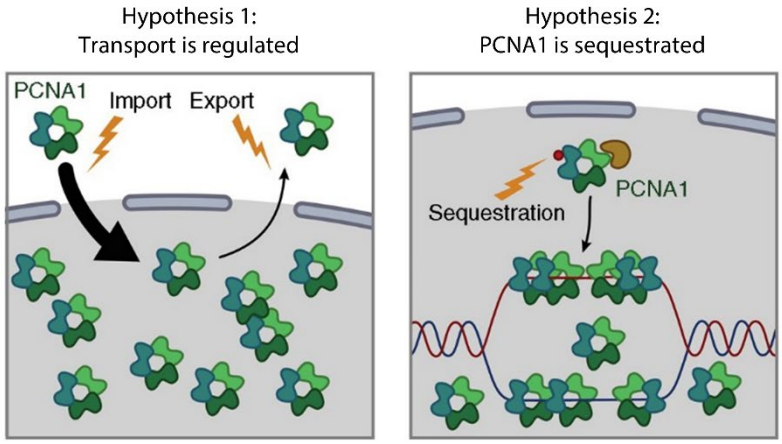

Figure 21 Nuclear accumulation of PCNA1 can be achieved via regulation of nucleo-cytoplasmic transport or regulation of PCNA1 binding in the nucleus. *Schematic describing two hypotheses on the mechanistic basis of S-phase-associated nuclear accumulation of PCNA1.*

To investigate which residues could be important for PCNA1::GFP accumulation, I first compared the sequence of human PCNA with *P. falciparum* PCNA1 (Fig. 22A). PCNA1 showed an approximately 36% conservation when compared to human PCNA, with only a single *Plasmodium* specific insertion towards the C-terminus (Fig. 22A, grey box). Human PCNA has been extensively investigated, which included the profiling of functionally relevant posttranslational modifications of amino acid residues (Moldovan, Pfander and Jentsch, 2007; Boehm, Gildenberg and Washington, 2016; Kondratick *et al.*, 2016; Billon and Côté, 2017; Billon *et al.*, 2017; de March *et al.*, 2017; González-Magaña and Blanco, 2020; Wang *et al.*, 2022). I found several of these amino acids, such as lysine (K) 13, 14, 20, 77, 80, 248 (259 in P. falciparum PCNA1) and 254 (265 in P. falciparum PCNA1) conserved in *P. falciparum* PCNA1 (Fig. 22A), indicating that they could be involved in the regulation of *P. falciparum* PCNA1 accumulation and function. Additionally, previous reports indicated that tyrosine (Y) 213 of P. falciparum PCNA1 is involved in nuclear localisation of PCNA1 (Banu *et al.*,

2018). Similarly, tyrosine 114, which is replaced by a structurally similar phenylalanine (F) in *P. falciparum* (Fig. 22A), has been shown to be essential for trimerization of human PCNA (Jónsson *et al.*, 1995; Bouayad *et al.*, 2012).

To investigate the role of nucleo-cytoplasmic transport in PCNA1::GFP accumulation, I also searched for potential nuclear transport signal sequences within *P. falciparum* PCNA1. Although in other organisms PCNA homologues are frequently exclusively nuclear, during granulocytic differentiation human PCNA is exported from the nucleus of developing neutrophils (Bouayad *et al.*, 2012). Previous studies indicated that this export is dependent on a nuclear export sequence (NES) between I11-L22, which is well conserved in *P. falciparum* (Fig. 22A, yellow box) (Bouayad *et al.*, 2012). Strikingly, this motif included three lysine residues which have been shown to be modified in human PCNA (K13, 14 and 20) (Billon *et al.*, 2017; González-Magaña and Blanco, 2020). I also investigated potential signal sequences for nuclear import. Studies of human PCNA indicated the presence of a nuclear localisation signal (NLS) between F100-S120, which was again well preserved in *P. falciparum* PCNA1 and which included several conserved lysine residues as well as a conserved phenylalanine (Fig. 22A, green box) (Kim and Lee, 2008). In contrast to the conserved residues within the NES however, there are no reports of modification of these residues in human PCNA (González-Magaña and Blanco, 2020).

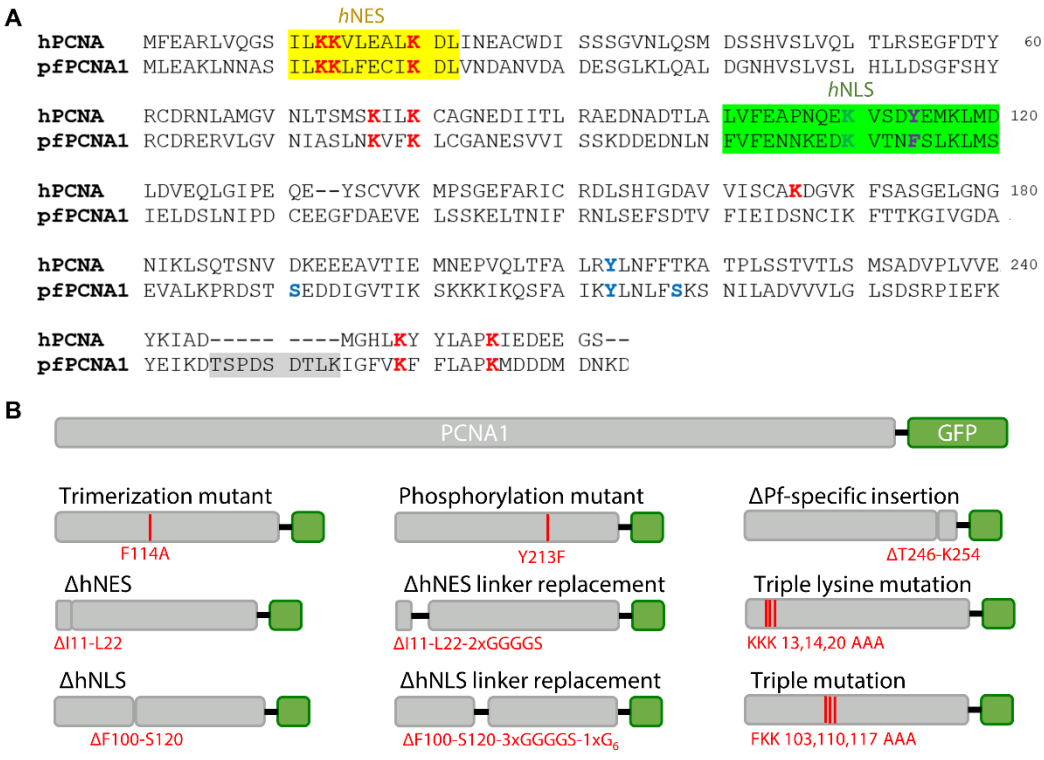

Figure 22 Comparison of human PCNA and* P. falciparum *PCNA1 allows identification of potential functional residues and signal sequences. *(A) Sequence comparison of human PCNA and* P. falciparum *PCNA1. Potential NES identified in human PCNA (hNES) marked in yellow, potential NLS identified in human PCNA (hNLS) in green with critical lysine residue in green,* Plasmodium*-specific insertion in grey; (potentially) modified lysine residues marked in red; potential phosphorylation sides in blue; residue essential for trimerization in purple. (B) Schematic overview of WT PCNA1::GFP as well as all PCNA1::GFP mutants expressed episomally; mutations and deletions not drawn to scale.*

To analyse the role of these residues and potential signal sequences, we created a panel of nine PCNA1 mutants and episomally expressed them as a GFP fusion protein from an overexpression plasmid (Fig. 22B). In two mutants, we introduced the point mutations F114A and Y213, respectively, to investigate the role of trimerization and possible phosphorylation for PCNA1 accumulation. We also created a mutant in which we removed the *Plasmodium*-specific insertion between T246-L253 (Fig. 22B).

Four mutants were designed to investigate the predicted NES sequence between I11-L22 (hNES) and the predicted NLS sequence between F100-S120 (hNLS), which were identified based on sequence homology to human PCNA. In one variant, we deleted the entire NES and NLS sequence (Fig. 22B). In another variant, we replaced the NES and NLS sequence with a linker of similar size to avoid potential structural repercussions of the deletion (Fig. 22B). In addition, we created a third variant for the NES and NLS motifs, in which we mutated only three conserved residues within the putative signal sequence to alanine, as these residues showed functional relevance in human PCNA (González-Magaña and Blanco, 2020). For the putative NES these three mutations were KKK13,14,20AAA, while in the putative NLS FKK103,110,117AAA were mutated (Fig. 22B).

The localisation of all mutants was analysed by IFA, and their ability to accumulate within nuclei during S-phase was evaluated using live-cell microscopy (Fig. 23). While the three mutants carrying the single point mutations F114A and Y213F as well as the deletion ΔT246-L253 showed no difference compared to PCNA1::GFP (Fig. 23A, Fig. 13A), all mutations within the predicted nuclear transport signal sequences abolished proper PCNA1::GFP behaviour to different degrees (Fig. 23B-D). In comparison with PCNA1::GFP, which shows a higher signal in the nucleus even in non-DNA replicating cells (Fig. 12A and B, Fig. 23B and C), PCNA1 mutants with deletion of the signal sequence, either with (data not shown) or without replacement by a linker, showed a completely even protein distribution across the parasite (Fig. 23B and C). Similarly, none of the mutants were able to accumulate in nuclei undergoing S-phase (Fig. 23D), indicating that removal of these sequences abolishes PCNA1 function. In contrast, the two PCNA1 mutants each carrying three point mutations within the predicted signal sequences, showed a higher signal intensity in the nucleus than in the cytoplasm in non-replicating cells (Fig. 23B and C), yet no nuclear accumulation in S-phase (Fig. 23D). This indicates that these residues are critical for nuclear accumulation of PCNA1 during S-phase.

[Construction and analysis of mutants was done by and with A. Kudulyte, an Erasmus+ student, who I supervised during her internship.]

4.2.2 Minimal PCNA1 motives target different cellular compartments

Our analysis of different PCNA1 mutants indicated that conserved residues within predicted nuclear transport signal sequences were essential for PCNA1::GFP accumulation. To investigate if these sequences are functional nuclear transport signal sequences and able to target proteins to the nucleus or to cause export from the nucleus, we aimed to isolate putative PCNA1 signal sequences, fuse them to GFP and express them as episomal constructs to analyse their localisation and behaviour. While previous reports indicate the presence of an NLS at F100-S120

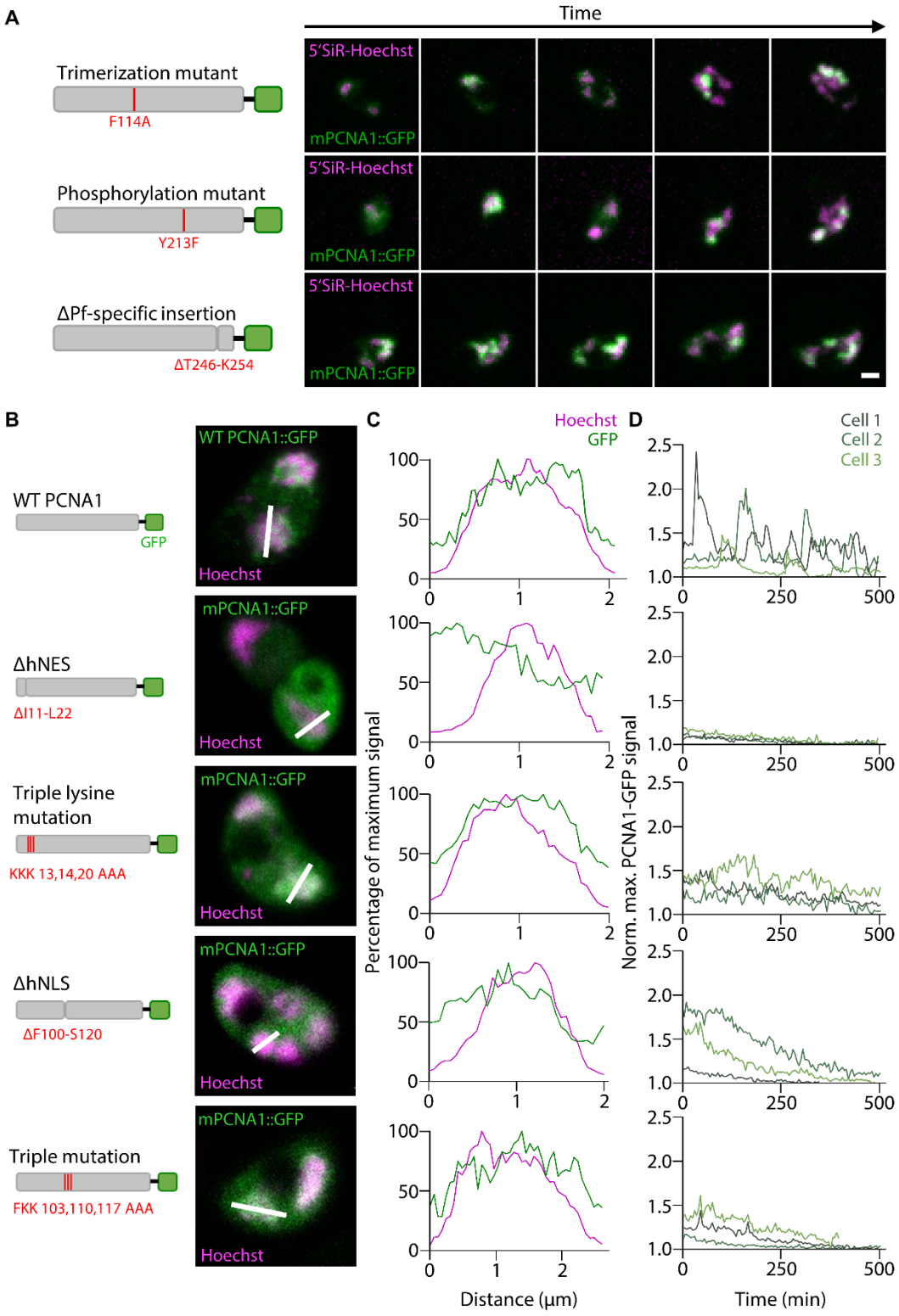

Figure 23 Conserved residues within potential nuclear transport sequences abolish PCNA1::GFP accumulation during S-phase but not nuclear localisation. *(A) Time-lapse microscopy of parasites stained with 5-SiR Hoechst (magenta) and expressing mutant PCNA1::GFP (green); scale bar, 2 μm. Top, PCNA1 with mutation of F114A; middle, Y213F; bottom, deletion of T246-K254 (B) Representative images showing localisation of WT and mutated PCNA1::GFP (green) in IFA using mouse α-GFP and α-mouse Alexa488; top, WT PCNA1::GFP without antibody staining for reference; nuclei stained with Hoechst (magenta). Lines represent profiles quantified in (C). Images generated by A. Kudulyte, who I supervised during her internship. (C) Normalized pixel intensity values for GFP (green) and Hoechst (magenta) across the line profile shown in (B). (D) Normalized maximal GFP signal over time for time-lapse microscopy of three representative cells either expressing WT PCNA1::GFP or different PCNA1::GFP mutations. Values were normalized to the lowest value over time. Peaks represent nuclear accumulation events.*

(hNLS) and an NES I11-L22 (hNES) based on sequence homology to human PCNA (Fig. 22A) (Kim and Lee, 2008; Bouayad *et al.*, 2012), we hypothesised that *P. falciparum* PCNA1 carries additional *Plasmodium*-specific signal sequences. We therefore screened PCNA1 for putative nuclear import and nuclear export signal sequences using the online prediction tools NLStradamus, cNLS Mapper, SeqNLS, LocNES and NetNES (la Cour *et al.*, 2004; Kosugi *et al.*, 2009; Nguyen Ba *et al.*, 2009; Lin and Hu, 2013; Xu *et al.*, 2015).

Screening revealed three distinct areas with potential signal sequences (Fig. 24A). The first area was between K5-D41, where the previously described hNES is located (Fig. 24A, grey box). Interestingly, while both NetNES and LocNES predicted possible NES between K5-I19, SeqNLS as well as the cNLS Mapper also predicted the presence of an NLS between S10-D41 (Fig. 24A). Such overlapping signal sequences could work in tandem to facilitate a dynamic regulation of nuclear import and export by activating or inhibiting the NLS or NES through targeted protein modification (Tavolieri *et al.*, 2019). Strikingly, the overlap between these predicted sequences included the previously investigated conserved lysine residues K13 and 14 which are essential for PCNA1::GFP accumulation (Fig. 24A). A second patch of predicted signal sequences was identified between F114-I128, where LocNES as well as NetNES both predicted the presence of an NES (Fig. 24A). This contrasted with previous studies, which reported the presence of an NLS between F100-S120 in human PCNA (hNLS). Again, one of the previously investigated conserved amino acids essential for PCNA1::GFP accumulation, namely K117, localised to the overlap between the predicted NES and hNLS (Fig. 24A). A third patch of potential signal sequences was located between K200-F209 as reported by all three different NLS prediction tools (Fig. 24A). Intriguingly, this NLS was only present in *P. falciparum* PCNA1 and not PCNA2 or mouse, rice and human PCNA, and contains a stretch of several lysine residues (Fig. 24B).

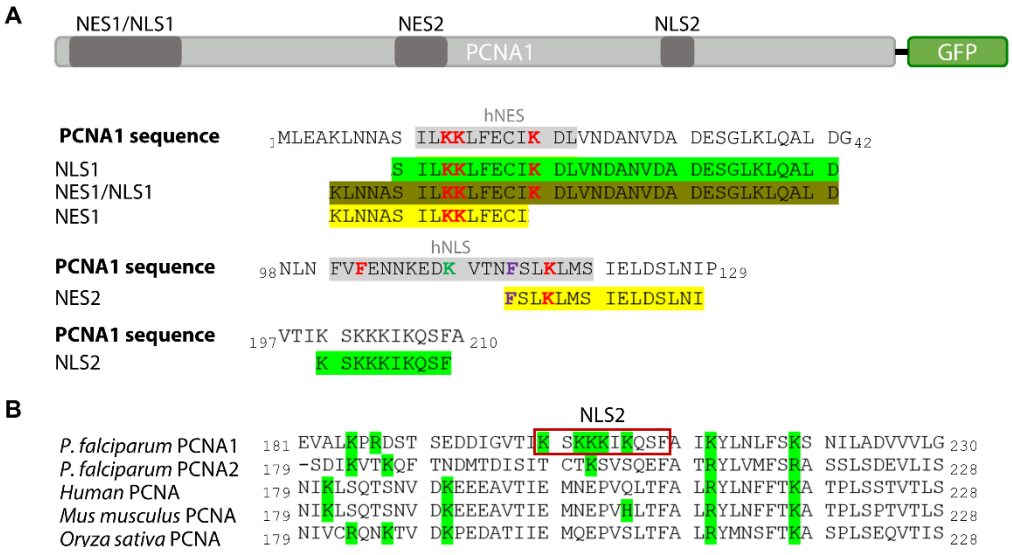

Figure 24* P. falciparum *PCNA1 carries multiple predicted nuclear transport signal sequences, including a* P. falciparum *PCNA1-specific NLS. *(A) Location and sequence of different predicted nuclear transport sequences. NES marked in yellow, NLS marked in green, overlapping NES and NLS marked in olive. Previously mutated residues in red, green and purple. Location of conserved nuclear transport sequences in human marked in grey. (B) Sequence comparison of P. falciparum PCNA1 with* P. falciparum *PCNA2, human PCNA,* Mus musculus *(mouse) PCNA and* Oryza sativa subsp. japonica *(rice) PCNA in the region from E181 to G230. Predicted NLS2 marked in red; positively charged amino acids (K, R, H) highlighted in green.*

We then fused these predicted signal sequences from WT PCNA1 to GFP separated by a linker (Fig. 25A). We also included a peptide covering both the NES and NLS spanning from K5-D41 to investigate how the combination of these putative signal sequences affects their localisation. In total, five peptides were used: K5-I19 (NES1), S10-D41 (NLS1 – which also included the sequence for hNES), K5-D41 (NES1/NLS1), F114-I28 (NES2) and K200-F209 (NLS2) (Fig. 24A and Fig. 25A). These PCNA1-derived peptides were then overexpressed in *P. falciparum* 3D7 parasites and their localisation analysed via IFA or, in case of NES1/NLS1::GFP, live cell imaging (Fig. 25B).

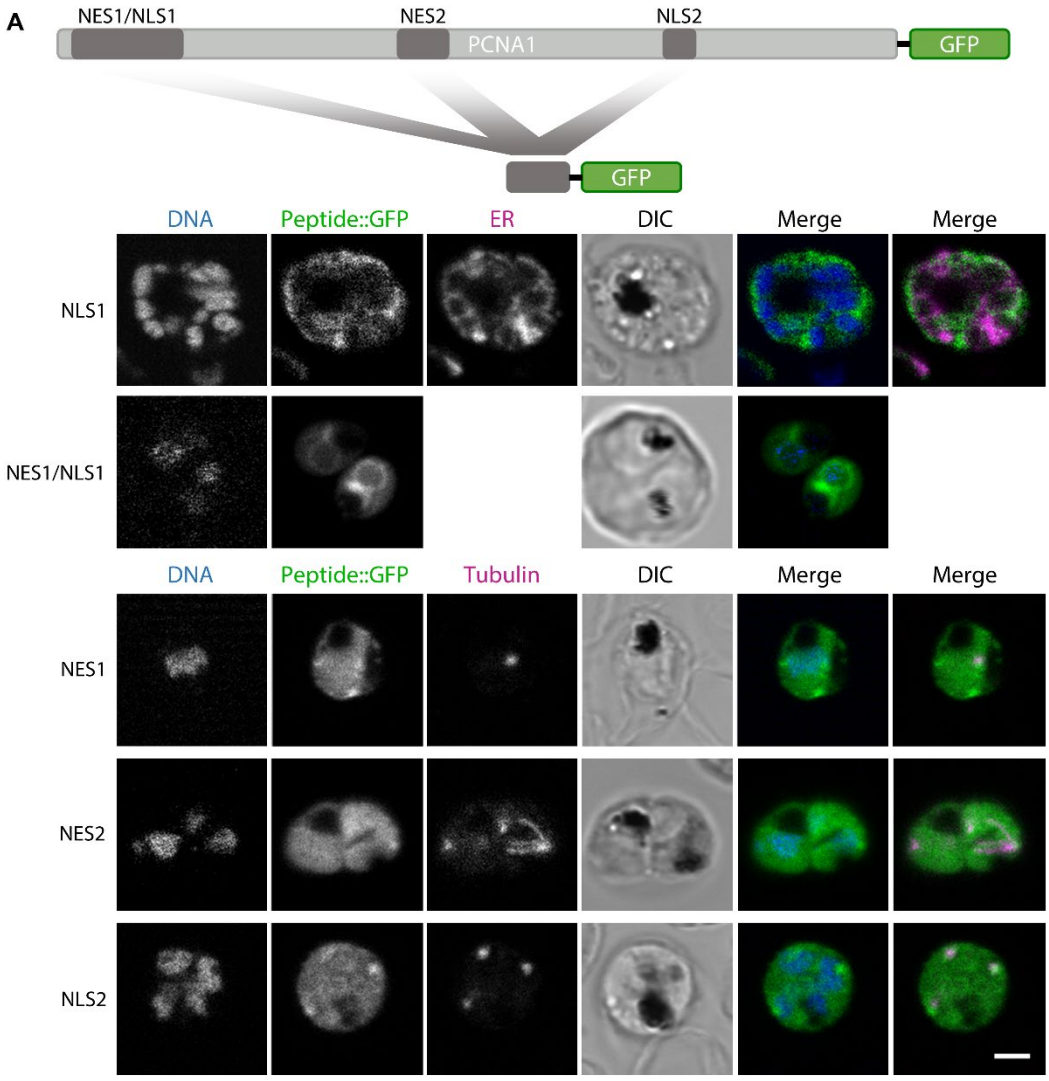

Figure 25 Different predicted nuclear transport signal sequences target GFP to different compartments. *(A) Schematic of peptide-GFP fusion proteins analysed. (B) Representative single slice confocal images of peptide-GFP fusion proteins analysed via IFA, except NES1/NLS1, which was analysed via live-cell imaging; native GFP in green; the ER was visualized using α-ERC (rabbit) and α-rabbit Atto647 (top panel, magenta); tubulin was visualized using mouse α-Tubulin-alpha and α-mouse-Atto594 (bottom panels, magenta); DNA was stained using Hoechst (blue); scale bar, 2 µm. Images generated by J. Niethammer, a student I supervised.*

The two peptides containing S10-D41 (NLS1::GFP and NES1/NLS1::GFP) showed the same specific localisation pattern, with a decreased signal in nuclei and an uneven signal in the cytoplasm. The observed high signals do not colocalize with the endoplasmic reticulum (ER) (Fig. 25B), indicating that S10-D41 of PCNA1 could contain a signal sequence targeting the cytoplasm. The depletion of GFP from

the nucleus further supports the hypothesis that this region acts as NES and is in line with previous reports of I11-L22 acting as a NES in human PCNA (Bouayad *et al.*, 2012). NES1::GFP, NES2::GFP and NLS2::GFP showed an even distribution across the parasite, with foci of high intensity near the nucleus in some parasites (Fig. 25B). As some of these foci appeared to be in close proximity to the DNA-free, protein-rich intra-nuclear department associated with the centriolar plaque, we investigated if these foci were specifically present at the centriolar plaque. Strikingly, while IFA using antibodies against α-tubulin, a marker for the intranuclear part of the centriolar plaque, showed that NES1::GFP and NES2::GFP foci did not consistently colocalize with the centriolar plaque (Fig. 25B), the high signal foci of the ten-amino acid-long NLS2::GFP construct did specifically localise to the centriolar plaque (Fig. 25B).

It is possible that the K200-F209 peptide is targeted to the centriolar plaque due to interaction with specific proteins. In this case, this ten-amino acid-long peptide could contain a specific interaction motif. Searching for *P. falciparum* proteins containing this KxKKKxK motif using the protein motif search tool of the online database PlasmoDB resulted in the identification of 819 proteins (Tab. S2). These included proteins such as a putative anaphase-promoting complex subunit 1 protein (PF3D7_0728100), the putative centrosomal protein CEP120 (PF3D7_0504700), the putative eukaryotic translation initiation factor 2-alpha kinase 2 (PF3D7_0107600), and the schizont egress antigen-1 (PF3D7_1021800) which is involved in genome segregation in the schizont (Perrin *et al.*, 2021). It also contained a putative spindle pole body protein (PF3D7_0303500), which was independently analysed in a different project and was shown to localise at the centriolar plaque (M. Machado, unpublished data). Gene ontology (GO) term enrichment analysis on cellular components, biological processes and molecular function of these 819 proteins revealed that they are predicted to be predominantly nuclear and involved in RNA processing and ribosome biogenesis but also cell cycle regulation (Fig. S1) (Lu *et al.*, 2021). Intriguingly, molecular function prediction implicated these proteins mainly in kinase activity, which is central to the regulation of cell cycle processes (Fig. S1C). This analysis suggest that K200-F209 may indeed contain a specific motif targeting proteins to the centriolar plaque.

[Identification, construction and analysis of PCNA1-derived peptides was done by J. Niethammer, who I supervised during her studies to obtain a B.Sc.]

4.2.3 *P. falciparum* S-phase is a spatially regulated process

S-phase in *P. falciparum* is initiated by the kinase CRK4 (Ganter *et al.*, 2017). Recent studies in our lab have shown that CRK4 predominantly localises close to the centriolar plaque and is enriched in microtubule-containing areas (M. Machado, unpublished data). Together with the observation that the small, *Plasmodium*-specific PCNA1 derived NLS2 peptide targets the centriolar plaque, this prompted us to investigate the role of the centriolar plaque during S-phase by analysing the spatiotemporal dynamics of PCNA1::GFP accumulations within individual nuclei. For this, I employed live-cell imaging using a Zeiss LSM900 equipped with an Airyscan 2 detector in the super resolution mode, which allows live-cell imaging at a resolution below the diffraction limit with low photo-toxicity (Huff, 2015). Imaging was carried out using our nuclear cycle sensor cell line expressing

3xNLS::mCherry and PCNA1::GFP, and parasites were additionally stained with the live-cell compatible tubulin dye SPY650-tubulin to visualize microtubule structures and the position of the centriolar plaque (Simon *et al.*, 2021). Imaging was carried out in 3D for several hours at a time resolution of 10 minutes. The increased resolution of this microscope system allowed us to see the dynamics of PCNA1::GFP accumulations within the nucleus (Fig. 26). Accumulation of PCNA1::GFP was not random, but confined to sub-nuclear areas and always initiated in close proximity to the centriolar plaque (Fig. 26). From there PCNA1::GFP accumulations progressed as a wave through the nucleus and ended in the nuclear periphery (Fig. 26), indicating that the intranuclear progression of DNA-replication is a tightly regulated process, potentially initiated and organized by proteins residing close to or in the centriolar plaque.

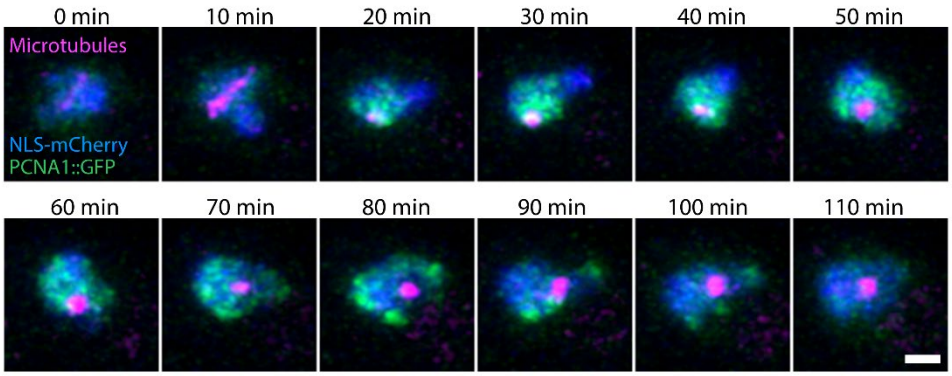

Figure 26 DNA replication follows a spatial pattern within nuclei and is initiated close to the centriolar plaque. *Time-lapse images of a nucleus of a* P. falciparum *cell episomally expressing 3xNLS::mCherry (blue) and PCNA1::GFP (green) additionally stained with SPY650-tubulin to visualize microtubules (magenta); scale bar, 1 µm.*

4.3 Investigating the nuclear export of PCNA1::GFP

Although our previous results indicated that PCNA1 indeed does contain signal sequences to target PCNA1 to specific compartments, the mechanism underlying this transport is unclear. The PCNA1-derived peptides containing S10-D41 showed an uneven distribution in the cytoplasm as well as low signals in the nucleus, indicating it could act as a NES (Fig. 25B).

Independent regulation of nuclear import in a nucleus-specific manner is difficult to achieve, as the components of the import system are located within the cytoplasm, which is shared by all nuclei (Frankel and Knoll, 2009). In comparison, independent regulation of nuclear export is conceptionally easier as the components of the export machinery are located within the individual nuclei (Frankel and Knoll, 2009). Thus, the regulation of nuclear export could provide a mechanistic basis for the asynchrony of DNA replication. In addition, to function in multiple nuclei, PCNA1 must be exported from the nucleus after accumulation. Nuclear export is therefore central to PCNA1 function, and in the last part of my thesis I focused on investigating possible mechanisms of PCNA1 nuclear export.

4.3.1 Establishing a system to investigate nuclear export in *P. falciparum*

Human PCNA can be exported from the nucleus via the export receptor exportin-1 (Bouayad *et al.*, 2012). Exportin-1 has been shown to transport the majority of

proteins from the nucleus and its function is well characterized in other organisms (Hutten and Kehlenbach, 2007; Frankel and Knoll, 2009). Study of exportin-1 dependent nuclear export is facilitated by the availability of several specific exportin-1 inhibitors, which are derived from the fungal compound leptomycin B (LMB) (Hamamoto, Uozumi and Beppu, 1985; Kudo *et al.*, 1998; Wang and Liu, 2019). LMB specifically and covalently binds to a cysteine residue (C528) within the NES-binding groove of exportin-1, thereby blocking cargo recognition (Sun *et al.*, 2013). Although previous studies have used LMB in *P. falciparum* to investigate the export of *Plasmodium* proteins from the nucleus (Panchal *et al.*, 2014), our preliminary analysis indicated that WT *P. falciparum* is insensitive to LMB due to a point mutation exchanging the cysteine residue that is targeted by LMB with an isoleucine (I637) (Fig. 27A and B).

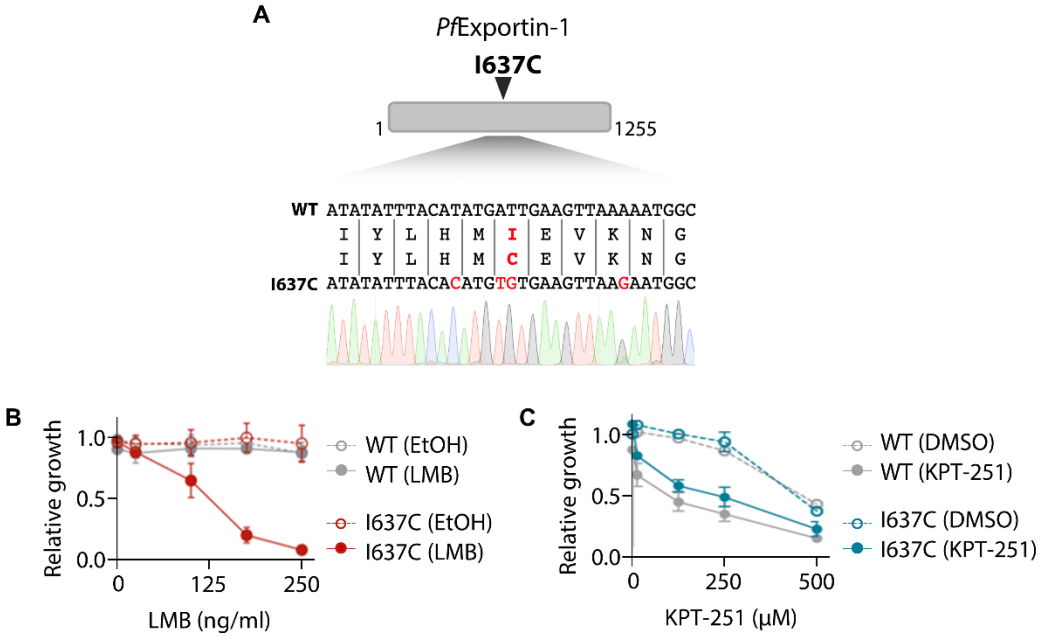

Figure 27 Mutation of I637C in* P. falciparum *exportin-1 sensitises cells to the export inhibitor LMB. *(A) Schematic overview of* P. falciparum *exportin-1 with location of a residue (red) critical for binding the inhibitor LMB, including genomic and amino acid sequence comparison of WT exportin-1 and the I637C mutant with base calling peaks for the mutant; changes in genomic sequence are marked in red. (B) Relative growth of WT and exportin-1 I637C mutant parasites over two cycles during incubation with different concentrations of the inhibitor LMB or equivalent volumes of the carrier ethanol; growth was normalized to WT parasite growth. (C) Relative growth of WT and exportin-1 I637C mutant parasites over two cycles during incubation with different concentrations of the inhibitor KPT-251 or equivalent volumes of the carrier DMSO; growth was normalized to WT parasite growth. (B) and (C) Data generated by A. Kudulyte, who I supervised during her internship.*

To harness the power of an exportin-1 specific inhibitor, we genetically engineered *P. falciparum* and constructed a mutant sensitive to LMB. For this we employed CRISPR-Cas9 gene editing and exchanged I637 with a cysteine (I637C) (Fig. 27A). We generated transfection vectors using two different guide RNAs with high predicted efficiency scores and transfected them into *P. falciparum* 3D7 parasites. As we ultimately wanted to investigate the nuclear export of PCNA1, we also co-transfected both the plasmid for episomal overexpression of 3xNLS::mCherry and the plasmid for episomal overexpression of PCNA1::GFP together with the exportin-1 targeting CRISPR-Cas9 plasmids. In total four transfections were carried out and the two CRISPR-Cas9 vectors were transfected both with and without the plasmids for our nuclear cycle sensor system. Only one of the four

transfections recovered – CRISPR-D-I637C – which contained the desired I637C mutation and showed expression of 3xNLS::mCherry and PCNA1::GFP (Fig. 27A and Fig. 28). This CRISPR-D-I637C cell line was highly sensitive to LMB in growth assays, while the corresponding carrier controls and LMB-treated WT parasites showed no growth reduction (Fig. 27A and B).

As an alternative way to inhibit exportin-1 function, we also tested the inhibitor KPT-251, which is an LMB derivative and has been reported to act on the same cysteine residue (Sun *et al.*, 2016). Strikingly, treatment with KPT-251 showed a ~50% reduction in parasite growth in WT parasites compared to the carrier control, but high concentrations of the inhibitor were needed to achieve growth reduction (Fig. 27C). Additionally, the toxicity of the carrier DMSO at high concentration caused a high mortality in the carrier control (Fig. 27C), which can confound analysis of nuclear export inhibition phenotypes. We also observed no increase in efficiency of KPT-251 in the CRISPR-D-I637C cell line, indicating that KPT-251 acts largely independent of cysteine binding in *P. falciparum*.

[Characterisation of LMB and KPT-251 in P. falciparum, as well as construction and analysis of CRISPR-D-I637C was done by A. Kudulyte, an Erasmus+ student I supervised during her internship.]

4.3.2 PCNA1::GFP is not transported via exportin-1

To test if exportin-1 inhibition influences PCNA1::GFP accumulation and redistribution to the cytoplasm after S- phase concludes, we treated unsynchronized parasites of the CRISPR-D-I637C cell line for 24 hours with 250 ng/ml LMB, which showed a ~90% growth reduction after two cycles in our growth assay (Fig. 27B). Subsequently, the treated parasites were imaged during schizogony at a time resolution of 5 minutes. Strikingly, accumulation of PCNA1::GFP was not disturbed over the course of nuclear multiplication and PCNA1::GFP readily redistributed to the cytoplasm after completion of S-phase (Fig. 28).

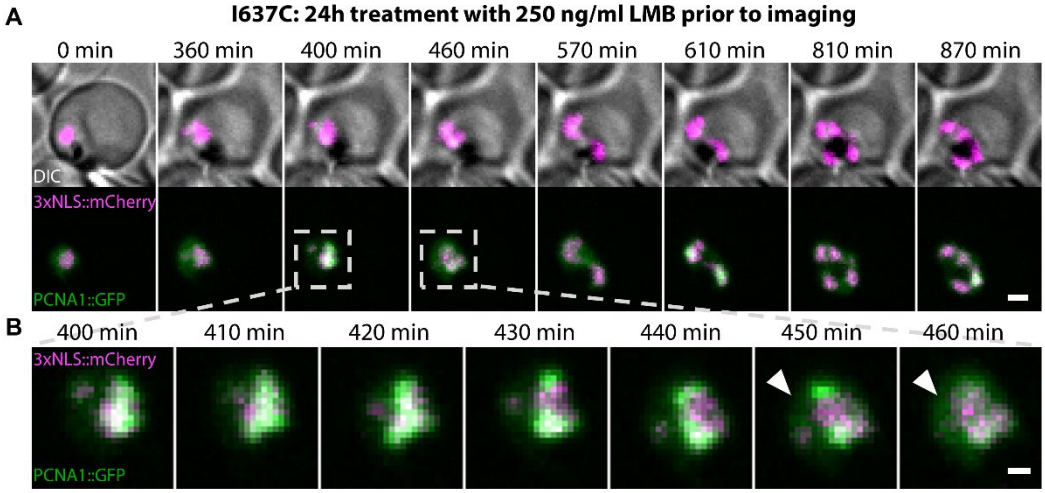

Figure 28 LMB treatment does not influence nuclear accumulation or redistribution of PCNA1::GFP during nuclear multiplication. *(A)Time-lapse images of* P. falciparum *parasites with the endogenous exportin-1 I637C mutation episomally expressing 3xNLS::mCherry (magenta) and PCNA1::GFP (green). Parasites were treated with 250 ng/ml LMB 24 hours prior to imaging. Insets mark first S-phase accumulation and redistribution to of PCNA1::GFP to the cytoplasm. Scale bar, 2 µm. (B) Close-up of insets marked in (A) with higher temporal resolution between timepoints. Arrows, redistribution of PCNA1::GFP to the cytoplasm. Scale bar, 1 µm.*

These findings indicate that exportin-1 does not transport PCNA1::GFP from the nucleus to the cytoplasm after nuclear accumulation, and that LMB treatment and inhibition of exportin-1 dependent nuclear export is not immediately lethal for *P. falciparum* schizonts in the first cycle after exposure to LMB. How exactly LMB treatment and inhibition of exportin-1 dependent nuclear export affects *P. falciparum* growth, which was severely affected after two growth cycles under the same LMB concentration in our growth assays, remains unclear.

[Analysis of PCNA1::GFP accumulation during LMB treatment was done together with A. Kudulyte, an Erasmus+ student I supervised during her internship.]

5 Discussion

Despite substantial efforts, malaria remains one of the leading causes of death in low-income countries, with over 600 000 fatalities estimated in 2021, most of which are children under the age of five (World Health Organisation, 2021). Disease severity is intimately linked with parasite burden, which in turn is caused by the rapid replication of asexual blood stage parasites (Dondorp *et al.*, 2005). During the blood stage of infection, parasites replicate via schizogony; an unusual mode of replication involving multiple asynchronous nuclear division events and the formation of a multinucleated parasite before daughter cell formation (Fig. 1 and 2) (Read *et al.*, 1993; Francia and Striepen, 2014). Although almost 150 years have passed ever since *Plasmodium* parasites were first observed in the blood of malaria patients (Laveran, 1881), little is known about the replication biology of asexual blood stage parasites (Matthews, Duffy and Merrick, 2018).

In this work, I aimed to uncover new biology and provide new knowledge on *Plasmodium* replication biology, starting by clarifying the organisation of S-phase and nuclear division during schizogony. Here, I was able to show that *P. falciparum* nuclei multiply via consecutive nuclear S- and M-phases, with S-phases being asynchronous (Fig. 8 and Fig. 9). To do so, I established a system for live-cell DNA quantification in single nuclei of a multinucleated parasite, which also enabled me to show that the accumulation of the replication protein PCNA1::GFP is a marker for DNA replication (Fig. 12 and Fig. 13). Consequently, PCNA1::GFP became a live-cell compatible protein marker for DNA replication in *Plasmodium* (Fig. 13). By utilising episomal overexpression of PCNA1::GFP in combination with the nucleus marker 3xNLS::mCherry during long-term live cell imaging (Fig. 13), I was then able to follow individual *P. falciparum* parasites during the schizont stage, quantifying both the dynamics of nuclear multiplication and the individual nuclear cycle phases in the early schizont (Fig. 14-16). This system also helped to show that nuclear multiplication stops once a certain number of nuclei are made, indicating that nuclear multiplication is controlled by a counter-type of stopping mechanism. Additionally, these insights lead to the development of a mathematical model of *P. falciparum* nuclear multiplication in collaboration with P. Binder from the Schwarz and Höfer research groups. This mathematical model allowed us to computationally extrapolate the quantitative data from the initial rounds of DNA replication and nuclear division to the entire course of nuclear multiplication, revealing that the spped of nuclear multiplication must decrease as it progresses (Fig. 17-19). This observation in turn lead us to hypothesize that there are limiting factors that restrict the speed of replication when multiple nuclei are present. We were able to gather evidence to support this hypothesis in cells with two nuclei: when DNA replication in these nuclei occurred synchronously, S-phases were significantly longer than S-phases, which occurred asynchronously (Fig. 20). In sum, I deciphered the organisation of DNA replication and nuclear division during blood stage schizogony, and shed light on potential evolutionary reasons for the development of asynchronous nuclear multiplication in *Plasmodium* during the blood stage. These results were published in *Science Advances* in 2022 (Klaus et al., 2022).

Trying to decipher how nuclear autonomy is achieved, I also investigated how one protein can behave different in different nuclei of the same cell. To this end I

analysed the molecular basis of S-phase specific accumulation of PCNA1 during nuclear multiplication (Fig. 21 and Fig. 22). I could show that nuclear accumulation of PCNA1::GFP during S-phase is dependent on conserved residues within predicted signal sequences and that during S-phase, PCNA1::GFP accumulations occur as distinct subnuclear high-signal foci (Fig. 23-26). Super-resolution live-cell imaging also allowed me to determine that these high PCNA1::GFP signal areas travel through the nucleus in a specific pattern, with accumulation being initiated close to the centriolar plaque and terminating in the nuclear periphery (Fig. 26). In parallel, I found that a short *P. falciparum* derived peptide, which is specific for *P. falciparum* PCNA1, targets the centriolar plaque, further implicating the centriolar plaque as a major hub of cell cycle control (Fig. 25).

As PCNA1::GFP rapidly shuttles between the nucleus and the cytoplasm during S-phase accumulation (Fig. 13), I also investigated potential mechanisms for nuclear transport to see if they contribute to the nuclear cycle specific behaviour of PCNA1 (Fig. 21). I found that PCNA1 may contain an active classical NES, which can target proteins to the cytoplasm when fused to GFP (Fig. 24 and Fig. 25). However, PCNA1 mutants with deletion of this NES sequence did not show a primarily nuclear phenotype as expected, but rather a decreased nuclear localisation (Fig. 23). Using similar experiments, I was not able to identify an NLS in *P. falciparum* PCNA1, despite reports from other organisms indicating that PCNA1 may contain a classical NLS (Fig. 22-25) (Kim and Lee, 2008). To investigate if I can stop the nuclear export of PCNA1, I also developed a system to inhibit the nuclear export receptor exportin-1, which transports most proteins out of the nucleus depending on classical NESs, and which has been implicated in the transport of human PCNA before (Bouayad *et al.*, 2012)(Fig. 27). Using this system, I was able to show that PCNA1 is most likely not transported by exportin-1 (Fig. 28).

All in all, I established a system to analyse the cell cycle of *P. falciparum* blood stage parasites (Fig. 12 and Fig. 13) and used it to characterize the basic parameters of nuclear multiplication during schizogony (Fig. 14-20) (Klaus *et al.*, 2021). In addition, I took initial steps to investigate the regulation of nuclear autonomy during asynchronous nuclear multiplication by investigating the molecular mechanisms of S-phase dependent nuclear accumulation of PCNA1 (Fig. 21-28). In the following I will discuss the implications of these results further.

5.1 Technological aspects and method development

The investigation of nuclear cycle dynamics, and especially the investigation of DNA replication, was hampered by the lack of a live-cell compatible marker that could be used to visualize DNA replication *in vivo* in stage parasites (Merrick, 2015; Matthews, Duffy and Merrick, 2018). Furthermore, long-term live-cell imaging was only possible at a low temporal resolution not suited to follow fast processes over several hours (Grüring *et al.*, 2011).

5.1.1 A novel nuclear cycle sensor system

In their 1993 publication on microtubule structures in *P. falciparum*, Read *et. al.,* already noted that: "… only by monitoring the passage of individual living parasites through schizogony, whilst being able to visualize accurately the succession of nuclear divisions, would this uncertainty [about the origin of different microtubule

structures within nuclei of the same cell] be clearly resolved" (Read *et al.*, 1993). Following this thought, I successfully developed a new tool to study the cell cycle dynamics of single, living *P. falciparum* parasites. Simultaneous episomal expression of the two reporter proteins 3xNLS::mCherry and PCNA1::GFP allows visualisation of the nuclei – and therefore nuclear division – as well as DNA replication in living cells (Fig. 10, Fig. 12 and Fig. 13). Notably, PCNA1::GFP represents a live-cell compatible marker for DNA replication, complementing previously established techniques, such as the incorporation of synthetic nucleosides during DNA replication, which require fixation to visualize areas where DNA synthesis takes place (Stanojcic *et al.*, 2017; McDonald and Merrick, 2022). Using this novel nuclear cycle sensor system, it is possible to follow the succession of nuclear division and DNA replication events in single nuclei of living cells using long-term live-cell imaging (Fig. 13-16). As both 3xNLS::mCherry and PCNA1::GFP are expressed as episomal copies without disturbing the endogenous genomic background of the cell, this expression system can be readily adapted to other *P. falciparum* strains and potentially other *Plasmodium* species, allowing the investigation of DNA replication and nuclear division in different cellular and biological contexts, such as liver stage schizogony or DNA replication in the activated male gametocyte (Matthews, Duffy and Merrick, 2018).

5.1.2 Advancements and constraints in live-cell microscopy

Long-term live-cell imaging of *Plasmodium* parasites was established in 2011 by Grüring *et. al.,* who used it at a temporal resolution of 20 to 60 min to investigate the entire parasite development and host cell modifications occurring during the blood stage (Grüring *et al.*, 2011; de Niz *et al.*, 2017). This temporal resolution however is not suitable to study the dynamics of nuclear division and DNA replication, which are fast processes that can be completed in under 30 min and are enacted in a complex 3-dimensional space. Together with C. Simon, I therefore established live-cell imaging of schizont stage parasites at high temporal and spatial resolution (acquisition of a large z-stack every 5-10 minutes for periods up to 24 hours) (Simon *et al.*, 2021; Klaus *et al.*, 2022). Imaging was successfully carried out in multiple confocal microscopy systems (spinning disk confocal microscopy, confocal point-scanning microscopy and Airyscan microscopy, see Fig. 10, Fig. 13 and Fig. 26), allowing me to visualise nuclear cycle dynamics in real time over long periods.

Still, long-term live-cell imaging at such depth is challenging and hampered by biological and physical constraints. In general, *Plasmodium* parasites are very sensitive to light (Wissing *et al.*, 2002). Strong illumination can induce acidification of the parasite cytoplasm and, in combination with the production of reactive oxygen species (ROS), lead to premature parasite death and aberrant behaviour (Wissing *et al.*, 2002; Icha *et al.*, 2017). Supplementation with media additives such as ascorbic acid to detoxify ROS (Icha *et al.*, 2017) could increase viability of parasites. However, each additional factor needs to be carefully tested to ensure that supplementation does not have side effects on parasite biology. Cell viability also depends on the photon load that parasites experience during imaging, which strongly depends on the microscopy system used (Magidson and Khodjakov, 2013; Tosheva *et al.*, 2020). Confocal point-scanning microscopy necessitates a

comparatively large light intensity to achieve signal-to-noise ratios suitable for detection and hence, in the context of this thesis, live-cell imaging with the Leica Sp8 point-scanning microscope was only possible for up to four hours at a high temporal resolution (see Fig. 10 and Fig. 13). In contrast, the Perkin Elmer spinning disk microscope allows acquisition using a lower light intensity, in part due to the very efficient EM-CCD camera equipped in our system, which allowed for imaging up to 24 hours. Thus, all data on schizogony dynamics presented in the results section was inferred from 3D time-lapse images acquired with this system (Fig. 13-20).

Long imaging at the spinning disk system however came at the expense of resolution. Imaging with the Perkin Elmer spinning disk microscope did not allow us to investigate intra-nuclear dynamics of PCNA1::GFP and made tracking of nuclei after the four-nuclei stage increasingly difficult. To overcome these limitations, other imaging systems could be explored (de Niz *et al.*, 2017). Recently, live-cell lattice light-sheet microscopy was successfully used to study merozoite invasion of red blood cells (Geoghegan *et al.*, 2021). The selective illumination, high speed, and high resolution of lattice light-sheet microscopy make it an attractive tool to study complex biological systems and could be beneficial to overcome phototoxicity and resolution barriers in our nuclear cycle sensor system (Chen *et al.*, 2014; de Niz *et al.*, 2017). Unfortunately, complex sample preparation and system configuration combined with a low number of systems available in general, and especially in enhanced biosafety conditions, currently limit accessibility of lattice-light sheet microscopy. An alternative could be Airyscan microscopy and 3D structured illumination microscopy (SIM) which can increase resolution around 1.7- and 2-fold, respectively (Gustafsson *et al.*, 2008; Huff, 2015; de Niz *et al.*, 2017). Indeed, here I could successfully adapt super-resolution Airyscan microscopy to allow long-term 3D imaging of *Plasmodium* parasites for up to 20 hours at high spatiotemporal resolution with up to three fluorescent markers (Fig. 26).

5.1.3 Fluorescent dyes in live-cell microscopy

The high resolution of the Airyscan system allowed me to investigate the intra-nuclear dynamics of PCNA1::GFP accumulation. During analysis of the intranuclear dynamics of PCNA1::GFP accumulation, visualisation of the centriolar plaque enabled me to determine that PCNA1::GFP accumulation foci travel through the nucleus in a distinct pattern. This was accomplished by using a cell permeable fluorescent dye, which allowed visualisation of the centriolar plaque without introduction of additional fluorescent markers, which is cumbersome and time-intensive (Fig. 10, Fig. 13 and Fig. 26). This strategy is commonly used in fluorescence microscopy and live-cell microscopy of *Plasmodium* parasites (Grüring and Spielmann, 2012; Broichhagen and Kilian, 2021; Strack, 2021).

Structures that can be visualized in this way include the microtubules and the DNA. Microtubules can be stained by fluorescent taxol derivatives and DNA can be visualized by Hoechst-derived probes (Lukinavičius *et al.*, 2014, 2015; Latt *et al.*, 2017), which are coupled with different dye moieties that show specific absorbance and emission spectra. Here, I was able to employ live-cell imaging in *P. falciparum* using two specific probes, one belonging to the SPY family of dyes, and one

belonging to a series of SiR-Hoechst derived compounds (Lukinavičius *et al.*, 2015; Bucevičius *et al.*, 2019; Wang *et al.*, 2019).

The SPY family of dyes are a relatively new group of cell-permeable probes with low background signal (Wang *et al.*, 2019). Recently, SPY555-tubulin allowed the visualisation of microtubules in live *P. falciparum* parasites during the schizont stage, enabling the characterization of microtubule dynamics (Simon *et al.*, 2021). As SPY probes are available in a wide range of absorbance and emission spectra, they are an attractive toolset to complement live-cell imaging using fluorescently tagged proteins (Wang *et al.*, 2019). Indeed, I was able to utilise SPY650-tubulin in combination with the nuclear cycle sensor system to correlate the position of the centriolar plaque with the spatiotemporal progression of DNA replication foci (Fig. 26).

Similarly, a number of live-cell compatible Hoechst-derived probes are available in the far-red spectrum to visualize DNA (Lukinavičius *et al.*, 2015). These cell-permeable probes bind selectively and stoichiometrically to the minor grove of double stranded DNA, but may cause cell cycle defects when used at high concentrations (Sen, Saurin and Higgins, 2018). However, recently, it was shown that the 5'-carboxyl isomers of these dyes show increased brightness and lower cytotoxicity (Bucevičius *et al.*, 2019). Using a preparation of the 5-SiR-Hoechst isomer, which can be used in the low nanomolar range, I was able to stain the DNA of living cells and monitor genome duplication in individual nuclei in real time for the first time in any *Plasmodium* system (Fig. 10 and Fig. 13). Moving forward, the quantification of the DNA content in living parasites will be of great benefit to correlate specific molecular processes to DNA replication without the need of additional fluorescent reporter proteins in already existing parasite strains.

5.1.4 Additional fluorescent reporter proteins for live-cell microscopy

While fluorescent dyes represent an attractive way to visualize cellular structures, there are no available live-cell compatible probes for many parasite compartments and structures. Lacking such probes, other fluorescent protein markers could be introduced into the nuclear cycle sensor system to correlate nuclear division and DNA replication with more complex, parasite-specific processes such as cytokinesis, mitochondrial fission, or ER-partitioning (Grüring *et al.*, 2011; Grüring and Spielmann, 2012; Rudlaff *et al.*, 2019).

To be compatible with the nuclear cycle sensor system, any additional fluorescent markers should be well-separated from the absorbance and emission spectra of GFP and mCherry. While there are many fluorophores with blue light excitation, which are compatible with both GFP and mCherry, the high energy of blue light could increase phototoxicity during imaging and reduce viability of parasites to unacceptable levels (Magidson and Khodjakov, 2013). Fluorescent proteins in the far-red spectra could circumvent this problem, as red and far-red light is comparatively more tolerated during imaging (Lukinavičius *et al.*, 2014, 2015). Many monomeric fluorophores with emission in the far-red spectrum, however, have absorbance spectra that largely overlap with that of mCherry, rendering them unsuitable for usage in our nuclear cycle sensor system (Wannier *et al.*, 2018). Other fluorophores in the far-red spectra include small proteins derived from the

bacterial phytochrome. These proteins show absorbance spectra that are well-separated from that of mCherry but require the cofactor biliverdin, which is generated by haem oxygenases during haemoglobin degradation (Shcherbakova *et al.*, 2016). While supplementation of biliverdin in cell culture can be problematic and has been shown to induce growth defects in *P. falciparum* cells (Alves *et al.*, 2016), some far-red fluorophores show high fluorescence in presence of endogenous levels of biliverdin (Shcherbakova *et al.*, 2016). As biliverdin is present at 63 nM in the supernatant of *P. falciparum* cell culture and *P. falciparum* encodes an essential haem oxygenase (Alves *et al.*, 2016), endogenous parasite biliverdin levels could be sufficient for usage of phytochrome-derived far-red fluorophores.

Alternatively, protein tags such as the Halo and SNAP tag could be used to generate additional reporter proteins, as they can be visualized by a range of different live-cell compatible dyes, some of which are in the far-red spectrum (Hoelzel and Zhang, 2020; Strack, 2021). These dyes show good specificity and signal to noise ratios as well as high cell tolerance, rendering them ideal for the study of cell cycle processes (Hoelzel and Zhang, 2020). In addition, simultaneous expression of two different proteins, one with the SNAP and one with a Halo tag enables flexibility in visualisation of different structures, as these tags can be selectively targeted by their respective dye partner. Therefore, although the need for pre-incubation of cells with these dyes requires a higher preparation time, tagging of reporter proteins with these peptide tags offers a good avenue to expand the nuclear cycle sensor system towards the visualisation of additional parasite cell cycle processes such as cytokinesis.

5.2 New aspects of *Plasmodium* biology

The unusual replication biology of *Plasmodium* parasites was noted early in malaria research. In 1986 Janse *et. al*., stained the DNA content of blood stage *P. berghei* parasites and found DNA replication takes place in the last 4-6 hours during schizogony, with DNA replication and genome segregation alternating (Janse *et al.*, 1986). Then, in 1993, Read *et. al.,* showed the presence of different spindle structures within nuclei of the same asexual blood stage parasite and – noting the presence of uneven numbers of nuclei – concluded that "there is an apparent asynchrony in chromosomal multiplication within a single parasite" (Read *et al.*, 1993). Yet, many aspects of the organisation of the cell cycle during *Plasmodium* blood stage proliferation remain unknown (Leete and Rubin, 1996; Arnot and Gull, 1998; Matthews, Duffy and Merrick, 2018). In my thesis I therefore aimed to characterize the organisation of DNA replication and nuclear division during schizogony and intended to use these insights to investigate the molecular mechanisms underlying nuclear autonomy.

5.2.1 The basic organisation of blood stage DNA replication and nuclear division

While flow cytometry was established as the primary method to profile DNA replication during asexual schizogony, it is unsuitable to study the organisation of DNA replication events on the level of single nuclei. Over the years, two models developed in the *Plasmodium* field regarding blood stage schizogony (Leete and Rubin, 1996; Arnot and Gull, 1998; Matthews, Duffy and Merrick, 2018). One hypothesised that all genomes are produced in a single event at the late

trophozoite/early schizont stage, which is then followed by multiple rounds of nuclear division to partition these genomes (Fig. 8A) (Arnot and Gull, 1998; Gerald, Mahajan and Kumar, 2011). The other model followed the argument of Janse *et. al.,* and assumed schizogony was completed through alternating rounds of DNA replication and nuclear division (Fig. 8A) (Janse *et al.*, 1986; Leete and Rubin, 1996; Arnot, Ronander and Bengtsson, 2011). Repeating the experiment of Janse *et. al.,* using *P. falciparum* parasites and 3D fluorescence microscopy at high resolution, I also found that the genome content of parasites is proportional to the number of nuclei (Fig. 8B), suggesting that individual genome duplication and segregation events are carried out sequentially. Lacking a nuclear envelope marker, I used individualised Hoechst foci as a proxy for nuclei, similar as Janse *et. al.,* did in 1986 (Janse *et al.*, 1986). Since it cannot be excluded that individual Hoechst foci are connected by membranous structures for which we do not have a marker, we also reconstructed parasite parts containing entire nuclei using 3D electron tomography (Fig. 9). While nuclei resided in close proximity, occasionally even deforming each other, their nucleoplasm was not connected, and they represented individual compartments (Fig. 9). This provides strong evidence that *P. falciparum* replicates through alternating rounds of DNA replication and nuclear division. Our data further suggests that individual nuclei not exceeding a genome content of 2. Additionally, I was able to follow genome duplication in single nuclei of *P. falciparum* cells containing two sibling nuclei, which showed that DNA replication is already asynchronous before nuclear division occurs (Fig. 8, Fig. 9 and Fig. 10).

5.2.2 The dynamics of *P. falciparum* blood stage nuclear multiplication

Despite limited resolution (see section 5.1.2), I was able to use our nuclear cycle sensor system to observe individual parasites as they underwent nuclear multiplication (Fig. 14-16, Tab. S1). I found that from the onset of DNA replication parasites took an average of 14 hours until egress. During this period, 11.5 hours elapsed between the onset of the first S-phase and the end of the last S-phase. At an average blood stage-cycle time of 44 hours in our case, this indicates that parasites spent approximately 25% of intraerythrocytic development multiplying their nuclei, which is largely compatible with studies following DNA replication by flow cytometry (Ganter *et al.*, 2017). During this time the percentage of nuclei undergoing DNA replication at any given point varies significantly (Fig. 13, Fig. 23 and Fig. 29).

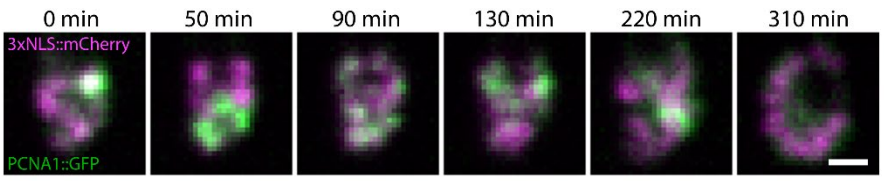

Figure 29* P. falciparum *blood stage parasites may replicate any number of nuclei at the same time. *Time-lapse images of a* P. falciparum *parasite expressing 3xNLS::mCherry (magenta) and PCNA1::GFP (green); scale bar, 2 µm.*

Parasites may have no nuclei undergoing DNA replication for short periods of time even if many nuclei are present, but at other timepoints may have all nuclei seemingly replicating their DNA at the same time (Fig. 29). This is in line with a study using nucleotide analogues to label nascent DNA in replicating nuclei, which

indicated that there is no limit on the number of simultaneously replicating nuclei (McDonald and Merrick, 2022).

The 14 hours in which parasites multiplied their nuclei included a time period at the end of the intraerythrocytic development of around 160 min, where no nuclear PCNA1::GFP accumulation was visible (Fig. 13 and Fig. 14). Towards the end of the intraerythrocytic development, nuclei align below to plasma membrane and a final round of nuclear division occurs, which is coupled to daughter cell formation (Francia and Striepen, 2014; Rudlaff *et al.*, 2020). Cytokinesis and daughter cell formation is initiated at approximately 3 hours before egress, and it was long suggested that daughter cell formation is synchronous and that a last synchronous round of DNA replication also occurs (Reilly *et al.*, 2007; Kono *et al.*, 2012; Francia and Striepen, 2014). Recent electron tomography data, however, suggests that while daughter cell formation occurs synchronously, the associated final round of nuclear division is not synchronous as nuclei divide at different times during daughter cell segmentation (Rudlaff *et al.*, 2020). Yet, it was not possible to investigate if a last synchronous round of DNA replication was coupled to cytokinesis.

Although I was not able to accurately segment nuclei and DNA replication events at these late timepoints, I was able to observe that during the last nuclear PCNA1::GFP accumulations before egress, some nuclei loose the signal before others (Fig. 14). Assuming that DNA replication is always accompanied by nuclear PCNA1::GFP accumulation, this observation indicates that there is no synchronous last round of DNA replication. Live-cell imaging data using inner membrane complex proteins indicates that cytokinesis starts 2.5-3 hours before egress (Kono *et al.*, 2012), which approximately coincides with the disappearances of the last nuclear PCNA1::GFP accumulations (Fig. 14). This suggests that the last DNA replication events conclude while cytokinesis is initiated, and it is tempting to speculate that the asynchrony of the last S-phases potentially mirrors the degree of asynchrony observed in the last nuclear divisions during the synchronous daughter cell formation (Rudlaff *et al.*, 2020). However, so far there is no data available to correlate the last DNA replications with the final nuclear division and daughter cell formation in single cells. Addition of fluorescently tagged cytokinesis markers such as MORN1, CINCH or GAP45 to our nuclear cycle sensor system in combination with live-cell imaging at an increased resolution, would help to investigate the final events of intraerythrocytic development (Kono *et al.*, 2012; Rudlaff *et al.*, 2019; Klaus *et al.*, 2022).

5.2.3 The dynamics of the individual nuclear cycle phases

Although crowding of the nuclei made tracking of events difficult once four nuclei were present in the parasite at the same time, I was able to quantify the duration of the individual nuclear cycle phases and the overall length of the nuclear cycles in early schizonts (Fig. 15). I was able to reconstruct around 70 lineage trees showing the pattern of the successive DNA replication and nuclear division events (Fig. 16). Shortly after the main results of my thesis were published (Klaus *et al.*, 2022), another study was published, which also investigated the nuclear cycle dynamics in *P. falciparum* and, in addition, in *P. knowlesi* (McDonald and Merrick, 2022). McDonald and Merrick used transgenic parasites expressing a *Herpes simplex* thymidine kinase, which permits the phosphorylation of nucleoside analogues into

nucleotides. Subsequently, these nucleotide analogues are incorporated into nascent DNA and can be detected by IFA after fixation (Merrick, 2015). In the recent study, McDonald and Merrick used pulsed labelling of DNA via nucleotide analogues to mark *de novo* DNA synthesis at different timepoints. (McDonald and Merrick, 2022). While this technique allows, e.g., the quantification of the speed of DNA replication forks, it does not permit to follow individual cells or nuclei over time. Another potential caveat is the sensitivity of thymidine kinase-expressing parasites to nucleotide analogues, with parasites experiencing growth phenotypes during schizogony at an IC_{50} below 100 nM (Merrick, 2015).

In spite of these major experimental differences, this study also found that *P. falciparum* proliferates via asynchronous rounds of DNA replication and nuclear division. McDonald and Merrick suggest that 70% of S-phases in *P. falciparum* parasites containing one nucleus take 40-75 min, which is in line with my observation that the first S-phase takes 54 ± 19 min (Fig. 15C) (McDonald and Merrick, 2022). In accordance with a study investigating the dynamics of microtubule rearrangement during blood stage schizogony (Simon *et al.*, 2021), McDonald and Merrick and I found that all phases of the first nuclear cycle were longer than those of the second nuclear cycle (McDonald and Merrick, 2022). This could be caused by on-going transcriptional activity at the onset of S-phase. Indeed, the total RNA-content of parasites peaks at this time point, possibly leading to a delay in genome duplication and segregation (Machado, Steinke and Ganter, 2021).

After the first nuclear cycle, I found that the duration of S-phase decreased to approximately 40 min and was relatively constant in nuclei of the second and third generation (Fig. 15C). McDonald and Merrick also report that the duration of S-phases decreases after the first nuclear cycle, but the authors further suggest that S-phases continue to get shorter as nuclear multiplication continues (McDonald and Merrick, 2022). In addition, they report that the time between S-phases become longer as nuclear multiplication continues (McDonald and Merrick, 2022). Our mathematical simulation of *P. falciparum* nuclear multiplication indicates that it slows down over time (Fig. 19). As we could not accurately quantify the DNA replication dynamics in later generations of nuclei, it is possible that this slow-down is achieved by extending the time between S-phases, with S-phases continuing to get shorter. However, our experimental data show that nuclei which replicate their DNA simultaneously, have longer S-phases (Fig. 20). This suggest that S-phases get longer as nuclear multiplication continues and more nuclei undergo S-phase at the same time. Live-cell microscopy using our nuclear cycle sensor system with increased resolution to track nuclei longer will help to resolve these differences.

In their study, McDonald and Merrick readily observed nuclei that replicated once and then did not initiate another S-phase for periods up to 5 hours (McDonald and Merrick, 2022). This ‘stalling’ phenomenon was detected in all schizont stages regardless of the number of nuclei and stalling was more common in parasites with 2-6 nuclei, with approximately 10% of nuclei being stalled (McDonald and Merrick, 2022). This is a clear difference to my data, as I did not observe stalling of nuclei (Fig. 13, Fig. 20, Fig. 23 and Fig. 28). While it cannot be excluded that the resolution of our live-cell microscopy does not permit the detection of such stalling, it may be possible that stalling of nuclei is induced by incubation with

nucleotides analogues over an extended time, due to their toxicity during nuclear multiplication (Merrick, 2015). Again, additional live-cell microscopy at increased resolution should allow more robust tracking of nuclei, testing if nuclei after S-phase can stall before entering a subsequent S-phase.

5.2.4 Blood stage DNA replication is a rate-limited process

When we simulated nuclear multiplication using a mathematical model, our results indicated that nuclear multiplication decelerates as parasite development progresses (Fig. 19). As we observed more and more nuclei undergoing DNA replication at the same time in late schizonts, we hypothesised that this deceleration may be caused by a factor that becomes increasingly limiting over time. Indeed, when comparing the duration of S-phases in parasites with two nuclei (S_2), we found that synchronous S_2-phases were significantly longer than S_2-phases that overlapped or were completed sequentially (Fig. 20I). While we did not find any other difference in the duration of the following SD- and DS-phases (Fig. 20F and G), we observed that synchronous S_2-phases are often preceded by a particularly long SD_1- and short DS_2-phases (Fig. 20B and C). This suggests that the closer S-phases follow to the preceding nuclear division, the higher the likelihood that these S-phases will initiate synchronously. We also observed that asynchrony is introduced after nuclear division and before S-phase, which is likely the time when a putative S-phase initiating factor locates to or activates in the nuclei (Fig. 13F). It is therefore tempting to speculate that when nuclear division is delayed, S-phase is initiated while two nuclei are still connected, leading to synchronous S-phases.

Synchronous and therefore prolonged S-phases caused a delay in the nuclear cycle (Fig. 20J). In combination with our observation that nuclear multiplication is stopped once a certain number of nuclei is reached (counter-type stopping mechanism) (Fig. 18) (Facchetti, Chang and Howard, 2017; Simon, Stürmer and Guizetti, 2021), this indicates that synchronous S-phases cause an overall delay in nuclear multiplication. Therefore, parasites with higher asynchrony, especially of their S-phase, may be able to allocate their resources more effectively, and complete intraerythrocytic development earlier.

The ability to allocate resources more efficiently could be an evolutionary adaptation the environment the parasite resides in during the blood stage: the erythrocyte. Lacking a nucleus, mitochondria, and most metabolic processes apart from glycolysis, the erythrocyte is a particularly resource-poor environment and parasites are dependent on the steady influx of nutrients from the blood plasma (Moras, Lefevre and Ostuni, 2017; Counihan, Modak and de Koning-Ward, 2021). Asynchronous nuclear cycling therefore could have evolved to use the limited resources of the erythrocyte more steadily. Curiously, asynchrony itself may also be strengthened by a limited resource. For example, if a certain amount of a limited resource is required for efficient S-phase, a nucleus entering S-phase before another may bind or use this resource to a degree that other nuclei may not be able to efficiently enter S-phase until the factor is replenished or redistributed. Depending on the kinetics of this process, resource limitation could therefore also drive asynchrony. However, the depletion of a limited resource by one nucleus requires an initial symmetry breaking event to enable one sister nucleus to start S-phase before the other in order to bind the resource first. Therefore, while resource

limitations may increase asynchrony, they cannot be responsible for nuclear asynchrony alone.

Our data suggests that DNA replication is affected by one or more limiting factor(s) (Fig. 20), but it is unclear what these factors may be. To be able to influence the DNA replication dynamics of two individual nuclei, this factor must be shared and diffusible between the nuclei. In principle, three different types of potential limiting factors can be considered.

As parasites are dependent on nutrients acquired from the blood plasma, extrinsic metabolic factors provided by the medium, such as hypoxanthine, which is essential for nucleic acid synthesis, could be available in only limited amounts (Tewari *et al.*, 2019). Metabolic factors such as glucose have been shown to influence the replication dynamics and number of daughter cells and could therefore also influence the dynamics of DNA replication events (Mancio-Silva *et al.*, 2017; Ch'Ng *et al.*, 2021). However, cells cultured in the same medium and often only separated by a few micrometres, still display different replication dynamics and produce different numbers of daughter cells, arguing against an effect of external factors (Fig. 16 and Fig. 19).

During the blood stage, the parasite also depends on the content of the erythrocyte, which is scavenged by the parasite for nutrients and energy (Lew, Tiffert and Ginsburg, 2003). Nuclear multiplication dynamics could also depend on the intracellular environment of the host cell, which differs for each parasite due to, e.g., the variability in age of erythrocytes and, in our laboratory settings, for each blood donor. Yet, I observed several cases of two parasites residing in the same host cell, with both parasites progressing through schizogony, and some of these parasites completed the intraerythrocytic development, seemingly producing daughter cell numbers comparable to single infections (Fig. 30).

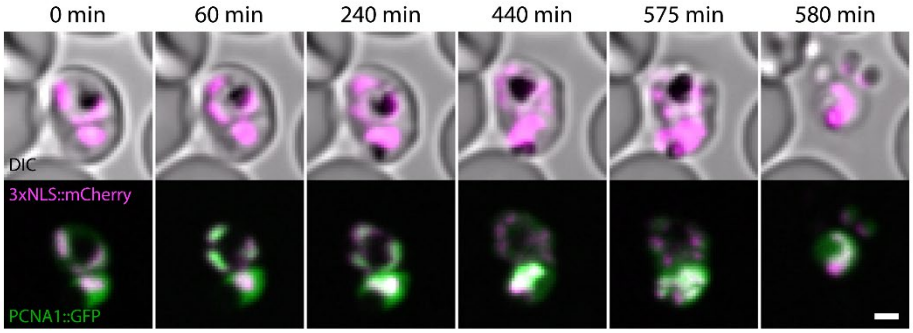

Figure 30 One parasite of a* P. falciparum *double infection may complete schizogony. *Time-lapse images of two* P. falciparum *parasite expressing 3xNLS::mCherry (magenta) and PCNA1::GFP (green) residing in the same blood cell; scale bar, 2 µm. Note, fully formed merozoites can be observed in the last time point.*

Together with observations that *Plasmodium* digests more haemoglobin then required to saturate its metabolic needs (Lew, Tiffert and Ginsburg, 2003), this suggests that the erythrocyte's resources might not be limiting. Therefore, parasite intrinsic factors may influence single-cell replication dynamics to a higher degree.

Indeed, differences in nuclear multiplication dynamics may be caused by variable expression of parasite intrinsic factors, such as proteins of the replication machinery, which may be limiting for the speed of DNA replication (Tanaka *et al.*,

2011). Additionally, as intercellular parasites, the levels of exogenous factors within the *P. falciparum* cells are dependent on the presence and activity of dedicated *Plasmodium* transporters (Counihan, Modak and de Koning-Ward, 2021). Thus, parasite specific expression levels of these transporters could lead to differences in the levels of nutrients present in the cells. Similarly, differences in expression levels of replication factors such as PCNA1 may cause different replication dynamics.

In our system, the duration of the S_1-phase does not correlate with the expression levels of PCNA1::GFP, which is highly overexpressed (Fig. 31). This is unsurprising, considering that tagged PCNA1 alone cannot support parasite replication (Fig. 11). Although the formation of replication foci by episomally expressed PCNA1::GFP indicates that it can take part in DNA replication (Fig. 11, 12 and 26), PCNA1::GFP is possibly only incorporated at a maximum of two units per trimer and thus endogenous levels of PCNA1 may be deciding for the speed of DNA replication. In addition, there are many other replication proteins besides PCNA1 whose expression levels could be limiting for S-phase (Maga and Hübscher, 2003). Lastly, in other organism such as yeast, the speed of DNA replication is dependent on proteins involved in origin firing (Fig. 5), which are present at low copy numbers in the cell, and are deciding for how many replication forks are activated at any given time (Tanaka *et al.*, 2011; Boos and Ferreira, 2019). Although there are no known homologues for many of these proteins in *Plasmodium* (Ganter *et al.*, 2017), it cannot be excluded that they are present in a divergent form and that similar principles for influencing S-phase duration apply in *P. falciparum* blood stage S-phase.

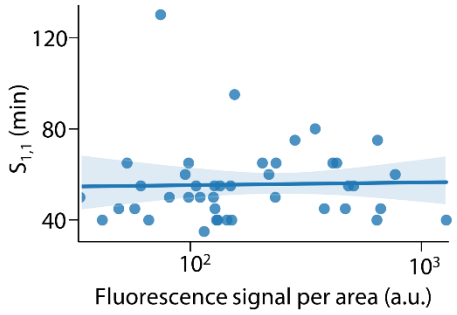

Figure 31 The speed of DNA replication does not correlate with expression level of PCNA1::GFP. *Correlation of the duration of the first S-phase and GFP fluorescence levels five minutes before start of $S_{1,1}$; a.u., arbitrary units. Solid line, linear regression; band, bootstrapped 95% confidence interval; Spearman's rho = 0.14, p = 0.37. Data visualisation and statistical analysis by P. Binder.*

5.2.5 Possible mechanisms driving asynchrony of nuclear multiplication

Despite being genetically identical, cultured in the same environment and nuclei originating from a single parent nucleus, parasites showed unique nuclear lineage trees with nuclei acting seemingly autonomously (Fig. 16). This variability is largely introduced in the time after nuclear division and before the onset of S-phase (Fig. 15F), a period which shares analogy with the G1-phase of the cell cycle.

Differences in the length of the cell cycle in genetically identical cells cultured in the same environment have been noted previously in other cases (Fox and Pardee, 1970; Spudich and Koshland, 1976; Hartwell and Unger, 1977; Sennerstam and

Strömberg, 1984; Zetterberg and Larsson, 1985). In yeast and mammalian cells, these differences are also caused by fluctuations of the G1-phase duration, which may arise due to size difference – which has been particularly well-documented in yeast – but can also be caused by molecular noise (Tyson, Lord and Wheals, 1979; Lord and Wheals, 1983; Gascoigne and Taylor, 2008; Holland and Cleveland, 2008). Specifically, fluctuations in low-abundance regulatory proteins result in significant differences in the cell cycle dynamics of genetically identically cells (Bean, Siggia and Cross, 2006; Talia *et al.*, 2007). While the large variability in the DS-phase duration during nuclear multiplication indicates that nuclear asynchrony may arise through similar mechanisms (Fig. 15F), it is unclear which pathways and proteins are involved.

In another organism where multiple nuclei share the same cytoplasm and display asynchronous behaviour, the filamentous fungi *A. gossypii*, asynchrony is likewise initiated during the G1 interval in sister nuclei originating from the same parent nucleus (Gladfelter, 2006; Gladfelter, Hungerbuehler and Philippsen, 2006; Nair *et al.*, 2010). During the G1-phase in most eukaryotic organisms, cells usually pass a 'commitment point', a specific point in a regulatory feedback loop where cells commit to re-entry into the cell cycle and ultimately initiate S-phase (Bertoli, Skotheim and de Bruin, 2013). In *A. gossypii*, asynchrony is dependent on this G1 regulatory feedback loop and both the upregulation of activators or the downregulation of inhibitors in this feedback loop cause nuclei to become more synchronous (Nair *et al.*, 2010). At the centre of this regulatory system lies the synthesis of the G1 cyclin 3, whose increased expression starts the molecular cascade leading to S-phase initiation by facilitating the export of the translational repressor Whi5 from the nucleus (Cooper, 2006). In *A. gossypii*, asynchrony is ultimately achieved by limiting the diffusion of cyclin 3 transcripts through binding to the aggregation prone RNA-binding protein Whi3 (Lee *et al.*, 2013; Gerbich *et al.*, 2020). Thus, cell cycle transcripts and their products are spatially restricted and unequally distributed, leading to different levels of cyclin 3 in different nuclei and asynchronous G1 to S-phase transition in these multinucleated cells (Lee *et al.*, 2013; Gerbich *et al.*, 2020).

In *A. gossypii*, like in most other model organisms, the regulation of the cell cycle and S-phase entry involves highly conserved proteins of the CDK and cyclin family. *Plasmodium* parasites, however, largely dispense with this dogma and encode a divergent set of cell cycle proteins seemingly lacking many canonical proteins – including G1-, S-, and M-phase cyclins (Matthews, Duffy and Merrick, 2018). What then regulates entry into S-phase in *Plasmodium* parasites?

Previous studies show that the *Plasmodium*-specific kinase CRK4 is pivotal in initiating S-phase in all generations of nuclei (Ganter *et al.*, 2017). CRK4 functions appears somewhat analogous to the function of the cell cycle kinase CDK2, which drives G_1- to S-phase transition in mammals and yeast and is regulated via phosphorylation and binding of cyclins (Ganter *et al.*, 2017). While CRK4 carries multiple inserts in its kinase domain that most likely block cyclin binding, it is differentially phosphorylated as schizogony progresses, indicating a possible phosphorylation-dependent regulation (Ganter *et al.*, 2017). Recent, unpublished data from our lab indicate that CRK4 preferentially localises to microtubule-

enriched structures within the nucleus, including the centriolar plaque, and that it is also involved in regulating microtubule-rearrangement at the G1- to S-phase transition, rendering it a master regulator of nuclear cycle progression (M. Machado, unpublished data). Uneven distribution or activation of CRK4 could therefore cause the observed asynchronous S-phase initiation in nuclei of a schizont and, thus, lead to asynchronous nuclear multiplication in *P. falciparum*. However, how this uneven distribution or activation could be achieved and which other proteins could be involved, is unclear.

5.2.6 Functional analysis of different PCNA1 residues and motifs

The basis for any mechanism of nuclear autonomy is the asynchronous distribution or recruitment of effector proteins to the different sister nuclei. To date only few proteins have been identified that show a clear nuclear-cycle dependent phenotype (Reininger *et al.*, 2011; Simon *et al.*, 2021). A prime example of such a protein is PCNA1, which shows a very specific nuclear-cycle dependent behaviour and can be readily overexpressed (Fig. 12 and Fig. 13), enabling characterization of WT and mutant proteins. Investigation of the molecular determinants of heterogenous PCNA1 accumulation could therefore reveal potential regulatory mechanism of nuclear autonomy.

Many of the functional amino acid residues of human and yeast PCNA are conserved in *Plasmodium* PCNA1, allowing a certain degree of functional prediction (Fig. 22). Similarly, structural comparison between *P. falciparum* PCNA1 and human PCNA allows an estimation of potential structural repercussions of mutations (Fig. 32). In this thesis, I investigated a range of conserved, sometimes possibly modified residues, some of which are located in amino acid stretches that are predicted to contain nucleo-cytoplasmic transport sequences (Fig. 22-25 and Fig. 32A) (Kim and Lee, 2008; Bouayad *et al.*, 2012).

Mutation of Y114 to alanine caused loss of trimerization in human and yeast PCNA (Jónsson *et al.*, 1995; Bouayad *et al.*, 2012), which should critically impair PCNA function. In contrast, when I mutated the homologous F114 to alanine I did not observe changes in PCNA1 accumulation in *P. falciparum* (Fig. 23A). Likewise, deletion of a *Plasmodium*-specific insertion between T246-K254 did not influence PCNA1 accumulation (Fig. 23A). The absence of any effect on accumulation suggests either that these mutations did not have the predicted effect (e.g., F114A did not affect trimerization), that these mutations are not important for accumulation, or that these mutations only induced small defects that could be masked by incorporation of both endogenous and mutant PCNA1 into functional trimers.

Episomally expressed PCNA1::GFP readily forms replication foci, indicating it is functional, incorporated into trimers, and participates in DNA replication (Fig. 11, 12 and Fig. 26). However, we were not successful in tagging the endogenous PCNA1, indicating that tagged PCNA1 alone is not able to support normal parasite growth. Consequently, formation of functional trimers might depend on the incorporation of at least one endogenous and non-tagged PCNA1. A similar phenomenon has been observed for tagged versions of the structural HIV protein Gag, which depends on the presence of untagged Gag to form fully infectious viral

particles (Müller *et al.*, 2004). Depending on the severity of the introduced mutation, endogenous WT PCNA1 may therefore compensate for slight defects in function of the mutant units. Previously, yeast PCNA carrying the Y114A mutation was shown to be able to form trimers with WT yeast PCNA although at a much lower rate (Jónsson *et al.*, 1995). Hence, in *P. falciparum* endogenous PCNA1 may also buffer for small defects of mutant PCNA1 proteins. To investigate if the three mutations have any functional relevance, a more stringent comparison of PCNA1::GFP mutants in the cytosolic and nuclear fraction pre- and post S-phase could be done to analyse if these mutants are incorporated into replication foci at a lower rate. Additionally, a combination of inducible deletion of endogenous PCNA1 with the overexpression of PCNA1 mutants would uncover if these mutants show a specific phenotype in absence of endogenous PCNA1.

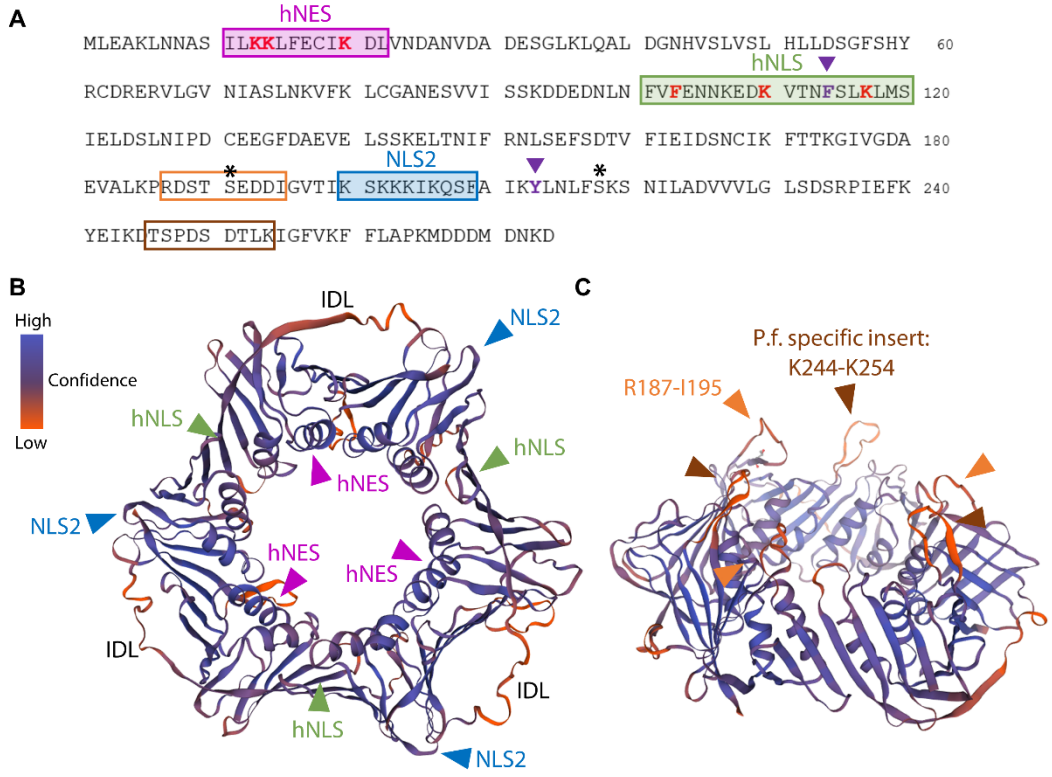

Figure 32 Localisation of functional residues within the PCNA1 trimer. *(A) Sequence of* P. falciparum *PCNA1 with highlighted residues and motifs that were investigated. Magenta, NES in human PCNA; green, NLS in human PCNA; blue,* Plasmodium*-specific NLS; orange box, exposed loop with low conservation; brown box,* Plasmodium*-specific insertion. Functionally important mutated residues are marked in red, residues where mutation had no effect on nuclear accumulation of PCNA1::GFP in purple, and residues where phosphoproteomic data indicates phosphorylation in* P. falciparum *with an asterisk. (B, C) Predicted structure of the* P. falciparum *PCNA1 trimer in top view (B) and side view (C). Location of different nuclear transport signal sequences is marked by arrows, with colours corresponding to (A). Interdomain loop (IDL) and position of DNA is indicated in (B). (B,C) Structure prediction via SWISS-MODEL on basis of 5tup.1A. template (University of Basel, Biozentrum).*

5.2.7 Y213F does not show an effect on nuclear accumulation

One of the mutations I analysed in this thesis was Y213F, which had previously been suggested to impair PCNA1 function and decrease the nuclear fraction of PCNA1 (Banu *et al.*, 2018). In contrast, mutation of Y213F in PCNA1::GFP did not influence transient nuclear accumulation during S-phase (Fig. 23A and Fig. 32A).

Similar to the system I used here, Banu *et. al.*, overexpressed PCNA1::GFP fusion protein with the mutations Y213A or S191A in addition to the endogenous PCNA1 (Banu *et al.*, 2018), but in contrast to our studies, Banu *et. al.,* analysed the localisation of their PCNA1 mutants via single snap-shots of live parasites. When analysing the localisation of these mutants, the authors state that "Interestingly, majority of the parasites expressing Y213F-PCNA1-GFP showed diffused GFP signals distributed all over the parasite, while parasites expressing S191A-PCNA1-GFP showed nuclear foci in many cells.", giving percentages of foci bearing parasites at 59.25% for PCNA1::GFP, 26.23% for the S191A mutant and 17.64% for the Y213F mutant (Banu *et al.*, 2018). The authors further perform sub-cellular fractionation Western blots and genotoxic survival assays and conclude that the Y213F mutant shows a loss of function and a decreased nuclear retention, while the S191A mutant does not (Banu *et al.*, 2018). However, given the provided information in the publication, an in-depth comparison of the respective observations is difficult. While it is possible that the reduction of the nuclear fraction in the Y213F mutant observed by Banu *et. al.,* does not translate into disturbed nuclear accumulation but rather changed accumulation dynamics, it is also possible that the Y213F mutation does not have any effect on PCNA1 function (Banu *et al.*, 2018). The functional relevance of the Y213F mutation is further questioned by the available phosphoproteomic data, which indicate that PCNA1 is phosphorylated at S191 and S218 but not at Y213 (Fig. 22A and Fig. 32A) (Solyakov *et al.*, 2011; Treeck *et al.*, 2011; Lasonder *et al.*, 2012; Pease *et al.*, 2013).

Although neither S191 nor S218 are conserved in human PCNA (Fig. 22A), their phosphorylation indicates that both residues may have a functional relevance and may be involved in PCNA1 nuclear accumulation. Despite the aforementioned study by Banu *et al*. (Banu *et al.*, 2018), revisiting the functional relevance of the S191A mutation could lead to valuable insight on mechanisms of PCNA1 accumulation. Mutation of both residues should therefore be undertaken and their impact on protein function and localisation investigated.

5.2.8 S-phase PCNA1 accumulation is likely caused by association to DNA

To dissect the contribution of nuclear transport and DNA binding to nuclear PCNA1 accumulation, I also investigated two well-conserved regions which have been shown to contain nuclear transport signals in human PCNA1 (Fig. 22 and Fig. 32) (Kim and Lee, 2008; Bouayad *et al.*, 2012). Within these regions I investigated several well-conserved residues with a functional relevance in human PCNA (González-Magaña and Blanco, 2020).

The first region I analysed was I11-L22 (Fig. 22A, for further discussion see below), which contains the conserved lysine residues K13, K14 and K20 that were mutated to alanine (Fig. 22). This KKK13,14,20AAA mutant was not able to accumulate during S-phase but displayed proper localisation in non-replicating cells, with a higher signal in the nucleus than in the cytoplasm (Fig. 23B). K13 and K14 are part of the basic amino acids within the PCNA channel and interact with the DNA backbone via their positive charge (González-Magaña and Blanco, 2020). Their acetylation is implicated in chromatin dissociation and protein degradation during DNA damage response in human cells (Cazzalini *et al.*, 2014; González-Magaña

and Blanco, 2020). Likewise, K20 is critically involved in clamp sliding, and its acetylation is involved in the DNA damage response in human PCNA (Billon and Côté, 2017; Billon *et al.*, 2017). Acetylation of lysine residues results in neutralisation of their positive charge and is predicted to be the cause of decreased DNA association (Billon and Côté, 2017; González-Magaña and Blanco, 2020). Additionally, mutation of at least three charged residues to alanine within the yeast PCNA channel stopped loading of PCNA to the DNA (McNally *et al.*, 2010). Here, mutation of not one but all three of the residues K13, K14 and K20 to the neutral amino acid alanine may therefore not only impair DNA binding, but also loading of PCNA1 to the DNA. Thus, the observed loss of nuclear accumulation of the KKK13,14,20AAA mutant may be caused by its inability to interact with the DNA. This finding would suggest that nuclear accumulation of PCNA1 may be a result of sequestration of PCNA1 due to DNA association during S-phase.

The second stretch of conserved residues I investigated was contained within F100-S120 (Kim and Lee, 2008) (Fig. 22, for further discussion see below). As with the KKK13,14,20AAA mutant, mutation of the three conserved residues F103, K110 and K117 to alanine led to an inability to accumulate in the nucleus during S-phase while not influencing the protein's basal localisation. This indicates that this mutant is not defective in nuclear transport, but cannot participate in nuclear accumulation upon entry into S-phase (Fig. 23B). The FKK103,110,117 residues are located close to the PCNA-PCNA monomer interaction surface, but previous reports on human PCNA indicate that mutations of K110 and K117 do not interfere with PCNA trimer formation (Naryzhny, Zhao and Lee, 2005). Instead, human PCNA has previously been suggested to form transient double homotrimer complexes depending on K110, and mutating K110 to alanine has identified this residue as critical to target human PCNA to DNA replication and repair foci, while not interfering with its nuclear localisation (Naryzhny, Zhao and Lee, 2005; Kim and Lee, 2008). In analogy, the FKK103,110,117AAA mutant could be unable to target replication foci in *P. falciparum*, again supporting the hypothesis that nuclear accumulation is caused by incorporation of PCNA1 into active replication sites.

In our analysis, we included a mutation of F103 to alanine, which has no previous functional annotation but was highly conserved in *Plasmodium* PCNA. While F103 is part of a beta sheet at the outer surface of the PCNA trimer, its phenyl side chain reaches into the protein and is therefore unlikely to be involved in interaction with other proteins. However, it cannot be excluded that mutation of F103 influences the structure or stability of PCNA1, which could contribute to the observed phenotype of the FKK103,110,117AAA mutant. Subsequently, mutation of K110 and K117 alone should be done to test this possibility.

5.2.9 Potential nuclear transport signal sequences in PCNA1 may be non-functional

While the phenotype of the triple mutants indicates that accumulation during S-phase is probably caused by chromatin association, *Plasmodium* PCNA1 must still be rapidly imported to and exported from the nucleus to exert its function in multiple nuclei of *P. falciparum*. Regulation of nuclear transport may also be involved in facilitating the nuclear accumulation of PCNA1 during S-phase, and

thus, a better understanding of the principles governing the nucleo-cytoplasmic transport of PCNA1 is advantageous.

There are two publications that suggest that PCNA carries nuclear transport signal sequences (Kim and Lee, 2008; Bouayad *et al.*, 2012). The paper by Kim and Lee suggests that F100-S120 acts as an NLS in human PCNA to target the always-nuclear human PCNA to the nucleus after expression (Kim and Lee, 2008). The paper by Bouayad *et al.* suggests that in human PCNA I11-L22 acts as an NES, which is used to expel human PCNA from the nucleus during granulocytic differentiation (Bouayad *et al.*, 2012). Both regions are well conserved in *Plasmodium* PCNA1 (Fig. 22A), indicating they could function in the same manner *P. falciparum*. To investigate these regions, I combined a mutational and a synthetic approach by either deleting these regions and analysing the localisation of the resulting mutants (Fig. 22B and Fig. 23B), or by fusing predicted nuclear transport signals to GFP to test if they are sufficient to target GFP to different cellular compartments (Fig. 24 and Fig. 25).

The first region I analysed was I11-L22, which was suggested to act as a classical NES in human PCNA (Bouayad *et al.*, 2012). Classical NESs facilitate nuclear export through the export receptor exportin-1 on accord of their hydrophobic sequence often containing leucines (Xu, Farmer and Chook, 2010). Exportin-1, which is well-conserved in *P. falciparum*, is responsible for the export of the majority of proteins from the nucleus and thus classical NESs are the largest and most-well characterized family of nuclear export sequences (Frankel and Knoll, 2009; Xu, Farmer and Chook, 2010). In their study, Bouayad *et. al.,* based their conclusion that I11-L22 acts as a classical NES on experiments where they fused I11-L22 to GFP and saw a nuclear exclusion phenotype in localisation studies, which could be reversed by chemical inhibition of exportin-1 (Bouayad *et al.*, 2012; Sun *et al.*, 2013).

Similarly, I fused predicted signal sequences between K5-D41 both alone (K5-I19, NES1 and S10-D41, NLS1) and as a combined peptide (K5-D41, NES1/NLS1) with GFP, and episomally overexpressed them in *P. falciparum* to investigate their location (Fig. 25 and Fig. 33). Only the peptides containing S10-D41 showed a specific localisation, with lower signal intensity in the nuclei than in the cytoplasm (Fig. 25 and Fig. 33). This pattern is compatible with the presence of an NES between S10-D41. Additionally, as discussed, S10-D41 also contains I11-L22 which acted as an NES in human cells, further strengthening the evidence for a functional NES in this region (Bouayad *et al.*, 2012).

In contrast, I found that deletion of I11-L22 from full length PCNA1, with and without linker replacement, does not show the predicted phenotype for removal of an NES, which would be a primarily nuclear protein localisation (Fig. 33). Instead, this deletion mutant was distributed evenly across the cell, with a decreased nuclear localisation more compatible with deletion of an NLS or a complete loss of targeted protein transport (Fig. 23B and Fig. 33). While unexpected, this distribution is also consistent with the studies by Bouayad *et. al.,* which showed that point mutations of leucines within I11-L22 as well as deletion of I11-L22 in human PCNA led to an even distribution of mutant human PCNA across the cell (Bouayad *et al.*, 2012).

Bouayad *et. al.,* speculated that this may be due to a dual role of this amino acid stretch in both nuclear export and nuclear import and that any disruption of this sequence may lead to phenotype that is associated with removal of an NLS (Bouayad *et al.*, 2012).

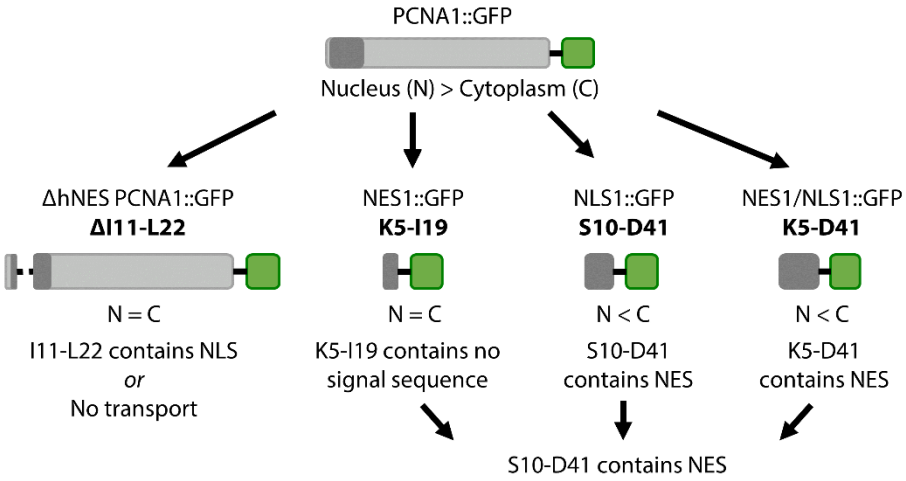

Figure 33 Schematic overview of mutants and peptides derived from* P. falciparum *PCNA1 K5 to D41*. Dark grey, K5-D41, green, GFP tag. Protein localisation and distribution indicated below peptide; N, nucleus; C, cytoplasm. Not drawn to scale.*

However, none of the peptides derived from the regions around I11-L22 had a localisation compatible with an NLS when fused to GFP (Fig. 25 and Fig. 33). This observation indicates that if an NLS is also present at this position it may be weaker than a putative NES at the same location and may only be functional in combination with other PCNA1 NLSs. As I could not unequivocally identify any other NLSs within the PCNA1 sequence (Fig. 23B, Fig. 25 and Fig. 34), perhaps it is more parsimonious to assume that deletion of I11-L22 causes major disturbances in the protein structure, leading to loss of any transport activity. Supporting this hypothesis, the observed even distribution of the I11-L22 deletion mutant is closely reminiscent of that of only GFP (Mogollon *et al.*, 2016). Further mutational experiments, including the expression of only the I11-L22 and L23-D41 peptide or mutation of single hydrophobic residues, which may be important for NES activity will help to disentangle these phenotypes.

Further raising questions on the significance of the identified NES, Bouayad *et. al.,* showed that nuclear export of human PCNA can be stopped via chemical inhibition of exportin-1 – but only in the monomeric form of PCNA, which had to be induced by mutation (Bouayad *et al.*, 2012). This was explained by I11-L22 being buried within the PCNA channel and not accessible as an NES in the PCNA trimer (Bouayad *et al.*, 2012) (Fig. 32). Monomeric PCNA is thought to be a largely non-functional, although it is present in the nucleus of HeLa cells (Chiara *et al.*, 2013). Hence, even if *P. falciparum* PCNA1 does contains an N-terminal NES and/or an NLS between S10-D41, both signal sequences may be non-functional or only functional under specific conditions. It may be possible that posttranslational modifications lead to decreased chromatin association and increased levels of monomeric PCNA1, which could facilitate access of the nuclear export machinery to the NES and expulsion of PCNA1 from the nucleus.

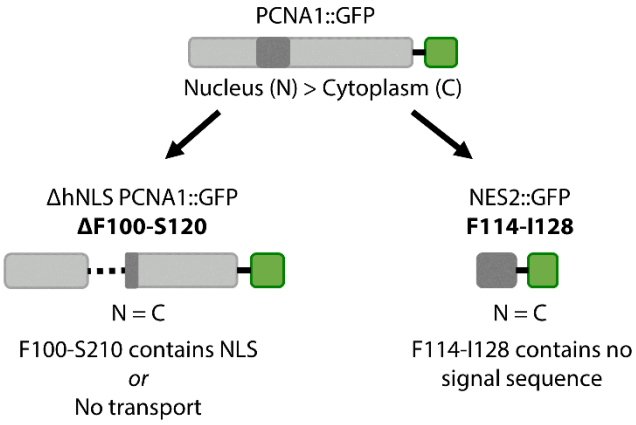

Figure 34 Schematic overview of mutants and peptides derived from* P. falciparum *PCNA1 F100 to I128. *Dark grey, F100-I128, green, GFP tag. Protein localisation and distribution indicated below peptide; N, nucleus; C, cytoplasm. Not drawn to scale*

Another region I analysed for nuclear transport signal sequences was F100-S120, which contained the residues F103, K110 and K117 (see section 5.2.8) and was suggested to act as a classical NLS in human PCNA (Fig. 22, Fig. 23B and Fig. 32) (Kim and Lee, 2008). In contrast to NESs, classical NLSs generally depend on clusters of basic lysine residues to facilitate interaction with import receptors of the importin family, which are well-conserved in *P. falciparum* (Frankel and Knoll, 2009; Lu *et al.*, 2021). Deletion of F100-S120 in *P. falciparum* PCNA1 with or without linker replacement led to decreased nuclear localisation and even distribution throughout the cell (Fig. 23B and Fig. 34). A similar phenotype was observed in human PCNA upon deletion of this region and was attributed to the deletion of an NLS (Kim and Lee, 2008). However, the F100-S120 fragment is comparatively large and covers the PCNA-PCNA monomer interaction interface (Fig. 32), including several residues, which has been shown to be essential for trimerization (Jónsson *et al.*, 1995; Freudenthal *et al.*, 2009). Therefore, similar to the I11-L22 deletion mutants, the observed localisation of the F100-S120 deletion mutants could also be due to a complete loss of trimerization capabilities or loss of proper protein structure. Supporting this hypothesis, the fusion protein of F114-I28 (NES2) with GFP did not show a specific localisation (Fig. 25 and Fig. 34). Yet, this peptide only partly covered the F100-S120 region, and thus it cannot be excluded that it was missing critical residues for nuclear targeting. To investigate whether F100-S120 does contain an NLS or not, the F100-S120 peptide could be excised and fused to GFP to investigate if it is sufficient to direct GFP to the nucleus.

5.2.10 A unique PCNA1 motif targets the centriolar plaque

P. falciparum PCNA1 displays a strikingly different behaviour compared to the PCNA of other organisms, where it is usually exclusively nuclear (Maga and Hübscher, 2003). The transient nuclear accumulation and nucleo-cytoplasmic shuttling of *P. falciparum* PCNA1 may hence be caused by *Plasmodium*-specific motifs and modifications. One of the sequences we identified via software prediction, the NLS2 between K200-F209, was not conserved in either human, mouse or rice PCNA and was also not present in *P. falciparum* PCNA2 (Fig. 24). This stretch of amino acids is located in a loop connecting two beta sheets on the

outside surface of the PCNA1 trimer (Fig. 32), but not close to the inter-domain loop between I121 and E132, which is known to interact with many proteins such as the flap endonuclease 1 (Fen1) or the DNA ligase 1 (Fig. 32) (Maga and Hübscher, 2003; Moldovan, Pfander and Jentsch, 2007). PCNA1 K200-F209 is lysine rich, containing five lysine residues within seven amino acids, all of which are likely surface exposed, suggesting these residues are well-accessible and potentially functional (Fig. 24 and Fig. 32).

When fusing the *Plasmodium*-specific K200-F209 peptide to GFP and analysing its localisation, it targeted the centriolar plaque (Fig. 23B). The centriolar plaque has previously been proposed to act as a hub for cell cycle coordination and many cell cycle proteins such as the kinase Ark-1 and the S-phase promoting kinase CRK4 can be found there (Arnot, Ronander and Bengtsson, 2011, M. Machado, unpublished data). When searching for *P. falciparum* proteins containing this KxKKKxK motif, the 819 identified proteins were predicted to be predominantly nuclear – which is not unexpected as lysine-rich regions often act an NLS – involved in ribosome biogenesis and cell cycle regulation, and predicted to have kinase activity, which is central to the regulation of cell cycle processes (Fig. S1) (Lu et al., 2021). It is therefore possible that the K200-F209 peptide is targeted to the centriolar plaque due to interaction with cell cycle coordinating proteins. To further test if this motif is indeed critical for PCNA1 centriolar plaque localisation and function, a mutant in which this sequence is replaced by the sequence of human PCNA will need to be generated and analysed for its function and localisation.

5.2.11 Spatiotemporal coordination of PCNA1::GFP accumulation during S-phase

As the localisation of the K200-F209 peptide indicated a role of the centriolar plaque in PCNA1 accumulation, I revisited the organisation of PCNA1 accumulation within nuclei during S-phase. I found that PCNA1::GFP accumulation was always initiated close to the centriolar plaque before continuing as a wave across the nucleus and terminating in the nuclear periphery (Fig. 26). Consistent with the previous observation that the K200-F209 peptide specifically targets the centriolar plaque, this localisation further implicates the centriolar plaque as the main organising centre for S-phase entry and nuclear cycle progression.

Furthermore, the presence of high PCNA1::GFP signal patches only in some areas of the nucleus provides additional support to the hypothesis that S-phase accumulation is caused by chromatin association. Subnuclear patches of high PCNA1::GFP signal most likely represent active replication factories where PCNA1::GFP is bound to the DNA at a high rate (Meister, Taddei and Gasser, 2006; Meister *et al.*, 2007). The associated drop in the unbound fraction of PCNA1::GFP in the nucleoplasm may cause a change in the cytoplasm/nucleus equilibrium of PCNA1::GFP and result in an influx of PCNA1::GFP into the nucleus, and consequently the observed depletion of cytoplasmic PCNA1::GFP (Fig. 13). Analysis of the protein content of PCNA1::GFP within the replication foci, the nucleoplasm and the cytoplasm over time will enable further testing of this hypothesis.

The consistent progression of replication foci from areas close to the centriolar plaque towards the nuclear periphery (Fig. 26) suggests that S-phase is a spatially coordinated process with a pre-defined sequence, similar to the DNA replication patterns observed in mammalian cells (Leonhardt *et al.*, 2000; Boos and Ferreira, 2019). Here, the spatial sequence of origin activation is partially dictated by chromatin state and transcriptional activity, with euchromatin being replicated first and heterochromatin being replicated last (Dimitrova and Gilbert, 2000; Petryk *et al.*, 2016; Devbhandari *et al.*, 2017). Although chromosomes do seemingly not condense (Read *et al.*, 1993; Gerald, Mahajan and Kumar, 2011), they are likely organized in the nuclei of *P. falciparum*. The *Plasmodium* centromeres are clustered and have been suggested to be associated to the mitotic spindle close to the centriolar plaque during all stages of the nuclear cycle (Hoeijmakers *et al.*, 2012; Simon *et al.*, 2021). Unlike in mammalian cells, *Plasmodium* centromeric regions are not heterochromatic (Hoeijmakers *et al.*, 2012) while telomeres are usually located at the nuclear periphery and show heterochromatin markers (Freitas-Junior *et al.*, 2000; Hernandez-Rivas *et al.*, 2010). *P. falciparum* S-phase may therefore follow similar patterns as mammalian S-phase, with the euchromatic centromeric regions close to the centriolar plaque being replicated first and heterochromatic telomeres at the nuclear periphery being replicated last. The early replication of centromeric regions is not unique to *Plasmodium* and has been observed in the heterochromatic pericentromeric regions of yeast before, suggesting an active regulation of origin firing (Hayashi *et al.*, 2009; Natsume *et al.*, 2013).

In addition to helping understand the intra-S-phase dynamics in *P. falciparum*, the identification of nuclear PCNA1::GFP accumulations as replication foci also has implications for the mechanism behind nuclear accumulation of PCNA1. If nuclear accumulation of PCNA1::GFP is predominantly caused by DNA association, and if the progression of subnuclear PCNA1::GFP foci represents the stepwise firing of origins and formation of replication foci, then nuclear accumulation of PCNA1::GFP may simply be a consequence of increased availability of active replication forks and not directly regulated. During origin firing, licensed origins are converted to active replication forks via a well-described cascade involving the pre-initiation complex (Fig. 5) (Boos and Ferreira, 2019). The DNA at the activated origin subsequently opens, and only then the origin may acquire replication factors such as the RFC complex and PCNA (Fig. 5) (Boos and Ferreira, 2019). Therefore, it is possible that DNA association of the RFC complex and PCNA1 – and subsequently PCNA1 loading and accumulation at replication foci – is simply only possible once origins are activated.

In yeast, firing involves several proteins including Sdl3 and Sdl7, that transiently associate with licensed origins during firing to provide a platform for regulation of origin conversion (Fig. 5) (Boos and Ferreira, 2019). Once an origin is activated, these proteins detach from the origin to continue the conversion of other licensed origins (Fig. 5). In that case, it is possible that accumulation is not regulated at the level of PCNA1 loading but rather at origin firing, when PCNA1 is not yet associated with the DNA. In accordance with this hypothesis, establishment of the pre-initiation complex is the central regulating step in origin firing, with many of the involved factors being limiting for origin firing and S-phase duration in yeast

and other model organisms (Tanaka *et al.*, 2011; Boos and Ferreira, 2019). However, while regulation of origin firing proteins may be the critical step ultimately leading to PCNA1 accumulation, it cannot be excluded that PCNA1 itself and its interaction partners are posttranslationally regulated to accommodate effective replication fork association and loading.

5.2.12 Nuclear export in *P. falciparum*

Although my results indicate that PCNA1::GFP accumulation is predominantly caused by increased chromatin association at active DNA replication sites, PCNA1::GFP must still be imported into the nucleus before it can be loaded onto the DNA. While in non-replicating cells PCNA1::GFP levels are already higher in the nucleus than in the cytoplasm, there is still a substantial pool of cytoplasmic PCNA1::GFP (Fig. 12). Moreover, the reversible depletion of this cytoplasmic pool during S-phase indicates that PCNA1 is transferred from the cytoplasm to the nucleus during DNA replication, meaning it is used during S-phase (Fig. 13B). It is thus likely that nuclear transport is vital for PCNA1 function. While the PCNA1 monomer itself is small enough to potentially enter the nucleus by passive diffusion, the PCNA1::GFP fusion protein exceeds the most commonly used size limit of 30–60 kD for passive transport and the rapid depletion of the cytoplasmic PCNA1::GFP pool further indicates active transport (Timney *et al.*, 2016) (Fig. 13B). In addition, human PCNA is actively transported in and out of the nucleus via the import factor importin-β and the export factor exportin-1 respectively (Kim and Lee, 2008; Bouayad *et al.*, 2012).

To be able to facilitate efficient S-phase in multiple nuclei of a schizont, redistribution of PCNA1 to the cytoplasm after completion of DNA replication is essential. Moreover, decreasing the PCNA1 export rate in a given nucleus would constitute an attractive mechanism to increase the intranuclear pool of PCNA1 available for S-phase. I therefore investigated how PCNA1 is exported from the nucleus in *P. falciparum*. However, little is known about nucleo-cytoplasmic transport in *P. falciparum* in general. As previous publications indicated that human PCNA is transported from the nucleus via exportin-1 and my results indicated that PCNA1 carries a classical NES at the same position as human PCNA (Fig. 23B and Fig. 25), I focused my research on exportin-1 dependent nuclear export.

Exportin-1 dependent nuclear export is commonly studied using small drugs of the class of selective inhibitors of nuclear export (SINE) (Wang and Liu, 2019). SINE have been developed as anti-cancer drugs, with a large range of available compounds (Wang and Liu, 2019). The prototype for many SINE is the antifungal compound LMB, which blocks cargo recognition of exportin-1 through selective and covalent binding to C528 in the NES binding groove of mammalian exportin-1 (Hamamoto, Uozumi and Beppu, 1985; Kudo *et al.*, 1998; Sun *et al.*, 2013). Despite previous reports indicating that *P. falciparum* is sensitive to LMB, we found that *P. falciparum* 3D7 parasites are refractory to LMB treatment, likely due to the presence of an isoleucine in the position 637, which represents the homologous residue to C528 in mammalian exportin-1 (Fig. 27A and B) (Panchal *et al.*, 2014). In contrast, the LMB derived SINE KPT-251 induced a 50% growth reduction of *P. falciparum* 3D7 parasites compared to the carrier control (Fig. 27C), indicating that KPT-251 is at least partially functional despite reports of its mode

of action being the same as LMB (Etchin *et al.*, 2013). Differences in the chemical structure of LMB and KPT-251 cause differences in the interaction profile with amino acids of the NES binding groove (Sun *et al.*, 2013). Binding of LMB is suggested to further stabilise after covalent conjugation of LMB to the target cysteine (Sun *et al.*, 2013). Without covalent binding, LMB may only be able to occupy the binding groove transiently, causing less or no inhibition. In turn, the observed residual inhibitory activity of KPT-251 could be due to its different NES groove interaction profile. Alternatively, parasite death upon treatment with KPT-251 may be due to parasite-specific off target effects of KPT-251 compared to LMB.

5.2.13 Nuclear export of PCNA1::GFP during nuclear multiplication

To investigate exportin-1 dependent nuclear export in *P. falciparum*, we constructed a new LMB-sensitive strain by exchanging I637 to a cysteine via CRISPR-Cas9 editing. The resulting parasite strain CRISPR-D-I637C (I637C) was sensitive to LMB (Fig. 27A and B). Strikingly, parasite death upon KPT-251 treatment was only minimally enhanced in the I637C strain, again indicating that KPT-251 acts largely independent of NES groove cysteine binding in *P. falciparum* (Fig. 27C).

Treatment of the I637C strain with 250 ng/ml LMB prior to imaging did not disturb nuclear accumulation and redistribution of PCNA1::GFP (Fig. 28). As we found that nuclear accumulation of PCNA1::GFP is not altered by LMB treatment, it is currently not possible to unequivocally show that LMB treatment indeed inhibits exportin-1 and that the inhibition of nuclear export is the reason for parasite death of the I637C cell line upon LMB treatment. To test this, export of known exportin-1 cargos with and without LMB treatment in the background of the I637C mutation could be analysed. For this, a mostly marker free strain of parasites carrying the I637C mutation must be generated. Then, a panel of known or predicted exportin-1 cargos should be screened to identify a good reporter. Observation of the localisation dynamics of such a reporter under LMB treatment will test the specificity of our I637C system and enable the future study of nuclear export in *P. falciparum*. It will also allow us to further investigate the nucleo-cytoplasmic transport of PNCA1 (Fig. 24A and Fig. 25

Surprisingly, we saw no effect on nuclear accumulation or redistribution of PCNA1::GFP after S-phase upon treatment of our I637C stain with LMB (Fig. 28). This indicates that PCNA1 is not transported via exportin-1 in *P. falciparum*, although the specificity of LMB treatment in the I637C stain remains to be analysed. Instead, PCNA1 may be exported from the nucleus through alternative nuclear export pathways. Sequence comparison of known components of the nuclear trafficking system indicates that *Plasmodium* parasites carry a minimal set of genes responsible for nuclear export (Frankel and Knoll, 2009). While many transport receptor orthologues for proteins such as the transporter associated with antigen processing (TAP) and exportin-4 to -6 are seemingly absent, *P. falciparum* encodes orthologues for the nuclear export receptors exportin-1, exportin-t, and exportin-7 (Frankel and Knoll, 2009). As its name suggests, exportin-t is usually involved in trafficking of tRNAs while exportin-7 represents an alternative nuclear export receptor for a broader range of proteins and may even be involved in nuclear

import as well (Aksu *et al.*, 2018). Thus, it may be possible that PCNA1 is exported from – and potentially also imported to – the nucleus via exportin-7 rather than exportin-1. Unlike exportin-1, which interacts with classical NESs carrying hydrophobic residues, exportin-7 interacts with NES that are rich in basic lysine residues and show a 3-dimensional structure, which complicates NES identification (Mingot *et al.*, 2004). Exportin-7 dependent nuclear export is one of the least studied nuclear export pathways, in part due to lack of tools for chemical inhibition. However, some progress has been made in recent years by employing the inducible expression of anti-exportin-7 nanobodies to block exportin-7 function (Aksu *et al.*, 2018). Inducible expression of such nanobodies may also enable the study of exportin-7 dependent nuclear trafficking for localisation of *P. falciparum* PCNA1.

5.3 Outlook

Using a combination of cutting-edge imaging techniques and novel tools together with mutagenesis approaches, I was able to characterize the fundamental aspects of organisation and regulation of *P. falciparum* cell cycle control during nuclear multiplication (Klaus *et al.*, 2022). Building on the methods and the knowledge that I gained during my PhD, our research can now be expanded to uncover novel insights into *Plasmodium* biology. The discovery of new *Plasmodium* biology might be achieved through improvement of imaging systems as well as development of novel experimental tools. In the following I will present experimental strategies that can be used to improve or expand the approaches I established during my thesis.

5.3.1 Imaging the *P. falciparum* blood stage nuclear cycle at a higher resolution

While the data generated using a spinning disk confocal microscope provides significant insights into *Plasmodium* replication biology, many open questions remain that would benefit from increased resolution during imaging. As I was able to adapt the Airyscan microscope for long-term 3D imaging (Huff, 2015) (Fig. 26), I generated a first pilot set of data using our nuclear cycle sensor system (Fig. 35). In this initial imaging session, I imaged twelve parasites in 3D at a time resolution of 5 min for a total of 21 hours. The enhanced resolution of the Airyscan microscope allowed for reliable tracking of S-phase events in the third generation of nuclei, and in some cases into the fourth generation of nuclei (Fig. 35B and C). In comparison, using the spinning disk microscope, nuclear cycle dynamics of the third generation of nuclei could only sporadically be determined and it was not possible to determine any nuclear cycle dynamics in the fourth generation of nuclei (Fig. 15). Additionally, the higher resolution of the Airyscan microscope allows the determination of the approximate number of daughter cells before egress, which was not possible during imaging with the spinning disk microscope. Correlation of the number of daughter cells with nuclear cycle dynamics will allow more robust conclusions regarding the effects of different replication dynamics.

Although ten out of twelve cells imaged using the Airyscan system survived for the duration of the imaging, these parasites exhibited altered cell cycle dynamics.

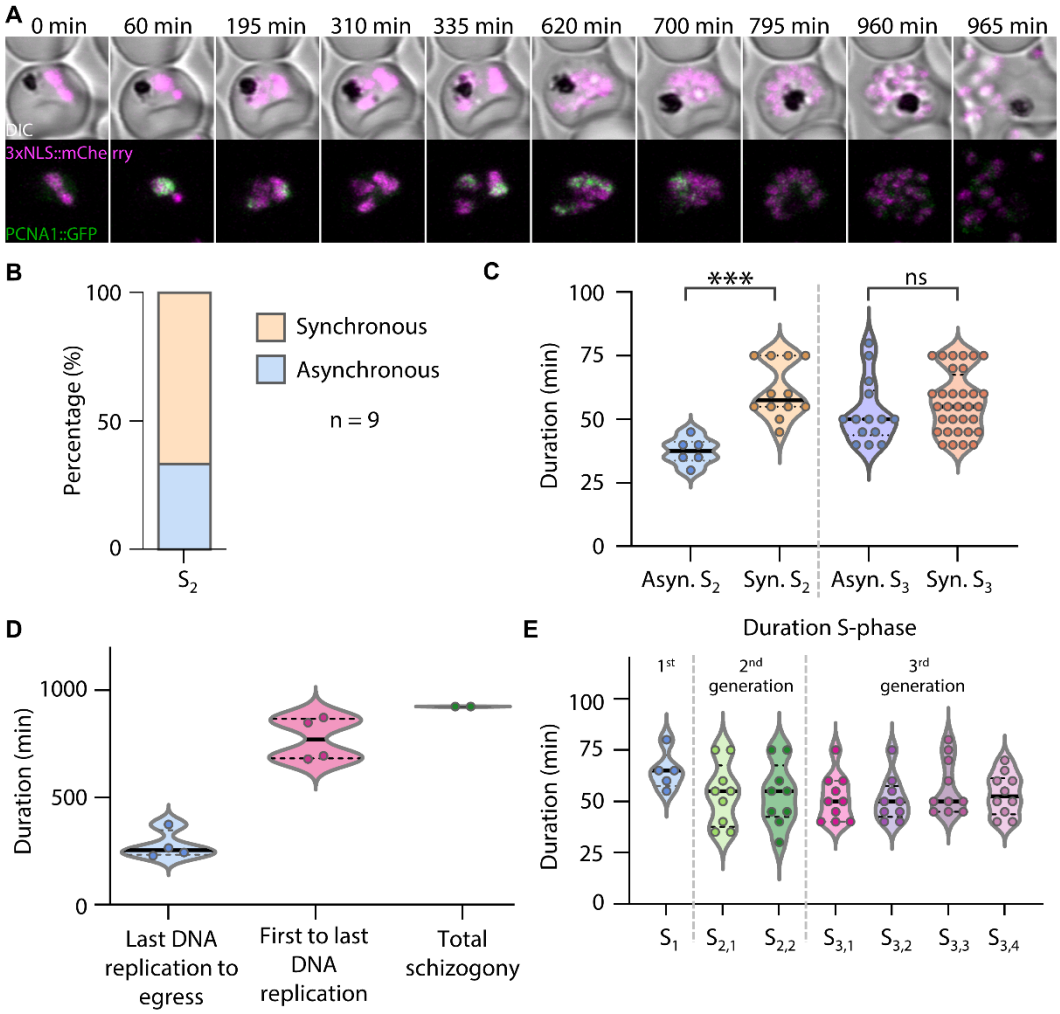

Figure 35 Imaging the nuclear cycle sensor line using the Airyscan system allows longer quantification of nuclear cycle events but introduces higher numbers of synchronous S-phases. *(A) Time-lapse images of a* P. falciparum *cell episomally expressing 3xNLS::mCherry (magenta) and PCNA1::GFP (green) acquired in the super-resolution mode with the Zeiss LSM900 equipped with an Airyscan 2 detector; scale bar, 2 µm. (B) Fraction of parasites imaged at the Airyscan system with synchronous or asynchronous $S_{2,1}$ and $S_{2,2}$. (C) Comparison of S_2-phase and S_3-phase duration of parasites undergoing synchronous or asynchronous S_2 or S_3-phases respectively in sister nuclei. Comparison of S2-phases; two-sided Mann-Whitney U-test, $n_1 = 12$, $n_2 = 6$, $P = 0.0002$; and comparison of S_3-phases; two-sided Mann-Whitney U-test, $n_1 = 32$, $n_2 = 14$, $P = 0.2950$; solid lines, median; dashed lines, quartiles. ns, not significant; ***$P < 0.001$. (D) Quantification of overall schizogony parameters of* P. falciparum*; last DNA replication was defined as last detectable nuclear accumulation of PCNA1::GFP; solid lines, median; dashed lines, quartiles. (D) S-phase durations of three generations of nuclei in parasites; solid lines, median; dashed lines, quartiles.*

Specifically, I noticed an increased proportion of synchronous DNA replication events in parasites containing two nuclei (Fig. 35B). While only 25% of S-phases were synchronous in parasites with two nuclei when using the spinning disk microscope, 67% (6/9 parasites) of S-phases were synchronous in the set acquired using the Airyscan microscope (Fig. 35B). As before, synchronous S_2-phases displayed a prolonged duration (~ 58 min for synchronous S_2- compared to ~ 38 min for asynchronous S_2-phases (Fig. 35C)) which was comparable to the dynamics quantified using the spinning disk microscope (Fig. 15). Even in the third generation of nuclei, S_3-phases which occurred completely synchronously in pairs of sibling nuclei were slightly longer on average, but did not reach statistical significance (Fig. 35C). In the data set acquired at the Airyscan microscope, on average 773 min elapsed from onset of the first S-phase until the end of the last S-

phase in the four cells which could be analysed for the entire nuclear multiplication period (Fig. 35D), representing an approximately 10% increase in duration compared to cells imaged using the spinning disk microscope (Fig. 14). As three out of four of these cells showed synchronous S_2-phases and all cells showed synchronous S_3-phases in at least one pair of sibling nuclei, this prolongation of the total replication time could be potentially caused by the increase in synchronous events. This is in line with our data that *Plasmodium* nuclear multiplication is governed by a counter-type mechanism, which only stops nuclear multiplication once a certain number of nuclei is reached and therefore extends the duration of nuclear multiplication if there are delays in the initial nuclear cycles (Klaus *et al.*, 2022). Similarly, the higher median duration of the S_2- and S_3-phases (Fig. 35E) in this data set (~55 min in S_2 and ~50 min in S_3, compared to around 40 min for both S_2- and S_3-phases of cell acquired at the spinning disk microscope (Fig. 13C, Tab. S1)) could be caused by the higher frequency of synchronous DNA replication events, as the duration of asynchronous S_2-phases correlated well to that observed on the spinning disk (Fig. 15).

The increase in the number of synchronous replication events as well as the altered replication dynamics indicate that, at least in part, the observed nuclear cycle dynamics depend on the system that is used to acquire the time-lapse images. Our previous observations indicated that synchronous S-phases could be associated with delays in the preceding nuclear division (Fig. 20B-D). The higher photon load which parasites experience during imaging with the Airyscan system, could potentially cause photodamage, leading to nuclear division delays which consequently produces more synchronous S-phases. Consistent with this hypothesis, I observed a delayed cytokinesis and egress after conclusion of the last S-phase when imaging at the Airyscan system (median of 255 min compared to 163 min at the spinning disk system, see Fig. 35D and Fig. 14A), suggesting a possible mitotic defect.

The data set generated with the Airyscan microscope represents only a single biological replicate of twelve cells. Therefore, it needs to be repeated to gain significant data and make accurate conclusions. Nevertheless, the difference between the data generated by the spinning disk microscope and the data generated by the Airyscan microscope suggests that the nuclear multiplication dynamics quantified from spinning disk data could also be influenced by our imaging system and not accurately represent an unperturbed biological state. However, comparison of our data with independently generated datasets indicates that imaging using the spinning disk did not have a significant effect on nuclear multiplication dynamics. The total time of nuclear multiplication as determined as time from the onset of the first S-phase to egress is in accordance with flow cytometry data on DNA replication (Ganter *et al.*, 2017). Similarly, the duration of the individual nuclear cycle phases is comparable to those determined by McDonald and Merrick using a different technique to estimate DNA replication dynamics (McDonald and Merrick, 2022). Additionally, many of the conclusions presented in this study – there is no conserved pattern during schizogony, asynchrony is introduced in the DS-phase, and DNA replication is a rate limited process – are based on relative comparisons, which would not be affected by altered nuclear cycle phases durations or a higher

number of synchronous S-phase events (Klaus *et al.*, 2022). Importantly, these main conclusions are all supported by the data from the Airyscan microscope (Fig. 35B, C and E) (Klaus *et al.*, 2022).

Despite being only a single replicate, the Airyscan dataset already provides novel insights into *Plasmodium* biology, showing differences in nuclear cycle dynamics under different conditions. Moreover, this dataset shows the potential of Airyscan microscopy in elucidating some of the remaining question regarding nuclear multiplication dynamics, such as: can nuclei stall for hours during replication, and, does the S-phase duration decrease or increase over time as reported by McDonald and Merrick? While the Airyscan introduced some likely phototoxicity-related phenotypes during imaging, optimisation of acquisition parameters may minimize this effect (Magidson and Khodjakov, 2013; Icha *et al.*, 2017; Tosheva *et al.*, 2020). Importantly, I was able to show that my main findings on *P. falciparum* nuclear multiplication remain unchanged in this acquisition system. Therefore, Airyscan microscopy offers an exciting avenue to continue our research into *P. falciparum* replication dynamics.

5.3.2 Characterizing different schizogony phenotypes using the nuclear cycle sensor

In the first part of my thesis I accomplished a basic characterization of blood stage DNA replication and nuclear division dynamics, establishing key features of the organisation of *P. falciparum* schizogony. With many questions remaining, this data provides a base line for future studies and our nuclear cycle sensor system can now be used at a high temporal and spatial resolution to investigate a broad range of topics. I showed that nuclear multiplication is regulated by a counter that stops nuclear multiplication once a certain number of nuclei is reached (Fig. 18) (Facchetti, Chang and Howard, 2017; Simon, Stürmer and Guizetti, 2021; Klaus *et al.*, 2022). This poses questions on how and when the counter is set and which factors influence the final number of daughter cells. Using our nuclear cycle sensor system in tandem with high resolution imaging, we will now be able to observe *P. falciparum* development in cells cultured in conditions that have been shown to influence the number of daughter cells, such as low glucose (Mancio-Silva *et al.*, 2017; Ch'Ng *et al.*, 2021). By doing so we will be able to interrogate the correlation between multiplication dynamics and number of daughter cells. Additionally, it will be possible to use pulses of high or low glucose at different points of the parasite development to elucidate when the decision is made on how many daughter cells will be formed. Similarly, by adapting and transfecting our plasmids into existing mutant cell lines we will be able to investigate phenotypes that result in an aberrant number of daughter cells. Such a phenotype for example has been observed for the deletion of the histone deacetylase Sir2a, which produces an increased number of merozoites (Mancio-Silva *et al.*, 2013), and for the deletion of the atypical kinase CRK5 which has been shown to result in a reduced number of daughter cells (Dorin-Semblat *et al.*, 2012).

In general, the nuclear cycle sensor system will be useful to reveal mechanistic details of conditions known to perturbate schizogony and parasite replication. This could include conditions of differing metabolic context, such as low glucose or low

hypoxanthine, which are key nutrients (Mancio-Silva *et al.*, 2017; Tewari *et al.*, 2019), but also conditions such as high temperatures to simulate fever, and presence of antimalarial drugs. Indeed, I recently collaborated with R. Celada of the Lanzer research group (Center for Infectious Diseases, Heidelberg University Hospital, Heidelberg, Germany) to investigate the mode of action of the new antimalarial SC83288, which has been shown to act on the schizont stage but has no molecular functional target (Pegoraro *et al.*, 2017). We subjected highly synchronized parasites expressing our nuclear cycle sensor proteins to treatment with lethal concentrations of SC83288 and investigated the effect on nuclear multiplication dynamics (Fig. 36A). We were able to observe parasites from the onset of the first S-phase and could show that parasites treated with SC83288 were not able to complete the first nuclear division and usually died before or during DNA replication (R. Celada, unpublished data). Death was accompanied by redistribution of the nuclear 3xNLS::mCherry marker to the whole parasite, suggesting breakdown of either nucleo-cytoplasmic transport or nuclear lysis. Parasite death was also associated with a sudden stop of hemozoin movement in the food vacuole.

Strikingly, parasites treated with lethal concentrations of DMSO displayed no disruption in hemozoin movement but showed a similar loss of nucleus-specific 3xNLS::mCherry signal as well as highly aberrant nuclear shapes (Fig. 36B). These finding could point towards the existence of a nucleus breakdown pathway associated with parasite death, similar to that observed during apoptosis, which is not well studied in *Plasmodium* (Pollitt *et al.*, 2010; Lindenboim *et al.*, 2020). Altogether, this highlights the suitability of our nuclear cycle sensor system in profiling of schizogony associated phenotypes. Furthermore, the investigation of different aberrant schizogony phenotypes will also be helpful to fill gaps in our knowledge of *Plasmodium* biology.

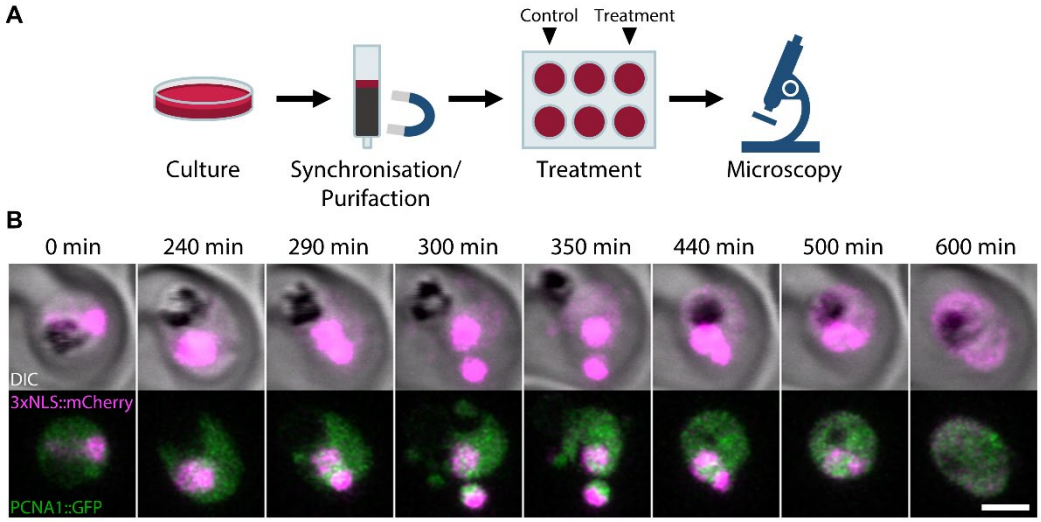

Figure 36 Parasites expressing 3xNLS::mCherry and PCNA1::GFP can be used to characterize drug effects, including cell death. *(A) Schematic of the experimental pipeline used to acquire synchronized and drug-treated cells for microscopy. (B) Time-lapse images of a* P. falciparum *cell episomally expressing 3xNLS::mCherry (magenta) and PCNA1::GFP (green). Parasites were treated with 5% DMSO just before start of imaging; scale bar, 2 µm. Preparation of cells was done in collaboration with R. Celada from the Lanzer research group.*

5.3.3 Profiling the *P. falciparum* PCNA1 interactome

My data indicates that the nuclear accumulation of PCNA1 is due to association of PCNA1 with the DNA and that proteins residing at the centriolar plaque are involved in initiating S-phase and therefore in the initiation of loading of PCNA1 to the DNA. PCNA1 is present in the nucleus before initiation of S-phase, but usually only starts associating with the DNA during firing of origins of replication when it is loaded onto the DNA by the replication factor C (RFC) (Fig. 5) (Moldovan, Pfander and Jentsch, 2007; Shiomi and Nishitani, 2017; González-Magaña and Blanco, 2020). While loading may be constitutive once replication origins are activated, it may also be achieved by regulation or modification of PCNA1 itself to permit interaction with replication fork proteins, or by activating PCNA1 interaction partners such as RFC complex to begin PCNA1 loading.

Identification of the PCNA1 interaction partners and their post-translational modifications before and after S-phase could help to identify how PCNA1 accumulation is regulation. To this end we established a pull-down of GFP tagged proteins and their interaction partners after crosslinking. This method has been successfully used in *P. falciparum* before to identify interaction partners of proteins involved in calcium homeostasis (Balestra *et al.*, 2021).

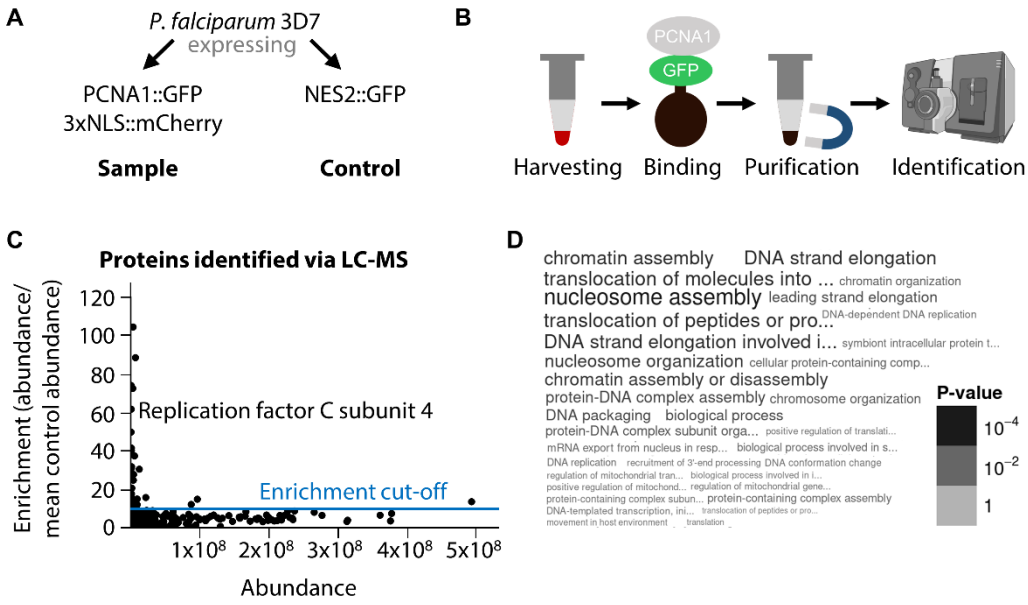

Figure 37 PCNA1 interacts with proteins involved in chromatin organization, DNA replication and parasite host interactions. *(A) Overview of cell lines used for pull-down and interaction partner identification experiments. (B) Schematic of workflow of pull-down and interaction partner identification experiments. (C) Protein fold enrichment (ratio of protein abundance within sample 1 as compared to the mean abundance of the two controls) plotted against the abundances of the respective protein. (D) Word cloud of biological processes of 10-fold enriched filtered proteins in sample 1 computed via Gene Ontology Enrichment. (C)-(D) Data generated, analysed and visualized by W. Straßburger, who I supervised during her studies to obtain a M.Sc. degree.*

In initial co-immunoprecipitation experiments, multinucleated parasites expressing either PCNA1::GFP or the non-specifically localised PCNA1-derived peptide NES2 (F114-I28) tagged with GFP were acquired in duplicate and crosslinked in solution (Fig. 25 and Fig. 37A). Subsequently, the GFP-containing proteins and their interaction partners were immunoprecipitated using magnetic anti-GFP nanobodies and analysed via by quantitative liquid chromatography mass

spectrometry (LC-MS) (Fig. 37B). Limiting analysis to proteins which were 10-fold or more enriched or only present in the PCNA1::GFP sample suggested that PCNA1::GFP interacts with the *Plasmodium* homologues of many canonical PCNA1 binding partners such as the components of the RFC complex (Fig. 37C, Tab. S3). GO-term analysis of highly enriched proteins indicates that PCNA1 interaction proteins are mainly involved in chromatin organization, DNA replication and parasite host interactions (Fig. 37F). Although this is largely in line with the known functions of PCNA proteins, further replicates will have to be generated to allow meaningful conclusions on the PCNA1 interactome and to see if *P. falciparum* PCNA1 exerts its function via interaction with other interaction partners compared to the PCNA of other organisms.

Our preliminary results of the immunoprecipitation experiments indicate that isolation and identification of PCNA1 interaction partners is possible. This strategy will now enable not only the identification of PCNA1 interaction partners pre- and post-S-phase by comparing samples from mono- versus multinucleated parasites, but also permit comparison of the interaction partners of PCNA1 mutants and peptides with those of WT PCNA1. In addition, profiling of post-translation modifications such as acetylation and phosphorylation will allow first insights into the regulation of S-phase specific PCNA1 accumulation. Identified proteins can further be analysed for crosslinking sites, which will allow the reconstruction of protein complexes and signalling cascades in ideal cases. Hence, co-immunoprecipitation is an attractive tool to compliment mutation studies to further our understanding of the *Plasmodium* cell cycle machinery.

6 Conclusion

"To look ahead, and speculate on the next century of malariology, can best be done in two parts – how will malaria change and in what ways our understanding of it develop?"

D.J. Badley, London School of Hygiene and Tropical Medicine, London, UK, Opening lecture to the Malariology Centenary Conference 1998 (M.J. Dobson, the malariology centenary, Parassitologia 1999)

Despite over a hundred years of malaria research, many aspects of the fundamental biology of *Plasmodium* parasites remains unknown, including the basic organisation of the cell cycle (Matthews, Duffy and Merrick, 2018). In this thesis I characterized the organisation of the cell cycle in the human-infecting parasite *P. falciparum* during the blood stage of infection and identified several unique features of *Plasmodium* nuclear replication and division. These discoveries were enabled by the development of a new nuclear cycle sensor system to study DNA replication and nuclear division in living parasites (Fig. 12 and Fig. 13). This system involved the characterisation and validation of the novel DNA replication marker PCNA1::GFP, which is compatible with live-cell microscopy (Fig. 13). Using this system in combination with long-term live-cell imaging at high spatial and temporal resolution enabled me to analyse the dynamics of nuclear multiplication (Fig. 14-16). Importantly, my results allowed me to compile a model for cell cycle progression during nuclear multiplication in blood stage schizogony, where individual nuclei act as 'cells-within-cells' and undergo successive, asynchronous rounds of nuclear G1-, S- and M-like-phases. These observations included the quantification of nuclear cycle dynamics, which allowed me to determine that asynchrony during nuclear multiplication is most likely established at the nuclear G1- to S-phase transition (Fig. 15F). This discovery strongly implies that the S-phase promoting kinase PfCRK4 – a master regulator of G1- to S-phase transition and one of the few well-characterized cell cycle kinases in *P. falciparum* – is a central player in nuclear cycle progression and establishment of asynchrony during the blood stage of *P. falciparum* (Ganter *et al.*, 2017). In addition, I found that nuclear multiplication is stopped once a certain number of nuclei is reached and that the speed of DNA replication is a rate-limited process influenced by one or several limited factors (Fig. 18-20). Combining both observations indicates that the asynchrony of the nuclear cycle may allow resources to be used more steadily through the schizont stage, leading to shorter DNA replication times and consequently allow parasites to reach the final number of nuclei sooner. Thus, asynchrony may have evolved to facilitate a more efficient replication in erythrocytes. In addition, the presence of one or several factors limiting the speed of DNA replication could further potentiate asynchrony by restricting initiation or progression of replication in nuclei while other nuclei in the same cell are already undergoing S-phase.

In my thesis, I also investigated the molecular mechanisms of nuclear autonomy by analysing a protein which displays a strong nuclear cycle dependent behaviour: the DNA replication marker PCNA1::GFP which only accumulates in those nuclei that undergo S-phase. By profiling different amino acid residues and nuclear transport

signals, I was able to show that S-phase dependent nuclear accumulation of PCNA1::GFP is most likely caused by increased DNA binding (Fig. 22 and Fig. 23B). Using super-resolution live-cell imaging I could further demonstrate that PCNA1::GFP accumulations progress as a wave through the nucleus, with a defined pattern mirroring the replication pattern seen in other organisms (Fig. 26) (Essers *et al.*, 2005; Meister, Taddei and Gasser, 2006). These experiments not only suggest that S-phase is initiated close to the centriolar plaque, further implicating it as a central hub for cell cycle control, but also suggest that DNA binding of PCNA1::GFP occurs during the firing of licensed origins and the formation of replication foci in S-phase. This is in line with our knowledge on PCNA loading during canonical S-phase initiation, where replication forks only become available for PCNA binding towards the end of origin of replication firing, when new active replication forks are established (Fig. 5) (Yeeles *et al.*, 2015; Boos and Ferreira, 2019). Strikingly, origin firing is the result of CDK2 activity in mammalian and yeast cells, which is most likely accomplished by PfCRK4 in *Plasmodium* cells (Ganter *et al.*, 2017).

Taken together, these results offer a new working hypothesis for the molecular mechanisms of cell cycle control in *P. falciparum*. Uneven distribution or activation of PfCRK4 or a similar cell cycle regulator after nuclear division may lead to one nucleus initiating G1- to S-phase transition earlier than the other. Then, during S-phase initiation, origins of replications are fired, which ultimately results in opening of the DNA at the replication fork. This allows PCNA1 to be loaded onto the DNA, thereby sequestering it and causing the characteristic S-phase-dependent nuclear accumulation of PCNA1::GFP. Origins are most likely fired in a defined order starting at the centromeric regions around the inner body of the centriolar plaque and ending in the nuclear periphery, where the telomeres are located. Intriguingly, in other model organisms, proteins involved in conversion of a licensed to an active origin during origin firing are the limiting factor for the speed of S-phase, as they dictate at which rate origins are activated (Tanaka *et al.*, 2011; Boos and Ferreira, 2019). Consequently, they may also act as a limiting factor in *P. falciparum* replication, potentially causing the observed differences in the duration of synchronous and asynchronous S_2-phases (Fig. 20 and Fig. 35), and imposing limitations on nuclei initiating G1- to S-phase transition when another nucleus is already in S-phase by restricting firing of origins.

In the future, this novel nuclear cycle sensor system can be adapted for other *Plasmodium* research to learn more about the cell cycle of different *Plasmodium* species and life-cycle stages (Matthews, Duffy and Merrick, 2018). As replication is fundamental to life-cycle progression, a better understanding of the molecular mechanisms governing the cell cycle in other *Plasmodium* stages could offer new strategies and targets for intervention and research (Cowman *et al.*, 2016). To this end the nuclear cycle sensor system could be adapted to the rodent malaria parasite *P. berghei*, which can complete the *Plasmodium* life cycle in an easily accessible laboratory setting. Specifically, transferring the nuclear sensor system to *P. berghei* would allow research on DNA replication and nuclear division in other replicative stages such as the male gamete, the zygote, the oocyst stage, and the liver stage (Vaughan and Kappe, 2017; Singh *et al.*, 2021). Similarly, by using the nuclear

cycle sensor system in the human-infecting *P. knowlesi*, it will be possible to interrogate differences in the cell cycle which lead, e.g., to different numbers of progeny or different developmental dynamics (McDonald and Merrick, 2022).

Further research, including the comprehensive profiling of modifications and interaction partners of PCNA1 and different PCNA1 mutants, will allow us to uncover new knowledge of the divergent cell cycle biology of *Plasmodium* parasites. In addition, I have developed a novel system to study exportin-1 dependent nuclear export via chemical inhibition in *P. falciparum* (Fig. 27), opening the field of *Plasmodium* nuclear transport research. Importantly, differences in nuclear transport between *Plasmodium* and other organisms may facilitate the development of *Plasmodium*-specific nuclear transport inhibitors. Nuclear export inhibitors have shown potential as pharmaceutical agents before, and are being developed as potent anti-cancer drugs (Wang and Liu, 2019).

All in all, my findings on *Plasmodium* cell cycle regulation and nuclear export highlight the importance of understanding the fundamental cell biology of *Plasmodium* parasites, not only to uncover novel targets for intervention but also to expand our understanding of cell biology in general.

7 References

Absalon, S. and Dvorin, J.D. (2021) “Depletion of the mini-chromosome maintenance complex binding protein allows the progression of cytokinesis despite abnormal karyokinesis during the asexual development of Plasmodium falciparum,” *Cellular Microbiology*, 23(3). Available at: https://doi.org/10.1111/cmi.13284.

Aikawa, M. and Beaudoin, R.L. (1968) “Studies on nuclear division of a malarial parasite under pyrimethamine treatment.,” *The Journal of cell biology*, 39(3), pp. 749–754. Available at: https://doi.org/10.1083/jcb.39.3.749.

Aikawa, M., Huff, C.G. and Sprinz, H. (1967) “Fine structure of the asexual stages of Plasmodium elongatum.,” *The Journal of cell biology*, 34(1), pp. 229–249. Available at: https://doi.org/10.1083/jcb.34.1.229.

Aksu, M. *et al.* (2018) “Xpo7 is a broad-spectrum exportin and a nuclear import receptor,” *Journal of Cell Biology*, 217(7), pp. 2329–2340. Available at: https://doi.org/10.1083/jcb.201712013.

Alves, E. *et al.* (2016) “Biliverdin targets enolase and eukaryotic initiation factor 2 (eIF2α) to reduce the growth of intraerythrocytic development of the malaria parasite Plasmodium falciparum,” *Scientific reports*, 6. Available at: https://doi.org/10.1038/SREP22093.

Arnot, D.E. and Gull, K. (1998) “The Plasmodium cell-cycle: Facts and questions,” in *Annals of Tropical Medicine and Parasitology*. Ann Trop Med Parasitol, pp. 361–365. Available at: https://doi.org/10.1080/00034989859357.

Arnot, D.E., Ronander, E. and Bengtsson, D.C. (2011) “The progression of the intra-erythrocytic cell cycle of Plasmodium falciparum and the role of the centriolar plaques in asynchronous mitotic division during schizogony,” *International Journal for Parasitology*, 41(1), pp. 71–80. Available at: https://doi.org/10.1016/j.ijpara.2010.07.012.

Baer, K. *et al.* (2007) “Release of hepatic Plasmodium yoelii merozoites into the pulmonary microvasculature,” *PLoS Pathogens*, 3(11), pp. 1651–1668. Available at: https://doi.org/10.1371/journal.ppat.0030171.

Balestra, A.C. *et al.* (2021) “Ca^{2+} signals critical for egress and gametogenesis in malaria parasites depend on a multipass membrane protein that interacts with PKG,” *Science Advances*, 7(13). Available at: https://doi.org/10.1126/sciadv.abe5396.

Bannister, L.H. *et al.* (2000) “A brief illustrated guide to the ultrastructure of Plasmodium falciparum asexual blood stages,” *Parasitology Today* [Preprint]. Available at: https://doi.org/10.1016/S0169-4758(00)01755-5.

Banu, K. *et al.* (2018) “Role of tyrosine residue (Y213) in nuclear retention of PCNA1 in human malaria parasite Plasmodium falciparum,” *FEMS Microbiology Letters*, 365(17). Available at: https://doi.org/10.1093/femsle/fny182.

Barnum, K.J. and O’Connell, M.J. (2014) “Cell cycle regulation by checkpoints,” *Methods in Molecular Biology*, 1170, pp. 29–40. Available at: https://doi.org/10.1007/978-1-4939-0888-2_2.

Basu, S. *et al.* (2022) “Core control principles of the eukaryotic cell cycle,” *Nature*, 607(7918), p. 381. Available at: https://doi.org/10.1038/s41586-022-04798-8.

Bean, J.M., Siggia, E.D. and Cross, F.R. (2006) “Coherence and timing of cell cycle start examined at single-cell resolution,” *Molecular cell*, 21(1), pp. 3–14. Available at: https://doi.org/10.1016/J.MOLCEL.2005.10.035.

Bertoli, C., Skotheim, J.M. and de Bruin, R.A.M. (2013) “Control of cell cycle transcription during G1 and S phases,” *Nature Reviews Molecular Cell Biology*, 14(8), pp. 518–528. Available at: https://doi.org/10.1038/nrm3629.

Billon, P. *et al.* (2017) “Acetylation of PCNA Sliding Surface by Eco1 Promotes Genome Stability through Homologous Recombination,” *Molecular Cell*, 65(1), pp. 78–90. Available at: https://doi.org/10.1016/j.molcel.2016.10.033.

Billon, P. and Côté, J. (2017) “Novel mechanism of PCNA control through acetylation of its sliding surface,” *Molecular & Cellular Oncology*, 4(2), p. e1279724. Available at: https://doi.org/10.1080/23723556.2017.1279724.

Birnbaum, J. *et al.* (2017) “A genetic system to study Plasmodium falciparum protein function,” *Nature Methods*, 14(4), pp. 450–456. Available at: https://doi.org/10.1038/nmeth.4223.

Blasco, B., Leroy, Di. and Fidock, D.A. (2017) “Antimalarial drug resistance: linking Plasmodium falciparum parasite biology to the clinic,” *Nature medicine*, 23(8), pp. 917–928. Available at: https://doi.org/10.1038/NM.4381.

Boehm, E.M., Gildenberg, M.S. and Washington, M.T. (2016) “The Many Roles of PCNA in Eukaryotic DNA Replication,” in, pp. 231–254. Available at: https://doi.org/10.1016/bs.enz.2016.03.003.

Böhme, U. *et al.* (2019) “Progression of the canonical reference malaria parasite genome from 2002–2019,” *Wellcome Open Research*, 4, p. 58. Available at: https://doi.org/10.12688/wellcomeopenres.15194.2.

Boos, D. and Ferreira, P. (2019) “Origin Firing Regulations to Control Genome Replication Timing,” *Genes*, 10(3), p. 199. Available at: https://doi.org/10.3390/genes10030199.

Bouayad, D. *et al.* (2012) “Nuclear-to-cytoplasmic relocalization of the proliferating cell nuclear antigen (PCNA) during differentiation involves a chromosome region maintenance 1 (CRM1)-dependent export and is a prerequisite for PCNA antiapoptotic activity in mature neutrophils,” *Journal of Biological Chemistry*, 287(40), pp. 33812–33825. Available at: https://doi.org/10.1074/jbc.M112.367839.

Boyle, M.J. *et al.* (2010) “Interactions with heparin-like molecules during erythrocyte invasion by Plasmodium falciparum merozoites,” *Blood*, 115(22), pp. 4559–4568. Available at: https://doi.org/10.1182/blood-2009-09-243725.

Broichhagen, J. and Kilian, N. (2021) “Chemical Biology Tools To Investigate Malaria Parasites,” *ChemBioChem*, 22(13), pp. 2219–2236. Available at: https://doi.org/10.1002/CBIC.202000882.

Bucevičius, J. *et al.* (2019) “Rhodamine-Hoechst positional isomers for highly efficient staining of heterochromatin,” *Chemical Science*, 10(7), pp. 1962–1970. Available at: https://doi.org/10.1039/c8sc05082a.

Byung, J.K. and Lee, H. (2006) “Importin-β mediates Cdc7 nuclear import by binding to the Kinase Insert II domain, which can be antagonized by importin-α,” *Journal of Biological Chemistry*, 281(17), pp. 12041–12049. Available at: https://doi.org/10.1074/jbc.M512630200.

Carter, L.M. *et al.* (2013) “Stress and sex in malaria parasites,” *Evolution, Medicine, and Public Health*, 2013(1), pp. 135–147. Available at: https://doi.org/10.1093/emph/eot011.

Carter, R. and Mendis, K.N. (2002) “Evolutionary and historical aspects of the burden of malaria,” *Clinical Microbiology Reviews*. American Society for Microbiology (ASM), pp. 564–594. Available at: https://doi.org/10.1128/CMR.15.4.564-594.2002.

Carvalho, T.G., Doerig, C. and Reininger, L. (2013) “Nima- and Aurora-related kinases of malaria parasites,” *Biochimica et Biophysica Acta (BBA) - Proteins and Proteomics*, 1834(7), pp. 1336–1345. Available at: https://doi.org/10.1016/j.bbapap.2013.02.022.

Cazzalini, O. *et al.* (2014) “CBP and p300 acetylate PCNA to link its degradation with nucleotide excision repair synthesis,” *Nucleic Acids Research*, 42(13), pp. 8433–8448. Available at: https://doi.org/10.1093/nar/gku533.

Chal, J. and Pourquié, O. (2017) “Making muscle: Skeletal myogenesis in vivo and in vitro,” *Development (Cambridge)*. Company of Biologists Ltd, pp. 2104–2122. Available at: https://doi.org/10.1242/dev.151035.

Chen, B.C. *et al.* (2014) “Lattice light-sheet microscopy: imaging molecules to embryos at high spatiotemporal resolution,” *Science (New York, N.Y.)*, 346(6208). Available at: https://doi.org/10.1126/SCIENCE.1257998.

Chiara, A. de *et al.* (2013) “Characterization of cytosolic proliferating cell nuclear antigen (PCNA) in neutrophils: antiapoptotic role of the monomer,” *Journal of Leukocyte Biology*, 94(4), pp. 723–731. Available at: https://doi.org/10.1189/JLB.1212637.

Chilkova, O. *et al.* (2007) “The eukaryotic leading and lagging strand DNA polymerases are loaded onto primer-ends via separate mechanisms but have comparable processivity in the presence of PCNA,” *Nucleic Acids Research*, 35(19), pp. 6588–6597. Available at: https://doi.org/10.1093/nar/gkm741.

Ch’Ng, J.H. *et al.* (2021) “Enhanced virulence of Plasmodium falciparum in blood of diabetic patients,” *PloS one*, 16(6). Available at: https://doi.org/10.1371/JOURNAL.PONE.0249666.

Cohen, J.M., Okumu, F. and Moonen, B. (2022) “The fight against malaria: Diminishing gains and growing challenges,” *Science Translational Medicine*, 14(651). Available at: https://doi.org/10.1126/scitranslmed.abn3256.

Cooper, K. (2006) “Rb, whi it’s not just for metazoans anymore,” *Oncogene 2006 25:38*, 25(38), pp. 5228–5232. Available at: https://doi.org/10.1038/sj.onc.1209630.

Coronado, L.M., Nadovich, C.T. and Spadafora, C. (2014) “Malarial hemozoin: From target to tool,” *Biochimica et Biophysica Acta - General Subjects*. Elsevier B.V., pp. 2032–2041. Available at: https://doi.org/10.1016/j.bbagen.2014.02.009.

Counihan, N.A., Modak, J.K. and de Koning-Ward, T.F. (2021) “How Malaria Parasites Acquire Nutrients From Their Host,” *Frontiers in Cell and Developmental Biology*, 9, p. 582. Available at: https://doi.org/10.3389/FCELL.2021.649184/BIBTEX.

la Cour, T. *et al.* (2004) “Analysis and prediction of leucine-rich nuclear export signals,” *Protein Engineering, Design and Selection*, 17(6), pp. 527–536. Available at: https://doi.org/10.1093/protein/gzh062.

Cowman, A.F. *et al.* (2016) “Malaria: Biology and Disease,” *Cell*, 167(3), pp. 610–624. Available at: https://doi.org/10.1016/j.cell.2016.07.055.

Cox, F.E. (2010) “History of the discovery of the malaria parasites and their vectors,” *Parasites and Vectors*. BioMed Central, p. 5. Available at: https://doi.org/10.1186/1756-3305-3-5.

Cox, F.E.G. (2002) “History of human parasitology,” *Clinical Microbiology Reviews*. American Society for Microbiology (ASM), pp. 595–612. Available at: https://doi.org/10.1128/CMR.15.4.595-612.2002.

Crabb, B.S. *et al.* (1997) “Stable transgene expression in Plasmodium falciparum,” *Molecular and Biochemical Parasitology*, 90(1), pp. 131–144. Available at: https://doi.org/10.1016/S0166-6851(97)00143-6.

Crosby, M.E. (2007) “Cell Cycle: Principles of Control,” *The Yale Journal of Biology and Medicine*, 80(3), p. 141.

Deshmukh, A.S. *et al.* (2012) “The role of N-terminus of Plasmodium falciparum ORC1 in telomeric localization and var gene silencing,” *Nucleic Acids Research*, 40(12), pp. 5313–5331. Available at: https://doi.org/10.1093/nar/gks202.

Devbhandari, S. *et al.* (2017) “Chromatin Constrains the Initiation and Elongation of DNA Replication,” *Molecular cell*, 65(1), pp. 131–141. Available at: https://doi.org/10.1016/J.MOLCEL.2016.10.035.

van Dijk, M.R. *et al.* (1997) “Replication, expression and segregation of plasmid-borne DNA in genetically transformed malaria parasites,” *Molecular and Biochemical Parasitology*, 86(2), pp. 155–162. Available at: https://doi.org/10.1016/S0166-6851(97)02843-0.

Dimitrova, D.S. and Gilbert, D.M. (2000) “Temporally coordinated assembly and disassembly of replication factories in the absence of DNA synthesis,” *Nature cell biology*, 2(10), pp. 686–694. Available at: https://doi.org/10.1038/35036309.

Dobson, M.J. (1999) “The malariology centenary.,” *Parassitologia*, 41(1–3), pp. 21–32. Available at: https://europepmc.org/article/med/10697830 (Accessed: August 17, 2022).

Doench, J.G. *et al.* (2014) “Rational design of highly active sgRNAs for CRISPR-Cas9-mediated gene inactivation,” *Nature Biotechnology*, 32(12), pp. 1262–1267. Available at: https://doi.org/10.1038/nbt.3026.

Dondorp, A.M. *et al.* (2005) “Estimation of the Total Parasite Biomass in Acute Falciparum Malaria from Plasma PfHRP2,” *PLoS Medicine*. Edited by S. Krishna, 2(8), p. e204. Available at: https://doi.org/10.1371/journal.pmed.0020204.

Dorin-Semblat, D. *et al.* (2011) “Plasmodium falciparum NIMA-related kinase Pfnek-1: sex specificity and assessment of essentiality for the erythrocytic asexual cycle,” *Microbiology*, 157(10), pp. 2785–2794. Available at: https://doi.org/10.1099/mic.0.049023-0.

Dorin-Semblat, D. *et al.* (2012) “Experimental Tools for the Study of Protein Phosphorylation in Plasmodium,” in. Humana Press, Totowa, NJ, pp. 241–257. Available at: https://doi.org/10.1007/978-1-62703-026-7_16.

Essers, J. *et al.* (2005) “Nuclear Dynamics of PCNA in DNA Replication and Repair,” *Molecular and Cellular Biology*, 25(21), pp. 9350–9359. Available at: https://doi.org/10.1128/mcb.25.21.9350-9359.2005.

Etchin, J. *et al.* (2013) “Antileukemic activity of nuclear export inhibitors that spare normal hematopoietic cells,” *Leukemia*, 27(1), pp. 66–74. Available at: https://doi.org/10.1038/leu.2012.219.

Facchetti, G., Chang, F. and Howard, M. (2017) “Controlling cell size through sizer mechanisms,” *Current Opinion in Systems Biology*. Elsevier Ltd, pp. 86–92. Available at: https://doi.org/10.1016/j.coisb.2017.08.010.

Farrell, J.A. and O’Farrell, P.H. (2014) “From egg to gastrula: How the cell cycle is remodeled during the drosophila mid-blastula transition,” *Annual Review of Genetics*, 48, pp. 269–294. Available at: https://doi.org/10.1146/annurev-genet-111212-133531.

Fox, T.O. and Pardee, A.B. (1970) “Animal cells: noncorrelation of length of G1 phase with size after mitosis,” *Science (New York, N.Y.)*, 167(3914), pp. 80–82. Available at: https://doi.org/10.1126/SCIENCE.167.3914.80.

Francia, M.E. and Striepen, B. (2014) “Cell division in apicomplexan parasites.,” *Nat Rev Microbiol*, 12(2), pp. 125–136. Available at: https://doi.org/10.1038/nrmicro3184.

Frankel, M.B. and Knoll, L.J. (2009) “The Ins and Outs of Nuclear Trafficking: Unusual Aspects in Apicomplexan Parasites,” *DNA and Cell Biology*, 28(6), pp. 277–284. Available at: https://doi.org/10.1089/dna.2009.0853.

Freitas-Junior, L.H. *et al.* (2000) “Frequent ectopic recombination of virulence factor genes in telomeric chromosome clusters of P. falciparum,” *Nature*, 407(6807), pp. 1018–1022. Available at: https://doi.org/10.1038/35039531.

Freudenthal, B.D. *et al.* (2009) “A charged residue at the subunit interface of PCNA promotes trimer formation by destabilizing alternate subunit interactions,” *Acta Crystallographica Section D Biological Crystallography*, 65(6), pp. 560–566. Available at: https://doi.org/10.1107/S0907444909011329.

Frischknecht, F. and Matuschewski, K. (2017) "*Plasmodium* Sporozoite Biology," *Cold Spring Harbor Perspectives in Medicine*, 7(5), p. a025478. Available at: https://doi.org/10.1101/cshperspect.a025478.

Ganter, M. *et al.* (2017) "Plasmodium falciparum CRK4 directs continuous rounds of DNA replication during schizogony," *Nature Microbiology*, 2(5), p. 17017. Available at: https://doi.org/10.1038/nmicrobiol.2017.17.

Gardner, M.J. *et al.* (2002) "Genome sequence of the human malaria parasite Plasmodium falciparum," *Nature 2002 419:6906*, 419(6906), pp. 498–511. Available at: https://doi.org/10.1038/nature01097.

Gascoigne, K.E. and Taylor, S.S. (2008) "Cancer Cells Display Profound Intra- and Interline Variation following Prolonged Exposure to Antimitotic Drugs," *Cancer Cell*, 14(2), pp. 111–122. Available at: https://doi.org/10.1016/j.ccr.2008.07.002.

Geoghegan, N.D. *et al.* (2021) "4D analysis of malaria parasite invasion offers insights into erythrocyte membrane remodeling and parasitophorous vacuole formation," *Nature Communications*, 12(1). Available at: https://doi.org/10.1038/s41467-021-23626-7.

Gerald, N., Mahajan, B. and Kumar, S. (2011) "Mitosis in the human malaria parasite plasmodium falciparum," *Eukaryotic Cell* [Preprint]. Available at: https://doi.org/10.1128/EC.00314-10.

Gerbich, T.M. *et al.* (2020) "Phosphoregulation provides specificity to biomolecular condensates in the cell cycle and cell polarity," *Journal of Cell Biology*, 219(7). Available at: https://doi.org/10.1083/jcb.201910021.

Ghorbal, M. *et al.* (2014) "Genome editing in the human malaria parasite Plasmodium falciparum using the CRISPR-Cas9 system," *Nature Biotechnology*, 32(8), pp. 819–821. Available at: https://doi.org/10.1038/nbt.2925.

Gladfelter, A.S. (2006) "Nuclear anarchy: asynchronous mitosis in multinucleated fungal hyphae," *Current Opinion in Microbiology*, 9(6), pp. 547–552. Available at: https://doi.org/10.1016/j.mib.2006.09.002.

Gladfelter, A.S., Hungerbuehler, A.K. and Philippsen, P. (2006) "Asynchronous nuclear division cycles in multinucleated cells," *Journal of Cell Biology*, 172(3), pp. 347–362. Available at: https://doi.org/10.1083/jcb.200507003.

Gollin, D. and Zimmermann, C. (2021) "Malaria: Disease Impacts and Long-Run Income Differences," *SSRN Electronic Journal* [Preprint]. Available at: https://doi.org/10.2139/ssrn.1012564.

Gómez-Escoda, B. and Wu, P.-Y. (2017) "Roles of CDK and DDK in Genome Duplication and Maintenance: Meiotic Singularities," *Genes*, 8(3), p. 105. Available at: https://doi.org/10.3390/genes8030105.

González-Magaña, A. and Blanco, F.J. (2020) "Human PCNA Structure, Function and Interactions," *Biomolecules*, 10(4), p. 570. Available at: https://doi.org/10.3390/biom10040570.

Grassi, B. (1900) "Studio di uno zoologo sulla malaria..."

Graumans, W. *et al.* (2020) "When Is a Plasmodium-Infected Mosquito an Infectious Mosquito?," *Trends in Parasitology*. Elsevier Ltd, pp. 705–716. Available at: https://doi.org/10.1016/j.pt.2020.05.011.

Grüring, C. *et al.* (2011) "Development and host cell modifications of Plasmodium falciparum blood stages in four dimensions," *Nature Communications*, 2(1). Available at: https://doi.org/10.1038/ncomms1169.

Grüring, C. and Spielmann, T. (2012) "Imaging of live malaria blood stage parasites," *Methods in Enzymology*, 506, pp. 81–92. Available at: https://doi.org/10.1016/B978-0-12-391856-7.00029-9.

Gubbels, M.-J. *et al.* (2020) “Fussing About Fission: Defining Variety Among Mainstream and Exotic Apicomplexan Cell Division Modes,” *Frontiers in Cellular and Infection Microbiology*, 10. Available at: https://doi.org/10.3389/fcimb.2020.00269.

Gulbis, J.M. *et al.* (1996) “Structure of the C-terminal region of p21(WAF1/CIP1) complexed with human PCNA,” *Cell*, 87(2), pp. 297–306. Available at: https://doi.org/10.1016/S0092-8674(00)81347-1.

Gupta, A. *et al.* (2006) “Analogous expression pattern of *Plasmodium falciparum* replication initiation proteins PfMCM4 and PfORC1 during the asexual and sexual stages of intraerythrocytic developmental cycle,” *FEMS Microbiology Letters*, 261(1), pp. 12–18. Available at: https://doi.org/10.1111/j.1574-6968.2006.00324.x.

Gupta, A., Mehra, P. and Dhar, S.K. (2008) “*Plasmodium falciparum* origin recognition complex subunit 5: functional characterization and role in DNA replication foci formation,” *Molecular Microbiology*, 69(3), pp. 646–665. Available at: https://doi.org/10.1111/j.1365-2958.2008.06316.x.

Gustafsson, M.G.L. *et al.* (2008) “Three-dimensional resolution doubling in wide-field fluorescence microscopy by structured illumination,” *Biophysical journal*, 94(12), pp. 4957–4970. Available at: https://doi.org/10.1529/BIOPHYSJ.107.120345.

Hamamoto, T., Uozumi, T. and Beppu, T. (1985) “Leptomycins A and B, new antifungal antibiotics III. Mode of action of leptomycin on schizosaccharomyces pombe,” *the journal of antibiotics*, 38(11), pp. 1573–1580. Available at: https://doi.org/10.7164/antibiotics.38.1573.

Hartwell, L.H. and Unger, M.W. (1977) “Unequal division in Saccharomyces cerevisiae and its implications for the control of cell division,” *The Journal of cell biology*, 75(2 Pt 1), pp. 422–435. Available at: https://doi.org/10.1083/JCB.75.2.422.

Hayashi, M.T. *et al.* (2009) “The heterochromatin protein Swi6/HP1 activates replication origins at the pericentromeric region and silent mating-type locus.,” *Nature Cell Biology*, 11(3), pp. 357–362. Available at: https://doi.org/10.1038/NCB1845.

Hekmat-Nejad, M. and Rathod, P.K. (1997) “Plasmodium falciparum: Kinetic interactions of WR99210 with pyrimethamine-sensitive and pyrimethamine-resistant dihydrofolate reductase,” *Experimental Parasitology*, 87(3), pp. 222–228. Available at: https://doi.org/10.1006/expr.1997.4228.

Hempelmann, E. and Krafts, K. (2013) “Bad air, amulets and mosquitoes: 2,000 years of changing perspectives on malaria,” *Malaria Journal*, 12(1), p. 232. Available at: https://doi.org/10.1186/1475-2875-12-232.

Hentzschel, F. and Frischknecht, F. (2022) “Still enigmatic: Plasmodium oocysts 125 years after their discovery,” *Trends in Parasitology*, 38(8), pp. 610–613. Available at: https://doi.org/10.1016/j.pt.2022.05.013.

Hernandez-Rivas, R. *et al.* (2010) “Telomeric Heterochromatin in Plasmodium falciparum,” *Journal of Biomedicine and Biotechnology*, 2010. Available at: https://doi.org/10.1155/2010/290501.

Hoeijmakers, W.A.M. *et al.* (2012) “*Plasmodium falciparum* centromeres display a unique epigenetic makeup and cluster prior to and during schizogony,” *Cellular Microbiology*, 14(9), pp. 1391–1401. Available at: https://doi.org/10.1111/j.1462-5822.2012.01803.x.

Hoelzel, C.A. and Zhang, X. (2020) “Visualizing and Manipulating Biological Processes by Using HaloTag and SNAP-Tag Technologies,” *ChemBioChem*, 21(14), pp. 1935–1946. Available at: https://doi.org/10.1002/CBIC.202000037.

van den Hoff, M.J. b., Moorman, A.F.M. and Lamers, W.H. (1992) “Electroporation in ‘intracellular’ buffer increases cell survival,” *Nucleic Acids Research*. Nucleic Acids Res, p. 2902. Available at: https://doi.org/10.1093/nar/20.11.2902.

Holland, A.J. and Cleveland, D.W. (2008) “Beyond genetics: surprising determinants of cell fate in antitumor drugs,” *Cancer cell*, 14(2), pp. 103–105. Available at: https://doi.org/10.1016/J.CCR.2008.07.010.

Huff, J. (2015) “The Airyscan detector from ZEISS: confocal imaging with improved signal-to-noise ratio and super-resolution,” *Nature Methods*, 12(12), pp. i–ii. Available at: https://doi.org/10.1038/nmeth.f.388.

Hutten, S. and Kehlenbach, R.H. (2007) “CRM1-mediated nuclear export: to the pore and beyond,” *Trends in Cell Biology*. Trends Cell Biol, pp. 193–201. Available at: https://doi.org/10.1016/j.tcb.2007.02.003.

Icha, J. *et al.* (2017) “Phototoxicity in live fluorescence microscopy, and how to avoid it,” *BioEssays*. John Wiley and Sons Inc. Available at: https://doi.org/10.1002/bies.201700003.

Inselburg, J. and Banyal, H.S. (1984) “Synthesis of DNA during the asexual cycle of Plasmodium falciparum in culture,” *Molecular and Biochemical Parasitology*, 10(1), pp. 79–87. Available at: https://doi.org/10.1016/0166-6851(84)90020-3.

Janouskovec, J. *et al.* (2019) “Apicomplexan-like parasites are polyphyletic and widely but selectively dependent on cryptic plastid organelles,” *eLife*, 8. Available at: https://doi.org/10.7554/eLife.49662.

Janse, C.J. *et al.* (1986) “DNA synthesis in Plasmodium berghei during asexual and sexual development,” *Molecular and Biochemical Parasitology*, 20(2), pp. 173–182. Available at: https://doi.org/10.1016/0166-6851(86)90029-0.

Johnson, R.T. and Rao, P.N. (1971) “Nucleo-cytoplasmic interactions in the achievement of nuclear synchrony in DNA systhesis and mitosis in multinucleate cells.,” *Biological Reviews*, 46(1), pp. 97–155. Available at: https://doi.org/10.1111/j.1469-185X.1971.tb01180.x.

Jónsson, Z.O. *et al.* (1995) “Tyrosine 114 is essential for the trimeric structure and the functional activities of human proliferating cell nuclear antigen.,” *The EMBO Journal*, 14(22), pp. 5745–5751. Available at: https://doi.org/10.1002/j.1460-2075.1995.tb00261.x.

Kilbey, B.J. *et al.* (1993) “Molecular characterisation and stage-specific expression of proliferating cell nuclear antigen (PCNA) from the malarial parasite, Plasmodium falciparum,” *Nucleic Acids Research*, 21(2), pp. 239–243. Available at: https://doi.org/10.1093/nar/21.2.239.

Kim, B.J. and Lee, H. (2008) “Lys-110 is essential for targeting PCNA to replication and repair foci, and the K110A mutant activates apoptosis,” *Biology of the Cell*, 100(12), pp. 675–686. Available at: https://doi.org/10.1042/bc20070158.

Kirkman, L.A., Lawrence, E.A. and Deitsch, K.W. (2014) “Malaria parasites utilize both homologous recombination and alternative end joining pathways to maintain genome integrity,” *Nucleic Acids Research*, 42(1), pp. 370–379. Available at: https://doi.org/10.1093/nar/gkt881.

Klaus, S. *et al.* (2022) “Asynchronous nuclear cycles in multinucleated Plasmodium falciparum facilitate rapid proliferation,” *Science Advances*, 8(13). Available at: https://doi.org/10.1126/sciadv.abj5362.

Kondratick, C.M. *et al.* (2016) “Identification of New Mutations at the PCNA Subunit Interface that Block Translesion Synthesis,” *PLOS ONE*, 11(6), p. e0157023. Available at: https://doi.org/10.1371/journal.pone.0157023.

de Koning-Ward, T.F. *et al.* (2000) “The selectable marker human dihydrofolate reductase enables sequential genetic manipulation of the Plasmodium berghei genome,” *Molecular and Biochemical Parasitology*, 106(2), pp. 199–212. Available at: https://doi.org/10.1016/S0166-6851(99)00189-9.

Kono, M. *et al.* (2012) “Evolution and Architecture of the Inner Membrane Complex in Asexual and Sexual Stages of the Malaria Parasite,” *Molecular Biology and Evolution*, 29(9), pp. 2113–2132. Available at: https://doi.org/10.1093/molbev/mss081.

Kosugi, S. *et al.* (2009) “Systematic identification of cell cycle-dependent yeast nucleocytoplasmic shuttling proteins by prediction of composite motifs,” *Proceedings of the National Academy of Sciences of the United States of America*, 106(25), pp. 10171–10176. Available at: https://doi.org/10.1073/pnas.0900604106.

Kudo, N. *et al.* (1998) “Leptomycin B inhibition of signal-mediated nuclear export by direct binding to CRM1,” *Experimental Cell Research*, 242(2), pp. 540–547. Available at: https://doi.org/10.1006/excr.1998.4136.

Kwiatkowski, D.P. (2005) “How Malaria Has Affected the Human Genome and What Human Genetics Can Teach Us about Malaria,” *The American Journal of Human Genetics*, 77(2), pp. 171–192. Available at: https://doi.org/10.1086/432519.

Lambros, C. and Vanderberg, J.P. (1979) “Synchronization of Plasmodium falciparum erythrocytic stages in culture,” *Journal of Parasitology*, 65(3), pp. 418–420. Available at: https://doi.org/10.2307/3280287.

Lasonder, E. *et al.* (2012) “The Plasmodium falciparum schizont phosphoproteome reveals extensive phosphatidylinositol and cAMP-protein kinase A signaling,” *Journal of proteome research*, 11(11), pp. 5323–5337. Available at: https://doi.org/10.1021/PR300557M.

Latt, S.A. *et al.* (2017) “Recent developments in the detection of deoxyribonucleic acid synthesis by 33258 Hoechst fluorescence.:,” *http://dx.doi.org/10.1177/23.7.1095650*, 23(7), pp. 493–505. Available at: https://doi.org/10.1177/23.7.1095650.

Laveran, A. (1881) “Un nouveau parasite trouvé dans le sang des malades atteints de fièvre palustre: origine parasitaire des accidents de l’impaludisme.”

Lee, C. *et al.* (2013) “Protein Aggregation Behavior Regulates Cyclin Transcript Localization and Cell-Cycle Control,” *Developmental Cell*, 25(6), pp. 572–584. Available at: https://doi.org/10.1016/j.devcel.2013.05.007.

Lee, M.C.S. *et al.* (2019) “Cutting back malaria: CRISPR/Cas9 genome editing of Plasmodium,” *Briefings in Functional Genomics*, 18(5), pp. 281–289. Available at: https://doi.org/10.1093/bfgp/elz012.

Lee, M.C.S. and Fidock, D.A. (2014) “CRISPR-mediated genome editing of Plasmodium falciparum malaria parasites,” *Genome Medicine*, 6(8), p. 63. Available at: https://doi.org/10.1186/s13073-014-0063-9.

Lee, S.-Y., Jang, C. and Lee, K.-A. (2014) “Polo-Like Kinases (Plks), a Key Regulator of Cell Cycle and New Potential Target for Cancer Therapy,” *Development & Reproduciton*, 18(1), pp. 65–71. Available at: https://doi.org/10.12717/dr.2014.18.1.065.

Leete, T.H. and Rubin, H. (1996) “Malaria and the cell cycle,” *Parasitology Today*, 12(11), pp. 442–444. Available at: https://doi.org/10.1016/0169-4758(96)10068-5.

Leonhardt, H. *et al.* (2000) “Dynamics of DNA Replication Factories in Living Cells,” *Journal of Cell Biology*, 149(2), pp. 271–280. Available at: https://doi.org/10.1083/jcb.149.2.271.

Lew, V.L., Tiffert, T. and Ginsburg, H. (2003) “Excess haemoglobin digestion and the osmotic stability ofPlasmodium falciparum–infected red blood cells,” *Blood*, 101(10), pp. 4189–4194. Available at: https://doi.org/10.1182/BLOOD-2002-08-2654.

Li, H. *et al.* (2021) “How the spleen reshapes and retains young and old red blood cells: A computational investigation,” *PLOS Computational Biology*, 17(11), p. e1009516. Available at: https://doi.org/10.1371/journal.pcbi.1009516.

Lim, M.Y.X. *et al.* (2016) “UDP-galactose and acetyl-CoA transporters as Plasmodium multidrug resistance genes,” *Nature Microbiology*, 1, p. 16166. Available at: https://doi.org/10.1038/nmicrobiol.2016.166.

Lindenboim, L. *et al.* (2020) “The nuclear envelope: target and mediator of the apoptotic process,” *Cell Death Discovery 2020 6:1*, 6(1), pp. 1–11. Available at: https://doi.org/10.1038/s41420-020-0256-5.

Lin, J. and Hu, J. (2013) “SeqNLS: Nuclear Localization Signal Prediction Based on Frequent Pattern Mining and Linear Motif Scoring,” *PLoS ONE*. Edited by A.R. Dalby, 8(10), p. e76864. Available at: https://doi.org/10.1371/journal.pone.0076864.

Liu, W. *et al.* (2010) “Origin of the human malaria parasite Plasmodium falciparum in gorillas,” *Nature*, 467(7314), pp. 420–425. Available at: https://doi.org/10.1038/nature09442.

Lord, P.G. and Wheals, A.E. (1983) “Rate of cell cycle initiation of yeast cells when cell size is not a rate-determining factor,” *Journal of cell science*, 59, pp. 183–201. Available at: https://doi.org/10.1242/JCS.59.1.183.

Loy, D.E. *et al.* (2017) “Out of Africa: origins and evolution of the human malaria parasites Plasmodium falciparum and Plasmodium vivax,” *International Journal for Parasitology*, 47(2–3), pp. 87–97. Available at: https://doi.org/10.1016/j.ijpara.2016.05.008.

Lu, J. *et al.* (2021) “Types of nuclear localization signals and mechanisms of protein import into the nucleus,” *Cell Communication and Signaling*, 19(1), pp. 1–10. Available at: https://doi.org/10.1186/S12964-021-00741-Y/FIGURES/1.

Lukinavičius, G. *et al.* (2014) “Fluorogenic probes for live-cell imaging of the cytoskeleton,” *Nature methods*, 11(7), pp. 731–733. Available at: https://doi.org/10.1038/NMETH.2972.

Lukinavičius, G. *et al.* (2015) “SiR–Hoechst is a far-red DNA stain for live-cell nanoscopy,” *Nature Communications 2015 6:1*, 6(1), pp. 1–7. Available at: https://doi.org/10.1038/ncomms9497.

Machado, M., Steinke, S. and Ganter, M. (2021) “Plasmodium Reproduction, Cell Size, and Transcription: How to Cope With Increasing DNA Content?,” *Frontiers in Cellular and Infection Microbiology*, 11. Available at: https://doi.org/10.3389/fcimb.2021.660679.

MacPherson, C.R. and Scherf, A. (2015) “Flexible guide-RNA design for CRISPR applications using Protospacer Workbench,” *Nature Biotechnology*. Nature Publishing Group, pp. 805–806. Available at: https://doi.org/10.1038/nbt.3291.

Maga, G. and Hübscher, U. (2003) “Proliferating cell nuclear antigen (PCNA): a dancer with many partners,” *Journal of Cell Science*, 116(15), pp. 3051–3060. Available at: https://doi.org/10.1242/jcs.00653.

Magidson, V. and Khodjakov, A. (2013) “Circumventing photodamage in live-cell microscopy,” *Methods in Cell Biology*, 114, pp. 545–560. Available at: https://doi.org/10.1016/B978-0-12-407761-4.00023-3.

Malumbres, M. (2014) “Cyclin-dependent kinases,” *Genome Biology*, 15(6), p. 122. Available at: https://doi.org/10.1186/gb4184.

Mamoun, C. ben *et al.* (1999) “A set of independent selectable markers for transfection of the human malaria parasite Plasmodium falciparum,” *Proceedings of the National Academy of Sciences of the United States of America*, 96(15), pp. 8716–8720. Available at: https://doi.org/10.1073/pnas.96.15.8716.

Mancio-Silva, L. *et al.* (2013) “Sir2a regulates rDNA transcription and multiplication rate in the human malaria parasite Plasmodium falciparum,” *Nature Communications 2013 4:1*, 4(1), pp. 1–6. Available at: https://doi.org/10.1038/ncomms2539.

Mancio-Silva, L. *et al.* (2017) “Nutrient sensing modulates malaria parasite virulence,” *Nature*, 547(7662), pp. 213–216. Available at: https://doi.org/10.1038/NATURE23009.

de March, M. *et al.* (2017) “Structural basis of human PCNA sliding on DNA,” *Nature Communications*, 8(1), p. 13935. Available at: https://doi.org/10.1038/ncomms13935.

Mastronarde, D.N. (2005) “Automated electron microscope tomography using robust prediction of specimen movements,” *Journal of structural biology*, 152(1), pp. 36–51. Available at: https://doi.org/10.1016/J.JSB.2005.07.007.

Matthews, H., Duffy, C.W. and Merrick, C.J. (2018) “Checks and balances? DNA replication and the cell cycle in Plasmodium,” *Parasites & Vectors*, 11(1), p. 216. Available at: https://doi.org/10.1186/s13071-018-2800-1.

Matuschewski, K. (2006) “Getting infectious: formation and maturation of Plasmodium sporozoites in the Anopheles vector,” *Cellular Microbiology*, 8(10), pp. 1547–1556. Available at: https://doi.org/10.1111/j.1462-5822.2006.00778.x.

McDonald, J. and Merrick, C.J. (2022) “DNA replication dynamics during erythrocytic schizogony in the malaria parasites Plasmodium falciparum and Plasmodium knowlesi,” *PLOS Pathogens*, 18(6), p. e1010595. Available at: https://doi.org/10.1371/journal.ppat.1010595.

McNally, R. *et al.* (2010) “Analysis of the role of PCNA-DNA contacts during clamp loading,” *BMC structural biology*, 10. Available at: https://doi.org/10.1186/1472-6807-10-3.

Mehnert, A.K., Simon, C.S. and Guizetti, J. (2019) “Immunofluorescence staining protocol for STED nanoscopy of Plasmodium-infected red blood cells,” *Molecular and Biochemical Parasitology*, 229, pp. 47–52. Available at: https://doi.org/10.1016/j.molbiopara.2019.02.007.

Mehra, P. *et al.* (2005) “Expression and characterization of human malaria parasite Plasmodium falciparum origin recognition complex subunit 1,” *Biochemical and Biophysical Research Communications*, 337(3), pp. 955–966. Available at: https://doi.org/10.1016/j.bbrc.2005.09.131.

Meister, P. *et al.* (2007) “Replication foci dynamics: replication patterns are modulated by S-phase checkpoint kinases in fission yeast,” *The EMBO Journal*, 26(5), pp. 1315–1326. Available at: https://doi.org/10.1038/sj.emboj.7601538.

Meister, P., Taddei, A. and Gasser, S.M. (2006) “In and out of the Replication Factory,” *Cell*, 125(7), pp. 1233–1235. Available at: https://doi.org/10.1016/j.cell.2006.06.014.

Merckx, A. *et al.* (2003) “Identification and initial characterization of three novel cyclin-related proteins of the human malaria parasite Plasmodium falciparum,” *Journal of Biological Chemistry*, 278(41), pp. 39839–39850. Available at: https://doi.org/10.1074/jbc.M301625200.

Merrick, C.J. (2015) “Transfection with thymidine kinase permits bromodeoxyuridine labelling of DNA replication in the human malaria parasite Plasmodium falciparum,” *Malaria Journal*, 14(1), p. 490. Available at: https://doi.org/10.1186/s12936-015-1014-7.

Milner, D.A. (2018) “Malaria pathogenesis,” *Cold Spring Harbor Perspectives in Medicine*, 8(1). Available at: https://doi.org/10.1101/cshperspect.a025569.

Mingot, J.-M. *et al.* (2004) “Exportin 7 defines a novel general nuclear export pathway,” *The EMBO Journal*, 23(16), pp. 3227–3236. Available at: https://doi.org/10.1038/sj.emboj.7600338.

Mitra, P. *et al.* (2015) “ Functional dissection of proliferating-cell nuclear antigens (1 and 2) in human malarial parasite Plasmodium falciparum: possible involvement in DNA replication and DNA damage response ,” *Biochemical Journal*, 470(1), pp. 115–129. Available at: https://doi.org/10.1042/bj20150452.

Mogollon, C.M. *et al.* (2016) “Rapid Generation of Marker-Free P. falciparum Fluorescent Reporter Lines Using Modified CRISPR/Cas9 Constructs and Selection Protocol,” *PLOS ONE*, 11(12), p. e0168362. Available at: https://doi.org/10.1371/JOURNAL.PONE.0168362.

Moldovan, G.-L., Pfander, B. and Jentsch, S. (2007) “PCNA, the Maestro of the Replication Fork,” *Cell*, 129(4), pp. 665–679. Available at: https://doi.org/10.1016/j.cell.2007.05.003.

Moras, M., Lefevre, S.D. and Ostuni, M.A. (2017) “From erythroblasts to mature red blood cells: Organelle clearance in mammals,” *Frontiers in Physiology*, 8(DEC), p. 1076. Available at: https://doi.org/10.3389/FPHYS.2017.01076/BIBTEX.

Moxon, C.A. *et al.* (2020) "New Insights into Malaria Pathogenesis," *Annual Review of Pathology: Mechanisms of Disease*, 15(1), pp. 315–343. Available at: https://doi.org/10.1146/annurev-pathmechdis-012419-032640.

Müller, B. *et al.* (2004) "Construction and Characterization of a Fluorescently Labeled Infectious Human Immunodeficiency Virus Type 1 Derivative," *Journal of Virology*, 78(19), p. 10803. Available at: https://doi.org/10.1128/JVI.78.19.10803-10813.2004.

Nair, D.R. *et al.* (2010) "A conserved G_1 regulatory circuit promotes asynchronous behavior of nuclei sharing a common cytoplasm," *Cell Cycle*, 9(18), pp. 3795–3803. Available at: https://doi.org/10.4161/cc.9.18.12999.

Naryzhny, S.N., Zhao, H. and Lee, H. (2005) "Proliferating Cell Nuclear Antigen (PCNA) May Function as a Double Homotrimer Complex in the Mammalian Cell," *Journal of Biological Chemistry*, 280(14), pp. 13888–13894. Available at: https://doi.org/10.1074/jbc.M500304200.

Natsume, T. *et al.* (2013) "Kinetochores coordinate pericentromeric cohesion and early DNA replication by Cdc7-Dbf4 kinase recruitment," *Molecular Cell*, 50(5), pp. 661–674. Available at: https://doi.org/10.1016/j.molcel.2013.05.011.

Ndwiga, L. *et al.* (2021) "A review of the frequencies of Plasmodium falciparum Kelch 13 artemisinin resistance mutations in Africa," *International journal for parasitology. Drugs and drug resistance*, 16, pp. 155–161. Available at: https://doi.org/10.1016/J.IJPDDR.2021.06.001.

Nguyen Ba, A.N. *et al.* (2009) "NLStradamus: A simple Hidden Markov Model for nuclear localization signal prediction," *BMC Bioinformatics*, 10(1), p. 202. Available at: https://doi.org/10.1186/1471-2105-10-202.

de Niz, M. *et al.* (2017) "Progress in imaging methods: Insights gained into Plasmodium biology," *Nature Reviews Microbiology*. Nature Publishing Group, pp. 37–54. Available at: https://doi.org/10.1038/nrmicro.2016.158.

Nosten, F. and White, N.J. (2007) "Artemisinin-Based Combination Treatment of Falciparum Malaria." Available at: https://www.ncbi.nlm.nih.gov/books/NBK1713/ (Accessed: August 13, 2022).

O'Donnell, R.A. *et al.* (2001) "Antibodies against merozoite surface protein (MSP)-119 are a major component of the invasion-inhibitory response in individuals immune to malaria," *Journal of Experimental Medicine*, 193(12), pp. 1403–1412. Available at: https://doi.org/10.1084/jem.193.12.1403.

Olotu, A. *et al.* (2016) "Seven-Year Efficacy of RTS,S/AS01 Malaria Vaccine among Young African Children," *New England Journal of Medicine*, 374(26), pp. 2519–2529. Available at: https://doi.org/10.1056/NEJMoa1515257.

O'Regan, L., Blot, J. and Fry, A.M. (2007) "Mitotic regulation by NIMA-related kinases," *Cell Division*, 2(1), p. 25. Available at: https://doi.org/10.1186/1747-1028-2-25.

Outlaw, D.C. and Ricklefs, R.E. (2011) "Rerooting the evolutionary tree of malaria parasites," *Proceedings of the National Academy of Sciences of the United States of America*, 108(32), pp. 13183–13187. Available at: https://doi.org/10.1073/pnas.1109153108.

Packard, R.M. (2011) *The Making of a Tropical Disease : A Short History of Malaria*. 1st edition.

Panchal, M. *et al.* (2014) "Plasmodium falciparum signal recognition particle components and anti-parasitic effect of ivermectin in blocking nucleo-cytoplasmic shuttling of SRP," *Cell Death and Disease*, 5(1), p. e994. Available at: https://doi.org/10.1038/cddis.2013.521.

Pappas, G., Kiriaze, I.J. and Falagas, M.E. (2008) "Insights into infectious disease in the era of Hippocrates," *International Journal of Infectious Diseases*. Elsevier, pp. 347–350. Available at: https://doi.org/10.1016/j.ijid.2007.11.003.

Patterson, S. *et al.* (2002) “Molecular characterization and expression of an alternate proliferating cell nuclear antigen homologue, PfPCNA2, in Plasmodium falciparum,” *Biochemical and Biophysical Research Communications*, 298(3), pp. 371–376. Available at: https://doi.org/10.1016/S0006-291X(02)02436-1.

Paul, F. *et al.* (1981) “SEPARATION OF MALARIA-INFECTED ERYTHROCYTES FROM WHOLE BLOOD: USE OF A SELECTIVE HIGH-GRADIENT MAGNETIC SEPARATION TECHNIQUE,” *The Lancet*, 318(8237), pp. 70–71. Available at: https://doi.org/10.1016/S0140-6736(81)90414-1.

Pease, B.N. *et al.* (2013) “Global analysis of protein expression and phosphorylation of three stages of Plasmodium falciparum intraerythrocytic development,” *Journal of proteome research*, 12(9), pp. 4028–4045. Available at: https://doi.org/10.1021/PR400394G.

Pegoraro, S. *et al.* (2017) “SC83288 is a clinical development candidate for the treatment of severe malaria,” *Nature Communications*, 8. Available at: https://doi.org/10.1038/NCOMMS14193.

Peng, D. and Tarleton, R. (2015) “EuPaGDT: a web tool tailored to design CRISPR guide RNAs for eukaryotic pathogens,” *Microbial Genomics*, 1(4). Available at: https://doi.org/10.1099/mgen.0.000033.

Perrin, A.J. *et al.* (2021) “Malaria Parasite Schizont Egress Antigen-1 Plays an Essential Role in Nuclear Segregation during Schizogony,” *mBio*, 12(2). Available at: https://doi.org/10.1128/mBio.03377-20.

Petryk, N. *et al.* (2016) “Replication landscape of the human genome,” *Nature communications*, 7. Available at: https://doi.org/10.1038/NCOMMS10208.

Pollitt, L.C. *et al.* (2010) “Investigating the evolution of apoptosis in malaria parasites: The importance of ecology,” *Parasites and Vectors*, 3(1), pp. 1–13. Available at: https://doi.org/10.1186/1756-3305-3-105/FIGURES/5.

Ponnudurai, T., Leeuwenberg, A. and Meuwissen, J. (1981) “Chloroquine sensitivity of isolates of Plasmodium falciparum adapted to in vitro culture.,” *undefined* [Preprint].

Pradhan, S. *et al.* (2019) “Molecular characterization and expression profile of an alternate proliferating cell nuclear antigen homolog PbPCNA2 in Plasmodium berghei,” *IUBMB Life*, 71(9), pp. 1293–1301. Available at: https://doi.org/10.1002/iub.2036.

Read, M. *et al.* (1993) “Microtubular organization visualized by immunofluorescence microscopy during erythrocytic schizogony in Plasmodium falciparum and investigation of post-translational modifications of parasite tubulin,” *Parasitology*, 106(3), pp. 223–232. Available at: https://doi.org/10.1017/S0031182000075041.

Reilly, H.B. *et al.* (2007) “Quantitative dissection of clone-specific growth rates in cultured malaria parasites,” *International Journal for Parasitology*, 37, pp. 1599–1607. Available at: https://doi.org/10.1016/j.ijpara.2007.05.003.

Reininger, L. *et al.* (2011) “An essential Aurora-related kinase transiently associates with spindle pole bodies during Plasmodium falciparum erythrocytic schizogony,” *Molecular Microbiology*, 79(1), pp. 205–221. Available at: https://doi.org/10.1111/j.1365-2958.2010.07442.x.

Ribaut, C. *et al.* (2008) “Concentration and purification by magnetic separation of the erythrocytic stages of all human Plasmodium species,” *Malaria Journal*, 7. Available at: https://doi.org/10.1186/1475-2875-7-45.

Robbins, J.A. *et al.* (2017) “The Malaria Parasite Cyclin H Homolog PfCyc1 Is Required for Efficient Cytokinesis in Blood-Stage *Plasmodium falciparum*,” *mBio*, 8(3). Available at: https://doi.org/10.1128/mBio.00605-17.

le Roch, K. *et al.* (2000) “Activation of a Plasmodium falciparum cdc2-related kinase by heterologous p25 and cyclin H. Functional characterization of a P. Falciparum cyclin homologue,”

Journal of Biological Chemistry, 275(12), pp. 8952–8958. Available at: https://doi.org/10.1074/jbc.275.12.8952.

Roques, M. *et al.* (2015) "Plasmodium P-Type Cyclin CYC3 Modulates Endomitotic Growth during Oocyst Development in Mosquitoes," *PLoS Pathogens*, 11(11). Available at: https://doi.org/10.1371/journal.ppat.1005273.

Ross, R. (1897) "On some peculiar pigmented cells found in two mosquitos fed on malarial blood," *British Medical Journal*, 2(1929), pp. 1786–1788. Available at: https://doi.org/10.1136/bmj.2.1929.1786.

Rougeron, V. *et al.* (2022) "A population genetic perspective on the origin, spread and adaptation of the human malaria agents Plasmodium falciparum and Plasmodium vivax," *FEMS Microbiology Reviews*, 46(1), pp. 1–24. Available at: https://doi.org/10.1093/FEMSRE/FUAB047.

Rudlaff, R.M. *et al.* (2019) "An essential contractile ring protein controls cell division in Plasmodium falciparum," *Nature Communications*, 10(1). Available at: https://doi.org/10.1038/s41467-019-10214-z.

Rudlaff, R.M. *et al.* (2020) "Three-dimensional ultrastructure of Plasmodium falciparum throughout cytokinesis," *PLOS Pathogens*, 16(6). Available at: https://doi.org/10.1371/journal.ppat.1008587.

Sachs, J. and Malaney, P. (2002) "The economic and social burden of malaria," *Nature*. Nature Publishing Group, pp. 680–685. Available at: https://doi.org/10.1038/415680a.

Sakaue-Sawano, A. *et al.* (2008) "Visualizing Spatiotemporal Dynamics of Multicellular Cell-Cycle Progression," *Cell*, 132(3), pp. 487–498. Available at: https://doi.org/10.1016/j.cell.2007.12.033.

Sato, S. (2021) "Plasmodium—a brief introduction to the parasites causing human malaria and their basic biology," *Journal of Physiological Anthropology*, 40(1), pp. 1–13. Available at: https://doi.org/10.1186/S40101-020-00251-9/TABLES/1.

Schindelin, J. *et al.* (2012) "Fiji: An open-source platform for biological-image analysis," *Nature Methods*, pp. 676–682. Available at: https://doi.org/10.1038/nmeth.2019.

Schrecker, M. *et al.* (2022) "Multistep loading of a DNA sliding clamp onto DNA by replication factor C," *eLife*, 11. Available at: https://doi.org/10.7554/eLife.78253.

Sennerstam, R. and Strömberg, J.O. (1984) "A comparative study of the cell cycles of nullipotent and multipotent embryonal carcinoma cell lines during exponential growth," *Developmental biology*, 103(1), pp. 221–229. Available at: https://doi.org/10.1016/0012-1606(84)90023-X.

Sen, O., Saurin, A.T. and Higgins, J.M.G. (2018) "The live cell DNA stain SiR-Hoechst induces DNA damage responses and impairs cell cycle progression," *Scientific Reports*, 8(1), pp. 1–8. Available at: https://doi.org/10.1038/s41598-018-26307-6.

Seydel, K.B. *et al.* (2015) "Brain Swelling and Death in Children with Cerebral Malaria," *New England Journal of Medicine*, 372(12), pp. 1126–1137. Available at: https://doi.org/10.1056/nejmoa1400116.

Sharma, R. *et al.* (2018) "Identification of a novel trafficking pathway exporting a replication protein, Orc2 to nucleus via classical secretory pathway in Plasmodium falciparum," *Biochimica et Biophysica Acta - Molecular Cell Research*, 1865(5), pp. 817–829. Available at: https://doi.org/10.1016/j.bbamcr.2018.03.003.

Shcherbakova, D.M. *et al.* (2016) "Bright monomeric near-infrared fluorescent proteins as tags and biosensors for multiscale imaging," *Nature Communications 2016 7:1*, 7(1), pp. 1–12. Available at: https://doi.org/10.1038/ncomms12405.

Sheriff, O. *et al.* (2021) "<scp> *Plasmodium falciparum* </scp> replication factor C subunit 1 is involved in genotoxic stress response," *Cellular Microbiology*, 23(2). Available at: https://doi.org/10.1111/cmi.13277.

Shiomi, Y. and Nishitani, H. (2017) "Control of genome integrity by RFC complexes; conductors of PCNA loading onto and unloading from chromatin during DNA replication," *Genes*, 8(2). Available at: https://doi.org/10.3390/genes8020052.

Siddiqui, F.A., Liang, X. and Cui, L. (2021) "Plasmodium falciparum resistance to ACTs: Emergence, mechanisms, and outlook," *International journal for parasitology. Drugs and drug resistance*, 16, pp. 102–118. Available at: https://doi.org/10.1016/J.IJPDDR.2021.05.007.

Simon, C.S. *et al.* (2021) "An extended DNA-free intranuclear compartment organizes centrosome microtubules in malaria parasites," *Life Science Alliance*, 4(11), p. e202101199. Available at: https://doi.org/10.26508/lsa.202101199.

Simon, C.S., Stürmer, V.S. and Guizetti, J. (2021) "How Many Is Enough? - Challenges of Multinucleated Cell Division in Malaria Parasites," *Frontiers in Cellular and Infection Microbiology*, 11. Available at: https://doi.org/10.3389/fcimb.2021.658616.

Singh, M. *et al.* (2021) "Plasmodium's journey through the Anopheles mosquito: A comprehensive review," *Biochimie*. Elsevier B.V., pp. 176–190. Available at: https://doi.org/10.1016/j.biochi.2020.12.009.

Sinka, M.E. (2013) "Global Distribution of the Dominant Vector Species of Malaria," in *Anopheles mosquitoes - New insights into malaria vectors*. InTech. Available at: https://doi.org/10.5772/54163.

Smith, R.C. and Barillas-Mury, C. (2016) "Plasmodium Oocysts: Overlooked Targets of Mosquito Immunity," *Trends in Parasitology*, 32(12), pp. 979–990. Available at: https://doi.org/10.1016/j.pt.2016.08.012.

Smith, R.C., Vega-Rodríguez, J. and Jacobs-Lorena, M. (2014) "The Plasmodium bottleneck: Malaria parasite losses in the mosquito vector," *Memorias do Instituto Oswaldo Cruz*, 109(5), pp. 644–661. Available at: https://doi.org/10.1590/0074-0276130597.

Smythe, E. and Ayscough, K.R. (2003) "The Ark1/Prk1 family of protein kinases. Regulators of endocytosis and the actin cytoskeleton," *EMBO Reports*. European Molecular Biology Organization, pp. 246–251. Available at: https://doi.org/10.1038/sj.embor.embor776.

Solyakov, L. *et al.* (2011) "Global kinomic and phospho-proteomic analyses of the human malaria parasite Plasmodium falciparum," *Nature communications*, 2(1). Available at: https://doi.org/10.1038/NCOMMS1558.

Spudich, J.L. and Koshland, D.E. (1976) "Non-genetic individuality: chance in the single cell," *Nature 1976 262:5568*, 262(5568), pp. 467–471. Available at: https://doi.org/10.1038/262467a0.

Stanojcic, S. *et al.* (2017) "Single-molecule analysis reveals that DNA replication dynamics vary across the course of schizogony in the malaria parasite Plasmodium falciparum," *Scientific Reports*, 7(1), p. 4003. Available at: https://doi.org/10.1038/s41598-017-04407-z.

Strack, R. (2021) "Organic dyes for live imaging," *Nature Methods 2021 18:1*, 18(1), pp. 30–30. Available at: https://doi.org/10.1038/s41592-020-01032-z.

Sturm, A. *et al.* (2006) "Manipulation of host hepatocytes by the malaria parasite for delivery into liver sinusoids," *Science*, 313(5791), pp. 1287–1290. Available at: https://doi.org/10.1126/science.1129720.

Sun, Q. *et al.* (2013) "Nuclear export inhibition through covalent conjugation and hydrolysis of Leptomycin B by CRM1," *Proceedings of the National Academy of Sciences*, 110(4), pp. 1303–1308. Available at: https://doi.org/10.1073/pnas.1217203110.

Sun, Q. *et al.* (2016) “Inhibiting cancer cell hallmark features through nuclear export inhibition,” *Signal Transduction and Targeted Therapy*. Springer Nature, p. 16010. Available at: https://doi.org/10.1038/sigtrans.2016.10.

Talia, S. di *et al.* (2007) “The effects of molecular noise and size control on variability in the budding yeast cell cycle,” *Nature*, 448(7156), pp. 947–951. Available at: https://doi.org/10.1038/NATURE06072.

Tanabe, K. *et al.* (2010) “Plasmodium falciparum accompanied the human expansion out of Africa,” *Current biology : CB*, 20(14), pp. 1283–1289. Available at: https://doi.org/10.1016/J.CUB.2010.05.053.

Tanaka, S. *et al.* (2011) “Origin Association of Sld3, Sld7, and Cdc45 Proteins Is a Key Step for Determination of Origin-Firing Timing,” *Current Biology*, 21(24), pp. 2055–2063. Available at: https://doi.org/10.1016/j.cub.2011.11.038.

Tan, M.S.Y. and Blackman, M.J. (2021) “Malaria parasite egress at a glance,” *Journal of Cell Science*, 134(5). Available at: https://doi.org/10.1242/jcs.257345.

Tavolieri, M. v. *et al.* (2019) “A novel overlapping NLS/NES region within the PH domain of Rho Guanine Nucleotide Exchange Factor (RGNEF) regulates its nuclear-cytoplasmic localization,” *European Journal of Cell Biology*, 98(1), pp. 27–35. Available at: https://doi.org/10.1016/j.ejcb.2018.11.001.

Taylor, T.E. *et al.* (2004) “Differentiating the pathologies of cerebral malaria by postmortem parasite counts,” *Nature Medicine*, 10(2), pp. 143–145. Available at: https://doi.org/10.1038/nm986.

Tewari, R. *et al.* (2010) “The systematic functional analysis of plasmodium protein kinases identifies essential regulators of mosquito transmission,” *Cell Host and Microbe*, 8(4), pp. 377–387. Available at: https://doi.org/10.1016/j.chom.2010.09.006.

Tewari, S.G. *et al.* (2019) “Short-term metabolic adjustments in Plasmodium falciparum counter hypoxanthine deprivation at the expense of long-term viability,” *Malaria Journal*, 18(1), pp. 1–13. Available at: https://doi.org/10.1186/S12936-019-2720-3/FIGURES/8.

Timney, B.L. *et al.* (2016) “Simple rules for passive diffusion through the nuclear pore complex,” *Journal of Cell Biology*, 215(1), pp. 57–76. Available at: https://doi.org/10.1083/jcb.201601004.

Tosheva, K.L. *et al.* (2020) “Between life and death: Strategies to reduce phototoxicity in super-resolution microscopy,” *Journal of Physics D: Applied Physics*. Institute of Physics Publishing, p. 163001. Available at: https://doi.org/10.1088/1361-6463/ab6b95.

Trager, W. and Jensen, J.B. (1976) “Human malaria parasites in continuous culture,” *Science*, 193(4254), pp. 673–675. Available at: https://doi.org/10.1126/science.781840.

Treeck, M. *et al.* (2011) “The phosphoproteomes of Plasmodium falciparum and Toxoplasma gondii reveal unusual adaptations within and beyond the parasites’ boundaries,” *Cell host & microbe*, 10(4), pp. 410–419. Available at: https://doi.org/10.1016/J.CHOM.2011.09.004.

Tyson, C.B., Lord, P.G. and Wheals, A.E. (1979) “Dependency of size of Saccharomyces cerevisiae cells on growth rate,” *Journal of bacteriology*, 138(1), pp. 92–98. Available at: https://doi.org/10.1128/JB.138.1.92-98.1979.

Vaughan, A.M. *et al.* (2012) “Complete Plasmodium falciparum liver stage development in liver-chimeric mice,” *Journal of Clinical Investigation*, 122(10), pp. 3618–3628. Available at: https://doi.org/10.1172/JCI62684.

Vaughan, A.M. and Kappe, S.H.I. (2017) “Malaria parasite liver infection and exoerythrocytic biology,” *Cold Spring Harbor Perspectives in Medicine*, 7(6). Available at: https://doi.org/10.1101/cshperspect.a025486.

Venugopal, K. *et al.* (2020) “Plasmodium asexual growth and sexual development in the haematopoietic niche of the host,” *Nature Reviews Microbiology*, 18(3), pp. 177–189. Available at: https://doi.org/10.1038/s41579-019-0306-2.

Waga, S. and Stillman, B. (1998) “The DNA replication fork in eukaryotic cells,” *Annual Review of Biochemistry*. Annual Reviews 4139 El Camino Way, P.O. Box 10139, Palo Alto, CA 94303-0139, USA , pp. 721–751. Available at: https://doi.org/10.1146/annurev.biochem.67.1.721.

Wagner, J.C. *et al.* (2014) “Efficient CRISPR-Cas9-mediated genome editing in Plasmodium falciparum,” *Nature Methods*, 11(9), pp. 915–918. Available at: https://doi.org/10.1038/nmeth.3063.

Waldecker, M. *et al.* (2017) “Differential time-dependent volumetric and surface area changes and delayed induction of new permeation pathways in *P. falciparum* -infected haemoglobinopathic erythrocytes,” *Cellular Microbiology*, 19(2), p. e12650. Available at: https://doi.org/10.1111/cmi.12650.

Wang, A.Y. and Liu, H. (2019) “The past, present, and future of CRM1/XPO1 inhibitors,” *Stem Cell Investigation*. AME Publishing Company. Available at: https://doi.org/10.21037/sci.2019.02.03.

Wang, L. *et al.* (2019) “A general strategy to develop cell permeable and fluorogenic probes for multicolour nanoscopy,” *Nature Chemistry 2019 12:2*, 12(2), pp. 165–172. Available at: https://doi.org/10.1038/s41557-019-0371-1.

Wang, Y.-L. *et al.* (2022) “The Functions of PCNA in Tumor Stemness and Invasion,” *International Journal of Molecular Sciences*, 23(10), p. 5679. Available at: https://doi.org/10.3390/ijms23105679.

Wannier, T.M. *et al.* (2018) “Monomerization of far-red fluorescent proteins,” *Proceedings of the National Academy of Sciences of the United States of America*, 115(48), pp. E11294–E11301. Available at: https://doi.org/10.1073/PNAS.1807449115/-/DCSUPPLEMENTAL.

Wassmer, S.C. *et al.* (2015) “Investigating the pathogenesis of severe malaria: A multidisciplinary and cross-geographical approach,” *American Journal of Tropical Medicine and Hygiene*, 93(3_Suppl), pp. 42–56. Available at: https://doi.org/10.4269/ajtmh.14-0841.

Westerveld, A. and Freeke, M.A. (1971) “Cell cycle of multinucleate cells after cell fusion,” *Experimental Cell Research*, 65(1), pp. 140–144. Available at: https://doi.org/10.1016/S0014-4827(71)80059-9.

Whitfield, J. (2002) “Portrait of a serial killer,” *Nature* [Preprint]. Available at: https://doi.org/10.1038/news021001-6.

Wissing, F. *et al.* (2002) “Illumination of the malaria parasite Plasmodium falciparum alters intracellular pH. Implications for live cell imaging,” *Journal of Biological Chemistry*, 277(40), pp. 37747–37755. Available at: https://doi.org/10.1074/jbc.M204845200.

World Health Organisation (2020) *The top 10 causes of death*, *The top 10 causes of death*. Available at: https://www.who.int/news-room/fact-sheets/detail/the-top-10-causes-of-death (Accessed: August 12, 2022).

World Health Organisation (2021) *World malaria report 2021*, *World Health Organisation*. Available at: https://www.who.int/teams/global-malaria-programme/reports/world-malaria-report-2021 (Accessed: August 12, 2022).

Wu, Y. *et al.* (1995) “Transfection of Plasmodium falciparum within human red blood cells,” *Proceedings of the National Academy of Sciences of the United States of America*, 92(4), pp. 973–977. Available at: https://doi.org/10.1073/pnas.92.4.973.

Xu, D. *et al.* (2015) “LocNES: a computational tool for locating classical NESs in CRM1 cargo proteins,” *Bioinformatics*, 31(9), pp. 1357–1365. Available at: https://doi.org/10.1093/bioinformatics/btu826.

Xu, D., Farmer, A. and Chook, Y.M. (2010) “Recognition of nuclear targeting signals by Karyopherin-β proteins,” *Current opinion in structural biology*, 20(6), p. 782. Available at: https://doi.org/10.1016/J.SBI.2010.09.008.

Yeeles, J.T.P. *et al.* (2015) “Regulated eukaryotic DNA replication origin firing with purified proteins,” *Nature*, 519(7544), pp. 431–435. Available at: https://doi.org/10.1038/nature14285.

Zetterberg, A. and Larsson, O. (1985) “Kinetic analysis of regulatory events in G1 leading to proliferation or quiescence of Swiss 3T3 cells,” *Proceedings of the National Academy of Sciences of the United States of America*, 82(16), pp. 5365–5369. Available at: https://doi.org/10.1073/PNAS.82.16.5365.

Zupa, E. *et al.* (2020) “The cryo-EM structure of a γ-TuSC elucidates architecture and regulation of minimal microtubule nucleation systems,” *Nature Communications*, 11(1), pp. 1–12. Available at: https://doi.org/10.1038/s41467-020-19456-8.

8 Acknowledgements

A PhD is always just as good as the environment it was created in, and I was lucky enough to find myself in an amazing one. There are no words to express my gratitude to the many people that made this experience what it was, so the only thing I can offer is my heartfelt thank you.

First and foremost, I want to say thank you to Dr. Markus Ganter for giving me a place and an opportunity to do my PhD. Markus, thank you for all the coffees and walks and scientific discussions. Thank you for your patience and your advice on many things big and small, and thank you for always supporting me and still reining me back in whenever I was spinning out of control with too many ideas and things I want to do. You showed me what it is to be a good scientist and a good group leader, and I will carry these lessons with me wherever I go. I would not have wanted anyone else as my Doktorvater.

I also want to thank Freddy Frischknecht for his open door, all his support, honesty and guidance, and for his unending enthusiasm for all things strange in this world. My official supervisor Prof. Dr. Michael Lanzer I wish to thank for all the input and support over the years to help me be a better scientist. A big thank you also goes to Dr. Julien Guizetti, for all his advice and the many discussion about parasite biology, and of course for sharing his passion for imaging. Over the years I also received some great support and advice during my TAC meeting from Prof. Dr. Frauke Melchior and Prof. Dr. Julien Bethúne, which I am very grateful for. I also want to thank Dr. Marina Lusic and Dr. Gautam Dey for readily agreeing to be in my PhD Defense committee.

A big part of my thesis was centred around microscopy which would have been only a fraction of the fun and success if it hadn't been for Dr. Vibor Laketa and Dr. Sylvia Olberg, who run the infectious disease imaging platform. Thank you for you open ears and your support in any situation. Likewise, none of the EM data would exist without the work of Dr. Charlotta Funaya, who I am very grateful to. Another big thank you goes to Miriam and Sandra, for all their support on the administrative side of things, and to Nadine and Ina, who were always ready to help me in the lab, even when they didn't have to. The same goes to the many members of the Frischknecht and Fackler Lab, who always lend me a helping hand whenever I needed it.

We would have only discovered half as much as we did about *Plasmodium* schizogony if it weren't for our great collaboration partners Patrick Binder and Dr. Nils Becker from the labs of Prof. Dr. Ulrich Schwarz and Prof. Dr. Thomas Höfer. Thank you for all of your patience and help, and the many great discussion about the workings of *Plasmodium* replication. I also want to thank Prof. Dr. Ulrich Schwarz for his many helpful suggestions on my project.

To Marta Machado, my partner in crime in the Ganter lab: obrigada por todos os bons tempos! Let's keep bombating together as much as we can. Then there are Caro, Yannik, Anja, and all the past and present people of the Ganter and Guizetti labs: Wendy, Aiste, Laura, Annika, Maruska, Katharina, Jana, Violetta, Alex, Ann-Kathrin, Johanna, Chris, Vanessa, Nic and Marius and everyone I may have

forgotten. Thank you for all the fun times working together, the trips to the zoo, the climbing forest and the river, the summer barbecues and the many other things we did together. Thanks to you all, I had a great time in the lab every day and you guys even made lab cleaning fun.

I was incredible fortunate that I had many great, diligent and hardworking students who supported me during my PhD. I want to thank them all; Mariya and Katharina for their work on trying to find exportin-1 cargo proteins, Jana for generating all the PCNA1 peptides, Violetta for her work on endogenously tagging PCNA1 and her informatics skills, and Ju for his amazing work in creating beautiful EM tomograms of our *Plasmodium* schizonts. A big thank you also goes to Laura for her tireless work on getting the exportin-1 inhibition system running. Likewise, a special thank you goes to Wendy for being my first student and still coming back for her Master thesis, and for all her amazing work on establishing the pull-downs; and to Aiste, who stuck with me from the beginning and shared all the fun and the pain and the glory of the many PCNA1 mutants, and who established the exportin-1 inhibition system in *P. falciparum*. Aiste, you were my rock in the lab and so much would not have been possible without you.

A PhD can be all-consuming, and it would have never worked out the way it did without the support of the people around me. Caro, thank you for all the walks and the talks and the fun times together; let's have many more. Annika, thank you for your enthusiasm and optimism and your friendship. Yes, we should definitely do more together! To my sport buddies, Cindy, Swetha and Samy, thank you guys for all the good games, the chats and the tasty food together. Any weather and time, I am always up to for a game with you guys. Likewise: ladies, to many more years of climbing and dining together. Although we may be separated by many hundreds of kilometres, I also want to thank Kai for sharing the pain and the glory of doing a PhD. A special shout-out goes to my brother Friedrich and his wife Kati for always providing support and cat photos whenever I need them. And finally, Franzi, thank you! Thank you for proof-reading this thesis, and being there to calm me down when my PhD-brain starts going crazy and thank you for just being an all-around amazing person and friend.

And then there are the people who make you who you are and have been with you every step of the way. Thank you Henrik and Mary and Christin. Thank you for being there for me whenever I need you, and for whatever I may need. I cherish every memory we make together. With you all I look forward to the future.

I would not be here altogether if it weren't for my parents. Mama und Papa, ihr habt mir die Welt gegeben. Ohne euch wäre nichts von alledem möglich gewesen und das Wissen, dass ihr hinter mir steht hat mir bei jedem Schritt auf dem Weg geholfen. Von euch habe ich gelernt, dass es immer das richtige ist, seinem Herzen zu folgen, und dass die Dinge am Ende immer gut ausgehen, egal wohin das Leben einen führt. Ich weiß, ich kann mich auf eure Liebe und eure Unterstützung und eure Hilfe in jeder Situation des Lebens verlassen. Der größte Dank gebührt euch.

9 Supplements

Table S1 *Duration of nuclear multiplication and nuclear cycle phases. Duration, mean duration; StD, standard deviation; n, number of data points.*

Cycle phase	Duration (min)	StD (min)	N
Total nuclear multiplication (Start S_1 to egress)	849	54	28
Total replication time (Start S_1 to last end S-phase)	694	58	30
End last S-phase to egress	163	33	64
S-phase S_1	54	19	54
S-phase to nuclear division SD_1	80	25	63
Nuclear division to S-phase $DS_{2,1}$	33	18	62
Nuclear division to S-phase $DS_{2,2}$	59	33	57
S-phase $S_{2,1}$	40	13	60
S-phase $S_{2,2}$	43	11	57
S-phase to nuclear division $SD_{2,1}$	50	12	36
S-phase to nuclear division $SD_{2,2}$	54	8	24
Nuclear division to S-phase $DS_{3,1}$	22	9	34
Nuclear division to S-phase $DS_{3,2}$	33	16	29
Nuclear division to S-phase $DS_{3,3}$	29	18	15
Nuclear division to S-phase $DS_{3,4}$	42	19	13
S-phase $S_{3,1}$	36	6	30
S-phase $S_{3,2}$	40	9	27
S-phase $S_{3,3}$	43	5	12
S-phase $S_{3,4}$	43	5	6

Table S2 P. falciparum *3D7 proteins containing four or more KxKKKxK motives as identified by the PlasmoDB protein motif finder. Proteins referenced in main text are marked in bold and grey. Spindle pole body protein shown for comparison.*

Gene ID	Product Description	Match Count
PF3D7_0417400	conserved *Plasmodium* protein, unknown function	12
PF3D7_0205000	conserved *Plasmodium* protein, unknown function	7
PF3D7_0419900	phosphatidylinositol 4-kinase, putative	7
PF3D7_0422200	erythrocyte membrane-associated antigen	7
PF3D7_1021700	VPS13 domain-containing protein, putative	7
PF3D7_1406200	transcription elongation factor SPT6, putative	7
PF3D7_0107600	**eukaryotic translation initiation factor 2-alpha kinase 2, putative**	**6**
PF3D7_0724700	bromodomain protein 6, putative	6
PF3D7_0922800	conserved *Plasmodium* protein, unknown function	6
PF3D7_1345400	conserved *Plasmodium* protein, unknown function	6
PF3D7_1444100	conserved *Plasmodium* protein, unknown function	6
PF3D7_0407700	conserved *Plasmodium* protein, unknown function	5
PF3D7_0504700	**centrosomal protein CEP120, putative**	**5**
PF3D7_0615400	ribonuclease, putative	5
PF3D7_0728100	**anaphase-promoting complex subunit 1, putative**	**5**
PF3D7_0728600	RING zinc finger protein, putative	5
PF3D7_0804700	conserved *Plasmodium* protein, unknown function	5
PF3D7_0829500	conserved *Plasmodium* protein, unknown function	5
PF3D7_1223500	conserved *Plasmodium* protein, unknown function	5
PF3D7_1324300	conserved *Plasmodium* membrane protein, unknown function	5
PF3D7_0104300	ubiquitin carboxyl-terminal hydrolase 1, putative	4
PF3D7_0403400	conserved *Plasmodium* protein, unknown function	4
PF3D7_0406500	NYN domain-containing protein, putative	4
PF3D7_0423300	conserved *Plasmodium* protein, unknown function	4
PF3D7_0521300	zinc finger protein, putative	4
PF3D7_0619300	conserved *Plasmodium* protein, unknown function	4
PF3D7_0802600	adenylyl cyclase beta	4

PF3D7_1021800	**schizont egress antigen-1**	**4**
PF3D7_1031600	protein GEXP15	4
PF3D7_1234100	bromodomain protein 5	4
PF3D7_1309200	protein phosphatase PPM6, putative	4
PF3D7_1408700	conserved protein, unknown function	4
PF3D7_1410300	WD repeat-containing protein, putative	4
PF3D7_1417300	cysteine protease ATG4, putative	4
PF3D7_1417600	ookinete surface and oocyst capsule protein OSCP, putative	4
PF3D7_1436100	conserved *Plasmodium* membrane protein, unknown function	4
PF3D7_1450700	conserved *Plasmodium* protein, unknown function	4
PF3D7_1457900	conserved *Plasmodium* protein, unknown function	4
***	***	***
PF3D7_0303500	**spindle pole body protein, putative**	**2**

Table S3 *Proteins enriched in pulldown of crosslinked proteins of* P. falciparum *parasites expressing PCNA1::GFP (sample, n = 1) compared to crosslinked proteins of* P. falciparum *parasites expressing NES2::GFP (controls, n = 2). Enrichment was calculated as mean abundance of a protein in the sample divided by mean abundance of a protein in the controls. GFP tagged sample bait protein PCNA1 is marked in bold and grey.*

Accession Nr.	Product Description	Enrichment
A0A144A0U2	40S ribosomal protein S30	25.11285
C0H5G3	60S ribosomal protein L18-2, putative	12.52684
Q8I1W9	Apical sushi protein	Not in control
Q8IBD0	CRA domain-containing protein, putative	12.43774
O96150	DNA-directed RNA polymerase II 16 kDa subunit, putative	74.37924
Q8IIR7	Endoplasmic reticulum-resident calcium binding protein	28.18584
Q8ILB0	ER membrane protein complex subunit 4	17.9831
Q8IEL0	ER membrane protein complex subunit 7, putative	10.22001
Q8I289	Heptatricopeptide repeat and RAP domain-containing protein, putative	11.29555
Q8IBV7	Histone H2B	13.98544
Q8IIV1	Histone H2B	13.94565
Q8IIV2	Histone H4	15.52191
C0H5L9	Membrane associated histidine-rich protein 1	16.35128
Q8I1Y0	Merozoite surface protein P41	10.16187
Q8ILB6	Mitochondrial acidic protein MAM33, putative	16.15238
Q8IKL8	MORN repeat protein, putative	25.44281
Q8I488	Parasite-infected erythrocyte surface protein	17.1376
Q8IIK8	Peptidyl-prolyl cis-trans isomerase	10.46652
O96287	Pfmc-2TM Maurer's cleft two transmembrane protein	Not in control
C6KSL5	Pfmc-2TM Maurer's cleft two transmembrane protein	88.84112
Q8IIY8	Pfmc-2TM Maurer's cleft two transmembrane protein	72.86341
Q8I207	PRESAN domain-containing protein	15.30598
Q8I206	PRESAN domain-containing protein	11.22888
Q8IFM0	PRESAN domain-containing protein	30.86775
Q8I3F1	PRESAN domain-containing protein	37.78014
P61074	**Proliferating cell nuclear antigen 1**	**305.856**
Q7K6A9	Proteasome subunit beta	Not in control
Q8IKK4	Replication factor C subunit 3	50.12952
Q8I512	Replication factor C subunit 4	62.04825
Q8IIQ1	Replication factor C subunit 5	32.18041
Q8I4R5	Rhoptry neck protein 3	104.7443
O96202	Ribosomal protein L12, mitochondrial, putative	12.27929
C0H4A6	Ribosomal protein L15	15.24546
A0A5K1K870	Ribosome-interacting GTPase 1, putative	41.86428
Q8IK38	Rifin	Not in control

Q8IEK9	RNA-binding protein, putative	38.78771
Q8I3Q6	Single-stranded DNA-binding protein, putative	14.12684
O96265	Small nuclear ribonucleoprotein Sm D2	Not in control
C0H5I5	Splicing factor subunit	12.26713
Q8IDP4	Thioredoxin 2	21.09733
Q8ILA1	Translocon component PTEX150	31.34986
Q8I259	Uncharacterized protein	Not in control
O96191	Uncharacterized protein	40.50986
Q8I490	Uncharacterized protein	12.43855
Q8IDG9	Uncharacterized protein	18.19378
Q8ILY8	Uncharacterized protein	19.95216

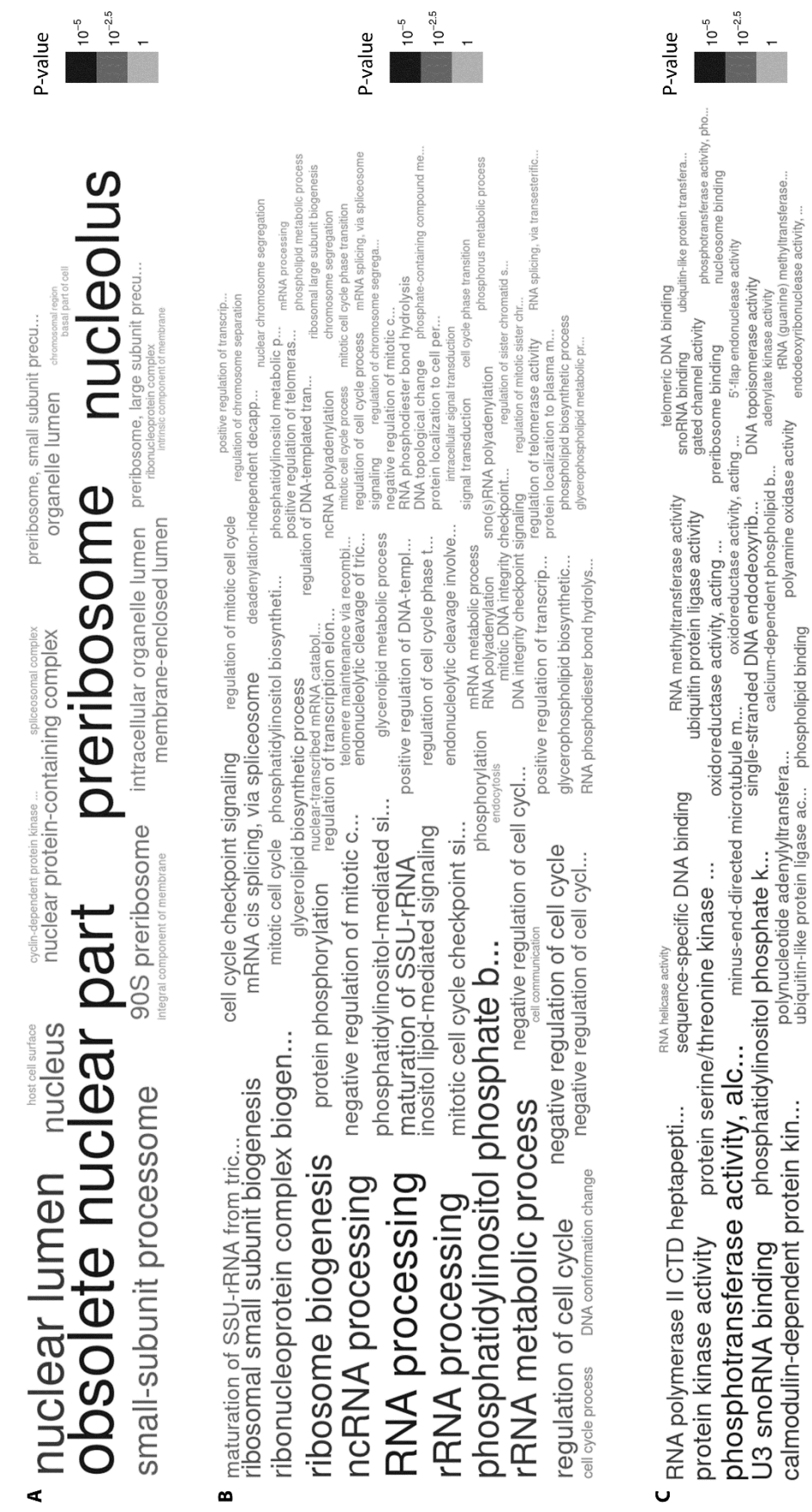

Figure S1 GO-Term enrichment for proteins containing the motif KxKKKxK. *(A) GO-Term enrichment for the cellular component. (B) GO-Term enrichment for biological processes (C) GO-Term enrichment for molecular functions. GO-term enrichment computed on* P. falciparum *3D7 using computed and curated association with a P-value cutoff of 0.05.*